

Justus-Liebig-Universität Giessen
Institut für Anorganische und Analytische Chemie



Reaction behavior of iron- and copper- complexes with tripodal ligands

Inaugural-Dissertation

zur Erlangung des Doktorgrades der Naturwissenschaften im Fachbereich Biologie und
Chemie der Justus-Liebig-Universität Gießen

Justus-Liebig-Universität Giessen
Institut für Anorganische und Analytische Chemie



Reaction behavior of iron- and copper- complexes with tripodal ligands

Inaugural-Dissertation

Zur Erlangung des Doktorgrades der Naturwissenschaften im Fachbereich Biologie und
Chemie der Justus-Liebig-Universität Gießen

vorgelegt von

Sandra Kisslinger

aus

Bautzen

Erstgutachter:

Prof. Dr. S. Schindler

Zweitgutachter:

Prof. Dr. R. Göttlich

Beim Prüfungsamt eingereicht am:

11.06.2012

Tag der mündlichen Prüfung:

22.08.2012

Acknowledgements

The work described in this thesis was carried out between July 2007 and July 2011 at the Institute for Inorganic and Analytical Chemistry at the Justus-Liebig-University of Gießen. My supervisor was Prof. Dr. Siegfried Schindler whom I would like to thank for his excellent guidance, patience and financial support during these years.

Further I would like to thank my lab mates, colleagues and friends Dr. Jörg Müller, Dr. Thomas Nebe, Alexander Beitat, Tobias Hoppe, Melanie Jopp, Dr. Anja Henß, Dr. Sabrina Turba, Lars Valentin, Stefan Schaub, Natascha Kempf, Cornelius Brombach, Janine Will, Sabrina Schäfer, Jennifer Blank, Dr. Jörg Astner, Sabine Löw, Jonathan Becker, Frank Mehlich, Dr. Ildikó Kerezsi, Janina Heck, Janine Capell and Dr. Christian Würtele for the team work and pleasant atmosphere.

I'm very grateful to our cooperation partners and would like to specially acknowledge Prof. Dr. Hans-Jörg Krüger and Dr. Harald Kelm of the Technische Universität Kaiserslautern, Prof. Dr. Franz Renz of the Leibnitz Universität Hannover, Dr. Sylvestre Bonnet of the Leiden Institute of Chemistry and Prof. Dr. Sonja Herres-Pawlis as well as Ramona Wortmann of the Ludwig-Maximilians-Universität München for their various assistances in this work.

For their great support of the X-Ray crystallographic measurements I wish to thank Alexander Beitat, Dr. Harald Kelm, Natascha Kempf, Dr. Olaf Walther, Dr. Christian Würtele, Günter Koch and Dr. Uwe Monkowius. For the SQUID measurements I want to thank Sipeng Zheng.

My thanks further go to the Institute of Inorganic and Analytical Chemistry as well as to the Institute for Organic Chemistry of the Justus-Liebig-University Gießen for their support of this work.

My special thanks go to my friends outside of the university who were always a foothold during these years.

I particularly want to thank my family and my fiancé Mario Kopsch for their never ending patience and great assistance during this time.

„Die Endlosigkeit des wissenschaftlichen Ringens sorgt unablässig dafür, daß dem forschenden Menscheist seine beiden edelsten Antriebe erhalten bleiben und immer wieder von neuem angefacht werden: Die Begeisterung und die Ehrfurcht...“

By
Max Planck
German Physicist (1858 – 1947)

for my family

Table of Contents

Table of Figures.....	II
Tables	III
Used Precursors and Ligands	IV
Abbreviations	V
Inaugural-Dissertation.....	1
1 Introduction	1
1.1 The Element Copper.....	1
1.2 Copper in Biology	1
1.3 The Element Iron.....	2
1.4 Magnetic Properties of Iron	3
1.5 Molecular Magnetism	4
1.6 Spin-Crossover.....	5
1.7 Spin Crossover Compounds as Molecular Switches.....	8
1.8 High- and Low-Spin Complexes within Bioinorganic Chemistry	9
1.9 Tripodal ligands	13
1.10 Projects.....	17
2 Copper Complexes with the Ligand apme	19
2.1 Syntheses and Characterization of Copper Complexes with the Ligand 2-Aminoethyl(2-pyridylmethyl)-1,2-ethanedi-amine (apme)	19
2.2 Synthesis of ligands and complexes.....	21
2.3 Investigation of the solution behavior of 1 and 2	27

2.4	Results of Electrochemistry.....	29
2.5	Results of time resolved UV-Vis Spectroscopy	30
2.6	Summary	32
2.7	Experimental Section	33
2.7.1	Materials and Methods.....	33
2.7.2	Single-Crystal X-ray Structure Determinations	34
2.7.3	Syntheses of Ligand and Complexes	35
3	Ligand Influence of Copper(I) Schiff Base Macrocyclic Complexes	39
3.1	Ligand Influence Over the Formation of Dinuclear [2+2] versus Trinuclear [3+3] CuI Schiff Base Macrocyclic Complexes	39
3.2	Results and Discussion	41
3.2.1	Synthesis of macrocycle components.....	42
3.2.2	Synthesis Metal free [2+2] Macrocyclic Ligands.....	43
3.2.3	Synthesis of CuI complexes.....	44
3.2.4	Solid State Characterization.....	45
3.2.5	NMR spectroscopy.....	49
3.2.6	MS Spectroscopy and the [2+2] vs. [3+3] Evolution Process.....	50
3.3	Conclusions.....	52
3.4	Experimental Section	53
3.4.1	Physical Methods.....	53
3.4.2	Materials and Synthesis.....	54
3.4.3	Ligand Synthesis.....	54
3.4.4	Synthesis of CuI complexes.....	59
3.4.5	X-ray diffraction studies.....	61
4	Open-Chain Copper(I) Complexes	63
4.1	Syntheses, Characterization and Properties of Open-Chain Copper(I) Complexes.....	63
4.2	Results and discussion.....	64
4.2.1	Syntheses and Characterization of L1, [Cu(L1)(CH ₃ CN)]PF ₆ (1) and [Cu ₂ (L1) ₂](ClO ₄) ₂ (2).....	64
4.2.2	Crystallographic Data.....	68
4.2.3	Discussion of the structure dependence on the counterion.....	70

4.2.4	Further variation of the counterions.	72
4.2.5	Investigation of the solution behavior of 1 and 2	73
4.2.6	Electrochemistry.	75
4.2.7	Copper(II) complexes.	76
4.2.8	Investigation of the oxidation reaction.	78
4.2.9	Copper complexes with the ligand L2.	80
4.2.10	Electrochemistry of [Cu(L2)(CH ₃ CN)]PF ₆	82
4.2.11	Investigation of the oxidation reaction of [Cu(L2)(CH ₃ CN)]PF ₆	83
4.2.12	[Cu ₂ (L2) ₂ Cl ₃]PF ₆ x 2 MeOH (6).	83
4.3	Conclusions.	84
4.4	Experimental Section	85
4.4.1	Materials and Methods	85
4.4.2	X-ray Structure Determination of L1 and 1 to 6.	86
4.4.3	Syntheses of Ligands and Complexes.	87
4.4.4	Investigation of the potential hydroxylation reaction of the ligand.	92
4.4.5	Quantitative investigation of H ₂ O ₂ formation upon oxidation.	92
5	Iron(II) complexes of apme-derivates	93
5.1	Synthesis, characterization and properties of iron(II) complexes with a series of tripodal ligands based on the parent ligand tris(2-pyridylmethyl)amine.	93
5.2	Results and Discussion	94
5.2.1	[Fe(imine2-apme)(NCS) ₂] (1)	95
5.2.2	[Fe(apme)(NCS) ₂] (2).	96
5.2.3	[Fe(HMe4apme)(NCS) ₃] (3).	97
5.2.4	[Fe(Me4apme)(NCS) ₂] (4)	98
5.2.5	Möbbsauer spectroscopy of [Fe(Me4apme)(NCS) ₂] (4)	99
5.2.6	Unpublished results: Magnetic susceptibility measurements of [Fe(imine2- apme)(NCS) ₂] (1)	100
5.2.7	Crystallographic Data.	102
5.2.8	IR-Spectroscopy of [Fe(apme)(NCS) ₂], [Fe(imine2-apme)(NCS) ₂], [Fe(Me4apme)(NCS) ₂] and [Fe(TMG2apme)(NCS) ₂]	104
5.3	Conclusions.	105
5.4	Experimental Section	106
5.4.1	Materials and Methods	106
5.4.2	Ligand synthesis.	106
5.4.3	Procedures for the synthesis of iron(II) complexes with the ligands imine2-apme, apme, HMe4apme and Me4apme.	106
5.4.4	X-Ray.	108

5.4.5	Mößbauer Spectroscopy	109
5.4.6	Magnetic susceptibility measurements	109
6	Tmpa related iron(II) complexes with methylene, imine and guanidine groups	110
6.1	Synthesis and Characterization of Iron(II) Thiocyanate Complexes with Derivatives of the Tris(2-pyridylmethyl) amine (tmpa) Ligand	110
6.2	Results and Discussion	113
6.2.1	Syntheses of ligands and complexes.	113
6.2.2	Structural properties of the complexes.	113
6.2.3	Crystallographic Data.	118
6.2.4	IR-Spectroscopy.....	120
6.2.5	Magnetic susceptibility measurements.	122
6.2.6	Mößbauer spectroscopy.	123
6.3	Summary	126
6.4	Experimental Section	126
6.4.1	Materials and Methods.	126
6.4.2	Complex Synthesis.....	129
6.4.3	X-Ray.....	132
6.4.4	Magnetic susceptibility measurements	133
6.4.5	Mößbauer Spectroscopy	133
7	Chelate ring size and spin-crossover in iron(II) complexes	134
7.1	Effect of chelate ring size in iron(II) thiocyanate complexes with tetradentate tripyridyl-alkylamine tripodal ligands	134
7.2	Results and Discussion	135
7.2.1	Synthesis of Ligands and complexes.	135
7.2.2	Mößbauer spectroscopy for [Fe(pmea)(NCS) ₂] (2).....	146
7.2.3	Magnetic susceptibility measurements for (1), (2), (3) and (4)	152
7.2.4	IR-Spectroscopy of 1 , 2 and 3	153
7.3	Conclusions.....	154
7.4	Experimental Section	154

7.4.1	Mößbauer Spectroscopy.	154
7.4.2	Magnetic susceptibility.	155
7.4.3	Raman and IR spectroscopy.	155
7.4.4	Ligand synthesis.	156
7.4.5	Complex Synthesis.....	156
7.4.6	X-Ray.....	157
8	Iron (II) Complexes with the ligand <i>o</i>-bipy	159
8.1	Synthesis and Characterization of [Fe(<i>o</i> -bipy)(NCS) ₂]	159
8.2	Results and Discussion	160
8.2.1	Crystallographic Data.	162
8.2.2	Electrochemistry.	163
8.2.3	Magnetic susceptibility measurements.	164
8.2.4	IR-Spectroscopy of [Fe(<i>o</i> -bipy)(NCS) ₂].....	165
8.3	Conclusions.....	166
8.4	Experimental Section	166
8.4.1	Materials and Methods.....	166
8.4.2	Synthesis of the complex [Fe(<i>o</i> -bipy)(NCS) ₂].....	167
8.4.3	Cyclic voltametry	167
8.4.4	X-Ray.....	167
8.4.5	Magnetic susceptibility measurements	168
9	Summary	169
	List of Crystal Structures.....	178
	Publications	184
	Presentations.....	185
	Curriculum Vitae	186
	Bibliography.....	188

Table of Figures

Figure 1-1: Ferromagnetic complex $[(\text{tmpa})\text{Fe}^{\text{II}}(\text{THBQ}^{2-})\text{Fe}^{\text{II}}(\text{tmpa})](\text{BF}_4)_2$ (top) ⁸ ; mixed Fe-Cu-Fe ferromagnetic complex (bottom). ¹⁰	4
Figure 1-2: $[\text{2Fe-2S}]$ cluster with tridentate capping ligand (antiferromagnetic). ¹⁴	5
Figure 1-3: Comparison of the orbital occupancy and crystal field stabilization energies (CFSE) of high-spin and low-spin for Fe^{2+} .	6
Figure 1-4: Representations of spin crossover curves: 1) gradual spin transition; 2) two step spin crossover with plateau; 3) abrupt spin transition with hysteresis. ²²	7
Figure 1-5: Electronic structure of Fe^{II} spin crossover compounds and mechanisms of LIESST and reverse-LIESST effect. ²²	8
Figure 1-6: Structures of some iron porphyrin complexes that mimic intermediates are similar to those known or presumed to occur within catalysis during cytochrome P450 turnover.	10
Figure 1-7: Modification of structure and spin state from the bond of oxygen at iron porphyrin. (a) high-spin iron(II)-desoxy form; (b) low-spin-iron(III) oxy form. ³⁶	11
Figure 1-8: Abbreviations used for tripodal ligands: left: tris(2-pyridylmethyl)amine (tmpa). Top row: (2-aminoethyl)bis(2-pyridyl-methyl)amine (uns-penp, R = H), N^1 -(2-aminoethyl)- N^1 -(2-pyridyl-methyl)-1,2-ethandiamine (apme, R = H) and tris(2-aminoethyl)amine (tren; R = H). Middle row: N^2, N^2 -bis[(2-pyridyl)methyl]-2-(2-pyridyl)ethylamine (pmea), N^2, N^2 -bis[2-(2-pyridyl)ethyl]-(2-pyridyl)methylamine (pmap) and tris[2-(2-pyridyl)ethyl]amine (tepa). Bottom row: tris((6-methylpyridin-2-yl)methyl)amine (6- Me_2 tmpa), 2-(6-methylpyridin-2-yl)- N, N -bis((6-methylpyridin-2-yl)methyl)ethanamine (6- Me_2 pmea), N^1, N^1 -bis((6-methylpyridin-2-yl)methyl)ethane-1,2-diamine (6- Me_2 -uns-penp; R = H) and N^1, N^1 -dimethyl- N^2, N^2 -bis((6-methylpyridin-2-yl)methyl)ethane-1,2-diamine (6- Me_2 - Me_2 uns-penp; R = CH_3).	13
Figure 1-9: First structurally characterized copper peroxido complex. ⁴⁹	14
Figure 1-10: Model complex for β -keto acid depending enzymes. ⁴¹	15
Figure 1-11: The ligands mac (mac = 3,6,9,17,20,23-hexaazatricyclo[23.3.1.1]triaconta-1(29),2,9,11(30),12(13),14,16,23, 25,27-decaene) and bsm2py (bsm2py = 6,20-bis(pyridin-2-yl)methyl,3,6,9,17,20,23-hexaazatricyclo[23.3.1.1]triaconta-1(29),2,9,11(30),12(13), 14,16,23,25,27-decaene).	17
Figure 1-12: The ligand (7E)- N^1 -benzylidene- N^2 -((E)-2-(benzylideneamino) ethyl)ethane-1,2-diamine (L^1).	18
Figure 1-13: The ligand o-bipy ⁸¹ .	18
Figure 2-1: Abbreviations used for tripodal ligands: tris(2-pyridylmethyl)amine (tmpa), N^1 -(2-aminoethyl)- N^1 -(2-pyridyl-methyl)-1,2-ethandiamin (apme, R = H) as well as bis[2-dimethylamino)ethyl]-(2-pyridylmethyl)amin (Me_4 apme, R = CH_3) (2-aminoethyl)bis(2-pyridyl-methyl)amine (uns-penp, R = H) as well as N^1, N^1 -dimethyl- N^2, N^2 -bis(2-pyridylmethyl)-1,2-ethandiamin (Me_2 uns-penp; $\text{R}^1 = \text{CH}_3$; R = H), tris(2-aminoethyl)amin (tren; R = H), N^1, N^1 -bis(2-(dimethylamino)ethyl)- N^2, N^2 -dimethylethane-1,2-diamine (Me_6 tren; R = CH_3).	20
Figure 2-2: Molecular structure of the cation of $[\text{Cu}_2(\text{apme})_2]^{2+}$ (1).	22
Figure 2-3: Molecular structure of the cation of $[\text{Cu}_2(\text{apme})_2]^{2+}$ (2).	23
Figure 2-4: Molecular structure of the cation of $[\text{Cu}(\text{apme})\text{Cl}]^+$ (3).	26
Figure 2-5: Molecular structure of the cation of $[\text{Cu}(\text{apme})(\text{DMF})]^+$ (4).	27
Figure 2-6: Low temperature NMR spectra of 2 in CD_3CN at -35°C , -5°C , $+5^\circ\text{C}$ and $+25^\circ\text{C}$.	28

Figure 2-7: Suggested monomer formed in solution.....	29
Figure 2-8: Cyclic Voltammogram of 2 (left) and 3 (right).....	29
Figure 2-9: Time resolved UV/vis spectra for the reaction of an in situ reaction of apme [Cu(CH ₃ CN) ₄]ClO ₄ and O ₂ in CH ₂ Cl ₂ at -87°C (left) and in acetone at -90°C (right); [complex] = 5 x 10 ⁻⁵ mol/L, [O ₂] = 5.1 x 10 ⁻³ mol/L in acetone, t = 1.47 s in CH ₂ Cl ₂ ; t = 0.76 s in acetone.	30
Figure 2-10: Possible pathways for copper(I) complexes to react with dioxygen.....	32
Figure 3-1: A) Synthetic strategy for the preparation of substituted N ² -triamines: H ₂ NC ₂ py, H ₂ NC ₂ PhOH and H ₂ NC ₂ Et. B) Macrocyclic ligands obtained from the [2+2] condensation of N ² -triamines and isophthalaldehyde, including proton labeling used.	40
Figure 3-2: The ligand mac (R = H)	41
Figure 3-3: Potential condensation products from the reaction of isophthalaldehyde and N ² - substituted triamine. For the labeling, the numerical values indicate the number of reacted units and in parenthesis the unreacted groups. For instance 1+1(n,o) means a condensation of one molecule of isophthalaldehyde and one of triamine. In parenthesis the (n) indicates an unreacted amine and (o) an unreacted aldehyde.	43
Figure 3-4: Ball and stick diagram for the X-ray crystal structure for Cu ^I complexes. (A) top, two representations of 2 ²⁺ ; bottom, two of 5 ³⁺ . (B) Left, 4 ³⁺ ; Right, 6 ³⁺ . Color codes: Cu, orange; N, blue; C, gray; O, red. H atoms are not shown.	46
Figure 3-5: Variable Temperature ¹ H NMR Spectra of 1(PF ₆) ₂ in d ₇ -DMF at -55, -15 and +25 °C (arrows mark the peaks of the second isomer).	49
Figure 3-6: ESI-MS spectra obtained for 2(CF ₃ SO ₃) ₂ (top) and 5(CF ₃ SO ₃) ₃ (bottom) in MeCN.	50
Figure 3-7: Graph of the 2 ²⁺ to 5 ³⁺ oligomerization evolution as a function of time monitored by MS spectroscopy. The inset shows the first 30 h. Units are the same as in the main graph.	51
Figure 4-1: Oxidation and intramolecular ligand hydroxylation of [Cu ₂ (mac)(CH ₃ CN) ₂](ClO ₄) ₂	64
Figure 4-2: Reduction of (7E)-N ¹ -benzylidene-N ² -((E)-2-(benzylideneamino) ethyl)ethane-1,2- diamine (L ¹) to N ¹ -benzyl-N ² -(2-(benzylamino)ethyl)ethane-1,2-diamine (L ²).....	64
Figure 4-3: Imine-aminal equilibrium of L ¹	65
Figure 4-4: Thermal ellipsoid plot of the molecular structure of L ¹ (50 % probability ellipsoids).....	65
Figure 4-5: Molecular structure of the cation of [Cu(L ¹)(CH ₃ CN)](PF ₆) (1)	66
Figure 4-6: Thermal ellipsoid plot of the molecular structure of the cation of [Cu ₂ (L ¹) ₂](ClO ₄) ₂ (2) (40% probability ellipsoids, C bound hydrogen atoms omitted for clarity).	66
Figure 4-7: Comparison of L ¹ with a 2,6-bis(pyrazole-2-yl)-pyridine derivative (R = H, Me, tBu).	67
Figure 4-8: Packing diagram of complex 2, view along the crystallographic a-axis (left), b-axis (middle) and c-axis (right) (hydrogen atoms omitted for clarity).	72
Figure 4-9: ¹ H NMR spectra of [Cu(L ¹)(CH ₃ CN)]PF ₆ in CD ₃ CN at -40, -20, -10 and +25 °C.	73
Figure 4-10: Thermal ellipsoid plot of the molecular structure of the cation of 3, [Cu(L ¹)(PPh ₃)] ⁺ (50 % probability ellipsoids, C bound H atoms omitted for clarity).	75
Figure 4-11: Thermal ellipsoid plot of the molecular structure of the cation of 4, [Cu ₂ (L ¹) ₂ (OCH ₃) ₂] ²⁺ (50 % probability ellipsoids, C bound H atoms of the ligand omitted for clarity).	76

Figure 4-12: Thermal ellipsoid plot of the molecular structure of the cation of 5 , $[\text{Cu}_2(\text{L}^1)_2(\text{OH})_2]^{2+}$, (50 % probability ellipsoids, C bound H atoms omitted for clarity). ...	77
Figure 4-13: Top left: UV-Vis spectrum of an oxidized solution of 1 in CH_2Cl_2 ; top right: UV-Vis spectrum of 5 in CH_2Cl_2 ; bottom: Time resolved UV-Vis spectra of an oxidized solution of 1 in CH_2Cl_2 , quenched with one equivalent water.	79
Figure 4-14: Cyclic Voltammetry of a 1:1 mixture of $[\text{Cu}(\text{CH}_3\text{CN})_4]\text{PF}_6$ and L^2 in CH_3CN ($v = 50, 100, 200 \text{ mV/s}$).	82
Figure 4-15: Molecular structure of the cation of $[\text{Cu}_2(\text{L}^2)_2\text{Cl}_3]^+$	84
Figure 5-1: Abbreviations used for tripodal ligands: tris(2-pyridylmethyl)amine (tpa), N^2, N^2 -bis[(2-pyridyl)methyl]-2-(2-pyridyl)ethylamine (pmea), (2-aminoethyl)bis(2-pyridyl-methyl)amine (uns-penp, $\text{R} = \text{H}$), N^1 -(2-aminoethyl)- N^1 -(2-pyridyl-methyl)-1,2-ethandiamine (apme, $\text{R} = \text{H}$) as well as bis[2-dimethylamino)ethyl]-(2-pyridylmethyl)amin (Me_4apme , $\text{R} = \text{CH}_3$).	94
Figure 5-2: Molecular structure of $[\text{Fe}(\text{imine}_2\text{-apme})(\text{NCS})_2]$ (1).	95
Figure 5-3: Molecular structure of $[\text{Fe}(\text{apme})(\text{NCS})_2]$ (2).	96
Figure 5-4: Molecular structure of $[\text{Fe}(\text{HMe}_4\text{apme})(\text{NCS})_3]$ (3).	98
Figure 5-5: Molecular structure of $[\text{Fe}(\text{Me}_4\text{apme})(\text{NCS})_3]$ (4).	99
Figure 5-6: Mößbauer spectra of $[\text{Fe}(\text{Me}_4\text{apme})(\text{NCS})_2]$ (4) between 40 and 298 K.	100
Figure 5-7: Magnetic susceptibility measurements using a SQUID magnetometer of $[\text{Fe}(\text{imine}_2\text{-apme})(\text{NCS})_2]$ (1) between 300 and 5 K (cooling mode) and 5 K and 300 K (heating mode).	101
Figure 5-8: IR-spectra of $[\text{Fe}(\text{apme})(\text{NCS})_2]$, $[\text{Fe}(\text{imine}_2\text{-apme})(\text{NCS})_2]$, $[\text{Fe}(\text{Me}_4\text{apme})(\text{NCS})_2]$ and $[\text{Fe}(\text{TMG}_2\text{apme})(\text{NCS})_2]$	105
Figure 6-1: Abbreviations used for tripodal ligands.	111
Figure 6-2: ORTEP plot of the molecular structure of $[\text{Fe}(6\text{-Me}_2\text{pmea})(\text{NCS})_2]$ (1). The Fe-N bonds linking the thiocyanate ligands to the iron ion are generally shorter than those linking the tripodal ligand to the iron ion (see Table 6-2). This is mainly due to electrostatic attractions between the metal ion and the monoanionic thiocyanate ligands. The Fe-N bond lengths of the two thiocyanate units differ substantially. Thus, the thiocyanate ligand which is positioned <i>trans</i> to that tertiary amine nitrogen atom interconnecting the three arms of the tripodal ligand displays the shortest Fe-N bond in each of the five complexes.	114
Figure 6-3: ORTEP plot of the molecular structure of $[\text{Fe}(6\text{-Me}_2\text{-Me}_2\text{uns-penp})(\text{NCS})_2]$ (2).	115
Figure 6-4: ORTEP plot of the molecular structure of $[\text{Fe}(\text{Me}_2\text{uns-penp})(\text{NCS})_2]$ (3).	116
Figure 6-5: ORTEP plot of the molecular structure of $[\text{Fe}(\text{imine-uns-penp})(\text{NCS})_2]$ (4).	117
Figure 6-6: ORTEP plot of the molecular structure of $[\text{Fe}(\text{TMG-uns-penp})(\text{NCS})_2]$ (5).	117
Figure 6-7: IR-Spectrum of $[\text{Fe}(6\text{-Me}_2\text{tpa})(\text{NCS})_2]$, $[\text{Fe}(6\text{-Me}_2\text{pmea})(\text{NCS})_2]$, $[\text{Fe}(6\text{-Me}_2\text{-uns-penp})(\text{NCS})_2]$ and $[\text{Fe}(6\text{-Me}_2\text{-Me}_2\text{uns-penp})(\text{NCS})_2]$ at 298 K.	121
Figure 6-8: IR-spectra of $[\text{Fe}(\text{Me}_2\text{uns-penp})(\text{NCS})_2]$, $[\text{Fe}(\text{imine-uns-penp})(\text{NCS})_2]$ and $[\text{Fe}(\text{TMG-uns-penp})(\text{NCS})_2]$ at 298 K.	121
Figure 6-9: Magnetic susceptibility measurements of top: $[\text{Fe}(6\text{-Me}_2\text{tpa})(\text{NCS})_2]$ (left), $[\text{Fe}(6\text{-Me}_2\text{pmea})(\text{NCS})_2]$ (right), bottom: $[\text{Fe}(6\text{-Me}_2\text{-uns-penp})(\text{NCS})_2]$ (left) $[\text{Fe}(6\text{-Me}_2\text{-Me}_2\text{uns-penp})(\text{NCS})_2]$ (right) between 5 K and 300 K.	122
Figure 6-10: Magnetic susceptibility measurements of top: $[\text{Fe}(\text{Me}_2\text{uns-penp})(\text{NCS})_2]$ (left), $[\text{Fe}(\text{imine-uns-penp})(\text{NCS})_2]$ (right) and bottom: $[\text{Fe}(\text{TMG-uns-penp})]$ between 5 K and 300 K.	123

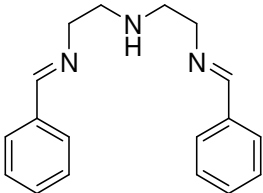
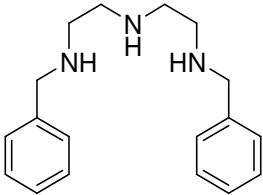
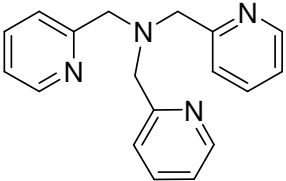
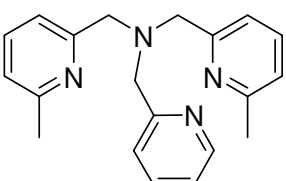
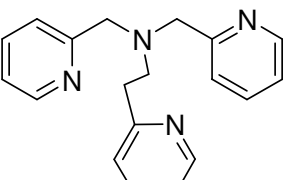
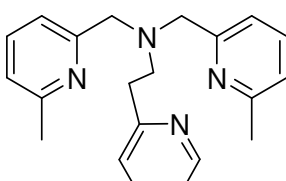
Figure 6-11: Mößbauer spectra of top: [Fe(6-Me ₂ tmpa)(NCS) ₂] and 1 ; middle: [Fe(6-Me ₂ -uns-penp)(NCS) ₂] and 2 and bottom: 3 and 4 between 298 and 40 K. (Note): The isomer shifts in this Figure are given relative to the cobalt source, while the isomer shifts in Table 6-4 are referenced versus an α -iron foil.)	125
Figure 7-1: Abbreviations used for tripodal ligands: tris(2-pyridylmethyl)amine (tmpa), N ² ,N ² -bis[(2-pyridyl)methyl]-2-(2-pyridyl)ethylamine (pmea), N ² ,N ² -bis[2-(2-pyridyl)ethyl]-(2-pyridyl)methylamine (pmap) and tris[2-(2-pyridyl)ethyl]amine (tepa).	135
Figure 7-2: Molecular structure of [Fe(tmpa)(NCS) ₂] (1).	141
Figure 7-3: Molecular structure of [Fe(pmea)(NCS) ₂] (2).	143
Figure 7-4: Racemic twin of [Fe(pmap)(NCS) ₂] (3).	144
Figure 7-5: Molecular structure of [Fe(tepa)(NCS) ₂] (4).	145
Figure 7-6: Temperature dependence of the HS and LS fits derived from ⁵⁷ Fe Mößbauer spectra on [Fe(pmea)(NCS) ₂] (2) between 10 and 300 K.	147
Figure 7-7: Temperature dependence of molar high spin ratio derived from ⁵⁷ Fe Mößbauer spectra of [Fe(pmea)(NCS) ₂] (2) between 10 and 300 K and under continuous green light irradiation (514.5 nm; 20 mW/cm ²) between 10 and 40 K indicating the presence of the LIESST effect.	147
Figure 7-8: Model of the LIESST effect.	148
Figure 7-9: ⁵⁷ Fe Mößbauer spectra of [Fe(pmea)(NCS) ₂] (2) before irradiation at 10 K shows 100% LS. At 20 K under green light irradiation (514.5 nm; 20 mW/cm ²) clearly shows a light-induced excited spin state trapping (LIESST) effect. At 100 K after irradiation reversibility is indicated. While at 175 K still the thermal spin transition is reproduced.	150
Figure 7-10: ⁵⁷ Fe Mößbauer spectra of [Fe(pmea)(NCS) ₂] (2) under continuous red light irradiation (820 nm; 40 mW/cm ²) indicate a LiPTH effect of the thermal spin transition seen in comparison to the thermal transition between 170 and 200 K. The LiPTH transition indicates a higher cooperativity among the centers.	151
Figure 7-11: Magnetic susceptibility χT vs T plot for [Fe(tmpa)(NCS) ₂] (1), [Fe(pmea)(NCS) ₂] (2), [Fe(pmap)(NCS) ₂] (3) and [Fe(tepa)(NCS) ₂] (4) measured at 1 Tesla in a SQUID magnetometer between 6 and 400 K.	152
Figure 7-12: IR-Spectra of [Fe(tmpa)(NCS) ₂] (1), [Fe(pmea)(NCS) ₂] (2) and [Fe(pmap)(NCS) ₂] (3) at RT.	153
Figure 8-1: The ligand bapbpy ²⁸⁵ compared to the ligand <i>o</i> -bipy ⁸¹	159
Figure 8-2: Molecular structure of the ligand <i>o</i> -bipy.	160
Figure 8-3: Molecular structure of [Fe(<i>o</i> -bipy)(NCS) ₂].	161
Figure 8-4: Electrochemistry of [Fe(<i>o</i> -bipy)(NCS) ₂] in DMF (RT) from 0 to 1.8 V.	164
Figure 8-5: SQUID measurements of [Fe(<i>o</i> -bipy)(NCS) ₂] between 30 K and 300 K.	165
Figure 8-6: IR-Spectrum for [Fe(<i>o</i> -bipy)(NCS) ₂].	166
Figure 9-1: Abbreviations used for tripodal ligands: from left: N ¹ -(2-aminoethyl)-N ¹ -(2-pyridyl-methyl)-1,2-ethandiamine (apme); Bis[2-Dimethylaminoethyl]-(2-pyridylmethyl)amine (Me ₄ apme); N ¹ -(propan-2-ylidene)-N ² -(2-(propan-2-ylideneamino)ethyl)-N ² -((pyridin-2-yl)methyl)ethane-1,2-diamine (Imine ₂ -apme); 2-(2-(bis((pyridin-2-yl)methyl)amino)ethyl)-1,1,3,3-tetramethylguanidine (TMG ₂ apme).	169
Figure 9-2: From left: Low temperature NMR spectra of [Cu ₂ (apme) ₂](CF ₃ SO ₃) ₂ in CD ₃ CN at -35°C, -5°C, +5°C and +25°C; right: Time resolved UV/vis spectra for the reaction of an in situ reaction of apme [Cu(CH ₃ CN) ₄]ClO ₄ and O ₂ in CH ₂ Cl ₂ at -87°C ; [complex] = 5 x 10 ⁻⁵ mol/L, [O ₂] = 5.1 x 10 ⁻³ mol/L in acetone, t = 1.47 s in CH ₂ Cl ₂ ; t = 0.76 s in acetone... ..	170

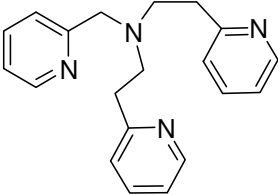
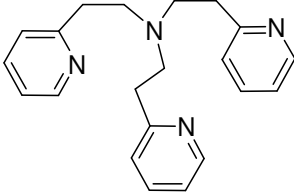
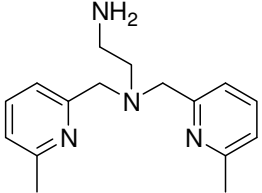
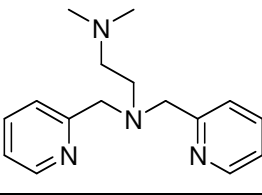
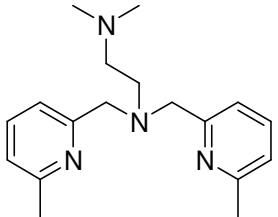
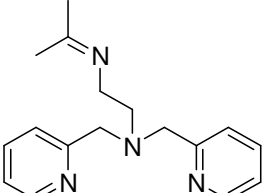
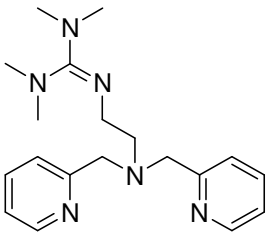
- Figure 9-3:** From left: Abbreviation of the ligand bsm2py (bsm2py = 6,20-bis(pyridin-2-yl)methyl,3,6,9,17,20,23-hexaazatricyclo[23.3.1.1]triaconta-1(29),2,9,11(30),12(13),14,16,23,25,27-decaene); middle: ESI-MS spectra obtained for $[\text{Cu}_2(\text{bsm2PhOH})(\text{MeCN})_2](\text{CF}_3\text{SO}_3)_2$ in MeCN (middle) right: ORTEP plot of $[\text{Cu}_3(\text{L}^4)](\text{CF}_3\text{SO}_3)_3 \cdot 1\text{EtOEt}$ 170
- Figure 9-4:** Molecular structure of left: $[\text{Fe}(\text{imine}_2\text{-apme})(\text{NCS})_2]$ and right: $[\text{Fe}(\text{apme})(\text{NCS})_2]$ 172
- Figure 9-5:** Molecular structure of left: $[\text{Fe}(\text{HMe}_4\text{apme})(\text{NCS})_3]$ and right: $[\text{Fe}(\text{Me}_4\text{apme})(\text{NCS})_2]$ 173
- Figure 9-6:** Abbreviations used for tripodal ligands: from left: tris((6-methylpyridin-2-yl)methyl)amine (6-Me₂tmpa), 2-(6-methylpyridin-2-yl)-N,N-bis((6-methylpyridin-2-yl)methyl)ethanamine (6-Me₂pmea), *N*¹,*N*¹-bis((6-methylpyridin-2-yl)methyl)ethane-1,2-diamine (6-Me₂-uns-penp) and *N*¹,*N*¹-dimethyl-*N*²,*N*²-bis((6-methylpyridin-2-yl)methyl)ethane-1,2-diamine (6-Me₂-Me₂uns-penp). 173
- Figure 9-7:** Abbreviation used for tripodal ligands: from left: 2-aminoethylbis(2-pyridylmethyl)amine (uns-penp); *N*¹,*N*¹-Dimethyl-*N*²,*N*²-Bis(2-pyridylmethyl)-1,2-ethandiamine (Me₂uns-penp); *N*¹-(propan-2-ylidene)-*N*²,*N*²-bis((pyridin-2-yl)methyl)ethane-1,2-diamine (Imine-uns-penp); 2-(2-(bis((pyridin-2-yl)methyl)amino)ethyl)-1,1,3,3-tetramethylguanidine (TMG-uns-penp). 174
- Figure 9-8:** Magnetic susceptibility measurements for the compounds of Chapter 6 (cooling mode) between 300 K and 5 K. 174
- Figure 9-9:** Abbreviations used for tripodal ligands: from left: tris(2-pyridylmethyl)amine (tmpa), *N*²,*N*²-bis[(2-pyridyl)methyl]-2-(2-pyridyl)ethylamine (pmea), *N*²,*N*²-bis[2-(2-pyridyl)ethyl]-(2-pyridyl)methylamine (pmap) and tris[2-(2-pyridyl)ethyl]amine (tepa). 175
- Figure 9-10:** left: Magnetic susceptibility χT vs *T* plot (heating mode) for $[\text{Fe}(\text{tmpa})(\text{NCS})_2]$, $[\text{Fe}(\text{pmea})(\text{NCS})_2]$, $[\text{Fe}(\text{pmap})(\text{NCS})_2]$ and $[\text{Fe}(\text{tepa})(\text{NCS})_2]$ measured at 1 Tesla in a SQUID magnetometer between 6 and 400 K. Right: ⁵⁷Fe Mößbauer spectra of $[\text{Fe}(\text{pmea})(\text{NCS})_2]$ before irradiation at 10 K shows 100% LS. At 20 K under green light irradiation (514.5 nm; 20 mW/cm²) clearly shows a light-induced excited spin state trapping (LIESST) effect. At 100 K after irradiation reversibility is indicated. While at 175 K still the thermal spin transition is reproduced. 176
- Figure 9-11:** From left: ORTEP plot of the complex $[\text{Fe}(\text{o-bipy})(\text{NCS})_2]$. Right: Magnetic susceptibility χT vs *T* plot (cooling and heating modes) for $[\text{Fe}(\text{o-bipy})(\text{NCS})_2]$ between 30 and 300 K. 177

Tables

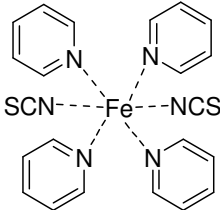
Table 2-1: Crystal data and structure refinement for 1 , 2 , 3 and 4 .	24
Table 2-2: Bond lengths [Å] and angles [°] for 1 , 2 , 3 and 4 .	25
Table 3-1: Crystallographic data for structures: L ² , 4 (SbF ₆) ₃ , 4 (PF ₆) ₃ , 2 (CF ₃ SO ₃) ₂ , 5 (CF ₃ SO ₃) ₃ and 6 (CF ₃ SO ₃) ₃	48
Table 3-2: Selected bond distances and angles for the first coordination sphere of one of the Cu ^I metal centers of complexes, 4 ³⁺ , 2 ²⁺ , 5 ³⁺ and 6 ³⁺ .	48
Table 4-1: Crystal data and structure refinement for L ¹ , 1 , 2 and 3 .	68
Table 4-2: Crystal data and structure refinement for 4 , 5 and 6 .	69
Table 4-3: Selected bond lengths [Å] and angles [°] for the compounds 1-6 .	69
Table 5-1: Selected crystallographic data unit cell parameters, and values of 1 , 2 , 3 and 4 .	102
Table 5-2: Selected bond lengths [Å] and angles [°] for compounds 1-4 .	103
Table 5-3: Range of N-Fe-N angles between <i>cis</i> and <i>trans</i> nitrogen atoms	104
Table 5-4: Fe-C-N angles thiocyanate trans to aliphatic amino and pyridine group	104
Table 6-1: Selected crystallographic data unit cell parameters, and values of [Fe(Me ₂ pmea)(NCS) ₂] (1), [Fe(6-Me ₂ -Me ₂ uns-penp)(NCS) ₂] (2), [Fe(Me ₂ uns-penp)(NCS) ₂] (3) [Fe(imine-uns-penp)(NCS) ₂] (4) and [Fe(TMGuns-penp)(NCS) ₂] (5).	118
Table 6-2: Selected bond lengths [Å] and angles [°] for the compounds 1-5 .	119
Table 6-3: Comparison of bond lengths (Å) between the iron ion and the nitrogen donor atoms of the tripodal ligand in [Fe(uns-penp)(NCS) ₂], [Fe(Me ₂ uns-penp)(NCS) ₂] (3), [Fe(6-Me ₂ -Me ₂ uns-penp)(NCS) ₂] (2).	120
Table 6-4: Isomer shifts δ_s relative to an α -iron foil and quadrupole splittings ΔE_Q of the complexes at room temperature and at 40 K.	124
Table 7-1: Selected crystallographic data, unit cell parameters, and values of [Fe(tmpa)(NCS) ₂] (1), [Fe(pmea)(NCS) ₂] (2), [Fe(pmap)(NCS) ₂] (3) and [Fe(tepa)(NCS) ₂] (4).	138
Table 7-2: Selected bond lengths [Å] and angles [°] for compounds 1-4 .	139
Table 7-3: Range of N-Fe-N angles between <i>cis</i> and <i>trans</i> nitrogen atoms.	140
Table 7-4: Fe-C-N angles thiocyanate trans to aliphatic amino and pyridine group.	140
Table 7-5: Temperature dependence of ⁵⁷ Fe Mößbauer parameter 2 between 10 and 300 K (see pmea) and under continuous irradiation (see pmea*). The green light irradiation (514.5 nm; 20 mW/cm ²) was performed at 10 K, 20K and 40K, while the effect of the red light irradiation (820 nm; 40 mW/cm ²) was observed at 170 K, 175 K, 195 K, and 200 K.	149
Table 8-1: Selected crystallographic data unit cell parameters, and values of L ¹ and 1	162
Table 8-2: Selected bond lengths [Å] and angles [°] for compound 1 .	163
Table 8-3: Range of N-Fe-N angles between <i>cis</i> and <i>trans</i> nitrogen atoms.	163

Used Precursors and Ligands

Name	Structure	Formular	Molar Mass [g/mol]
(7E)- <i>N</i> ¹ -benzylidene- <i>N</i> ² -((E)-2-(benzylideneamino)ethyl)ethane-1,2-diamine <i>L</i> ¹		C ₁₈ H ₂₁ N ₃	279,38 g/mol
<i>N</i> ¹ -benzyl- <i>N</i> ² -(2-(benzylamino)ethyl)ethane-1,2-diamine <i>L</i> ²		C ₁₈ H ₂₅ N ₃	283,41 g/mol
tris((pyridin-2-yl)methyl)amine tmpa (tpa)		C ₁₈ H ₁₈ N ₄	290,36 g/mol
<i>N,N</i> -bis((6-methylpyridin-2-yl)methyl)(pyridine-2-yl)methanamine 6-Me ₂ tmpa		C ₂₀ H ₂₂ N ₄	318,42 g/mol
2-(pyridin-2-yl)- <i>N,N</i> -bis((pyridin-2-yl)methyl)ethanamine pmea		C ₁₉ H ₂₀ N ₄	304,39 g/mol
<i>N,N</i> -bis((6-methylpyridin-2-yl)methyl)-2-(pyridin-2-yl)ethanamine 6-Me ₂ pmea		C ₂₁ H ₂₄ N ₄	332,44 g/mol

Name	Structure	Formular	Molar Mass [g/mol]
2-(pyridin-2-yl)-N-(2-(pyridin-2-yl)ethyl)-N-((pyridin-2-yl)methyl)ethanamine pmap		C ₂₀ H ₂₂ N ₄	318,42 g/mol
tris(2-(pyridin-2-yl)ethyl)amine tepa		C ₂₁ H ₂₄ N ₄	332,44 g/mol
N ¹ ,N ¹ -bis((6-methylpyridin-2-yl)methyl)ethane-1,2-diamine 6-Me ₂ -uns-penp		C ₁₆ H ₂₂ N ₄	270,18 g/mol
N ¹ ,N ¹ -Dimethyl-N ² ,N ² -Bis(2-pyridylmethyl)-1,2-ethandiamine Me ₂ uns-penp		C ₁₆ H ₂₂ N ₄	270,42 g/mol
N ¹ ,N ¹ -dimethyl-N ² ,N ² -bis((6-methylpyridin-2-yl)methyl)ethane-1,2-diamine 6-Me ₂ -Me ₂ uns-penp		C ₁₈ H ₂₆ N ₄	298,43 g/mol
N ¹ -(propan-2-ylidene)-N ² ,N ² -bis((pyridin-2-yl)methyl)ethane-1,2-diamine Imine-uns-penp		C ₁₇ H ₂₂ N ₄	282,38 g/mol
2-(2-(bis((pyridin-2-yl)methyl)amino)ethyl)-1,1,3,3-tetramethylguanidine TMG-uns-penp		C ₁₉ H ₂₈ N ₆	240,47 g/mol

Name	Structure	Formular	Molar Mass [g/mol]
N^1 -(2-Aminoethyl)- N^1 -(2-pyridylmethyl)-1,2-ethandiamine apme		$C_{10}H_{18}N_4$	194,15 g/mol
Bis[2-Dimethylaminoethyl]-(2-pyridylmethyl)amine Me ₄ apme		$C_{14}H_{26}N_4$	250,38 g/mol
N^1 -(propan-2-ylidene)- N^2 -(2-(propan-2-ylideneamino)ethyl)- N^2 -((pyridin-2-yl)methyl)ethane-1,2-diamine Imine ₂ -apme		$C_{16}H_{26}N_4$	274,40 g/mol
N'' -[Pyridin-2-ylmethyl-amino)- N'' -bis-ethyl]- N,N,N',N' -tetramethyl-guanidin TMG ₂ apme		$C_{16}H_{26}N_4$	390,57 g/mol
6,20-bis(pyridin-2-yl)methyl,3,6,9,17,20,23-hexaazatricyclo[23.3.1.1]triaconta-1(29),2,9,11(30),12(13),14,16,23,25,27-decaene bsm2py		$C_{38}H_{40}N_8$	584,76 g/mol
1,2-bis(6-(pyridin-2-yl)pyridin-2-yl)ethane o-bipy		$C_{22}H_{18}N_4$	338,41 g/mol

Name	Structure	Formular	Molar Mass [g/mol]
$[\text{Fe}(\text{py})_4(\text{NCS})_2]$	 <p>The structure shows a central iron atom (Fe) coordinated to four pyridine (py) rings and two isothiocyanate (NCS) groups. The pyridine rings are represented by hexagons with a nitrogen atom (N) at one vertex. The NCS groups are shown as SCN- and -NCS, with dashed lines indicating coordination to the central Fe atom.</p>	$\text{C}_{22}\text{H}_{20}\text{FeN}_6\text{S}_2$	488,41 g/mol

Abbreviations

aliph.	aliphatic
arom.	aromatic
CFSE	Crystal field stabilisation energy
d	doublet (NMR)
dd	doublet of doublet (NMR)
dt	doublet of triplet (NMR)
fac	facial
h	hour
\hbar	Plank constant/ 2π
HS-	high-spin
HV	high vacuum
L	ligand
LIESST	Light-induced Excited Spin State trapping
LS-	low-spin
m	multiplet
mer	meridional
MRT	magnetic resonance tomography
NEt ₃	triethylamine
P	Spin pairing energy
p. A.	pro Analysi (for analysis)
Pyr	Pyridin moiety
q	quartet (NMR)
s	singulet (NMR)
t	triplet (NMR)
τ	half life
χ	magnetic susceptibility
v	velocity (Mößbauer spectroscopy)

1 Introduction

1.1 The Element Copper

The element copper is one of the diamagnetic metals. It belongs to the “coin metals” along with gold and silver, because of its corrosion-resistance.¹ 5×10^{-3} percent of the earth crust contains copper. In pure form it can be found in small amounts in North America, Chile and Australia. Copper exists in bound form mainly within carbonates, oxides and sulfides. Despite its low deposit, copper has been known since about 7000 B.C..² Because of its nobility copper may appear as a pure metal and thus could be found this early. As a pure metal or alloyed with tin as bronze, copper is one of the oldest handling materials. The name “copper” comes from “aes cuprum” and means “ore of Cyprus”, a location where copper ore was used quite early in history.¹

1.2 Copper in Biology

Copper is a valuable micronutrient for bacilli, fungi, plants, animals and humans.¹⁻² Humans have about 3 mg/ kg copper in form of copper cations in their body and thus, copper – together with iron and zinc – belongs to the three most important transition metals in our body.¹⁻² Mollusks and arthropods contain copper by using hemocyanin instead of the iron containing hemoglobin of higher animals as an oxygen carrier protein. Plants need copper within plastocyanin for chlorophyll production. For some algae, small fungi and bacilli copper is already toxic in very small doses; but some microorganisms (for example bacilli of the type *Thiobacillus*) tolerate copper up to 50 g/L and dissolve also only slightly soluble copper compounds.²

Copper proteins are divided (based on spectroscopy) into type I, type II and type III copper proteins. Type I, also known as “blue copper proteins”, is found for example in plastocyanin of plants or azurin of bacilli. Because of its only slightly different coordination sphere, a reduction from Cu^{II} to Cu^{I} and vice versa is easy. Therefore, type I proteins catalyze electron transfer reactions within

organisms. Moreover, this function makes them very important for the electron transfer reaction cascades in photosynthesis.²

Type II copper proteins or “normal copper proteins” are catalysts for different types of reactions. They can act as oxidases and react with dioxygen without including dioxygen within the substrate molecule.² Further, monooxygenases catalyze the transfer of single atoms of dioxygen whereas dioxygenases catalyze the transfer of two dioxygen atoms into a substrate molecule. The third form of type II copper proteins acts as superoxide-dismutase and causes a disproportionation of superoxido-ions (O_2^-) into dioxygen and peroxide. Part of type II copper proteins are quercetine-dioxygenases, the galactose- and amine-oxidases as well as the dopamine- β -monooxygenases.²

Copper proteins of type III are always polynuclear and are involved in transportation or activation of dioxygen.² An example for transporting dioxygen can be found in hemocyanin, and as examples for dioxygen activation tyrosinase as well as catechol-oxidase can be named.³⁻⁶ Type III copper proteins are discussed in more detail in chapter 3.

There are still types of copper proteins that cannot be classified into the three types discussed above. These copper proteins are named “non-classic copper proteins” and can be divided into three groups: Metallothionins and proteins with Cu_A - and type (2-3) trimer copper proteins.² Also, Cytochrome-c-oxidases are an example for non-classic copper proteins.

1.3 The Element Iron

The element iron is one of the most common heavy metals, because the earth crust contains 4.7 percent iron. Genuine iron is found in about 86 percent of the lithosphere, and thus is the most common element on earth.¹ After aluminum, the element iron is the second numerous metal in the geosphere and the fourth numerous element in total. The earth crust contains predominantly oxides, carbonates and sulfides of iron. Weathering products mostly include trivalent iron, whereas magma precipitated out of rock is usually divalent. Elementary iron is quite rare and can be found mostly

within iron meteorites combined with nickel and other metals. Iron has been known historically as meteor iron since about 6000 years, and the Hethiters guarded the secret of iron processing since 3000 B.C.. After the collapse of the hethitic empire around 1200 B.C., the knowledge of working iron spread slowly and eventually initiated the so-called Iron Age. To this very day, the element iron is one of the most important metals and is used in many areas.

1.4 Magnetic Properties of Iron

The iron's magnetism is caused by the movement of electrons (magnetic moments) and their unpaired electronic spins. Atoms of solid bodies are arranged relatively immobile, thus the magnetic properties of solid state materials are primarily governed by the interactions between its atoms.⁷ The element iron is usually a ferromagnet, but exhibits paramagnetism at high temperatures.⁷ In this state, individual iron atoms have a magnetic moment, but all spins point in different directions and the total magnetism disappears above the Curie temperature (for iron 768° C).¹

Ferromagnetism, the common state for iron, was discovered as the first of all magnetic effects. Ferromagnetic iron has been used as a compass needle for a long time.¹ Below the Curie temperature a phase transition occurs because of an interaction between atomic magnetic moments and the spins become aligned. In this case, a permanent magnet is created.

Ferromagnetism can also be observed within nickel and cobalt compounds and at low temperatures additionally, for example, in gadolinium, dysprosium, holmium, erbium and terbium.

Some compounds, as for example FeO, NiCl₂, MnO and MnS, have an analogue to the Curie-temperature: the Neel-temperature.⁷ Beneath this Neel-temperature the spins arrange antiparallely and the compound shows antiferromagnetism. Above this Neel-temperature the compound is paramagnetic.

In the case of compounds with antiparallel spins, but two different kinds of cations, the spins do not annihilate each other exactly, but sum up to an effective magnetic moment. This form of magnetism is called ferrimagnetic, because its similarity to ferromagnetism.⁷ The most famous examples are ferrites of the type $M^{II}O \cdot Fe_2O_3$ (M^{II} among other compounds = Fe, Mn, Ni, Co, Zn, Cd, Mg, Cu).¹

1.5 Molecular Magnetism

Ferro-, ferri- and antiferromagnetism are not only found in solid state bodies, but also in various complexes. Here, magnetism manifests within single molecules or as interactions between two or more of them. One important example for ferromagnetic complexes is $[(t\text{mpa})Fe^{II}(\text{THBQ}^{2-})Fe^{II}(t\text{mpa})](\text{BF}_4)_2$ (THBQ = 2,3,5,6-tetrahydroxy-1,4-benzoquinone)⁸ as shown in Figure 1-1. Furthermore, the dinuclear compound $L_2Fe_2(\text{NO}_3)_2$ ($L = N',N$ -bis(3,5-di-*tert*-butylsalicylidene)-1,3-diaminobenzene)⁹ or a mixed Fe-Cu-Fe compound with two ferrocenium and one copper center (Figure 1-1) can be named.¹⁰

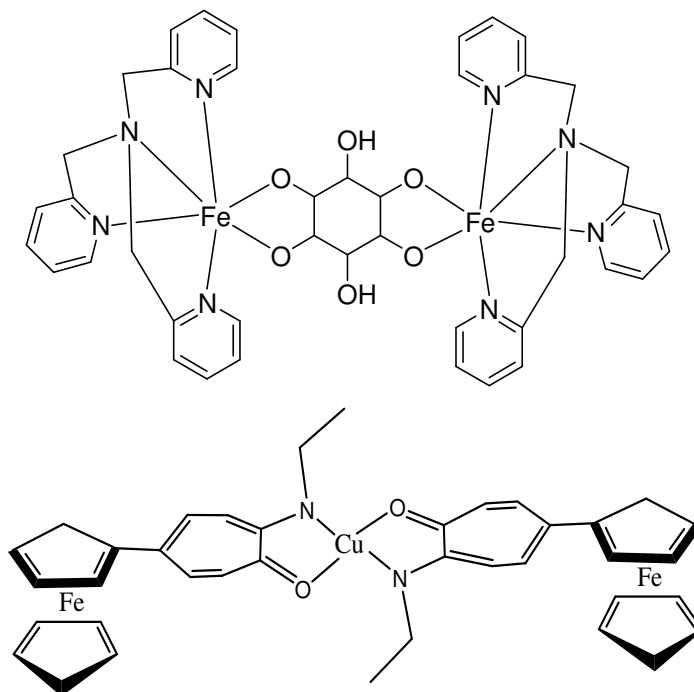


Figure 1-1: Ferromagnetic complex $[(t\text{mpa})Fe^{II}(\text{THBQ}^{2-})Fe^{II}(t\text{mpa})](\text{BF}_4)_2$ (top)⁸; mixed Fe-Cu-Fe ferromagnetic complex (bottom).¹⁰

Examples for antiferromagnetism within complexes are $[\text{Et}_3\text{NH}](\text{L}^1)\text{Fe}^{\text{III}}(\text{OMe})]$ ($\text{L}^1 = [N,N\text{-bis}(3,5\text{-di-tert-butyl-2-hydroxybenzyl})\text{aminoacetic acid}]$)¹¹ or $[\text{Fe}(\text{dm4bt})_3][\text{FeCl}_4]_2$ ($\text{dm4bt} = 2,2'\text{-dimethyl-4,4'}$ -bithiazole).¹² Furthermore, antiferromagnetism is found in clusters, as for example in the heptanuclear iron(III) oxide cluster $[\text{Fe}_7\text{O}_4(\text{OH})_2(\text{O}_2\text{CCMe}_3)_{11}(\text{bpm})_2(\text{H}_2\text{O})]$ ($\text{bpm} = 2,2'\text{-bipyrimidine}$) that shows a strong antiferromagnetic coupling between the seven iron atoms of the cluster.¹³ Clusters of $[2\text{Fe-2S}]$ show antiferromagnetism as well. Figure 1-2 shows such an antiferromagnetic cluster with five-coordinate iron atoms.¹⁴

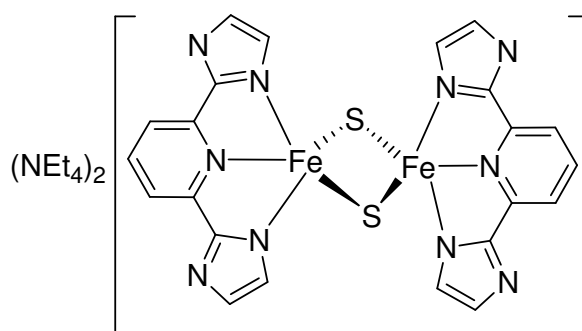


Figure 1-2: $[2\text{Fe-2S}]$ cluster with tridentate capping ligand (antiferromagnetic).¹⁴

Various ferrimagnetic complexes and clusters can also be named, like the hexanuclear cluster $[\{\text{Fe}^{\text{III}}(\text{Tp})(\text{CN})_3\}^{4-}\{\text{Fe}^{\text{II}}(\text{MeCN})(\text{H}_2\text{O})_2\}_2] \cdot 10\text{H}_2\text{O} \cdot 2\text{MeCN}$ ($\text{Tp} = \text{hydrotris(pyrazoly)borate}$)¹⁵, as well as the two cyano-bridged heterobimetallic chiral ferrimagnets with helical structures, $[\text{Mn}_3((R,R)\text{-Salcy})_3(\text{H}_2\text{O})_2\text{Fe}(\text{CN})_6 \cdot 2\text{H}_2\text{O}]_n$ and $[\text{Mn}_3((S,S)\text{-Salcy})_3(\text{H}_2\text{O})_2\text{Fe}(\text{CN})_6 \cdot 2\text{H}_2\text{O}]_n$ [$\text{Salcy} = N,N'\text{-(1,2-cyclohexanediylethylene)bis(salicylideneiminato)dianion}$].¹⁶

1.6 Spin-Crossover

In the 30s of the 20th century, the crystal-field theory was designed by physicists like John H. van Vleck and Hans Bethe. This theory is only an approximation to reality, but allows a good interpretation of electronic spectra/colors of transition metals and their magnetic properties.¹⁷

Fe^{2+} has a d^6 configuration, thus iron complexes can be either low-spin or high-spin, as shown in Figure 1-3.

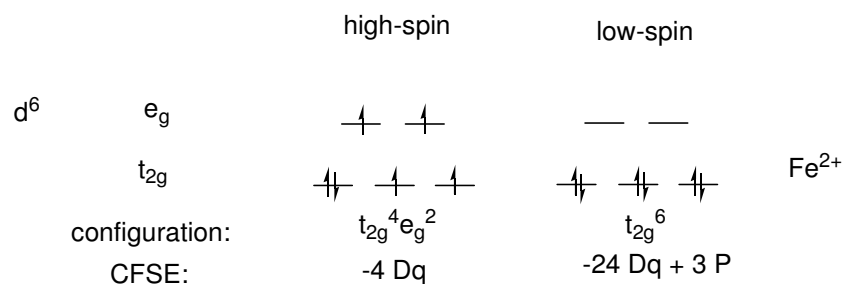


Figure 1-3: Comparison of the orbital occupancy and crystal field stabilization energies (CFSE) of high-spin and low-spin for Fe^{2+} .

In some cases, the energetic difference between the high-spin and low-spin form is very small and lies within an area of thermal excitation. An example for very well investigated compounds are six-coordinate iron(II) complexes with nitrogen donor ligands. In many cases a variation of temperatures excites a thermal induced spin-crossover between the paramagnetic high-spin and the energetic more stable diamagnetic low-spin state.¹⁷

A spin crossover, also called magnetic crossover, spin transition or spin equilibrium, occurs in different ways:¹⁸

1. A gradual spin crossover over a specific temperature range. This form of transition is found for example in the complex $[Fe(2-CH_3-phen)_3]X_2$ ¹⁹⁻²⁰, whereas the complex $[Fe(phen)_2(NCS)_2]$ ²¹ exhibits an abrupt spin crossover within a few Kelvin (Figure 1-4 (right) shows an abrupt spin transition).
2. Incomplete spin crossover either at very low or at high temperatures. This form generates a plateau instead of a true transition, which is called "residual paramagnetism" (RP).
3. A spin-crossover with hysteresis. This form of transition has proven as very efficient to study alterations of ligands and their effect on magnetic properties. Interestingly, this form of spin-transition is not only occurring in the solid state, but can be observed in solution as well.

Figure 1-4 shows three possibilities for spin crossover behavior.

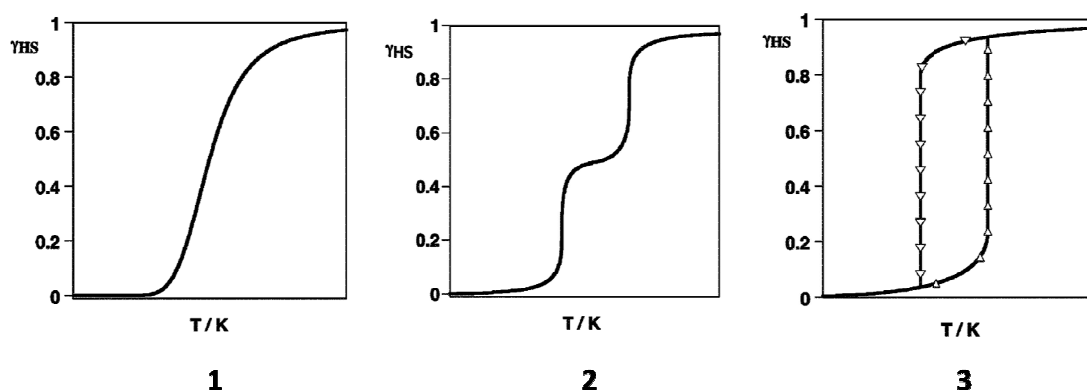


Figure 1-4: Representations of spin crossover curves: 1) gradual spin transition; 2) two step spin crossover with plateau; 3) abrupt spin transition with hysteresis.²²

The phenomenon of spin transition was discovered and characterized by Cambi in 1931.²³⁻²⁶ However, a temperature dependent spin-crossover of an iron(II) complex was not observed and investigated until about 30 years later.^{21, 27-28} It was found, that spin-crossover appears frequently within compounds composed of iron(II), cobalt(II) and iron(III), as well as sporadically within nickel(II), cobalt(III) and manganese(III) complexes.²⁹

As described above, a class of complex compounds can be found which changes spin from high-spin to low-spin after temperature decrease. During this procedure, both the optic and the magnetic properties change. Furthermore, a spin transition can occur, if the compound is pressurized. Here a destabilization of the HS state is desired, characterized by a larger volume than the LS state.²² At low temperatures, a change from a low-spin into a meta-stable high-spin state is observed after irradiating light into the complex. This state has a nearly infinite life-time and is called “Light-induced Excited Spin State Trapping” (LIESST) effect.³⁰⁻³² Decurtis and co-workers were the first to observe this effect within solid a state in 1984.³³ They radiated green light ($\lambda = 514.5$ nm) into the LS state of the complex $[\text{Fe}(\text{1-propyltetrazole})_6](\text{BF}_4)_2$ at temperatures below 50 K and registered a color change. The spin allowed $^1\text{A}_1 \rightarrow ^1\text{T}_1$ transition is stimulated by green light, but the $^1\text{T}_1$ change over decays after a few nanoseconds. However, there is a chance for the $^1\text{T}_1$ state to decay via double intersystem crossing over the $^3\text{T}_1$ spin state to the $^5\text{T}_2$ HS state, as can be seen in Figure 1-5. Here, the HS state has a

nearly indefinite life-time at low temperatures, because the $^5T_2 \rightarrow ^1A_1$ relaxation is spin forbidden. The metastable 5T_2 spin state can be converted into the 1A_1 LS state again by irradiating red light ($\lambda = 820$ nm) into the compound or by raising the temperature above 50 K. This effect is known as reverse LIESST effect.²²

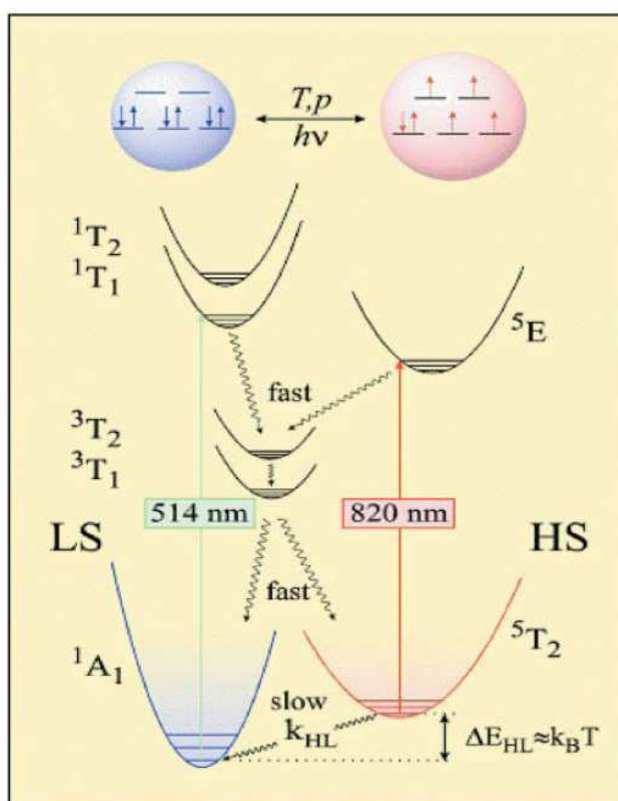


Figure 1-5: Electronic structure of Fe^{II} spin crossover compounds and mechanisms of LIESST and reverse-LIESST effect.²²

1.7 Spin Crossover Compounds as Molecular Switches

A molecular switch is a molecule that can be found in a bistable state with an “ON” and an “OFF” position. In “ON” position, a molecular switch has to perform some function or allow some device to do so. In “OFF” position a molecular switch has to stay inactive. This bistability can be exhibited by various means, for example a redox active molecule, an acid and its conjugated base or isomers of the same molecule. Usually, those switches are reversible.³⁴ Using the reversibility of SCO is another possibility for molecular switches. If it is possible to design a molecule that exhibits SCO at or above room temperature, it is possible to use them as molecular switches. Since the HS- and LS- state is

determined by electronic transitions of the d orbitals, the compound also always exhibits a change in color. It is very favorable for using a SCO compound for molecular switches, if the compound also shows a hysteresis effect. Here the critical temperature T_{down} (HS \rightarrow LS) is different from the critical temperature T_{up} (LS \rightarrow HS). In this situation, a system is bistable and both spin states can exist in a specific range of temperatures. This system has two colors as well: A pale color (HS) while coming from high temperatures and a dark color (LS) while coming from low temperatures.³⁵ Ideally both spin states can be activated here independently at the same temperature, essentially for using these molecules as for example storage media.

1.8 High- and Low-Spin Complexes within Bioinorganic Chemistry

High- and low-spin complexes also have an important task in nature.³⁶ Well-known within biochemistry are metalloproteins, so called oxygen-carrier or heme proteins, which play a valuable role for oxygen transport and storage. The substrate bond is a reversible bonding of dioxygen that is accompanied by a change of the redox state. One of these proteins is the iron containing hemoglobin that can be found in vertebrates and some invertebrates whereas the protein hemerythrin, which holds two non-heme iron atoms, is found in four strains of marine invertebrates.³⁶

Cytochrome P450 is an example for a compound in nature that shows spin crossover, but with a change of redox state. This protein can be found in several life-forms from bacilli to humans. It plays an important role within biosynthesis, metabolism, during detoxication of harmful substances and in some cases in creation of high active carcinogens. The inactive, substrate-free state contains one single low-spin iron(III) heme iron center. However, after adding camphor, 80% of the substrate changes into the high-spin form. During the catalytic cycle, electrons are transmitted to the protein and a high-spin iron(II) intermediate is formed. However, if CO is added, the low-spin iron(II) form can be achieved.³⁶ In Figure 1-6 porphyrin complexes are displayed. They mimic intermediates known or presumed to occur within catalysis during cytochrome P450 turnover.

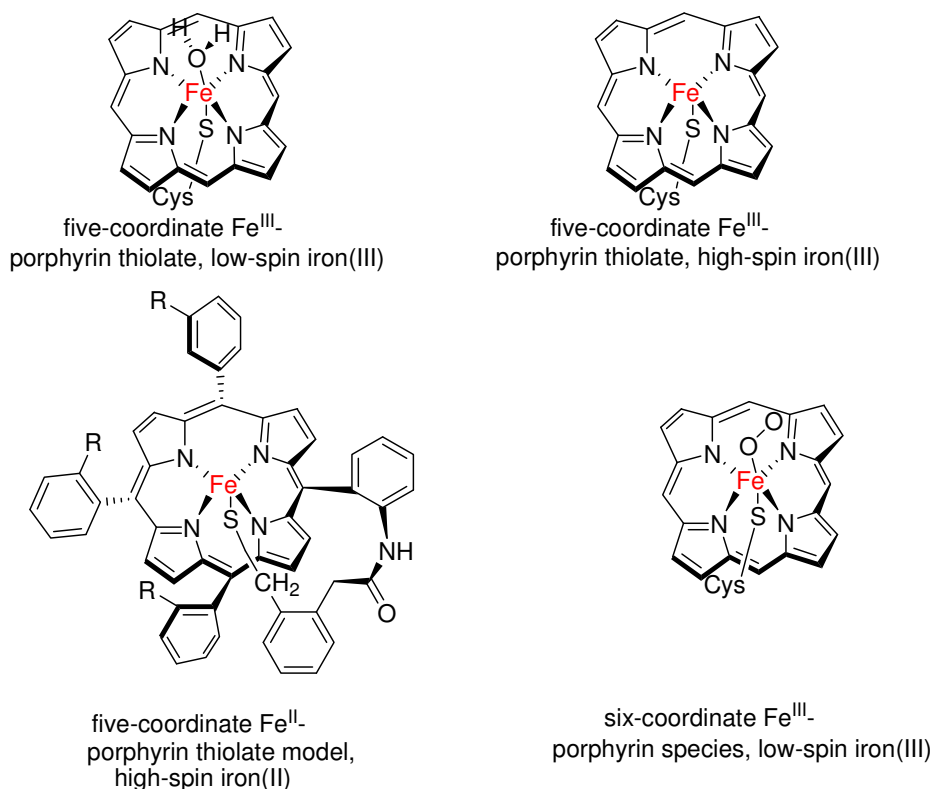


Figure 1-6: Structures of four iron porphyrin complexes that mimic intermediates similar to those known or presumed to occur within catalysis during cytochrome P450 turnover.³⁶

Furthermore, myoglobin and hemoglobin are of great interest. Dioxygen is bound by hemoglobin within the lungs and transferred to myoglobin within the tissues. During the transition of desoxy- into oxy-hemoglobin, the iron performs a motion in direction of the level of the porphyrin ring and then causes a cooperative O_2 -bonding because of the subunits of the hemoglobin. The protein has two different quaternary structures available, named as R (relaxed) and T (tense). Both conditions are in balance, but the T-unit has a lesser affinity to O_2 . Probably, interactions between the subunits interfere with the proximal histidin moiety during its motion, so the O_2 -bonding constant is lowered.³⁶

This mechanism requires the iron atom to move into the porphyrin ring plane to enable a bonding to the dioxygen molecule, which pulls the histidin residue in the same direction. Iron(II) is in a high spin state ($S = 2$) within the desoxy-hemoglobin and its covalent radius is too big to fit into the plane of the four nitrogen atoms. A bonding of O_2 leads to an iron(III)- O_2^- adduct complex and lowers the

covalent radius of iron. Now the iron center can shift into the ring plane of porphyrin and transforms into a low spin state ($S = 0$) as can be seen in Figure 1-7.³⁶ This case of different spin states is used within medical science during the functional MRT (fMRT). Here, dynamic processes can be displayed, for example in the brain. Active brain regions need more dioxygen and thus a higher blood supply takes place.³⁷

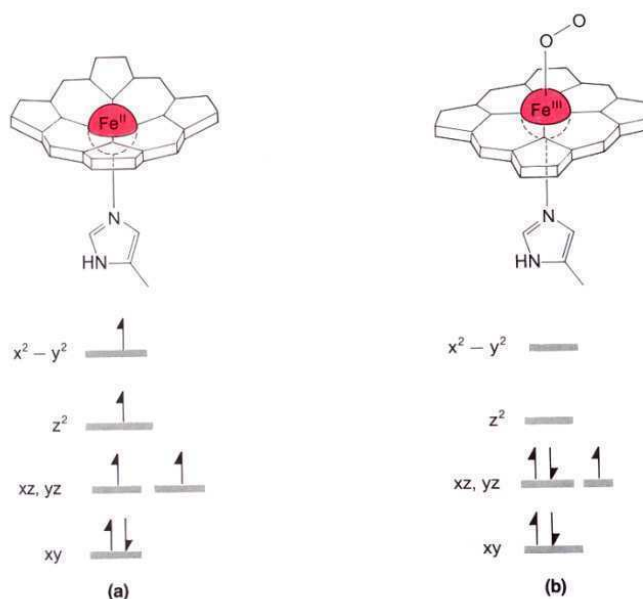


Figure 1-7: Modification of structure and spin state from the bond of oxygen at iron porphyrin. (a) high-spin iron(II)-desoxy form; (b) low-spin-iron(III) oxy form.³⁶

Hemerythrin are protein molecules which can be crystallized very easily and thus can be well investigated regarding their spectroscopic and magnetic properties. Mößbauer and EPR measurements of hemerythrin show two high-spin iron(II) ions in its desoxy form. Within oxy- and met-hemerythrin, two high-spin iron(II) centers are detected which are linked antiferromagnetically via a μ -oxy group. This coupling is strong enough to allow this compound to be diamagnetic in the ground state. The remaining paramagnetism at room temperature influences the characteristics of a solution of the protein, however.³⁶

Finding model compounds for iron proteins which are able to bind dioxygen reversibly was an early ambition.³⁶ A successful example is the $[\text{Fe}_2\text{O}(\text{O}_2\text{CR})_2]^{2+}$ unit of hemerythrin that was used in a variety of model compounds. $[\text{Fe}_2\text{O}(\text{O}_2\text{CCH}_3)_2(\text{HBpz}_3)_2]$ is one compound of this kind, HBpz_3^- is the

hydrotris(pyrazoyl)borate anion. It was possible to model magnetic and spectroscopic characteristics of the binuclear azidomet hemerythrin excellently.³⁶ The bridging oxido group of this model complex can be reversibly protonated, as already found for hemerythrin. During this protonation, a hydroxido bridged diiron(III) derivate is formed. If the compound is protonated at the μ -oxido ligand the Fe-O bond changes from 17.8 to 19.6 pm and the color changes from green-brown to orange. Furthermore, the antiferromagnetic interchange coupling constant is lowered noticeably after protonation. In addition, a model complex for desoxy hemerythrin was developed. $[\text{Fe}_2(\text{OH})(\text{O}_2\text{CCH}_3)_2(\text{Me}_3\text{TACN})_2]^{2+}$ that is similar to its natural analogue in structure and spectroscopy.

38-41

1.9 Tripodal ligands

Low molecular weight copper and iron complexes have been used in the past to model the active site of the according metalloproteins. In that context it was found that the tripodal ligand tris(2-pyridylmethyl)amine (tmpa; also abbreviated as tpa in the literature⁴²), is quite useful in various topics within the bioinorganic chemistry. The ligand tmpa can be seen in Figure 1-8.

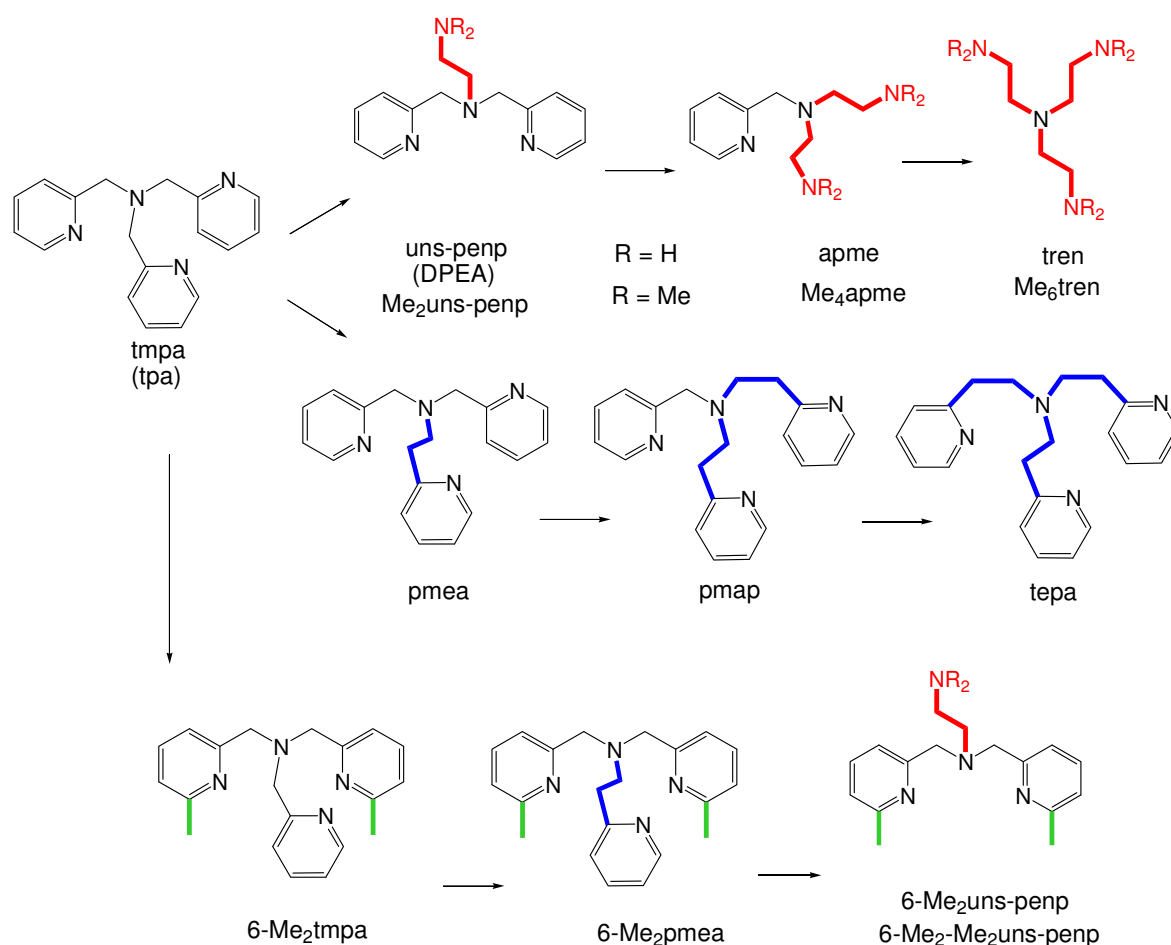


Figure 1-8: Abbreviations used for tripodal ligands: left: tris(2-pyridylmethyl)amine (tmpa). Top row: (2-aminoethyl)bis(2-pyridylmethyl)amine (uns-penp, R = H), N¹-(2-aminoethyl)-N¹-(2-pyridylmethyl)-1,2-ethandiamine (apme, R = H) and tris(2-aminoethyl)amine (tren; R = H). Middle row: N²,N²-bis[(2-pyridyl)methyl]-2-(2-pyridyl)ethylamine (pmea), N²,N²-bis[2-(2-pyridyl)ethyl]-(2-pyridyl)methylamine (pmap) and tris[2-(2-pyridyl)ethyl]amine (tepa). Bottom row: tris((6-methylpyridin-2-yl)methyl)amine (6-Me₂tmpa), 2-(6-methylpyridin-2-yl)-N,N-bis((6-methylpyridin-2-yl)methyl)ethanamine (6-Me₂pmea), N¹,N¹-bis((6-methylpyridin-2-yl)methyl)ethane-1,2-diamine (6-Me₂-uns-penp; R = H) and N¹,N¹-dimethyl-N²,N²-bis((6-methylpyridin-2-yl)methyl)ethane-1,2-diamine (6-Me₂-Me₂uns-penp; R = CH₃).

Tripodal ligands with a copper center were used to mimic the reversible binding of dioxygen at the active site of copper proteins.⁴³⁻⁴⁸ K. Karlin and coworkers reacted $[\text{Cu}(\text{tmpa})(\text{CH}_3\text{CN})]\text{PF}_6$ with dioxygen at low temperatures and were thus able to prepare the first binuclear peroxido-bridged copper(II) complex using the tripodal ligand tmpa.⁴⁹ Later studies using low-temperature stopped-flow techniques indicated a formation of a superoxido- prior to a peroxido complex.⁵⁰ Figure 1-9 shows this oxidized copper(II) complex $[\{\text{Cu}(\text{II})(\text{tmpa})\}_2(\text{O}_2)]^{2+}$. Further examples for copper dioxygen adduct complexes using tripodal ligands have been obtained by Weitzer et al.⁵¹⁻⁵², Schatz et al.⁵³⁻⁵⁵ and others.^{49, 56-62}

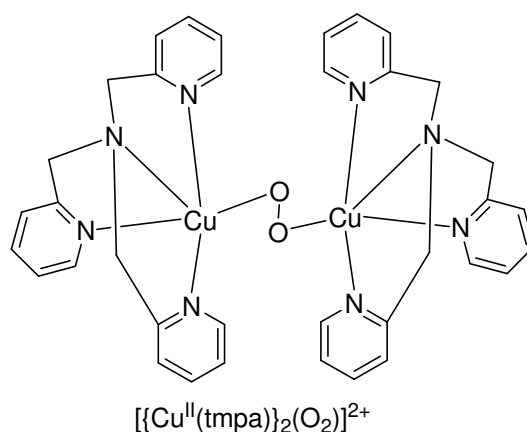


Figure 1-9: First structurally characterized copper peroxido complex.⁴⁹

To model the function of non-heme iron proteins, tripodal ligands are quite useful here as well.^{39-40, 63-64} For example Que et al. succeeded in the synthesis of the model complex $[\text{Fe}^{\text{II}}(6\text{-Me}_3\text{-tmpa})(\text{BF})]^+$ for enzymes that depend on α -keto acids (Figure 1-10).⁴¹ This complex was reacted with dioxygen and caused a quantitative conversion of benzoylformate to benzoic acid and CO_2 . This oxidative decarboxylation is a characteristic reaction for these kind of enzymes.⁶⁵⁻⁶⁶

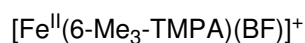
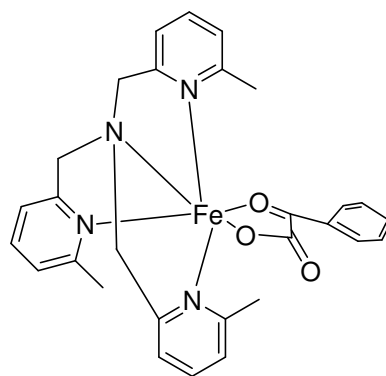


Figure 1-10: Model complex for α -keto acid depending enzymes.⁴¹

Tripodal ligands shown in Figure 1-8 can occupy four coordination positions of the central atom. Frequently the donor atoms are identical, however tripodal ligands can be composed of different atoms as well. Known donor atoms for this type of tripodal ligands are N, P, O and S. The “arms” can be varied by length and structure and led to a multitude of compounds.⁶⁷ Aliphatic and aromatic “arms” can be combined.

If each of the aromatic pyridine rings of the ligand tmpa is changed to aliphatic donor groups, 2-aminoethyl(2-pyridylmethyl)-1,3-ethanediamine (apme) and bis(2-pyridylmethyl)-1,2-ethanediamine (uns-penp; also named DPEA in the literature⁶⁸) as well as tris(2-aminoethyl)amine (tren), are obtained (Figure 1-8). Methylation of these ligands leads to the ligands Me₆tren, Me₂uns-penp and Me₄apme. If one of the aromatic amine “arms” in tmpa is extended by one CH₂-group, this leads to the ligand N²,N²-bis[(2-pyridyl)methyl]-2-(2-pyridyl)ethylamine (pmea), if two donor groups are extended, this leads to N²,N²-bis[2-(2-pyridyl)ethyl]-(2-pyridyl)methylamine (pmap) and three lead to tris[2-(2-pyridyl)ethyl]amine (tepa).

As a further possibility, the ligand tmpa can be varied by adding methyl groups into the aromatic ring (see Figure 1-8). In this work the six positions of two pyridine rings were chosen to compare the methylated variations with their parent ligands tmpa, pmea, uns-penp and Me₂uns-penp. The resulting ligands are tris((6-methylpyridin-2-yl)methyl)amine (6-Me₂tmpa; also abbreviated as 6-Me₂TPA in

the literature⁶⁹) if two methyl groups are introduced into the tmpa system, 2-(6-methylpyridin-2-yl)-N,N-bis((6-methylpyridin-2-yl)methyl)ethanamine (6-Me₂pmea), if the two shorter donor groups of pmea are methylated, and N¹,N¹-bis((6-methylpyridin-2-yl)methyl)ethane-1,2-diamine (6-Me₂-uns-penp) as well as N¹,N¹-dimethyl-N²,N²-bis((6-methylpyridin-2-yl)methyl)ethane-1,2-diamine (6-Me₂-Me₂uns-penp) if the two aromatic ligand groups of uns-penp or Me₂uns-penp are methylated.

Tripodal ligands with iron(II) centers further proved to be very interesting for studying the spin transition phenomenon (see above in Chapter 1-6). In early works, for example from Gütlich and co-workers, a spin transition was proven in an intermediate ligand field only.²⁹ The Tanabe-Sugano diagram⁷⁰ shows, that for an octahedral iron(II) complex with a weak ligand field the HS (⁵T₂) ground state is found, within a strong ligand field the LS (¹A₁) ground state. Thus, a spin transition can only be found within an area of an intermediate critical ligand field splitting Δ_{crit} . Toftlund and co-workers were the first to suggest SCO within iron(II) complexes, if the used ligands are composed of partially aliphatic and aromatic ligand parts with nitrogen donor atoms included.⁴² Here the same intermediate ligand field is expected, which the Tanabe-Sugano diagram requires to enable spin crossover. The work of F. Højland et al. demonstrated the forecasted result by using tmpa as a ligand. Later works used these conclusions and found other ligands that caused similar results; see for example the work of T. Buchen et al.⁷¹, G.S. Matouzenko et al.,^{68, 72} F. Renz et al.⁷³, Yu et al.⁷⁴, A. A. Yousif et al.³¹, Brehm et al.⁷⁵⁻⁷⁶ as well as most recent works by Li et al.⁷⁷⁻⁷⁸ and Wei et al.⁷⁹. A particular positive influence on this effect proved nitrogen bonded thiocyanate, as a co-ligand. This led to a variety of complexes of the group [Fe(X)(NCS)₂] (X = DPPA, bptn, bpen, phen, bipy, tmpa, pmea, uns-penp). Recently a Fe^{II} four square compound was found using tmpa without additional NCS-ligands, but with dicyanamide ligands and tetraphenylborate counter-ions. This compound shows a reversible single-crystal to single-crystal transformation and a complete two step spin crossover.⁸⁰

1.10 Projects

As discussed above, tripodal ligands derived from the parent tris(2-pyridylmethyl)amine (tmpa) play an important role in bioinorganic chemistry as well as for the design of iron(II) spin crossover complexes. In that context the following projects have been investigated in this thesis:

- Synthesis and characterization of copper complexes with the ligand 2-aminoethyl(2-pyridylmethyl)-1,2-ethanedi-amine (apme) and investigations with regard to the reactivity of the according copper(I) complexes towards dioxygen (Chapter 2).
- Investigation of ligand influence of copper complexes derived from macrocyclic ligands that are based partially on the ligand apme (see Figure 1-11 and Chapter 3).

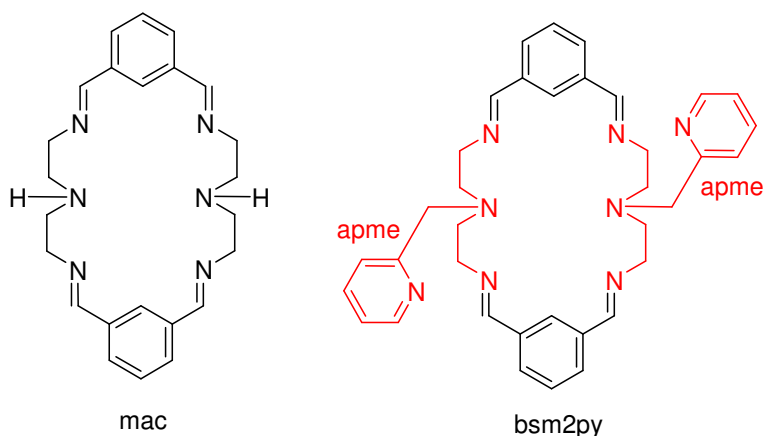


Figure 1-11: The ligands mac (mac = 3,6,9,17,20,23-hexaazatricyclo[23.3.1.1]triaconta-1(29),2,9,11(30),12(13),14,16,23,25,27-decaene) and bsm2py (bsm2py = 6,20-bis(pyridin-2-yl)methyl),3,6,9,17,20,23-hexaazatricyclo[23.3.1.1]triaconta-1(29),2,9,11(30),12(13), 14,16,23,25,27-decaene).

- Investigation of the reaction of the mononuclear copper(I) complex with dioxygen using "half" of the macrocycle mac (7E)-N¹-benzylidene-N²-((E)-2-(benzylideneamino)ethyl)ethane-1,2-diamine (L¹) as a ligand (see Figure 1-12 and Chapter 4).

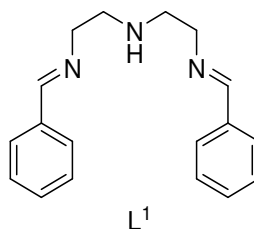


Figure 1-12: The ligand (7E)-N¹-benzylidene-N²-((E)-2-(benzylideneamino) ethyl)ethane-1,2-diamine (L^1).

- Synthesis and characterization of iron(II) complexes of the ligand apme and derivatives, as well as studies with regard to the spin crossover behavior of these compounds (Chapter 5).
- Synthesis and characterization of iron(II) complexes with tripodal ligands derived from uns-penp, tmpa and pmea, as well as studies with regard to the spin crossover behavior of these compounds (Chapter 6).
- Effects of chelate ring size in iron(II) complexes of derivatives of the ligands tmpa, pmea, pmap and tepa, as well as studies with regard to the spin crossover behavior (Chapter 7).
- Investigations of a thiocyanate trans coordinated iron(II) complex using the ligand *o*-bipy (see Figure 1-13), as well as studies with regard to the spin crossover behavior (Chapter 8).

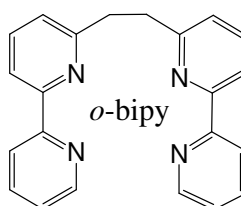


Figure 1-13: The ligand *o*-bipy⁸¹.

2 Copper Complexes with the Ligand apme

2.1 Syntheses and Characterization of Copper Complexes with the Ligand 2-Aminoethyl(2-pyridylmethyl)-1,2-ethanedi-amine (apme)

This work was published previously in the Journal of "Inorganic Biochemistry"

Utz, D.; Kisslinger, S.; Hampel, F.; Schindler, S., *J. Inorg. Biochem.* **2008**, *102*, 1236–1245 (doi:10.1016/j.jinorgbio.2008.01.028).

Modeling the reactivity of redox active copper enzymes that involve oxygen transfer during substrate oxidation (e. g. tyrosinase, a monooxygenase responsible for reactions such as *o*-hydroxylation of the benzene ring of the amino acid tyrosine)^{4-6, 82-83} has led to the synthesis and characterization of a large number of quite simple low molecular weight copper complexes that proved to be useful in studies on the activation of dioxygen.^{48, 60-61, 84-89}

During the course of these studies it was possible to isolate and to characterize several important "dioxygen" adduct complexes which represent important intermediates in substrate oxidation reactions.^{48, 58, 60-61, 84-90} In that regard it was quite an achievement when Karlin and coworkers could mimic the reversible binding of dioxygen at the active site of copper proteins using a copper(I) complex with the tetradentate tripodal ligand tris(2-pyridylmethyl)amine (tmpa, Figure 2-1). Furthermore, $[\text{Cu}_2(\text{tmpa})_2(\text{O}_2)]^{2+}$ could be isolated at low temperatures and was the first structural characterized copper(II) peroxido complex described in the literature.^{49, 91} Detailed kinetic analyses using low temperature stopped flow methods allowed to detect the formation of $[\text{Cu}(\text{tmpa})(\text{O}_2)]^+$, a superoxido complex, prior to the formation of $[\text{Cu}_2(\text{tmpa})_2(\text{O}_2)]^{2+}$.^{50, 92}

In our own work, based on these important results, we started to follow this kind of chemistry using derivatives of the compound tris(2-aminoethyl)amine (tren, Figure 2-1, R = H)^{51-52, 56, 60, 93} that can be regarded as the parental amine of tripodal ligands such as tmpa.⁶⁷

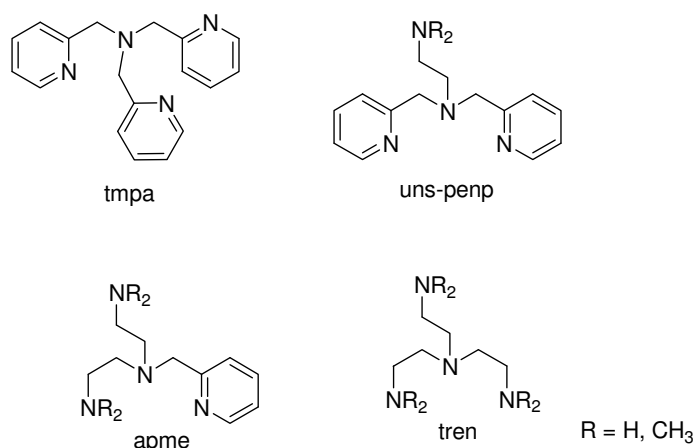


Figure 2-1: Abbreviations used for tripodal ligands: tris(2-pyridylmethyl)amine (tmpa), N¹-(2-aminoethyl)-N¹-(2-pyridyl-methyl)-1,2-ethandiamin (apme, R = H) as well as bis[2-(dimethylamino)ethyl]-(2-pyridylmethyl)amin (Me₄apme, R = CH₃) (2-aminoethyl)bis(2-pyridyl-methyl)amine (uns-penp, R = H) as well as N¹,N¹-dimethyl-N²,N²-bis(2-pyridylmethyl)-1,2-ethandiamin (Me₂uns-penp; R¹ = CH₃; R = H), tris(2-aminoethyl)amin (tren; R = H), N¹,N¹-bis(2-(dimethylamino)ethyl)-N²,N²-dimethylethane-1,2-diamine (Me₆tren; R = CH₃).

The advantage of the amine tren is, that it is commercially available and its modification is more easily accomplished compared with tmpa.^{54, 60, 93-94} Furthermore, stabilization of copper(II) complexes will be supported (hard nitrogen donor atoms) in contrast to tmpa that due to the soft nitrogen donor atoms of pyridine stabilizes copper(I) complexes to a much higher extent. Unfortunately, this is reflected in the syntheses of pure copper(I) with aliphatic amine ligands because they easily show disproportionation reactions.⁹³ In contrast, while using a tren derivative, tris(tetramethylguanidino)tren (TMG₃tren), as a ligand some of us succeeded for the first time in the isolation and structural characterization of [Cu(TMG₃(tren)O₂)SbF₆], an end-on superoxido copper complex.^{58, 90} This complex reflects very well the end-on dioxygen binding in the precatalytic enzyme complex of peptidylglycine-α-hydroxylating monooxygenase (PHM) that has been structurally characterized recently.⁹⁵

Furthermore, from a systematic study of modifying the ligand tmpa by a stepwise replacement of the pyridyl groups through amine groups we obtained the ligands (2-aminoethyl)bis(2-pyridyl-

methyl)amine (uns-penp, Figure 2-1) and 2-aminoethyl(2-pyridylmethyl)-1,2-ethanediamine (apme, Figure 2-1). Both compounds have been previously described in the literature,⁶⁷ however, so far only the methylated forms (as well as for tren; Figure 2-1, R = CH₃) proved to be useful for studies of the reactions of the according copper(I) complexes with dioxygen.^{55, 93} This is a consequence of the hydrogen atoms on the ligands that can lead to the decomposition of the formed peroxido complexes due to formation of hydrogen peroxide. This reaction has been observed for the tmpa system as well, if protic solvents were used during the oxidation reaction.

Due to the fact however, that little is known about the coordination chemistry of the ligand apme⁶⁷ we describe here the synthesis and characterization of its copper complexes.

2.2 Synthesis of ligands and complexes

The amine apme, also described as pdt in the literature, was first described by Fenton and coworkers who used it as a building block for the preparation of macrocyclic ligands.^{67, 96-99} However, the synthesis was problematic and yields were low. More recently alternative synthetic routes were provided by Skinner and coworkers¹⁰⁰⁻¹⁰¹ and by Cheng et al.¹⁰² We used a method here that is based on the method of Cheng et al., however we used a different second synthetic reaction step that provided apme in good yields. Here we performed an in situ reductive alkylation using 2-pyridylcarbaldehyde and NaBH(OAc)₃.¹⁰³ This route avoids the need of using the unpleasant chemical picolyl chloride and has been used by us and others for the synthesis of uns-penp, apme (reported herein) and the methylated forms of these amines (Figure 2-1).^{55, 104} Kugelrohr distillation of apme was necessary because otherwise it could be problematic to obtain pure samples. Apme prepared in this way has been recently used again for the preparation of a new interesting macrocyclic ligand and its metal complexes.¹⁰⁵ To the best of our knowledge so far only a zinc complex of apme, [Zn(apme)(H₂O)]²⁺ (prepared in aqueous solution), has been reported together with stability and acidity constants.¹⁰⁶ However, according to the Cambridge Structural Database no crystallographic characterization of a metal complex using apme as ligand has been reported so far.

Despite the fact that we were aware of the difficulties in the synthesis of copper(I) complexes with aliphatic amines (as described above) we successfully could react copper(I) complex salts $[\text{Cu}(\text{CH}_3\text{CN})_4]\text{ClO}_4$ and $[\text{Cu}(\text{CH}_3\text{CN})_4]\text{CF}_3\text{SO}_3$ with apme and obtained solid materials that could be structurally characterized. As observed previously for the copper(I) complex of uns-penp the formed complex is dinuclear and not mononuclear as would be expected for such a tripodal ligand system (and has been observed for the tmpa complex previously).⁵⁵ The molecular structure of the cation of **1** is shown in Fig. 2-2.

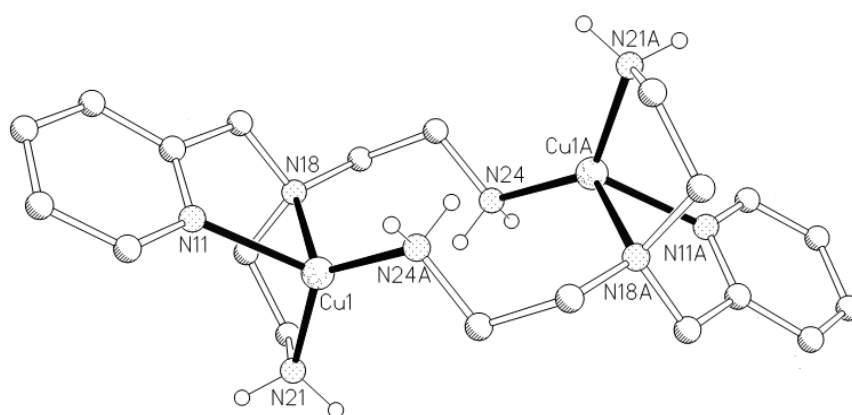


Figure 2-2: Molecular structure of the cation of $[\text{Cu}_2(\text{apme})_2]^{2+}$ (**1**).

The dinuclear complex displays a center of inversion in the middle of the Cu(1)-Cu(1A) axis. Each copper(I) ion is coordinated in a distorted trigonal pyramidal manner by one pyridine donor, one tertiary amine and two primary amine functions, with one arm of the ligand forming a bridge to the other copper(I) center. The trigonal plane is made up by N(21), N(11) and N(24A) with $\text{N}(24\text{A})\text{-Cu}(1)\text{-N}(21) = 134.13(6)^\circ$, $\text{N}(24\text{A})\text{-Cu}(1)\text{-N}(11) = 115.36(6)^\circ$ and $\text{N}(21)\text{-Cu}(1)\text{-N}(11) = 105.03(6)^\circ$, while N(18) forms the top of the pyramid. The copper(I) ions are shifted by 0.270 Å out of the equatorial planes towards N(18) and N(18A), respectively. The copper(I)-N-distances are in the normal range for such complexes, and the Cu(1)-Cu(1A) distance is with 4.487 Å quite similar to the reduced form of catechol oxidase, an enzyme related to tyrosinase.^{82, 107} The hydrogen atom H(21b) at the primary amine forms hydrogen bonds to the counterion with a distance of 2.408 Å for H(21b)-O(2) and 2.494 Å for H(21b)-O(1), respectively.

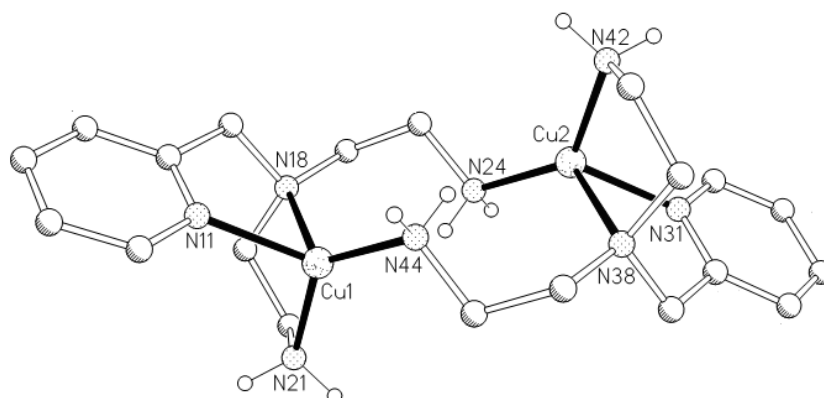


Figure 2-3: Molecular structure of the cation of $[\text{Cu}_2(\text{apme})_2]^{2+}$ (**2**).

2 that differs from **1** only by the anion is very similar to this complex. However, in contrast to **1**, **2** does not possess a center of inversion making the two copper(I) ions equivalent. Crystal data can be found in the Tables 2-1 and 2-2. A figure of the molecular structure of **2** is shown in Figure 2-3.

Table 2-1: Crystal data and structure refinement for **1**, **2**, **3** and **4**.

Compound	[Cu ₂ (apme) ₂](ClO ₄) ₂ (1)	[Cu ₂ (apme) ₂](CF ₃ SO ₃) ₂ (2)	[Cu(apme)Cl] BPh ₄ (3)	[Cu(apme)(DMF)] BPh ₄ (4)
Chemical formula	C ₁₀ H ₁₈ N ₄ CuClO ₄	C ₁₁ H ₁₈ N ₄ CuF ₃ O ₃ S	C ₃₇ H ₄₅ N ₅ CuClBO	C ₆₄ H ₇₂ N ₆ CuB ₂ O ₂
Formula weight	357.27	406.89	685.58	1042.44
Temperature (K)	173(2)	173(2)	173(2)	173(2)
Wavelength (Å)	0.71073	0.71073	0.71073	0.71073
Space group	P2 ₁ /c	P2 ₁ /n	P-1	Cc
a (Å)	9.6566(2)	14.7596(3)	10.9803(1)	17.9649(2)
b (Å)	10.1755(2)	10.1171(2)	12.4384(2)	12.8478(2)
c (Å)	14.5125(4)	21.7103(4)	13.6573(2)	25.478 (4)
α (°)	90	90	84.809(1)	90
β (°)	95.8830(10)	96.016(1)	71.945(1)	101.224(1)
γ (°)	90	90	77.020(5)	90
Volume (Å ³)	1418.50(6)	3224.0 (1)	1727.68(4)	5768.2 (4)
Z	4	8	2	4
Density calc. (Mg/m ³)	1.673	1.677	1.318	1.200
Absorption coeff. (mm ⁻¹)	1.746	1.534	0.747	0.427
R indices [I>2σ(I)]	R1(F _o) = 0.0300 wR2(F _o ²) = 0.0797	R1(F _o) = 0.0384 wR2(F _o ²) = 0.0973	R1(F _o) = 0.0365 wR2(F _o ²) = 0.0995	R1(F _o) = 0.0463 wR2(F _o ²) = 0.1122
R indices (all data)	R1(F _o) = 0.0349 wR2(F _o ²) = 0.0824	R1(F _o) = 0.0636 wR2(F _o ²) = 0.1083	R1(F _o) = 0.0454 wR2(F _o ²) = 0.1047	R1(F _o) = 0.0637 wR2(F _o ²) = 0.1209

$$R1(F_o) = \sum ||F_o| - |F_c|| / \sum |F_o|; wR2(F_o^2) = (\sum [w(F_o^2 - F_c^2)^2] / \sum [w(F_o^2)^2])^{1/2}$$

$$R(F_o) = \sum (|F_o - F_c|) / \sum (F_o); Rw(F_o) = \sum [(|F_o - F_c|) \cdot w^{1/2}] / \sum [F_o \cdot w^{1/2}]$$

Table 2-2: Bond lengths [Å] and angles [°] for **1**, **2**, **3** and **4**.

1				2			
Bond lengths		Bond angles		Bond lengths		Bond angles	
Cu(1)-N(24A)	1.988 (5)	N(24A)-Cu(1)-N(21)	134.13(6)	Cu(1)-N(44)	1.978 (9)	N(44)-Cu(1)-N(21)	132.88(8)
Cu(1)-N(11)	2.081 (5)	N(24A)-Cu(1)-N(11)	115.36(6)	Cu(1)-N(11)	2.067(2)	N(44)-Cu(1)-N(11)	117.40(8)
Cu(1)-N(21)	2.034 (6)	N(21)-Cu(1)-N(11)	105.03(6)	Cu(2)-N(24)	1.982 (9)	N(21)-Cu(1)-N(11)	104.14(8)
Cu(1)-N(18)	2.296 (4)	N(24A)-Cu(1)-N(18)	123.34(6)	Cu(2)-N(31)	2.071(2)	N(44)-Cu(1)-N(18)	125.00(8)
Fe(1)-N(1)	2.242(2)	N(21)-Cu(1)-N(18)	123.34(6)	Cu(1)-N(21)	2.034(2)	N(21)-Cu(1)-N(18)	82.53(7)
				Cu(1)-N(18)	2.351 (8)	N(11)-Cu(1)-N(18)	78.66(7)
				Cu(2)-N(42)	2.028(2)	N(24)-Cu(2)-N(42)	134.91(8)
				Cu(2)-N(38)	2.355 (9)	N(24)-Cu(2)-N(31)	115.69(8)
						N(42)-Cu(2)-N(31)	104.55(8)
						N(24)-Cu(2)-N(38)	123.53(8)
						N(42)-Cu(2)-N(38)	82.78(7)
						N(31)-Cu(2)-N(38)	78.11(7)
3				4			
Bond lengths		Bond angles		Bond lengths		Bond angles	
Cu(1)-N(21)	2.045 (5)	N(21)-Cu(1)-N(11)	81.64(6)	Cu(1)-N(10)	2.016(2)	O(1)-Cu(1)-N(10)	175.82(10)
Cu(1)-N(14)	2.064 (6)	N(21)-Cu(1)-N(14)	128.69(7)	Cu(1)-N(13)	2.060(2)	O(1)-Cu(1)-N(11)	93.5 (1)
Cu(1)-Cl(1)	2.2741(5)	N(11)-Cu(1)-N(14)	84.40(6)	Cu(1)-O(1)	1.960(2)	N(10)-Cu(1)-N(11)	82.8 (1)
Cu(1)-N(11)	2.046 (4)	N(21)-Cu(1)-N(17)	115.87(6)	Cu(1)-N(11)	2.032(3)	O(1)-Cu(1)-N(13)	97.7(1)
Cu(1)-N(17)	2.128 (5)	N(11)-Cu(1)-N(17)	83.87(6)	Cu(1)-N(16)	2.129(2)	N(10)-Cu(1)-N(13)	86.2(1)
		N(14)-Cu(1)-N(17)	111.28(7)			N(11)-Cu(1)-N(13)	127.6(1)
		N(21)-Cu(1)-Cl(1)	97.99(5)			O(1)-Cu(1)-N(16)	94.2(1)
		N(11)-Cu(1)-Cl(1)	179.39(4)			N(10)-Cu(1)-N(16)	85.20(9)
		N(14)-Cu(1)-Cl(1)	95.47(5)			N(11)-Cu(1)-N(16)	113.9(1)
		N(17)-Cu(1)-Cl(1)	96.73(4)			N(13)-Cu(1)-N(16)	116.0(1)

In contrast to copper(I) chemistry it is quite easy to obtain copper(II) complexes with this type of ligand. Here we used apme together with chloride as an additional co-ligand and obtained crystals of **3** suitable for X-ray crystallography. The molecular structure of the cation of **3** is shown in Figure 2-4.

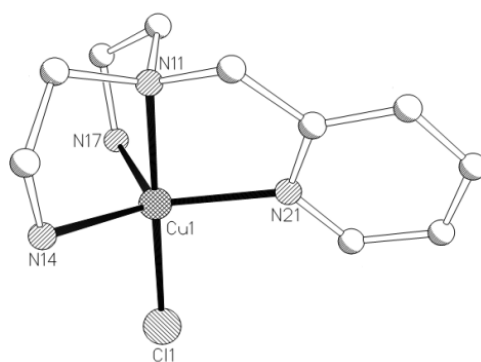


Figure 2-4: Molecular structure of the cation of $[\text{Cu}(\text{apme})\text{Cl}]^+$ (**3**).

In contrast to **1** and **2**, a mononuclear species is formed here with the copper(II) ion. The copper(II) ion is coordinated in a distorted trigonal bipyramidal manner with a τ factor of 0.85 ($\tau = 0$ for a square pyramidal, $\tau = 1$ for a trigonal bipyramidal geometry).¹⁰⁸ The pyridine and two primary amine donor atoms form the equatorial trigonal plane, while the tertiary amine group and the chloro ligand occupy the apical positions. The copper(II) ion is shifted by 0.244 Å out of the equatorial plane towards the chloro ligand. One DMF molecule from the solvent is included in the crystal lattice and disordered.

The crystal structure of **3** is very similar to $[\text{Cu}(\text{uns-penp})(\text{Cl})]^+$ and has nearly identical bond lengths and very similar bond angles.⁵⁵ In contrast to these compounds, reported copper(II)-chloro complexes of tren form dimers with trigonal-bipyramidal as well as square pyramidal geometries.¹⁰⁹⁻¹¹⁰ The complex $[\text{Cu}(\text{tmpa})\text{Cl}]^+$ shows a trigonal bipyramidal coordination of the copper(II)-center and the chloro- and the tertiary amino ligand can be found at apical positions.¹¹¹ Because of the higher symmetry this compound is probably less distorted than **3**, however it only shows small differences in bond lengths and angles as well.

During the crystallization of **3** complex **4** was obtained as a side product. The molecular structure of the cation of **4** is shown in Fig. 2-5.

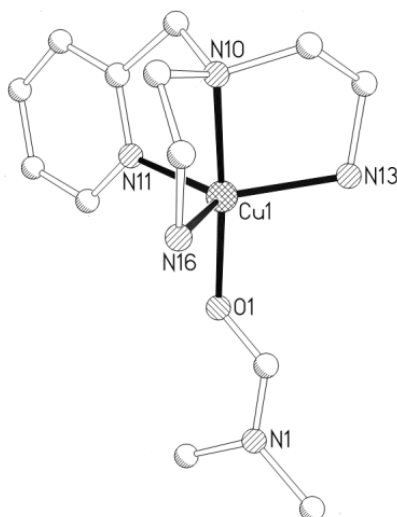


Figure 2-5: Molecular structure of the cation of $[\text{Cu}(\text{apme})(\text{DMF})]^+$ (**4**).

To the best of our knowledge, **4** is the first structurally characterized copper(II) complex containing four nitrogen donors and a coordinated DMF molecule which displays a distorted trigonal bipyramidal coordination sphere with a τ factor of 0.80. N(16), N(11) and N(13) form the trigonal equatorial plane with $\text{N}(11)\text{-Cu}(1)\text{-N}(16) = 113.85(10)^\circ$, $\text{N}(13)\text{-Cu}(1)\text{-N}(16) = 116.01(10)^\circ$ and $\text{N}(11)\text{-Cu}(1)\text{-N}(13) = 127.62(10)^\circ$. The tertiary amine donor N(10) and the oxygen donor of DMF occupies the apical positions with $\text{O}(1)\text{-Cu}(1)\text{-N}(10) = 175.82(10)^\circ$. All bond lengths are very similar to **3**, and the copper(II) ion is shifted by 0.190 Å out of the trigonal plane towards the O-donor. The $\text{Cu}(1)\text{-O}(1)$ distance is with 1.960(2) Å significantly shorter than in square pyramidal coordinated copper(II) complexes with 4 nitrogen donors and DMF as additional ligand.¹¹²⁻¹¹⁴ The crystals are racemic twins in 47:53 ratio.

2.3 Investigation of the solution behavior of **1** and **2**

The solution behavior of **1** and **2** was investigated by NMR spectroscopy. NMR spectra of both **1** and **2** in DMSO-d_6 at room temperature showed very broad unresolved signal indicating equilibria in solution. Therefore low temperature techniques were applied. The use of DMF-d_6 down to -55°C was unsuccessful because only very broad signals were observed in the spectra, while with CD_3CN at -35°C well resolved signals could be obtained. Fig. 2-6 shows the ^1H NMR spectra of **2** in CD_3CN at -35 , -5 , $+5$ and $+25^\circ\text{C}$.

The NMR spectrum at -35°C shows one broad signal for the NH protons at 2.39 ppm, two unresolved signals for the CH_2 groups in the ethylene units at 2.57 and 2.76 ppm and one sharp singlet for the CH_2 group at the pyridine ring at 3.95 ppm. In the aromatic region a multiplet for the protons in meta position to the pyridine nitrogen was observed at 7.38 ppm, a doublet of doublet for the para proton at 7.84 and a doublet for the ortho proton at 8.55 ppm. This highly symmetric pattern in the NMR spectrum does not fit to the molecular structure in the solid state but indicates the formation of a highly symmetric species in solution.

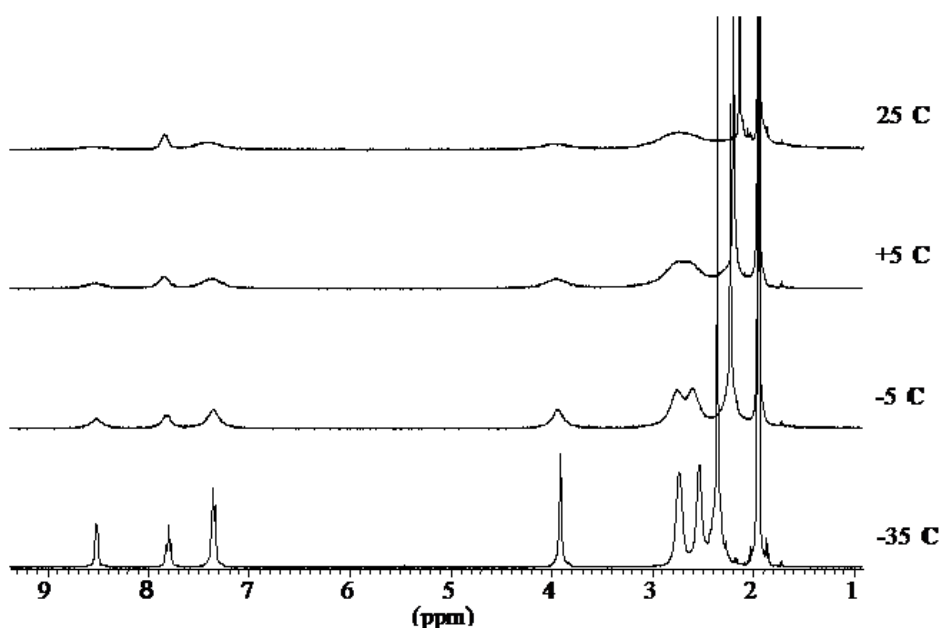


Figure 2-6: Low temperature NMR spectra of **2** in CD_3CN at -35°C , -5°C , $+5^{\circ}\text{C}$ and $+25^{\circ}\text{C}$.

Furthermore, the small signal at 1.95 ppm which is high field shifted compared to the main signal for CD_2HCN indicates the coordination of a solvent molecule. Therefore we suggest a mononuclear trigonal bipyramidal coordinated species, $[\text{Cu}(\text{apme})\text{CH}_3\text{CN}]^+$, in solution with the tertiary amine and one acetonitrile molecule in the axial positions and a symmetry plane through the pyridine ring, the acetonitrile molecule and the tertiary amine, dividing the molecule into two equivalent parts as shown in Fig. 2-7 (and as discussed above has been observed for the analogous type complex previously).⁵⁵ The two diastereotopic protons at each carbon atom in the chemically equivalent ethylene units result in two different signals for the syn and anti protons which show coalescence at $+5^{\circ}\text{C}$ due to decooordination, rotation and subsequent coordination of the N-donors to the copper(I) center

making the diastereotopic protons equivalent. The calculated value of ΔG^\ddagger for this process is 56 kJ (± 2 kJ).

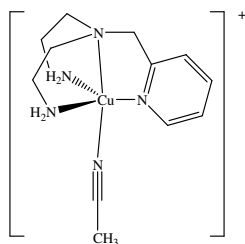


Figure 2-7: Suggested monomer formed in solution.

2.4 Results of Electrochemistry

The cyclic voltammogram of **2** shows a reversible oxidation behavior with two oxidation and reduction waves with the heights of the first redox wave significantly smaller than that of the second one. This redox behavior might be due to the presence of two different species in solution. The redox potentials are -0.46 V with $E_{\text{Ox}} = -0.41$ V and $E_{\text{Red}} = -0.51$ V and -0.24 V with $E_{\text{Ox}} = -0.18$ V and $E_{\text{Red}} = -0.30$ V, respectively, and are in the usual range for the Cu(I)/Cu(II) redox pair. For **3**, CV investigations show a reversible redox behavior with $E_{\text{Redox}} = -0.46$ V ($E_{\text{Red}} = -0.54$ V and $E_{\text{Ox}} = -0.38$ V) for the Cu(II)/Cu(I) redox couple. From the similar values for E_{Redox} for the first oxidation wave of **2** and for **3** we conclude that both species possess a very similar ligand environment.⁶⁷ So the first oxidation wave of **2** may be assigned to a mononuclear species in solution. The cyclic voltammograms of **2** and for **3** are shown in Figure 2-8.

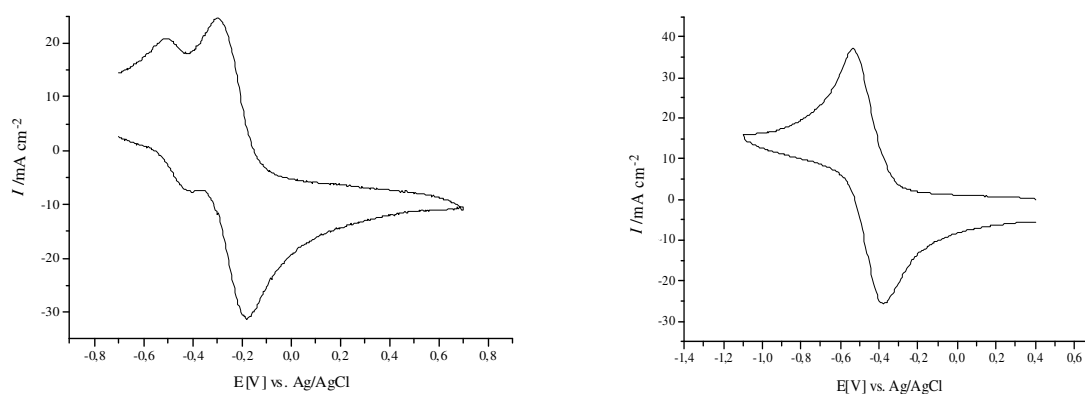


Figure 2-8: Cyclic Voltammogram of **2** (left) and **3** (right).

2.5 Results of time resolved UV-Vis Spectroscopy

The reactivity of the copper(I) complex **1** towards dioxygen was investigated using low temperature stopped-flow techniques to detect possible reactive copper "dioxygen adduct" complexes during the course of the reaction. This method has been applied successfully by us and others previously for the spectroscopic detection of copper superoxido or peroxido complexes.^{50-52, 60, 92, 115}

Time resolved spectra collected in CH_2Cl_2 at -87°C (Figure 2-9) showed the formation of a very labile species that decomposed under these conditions in less than a second. Therefore, resonance Raman spectra to further characterize this transient compound were not possible, however due to our previous work on such systems we can assign the well known UV-vis spectral features (for this type of compounds), the absorbance maximum at 400 nm ($\epsilon = 2000 \pm 200 \text{ M}^{-1}\text{cm}^{-1}$), to the mononuclear end-on superoxido complex $[(\text{apme})\text{Cu}(\text{O}_2)]^+$. This is supported furthermore by the fact, that we could fully characterize (including crystallography) such a species with a related tren based ligand recently.^{58, 116} No detailed kinetic study was possible because the reaction was too fast to be measured under these conditions.

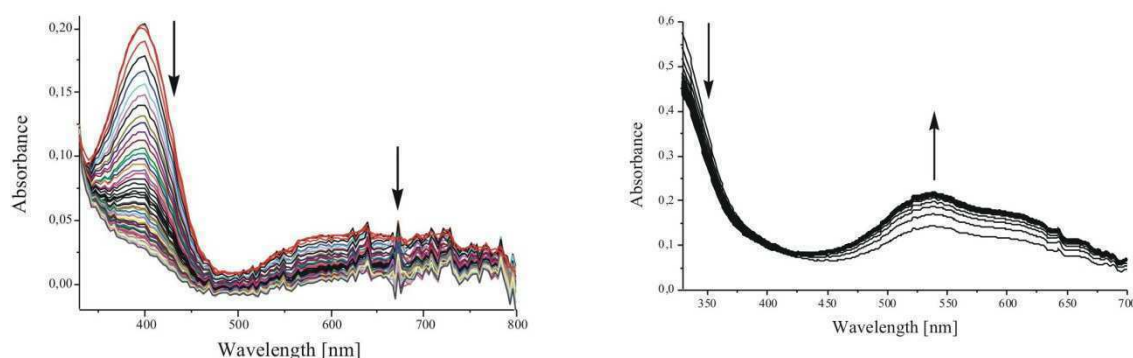


Figure 2-9: Time resolved UV/vis spectra for the reaction of an in situ reaction of apme $[\text{Cu}(\text{CH}_3\text{CN})_4]\text{ClO}_4$ and O_2 in CH_2Cl_2 at -87°C (left) and in acetone at -90°C (right); $[\text{complex}] = 5 \times 10^{-5} \text{ mol/L}$, $[\text{O}_2] = 5.1 \times 10^{-3} \text{ mol/L}$ in acetone, $t = 1.47 \text{ s}$ in CH_2Cl_2 ; $t = 0.76 \text{ s}$ in acetone.

Such reactions with dioxygen have turned out to be strongly dependant on solvent and therefore we tried acetone as an alternative as well (even so that it might be a problematic solvent for these studies due to possible imine formation under the conditions applied). Time resolved UV-vis spectra collected in acetone (Figure 2-9) showed an absorbance maximum at 539 nm ($\epsilon = 4400 \pm 200 \text{ M}^{-1}\text{cm}^{-1}$) and again can be assigned clearly due to the well known UV-vis spectral features (for this type

of compounds) as $[(\text{apme})\text{Cu}(\text{O}_2)\text{Cu}(\text{apme})]^{2+}$, a dinuclear peroxido species similar to the fully characterized complexes with related tren or tmpa based ligands.^{50-52, 92-93} However, again the reaction was too fast for a detailed kinetic analysis. A superoxido intermediate complex could not be observed under these conditions. This is different for the reactions of $[\text{Cu}_2(\text{uns-penp})_2]^{2+}$, where the decay of a superoxido complex ($\lambda_{\text{max}} = 426 \text{ nm}$) and the formation of a peroxido complex ($\lambda_{\text{max}} = 535 \text{ nm}$) was observed.⁵⁵

The results fit well to our previous investigations on the oxidation of copper complexes with tren based ligands and can be summarized in the following way: In dichloromethane the copper apme complex reacts extremely fast with dioxygen to form the very unstable superoxido complex similar as described for the tmpa system.^{50, 92} However, in contrast to the tmpa system it does not react further to a dinuclear copper peroxido complex. This is a consequence of the presence of protons in the ligand that allow a consecutive decomposition route leading finally to hydrogen peroxide (decomposing finally to water and dioxygen) and a copper(II) apme complex. This behavior is very similar to the reaction that has been observed spectroscopically for the related copper(I) complex of tren.⁶⁰ Furthermore, similar reaction behavior and the formation of hydrogen peroxide was observed again for the copper tmpa system if the reaction of $[\text{Cu}(\text{tmpa})(\text{CH}_3\text{CN})]^+$ with O_2 was performed in protic solvents such as methanol.

The reaction behavior of the complex in acetone is slightly more complex. Here we think that dinuclear species **1** is present in solution and thus providing a preorganized dinuclear complex for the fast formation of a dinuclear (or polynuclear) copper peroxido complex. Again related reactions were observed for copper complexes with tmpa and related ligands.^{92, 116} Different to these complexes is only that here as well as for the superoxide complex in dichloromethane the decomposition route to the according copper(II) complex and hydrogen peroxide exists thus preventing to obtain a more stable copper apme peroxido complex.

2.6 Summary

In summary we could prepare and characterize copper complexes with the ligand apme. Interestingly and as pointed out previously by Blackman, this ligand so far has not been used intensively in coordination chemistry despite the fact that it has been known for quite some time.⁶⁷ It allows, especially in bioinorganic chemistry, to study the effect of subsequent substitution of pyridyl arms through aliphatic amine groups (in the series with tmpa, uns-penp and tren; Figure 2-1) on the reactivity of the according metal complexes. Furthermore, similar to tren and to uns-penp it is a versatile ligand that can be easily modified (tren all three arms, apme two arms and uns-penp one arm) and it is likely that more use of this is made in the near future.^{54, 60}

In general there is a large number of possible pathways for copper(I) complexes to react with dioxygen to form a series of different possible reaction intermediates active in the oxidation of a substrate. Some of these reactions are shown in Figure 2-10.

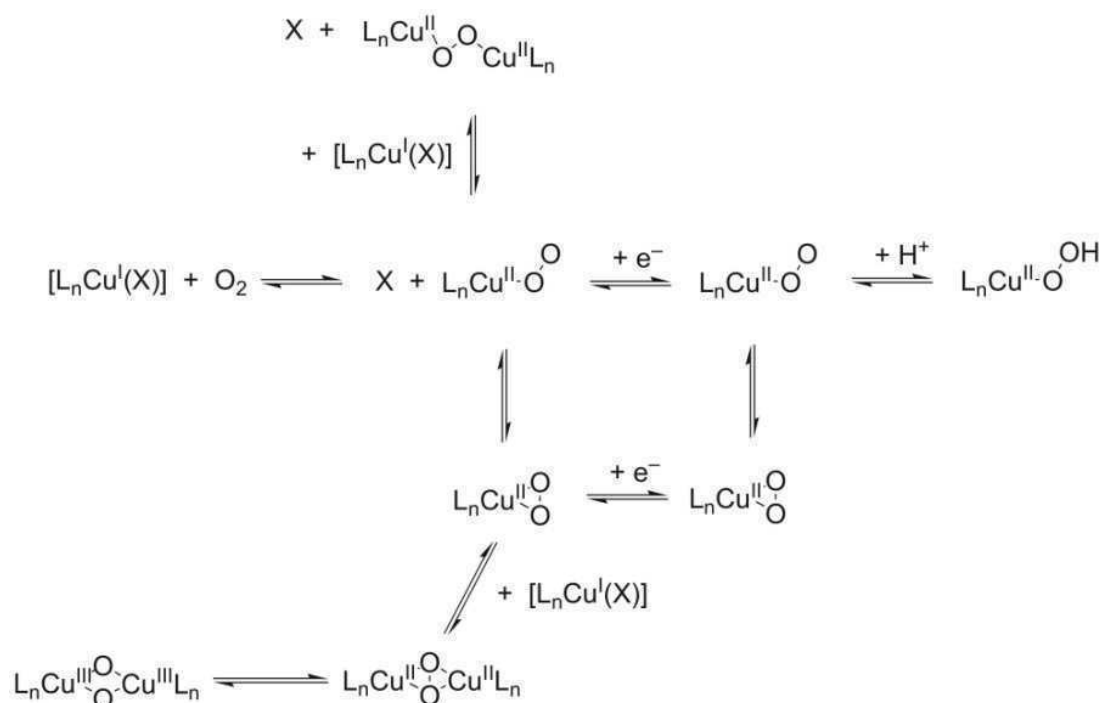


Figure 2-10: Possible pathways for copper(I) complexes to react with dioxygen.

Enzymes such as the copper monooxygenases dopamine β -monooxygenase (D β M) and peptidyl-glycine α -hydroxylating monooxygenase (PHM) are involved in neurohormone and neurotransmitter biosynthesis.¹¹⁷⁻¹¹⁸ Active-site substrate C-H hydroxylation reactions, which involve H-atom abstraction herein play an important role and mononuclear copper "dioxygen-adduct" complexes such as copper superoxide or copper hydroperoxide are considered as possible active intermediates.¹¹⁹ A recent crystallographic study of PHM supports this because in the active site of the enzyme an end-on coordination of a superoxido ligand to the copper(II) center has been observed.⁹⁵ With our previous crystallographic characterization of a model complex for this enzyme we recently could demonstrate that this compound itself actually does not affect C-H activation and that the true oxidant may be either the analogous mononuclear copper hydroperoxido complex or species derived from it, such as Cu(III)=O, a high valent copper oxido moiety.¹¹⁹

Due to the fact that reactions with the model complexes have been performed in aprotic solvents the question is open what happens in the natural systems in the presence of water. Our complexes described above might help here to further gain a better understanding on the reactive species responsible for the selective oxidation of substrates in aqueous systems. However, even so it could be demonstrated that mononuclear copper superoxido complexes could be observed under protic conditions, the compounds investigated so far are not stable enough for more detailed studies. Therefore, we hope that with a systematic modification of apme, uns-penp or tren the goal can be achieved to actually succeed in spectroscopically following reactions of dioxygen with copper(I) complexes in aqueous solutions at room temperature.

2.7 Experimental Section

2.7.1 Materials and Methods

Reagents and solvents used were of commercially available reagent quality. Organic solvents used in the syntheses of the copper(I) complexes were dried in the usual way.¹²⁰ $[\text{Cu}(\text{CH}_3\text{CN})_4]\text{X}$ ($\text{X}=\text{ClO}_4$, CF_3SO_3) was synthesized according to the literature.¹²¹

Preparation and handling of air-sensitive compounds was carried out in a glove box filled with argon (Braun, Germany; water and dioxygen less than 1 ppm). Samples for NMR spectra were prepared in the glove box.

Solutions for the collection of time-resolved UV/vis spectra in low-temperature stopped-flow measurements of the complexes were prepared in a glovebox and transferred to a low-temperature stopped-flow instrument by means of syringes. Dioxygen-saturated solutions were prepared by bubbling dioxygen through acetone or dichloromethane at 25°C. The reaction was studied under pseudo-first-order conditions ($[\text{complex}] \ll [\text{O}_2]$). Time-resolved UV/vis spectra of the reactions were recorded with a modified HI-TECH SF-3C low-temperature stopped-flow unit (Salisbury, U.K.) and evaluated with the program SPECFIT (Spectrum software Associates; Chapel Hill, USA).

^1H and ^{13}C NMR spectra were recorded on a DXP 300 AVANCE spectrometer (Bruker). Infrared spectra were recorded as KBr pellets on a ATJ Mattson Infinity 60 AR-FT-IR instrument. Elemental analyses were carried out on a Carlo Erba Element Analyser Model 1106 and FD-mass-spectra were measured on a JEOL JMS 700 instrument at 70 eV and a source temperature of 200°C. Cyclic voltammetry was carried out using an EG&G Model 263 Pentostat. The experiments utilized a two-chambered electrochemical cell in which the working solution compartment was separated from the other by a fine glass frit. Potentials are reported referenced to ferrocene (+0.42 V vs. the Ag/AgCl (1.0 M) reference electrode (BAS MF-1052)) used as the internal standard. The working and auxiliary electrodes were a glassy carbon disk and platinum wire, respectively. The measurements were performed at 25°C in absolute CH_3CN solutions containing 0.1 M $(\text{NBu})_4\text{PF}_6$ and a 10^{-3} M solution of $[\text{Cu}_2(\text{apme})_2](\text{CF}_3\text{SO}_3)_2$ or $[\text{Cu}(\text{apme})\text{Cl}]\text{BPh}_4$ respectively.

2.7.2 *Single-Crystal X-ray Structure Determinations*

X-Ray Structure Determination of **1**, **2**, **3** and **4**. Single crystals were coated with polyfluorether oil and mounted on a glass fiber. Data were collected with a Nonius KappaCCD area detector at 173(2) K (MoK_α , $\lambda = 71.073$ ppm, graphite-monochromator). The absorption corrections were performed using SCALEPACK with $T_{\min}=0.6224$, $T_{\max}=0.8447$ for **1**, $T_{\min}=0.7490$, $T_{\max}=0.8618$ for **2**, $T_{\min}=0.8650$,

$T_{\max}=0.9291$ for **3** and $T_{\min}=0.9195$, $T_{\max}=0.9195$ for **4**. Space groups were determined from systematic absences and subsequent least-squares refinement. The structure was solved by direct methods and refined on F^2 using full-matrix least-squares techniques. The parameters were refined using SHELXL-97.¹²² Non-hydrogen atoms were refined with anisotropic thermal parameters. Hydrogen atoms were fixed in idealized position using a riding model. The crystal of **3** was refined as racemic twin in 47:53 ratio. Scattering factors were taken from the literature.¹²³

2.7.3 Syntheses of Ligand and Complexes

Caution! Perchlorate salts are potentially explosive and should be handled with great care.

2.7.3.1 Synthesis of diphtaloyldiethylene-triamine

To a solution of 25 g (0.242 mol) diethylenetriamine in 250 mL MeOH were added 71.8 g (0.485 mol) phthalic anhydride at 60°C. The mixture was stirred for 45 min at 60°C and for 4 h at room temperature. The resulting yellow precipitate was filtered off, washed with 4 x 50 mL MeOH and 4 x 50 mL acetone and dried in vacuo to yield 28.011 g (77.1 mmol, 32%) of a white solid.

Anal. Calcd.: C: 66.12, H: 4.72, N: 11.56, Found: C: 66.29, H: 4.87, N: 11.34. $^1\text{H-NMR}$ (300 MHz, CDCl_3): δ = 1.40 (s, 1 H, N-H), 2.95 (t, 4 H, $^3J=6.0$ Hz, $\text{CH}_2\text{-N}$), 3.76 (t, 4 H, $^3J=6.0$ Hz, $\text{CH}_2\text{-NH}$), 7.66-7.74 (m, 8 H, H_{arom}). $^{13}\text{C}\{^1\text{H}\}\text{-NMR}$ (CDCl_3): δ = 33.62 ($\text{CH}_2\text{-NH}$), 43.26 ($\text{CH}_2\text{-N}$), 119.20, 128.22, 129.82 (C_{arom}), 164.51 (C=O). Field desorption mass spectrum (FD-MS) (70 eV, CHCl_3): m/z = 363 (100%) [P]⁺. IR (KBr, cm^{-1}): $\tilde{\nu}$ = 3329 $\nu(\text{N-H})$, 3086 $\nu(\text{C-H})$, 2943/2867 $\nu(\text{C-H})$, 1773/1713 $\nu(\text{imid})$, 1395 $\delta(\text{C-H})$, 718 $\delta(\text{C-H})$.

2.7.3.2 Synthesis of N^2 -pyridylmethyl-diphtaloyldiethylenetriamine

A suspension of 14.54 g (40 mmol) diphtaloyldiethylenetriamine and 6.43 g (60 mmol) 2-pyridinaldehyde in 200 mL 1,2-dichloroethane/100 mL CH_2Cl_2 was stirred for 15 min under nitrogen. To that mixture were added 17.80 g (84 mmol) $\text{NaB}(\text{OAc})_3\text{H}$ and the resulting suspension was stirred for 36 h at room temperature. Then 175 mL 2 N NaOH were added and the mixture was

stirred for another 45 min. The watery phase was separated and extracted three times with 150 mL CH_2Cl_2 . The organic phases were collected, dried over Na_2SO_4 and evaporated to dryness. The residue was stirred with 75 mL Et_2O and the resulting white solid was filtered off and dried in vacuo to yield 16.89 g (37.16 mmol; 93%) of N^2 -pyridylmethyl-diphtaloyldiethylentriamine.

Anal. Calcd.: C: 12.33, H: 4.88, N: 68.71, Found: C: 12.34, H: 4.99, N: 68.46. ^1H -NMR (300 MHz, CDCl_3): δ = 2.85 (t, $^3J=6.0$ Hz, 4 H, CH_2), 3.78 (t, $^3J=6.0$ Hz, 4 H, CH_2), 3.86 (s, 2 H, $\text{CH}_2\text{-py}$), 7.12 (m, 3 H, H_{py}), 7.70 (s, 8 H, H_{arom}), 8.40 (d, $^3J=4.9$ Hz, 1 H, H_{py}). $^{13}\text{C}\{^1\text{H}\}$ -NMR (CDCl_3): δ = 35.66 (CH_2), 51.93 (CH_2), 59.85 ($\text{CH}_2\text{-Py}$), 121.85, 123.01, 132.31, 133.64, 136.04, 148.72, 159.22 (C_{arom}), 168.16 (C=O). FD-MS (70 eV, CHCl_3): m/z = 454 (100%) $[\text{P}]^+$. IR (KBr, cm^{-1}): $\tilde{\nu}$ = 3065 $\nu(\text{C-H})$, 2982/2946/2806 $\nu(\text{C-H})$, 1770/1713 $\nu(\text{imid})$, 1400 $\delta(\text{C-H})$, 722 $\delta(\text{C-H})$.

2.7.3.3 Synthesis of N^2 -pyridylmethyldiethylene-triamine (apme)

To a suspension of 10.75 g (23.7 mmol) N^2 -pyridylmethyldiphtaloyl-diethylenetriamine in 270 mL EtOH 7.03 mL (142.0 mmol) $\text{N}_2\text{H}_4 \times \text{H}_2\text{O}$ (98%) were added and stirred under reflux for 3 h. The mixture was cooled to 4°C and the resulting white precipitate was filtered off and washed with 100 mL EtOH . The filtrate was evaporated to dryness and the yellow residue was redissolved in 50 mL CHCl_3 . The solution was washed with 30 mL of 3 N aqueous NaCl solution and the combined watery phases extracted three times with 3 x 40 mL CHCl_3 . The combined organic phases were dried over Na_2SO_4 . Evaporation of the solvent gave a yellow residue which was purified by Kugelrohr distillation at 250°C in vacuo to yield 2.80 g (14.41 mmol; 61% d. Th.) of a yellow oil.

^1H -NMR (300 MHz, CDCl_3): δ = 1.55 (s, 4 H, NH_2), 2.61 (t, 4 H, $^3J=6.0$ Hz, CH_2), 2.79 (t, 4 H, $^3J=6.0$ Hz, CH_2), 3.77 (s, 2 H, $\text{CH}_2\text{-Py}$), 7.15 (m, 1 H, H_{arom}), 7.44 (d, 1 H, $^3J=7.9$ Hz, H_{arom}), 7.63-7.69 (m, 1 H, H_{arom}), 8.53 (d, 1 H, $^3J=4.7$ Hz, H_{arom}). $^{13}\text{C}\{^1\text{H}\}$ -NMR (CDCl_3): δ = 39.77 (CH_2), 57.70 (CH_2), 60.89 ($\text{CH}_2\text{-Py}$), 121.96, 122.83, 136.39, 149.04, 160.02 (C_{arom}). FD-MS (70 eV, CHCl_3): m/z = 195 (100%) $[\text{P}]^+$, 389 (33%) $[\text{2P}]^+$. IR (KBr, cm^{-1}): $\tilde{\nu}$ = 3350/3285 $\nu(\text{N-H})$, 3052/3007 $\nu(\text{C-H})$, 2937/2842 $\nu(\text{C-H})$, 1589 $\delta(\text{NH}_2)$, 1435/1472 $\delta(\text{C-H})$, 760 $\delta(\text{C-H})$.

2.7.3.4 Synthesis of $[\text{Cu}_2(\text{apme})_2](\text{ClO}_4)_2$ (1).

To a solution of 0.194 g (1 mmol) apme in 20 mL MeOH were added 0.327 g (1 mmol) $[\text{Cu}(\text{CH}_3\text{CN})_4]\text{ClO}_4$ and the mixture was stirred for 45 min at room temperature. The resulting light yellow precipitate was filtered off, washed with Et_2O and dried in vacuo to yield 0.335 g (0.94 mmol; 94%) of the desired product. Recrystallisation of the product from *N,N*-dimethylformamide (DMF) and diffusion of Et_2O into the solution yielded light green crystals suitable for X-Ray diffraction analysis.

Anal. Calcd.: C: 33.62, H: 5.07, N: 15.68, Found: C: 33.71, H: 5.52, N: 15.63. ^1H -NMR (300 MHz, CD_3CN , -35°C): δ = 2.39 (s, 4 H, NH_2), 2.57 (s, 4 H, CH_2), 2.76 (s, 4 H, CH_2), 3.95 (s, 2 H, $\text{CH}_2\text{-Py}$), 7.38 (m, 2 H, H_{py}), 7.84 (dd, 1 H, H_{py}), 8.55 (d, 1 H, H_{py}). FD-MS (70 eV, CH_3CN): m/z = 257 (100%) $[\text{CuL}]^+$, 194 (10%) $[\text{L}]^+$. IR (KBr, cm^{-1}): $\tilde{\nu}$ = 3359/3306 $\nu(\text{N-H})$, 2969/2839 $\nu(\text{C-H})$, 1601 $\delta(\text{N-H})$, 1441 $\delta(\text{C-H})$, 1097 $\nu(\text{Cl-O})$, 760 $\delta(\text{C-H})$. UV/ vis (CH_3CN): $\lambda_{\text{max}}(\epsilon)$ = 216 (14.466), 226 (14.216), 244 (13.538), 290 (shoulder, 5402).

2.7.3.5 Synthesis of $[\text{Cu}_2(\text{apme})_2](\text{CF}_3\text{SO}_3)_2$ (2).

To a solution of 0.194 g (1 mmol) apme in 20 mL CH_3CN were added 0.377 g (1 mmol) $[\text{Cu}(\text{CH}_3\text{CN})_4]\text{CF}_3\text{SO}_3$ and the mixture was stirred for 30 min at room temperature. The resulting light yellow precipitate was filtered off, washed with Et_2O and dried in vacuo to yield 0.297 g (0.73 mmol; 73%) of the desired product. Diffusion of Et_2O into the mother solution yielded light yellow crystals suitable for X-Ray diffraction analysis.

Anal. Calcd.: C: 32.47, H: 4.45, N: 13.77, S: 7.88, Found: 32.68, H: 4.31, N: 13.68, S: 7.85. ^1H -NMR (300 MHz, CD_3CN , -35°C): δ = 2.39 (s, 4 H, NH_2), 2.57 (s, 4 H, CH_2), 2.76 (s, 4 H, CH_2), 3.95 (s, 2 H, $\text{CH}_2\text{-Py}$), 7.38 (m, 2 H, H_{py}), 7.84 (dd, 1 H, H_{py}), 8.55 (d, 1 H, $^3J=4.1$ Hz, H_{py}). ^{13}C -Distortionless Enhancement by Polarization Transfer-NMR (^{13}C -DEPT-NMR) (CD_3CN): δ = 41.41 (CH_2), 56.19 (CH_2), 60.64 ($\text{CH}_2\text{-Py}$), 124.85, 124.31, 137.93, 149.76 (C_{arom}). FD-MS (70 eV, CH_3CN): m/z = 257 (100%) $[\text{CuL}]^+$, 406 $[\text{CuL}(\text{CF}_3\text{SO}_3)]^+$. IR (KBr, cm^{-1}): $\tilde{\nu}$ = 3343/3297 $\nu(\text{N-H})$, 2958/2884/2834 $\nu(\text{C-H})$, 1606 $\delta(\text{N-H})$, 1443 δ

(C-H), 1278/1256/1152/1031/640 $\nu(\text{CF}_3\text{SO}_3)$, 756 $\delta(\text{C-H})$. UV-Vis (CH_3CN): $\lambda_{\text{max}}(\epsilon) = 214 (15.362), 224 (13.827), 242 (13.031), 290 (\text{shoulder}, 5110)$.

2.7.3.6 Synthesis of $[\text{Cu}(\text{apme})\text{Cl}]\text{BPh}_4$ (3**).**

To a solution of 0.194 g (1 mmol) apme in 20 mL CH_3CN were added 0.170 g (1 mmol) $\text{CuCl}_2 \times 2 \text{H}_2\text{O}$, 0.342 g (1 mmol) NaBPh_4 und 10 mL H_2O and the mixture was stirred for 30 min at room temperature. The resulting light green precipitate was filtered off, washed with Et_2O and dried in vacuo to yield 0.490 g (0.80 mmol; 80%) of the desired product. Recrystallisation of the crude product from DMF in the air yielded green crystals suitable for X-Ray diffraction analysis.

Anal. Calcd.: C: 66.68, H: 6.25, N: 9.15, Found: C: 67.04, H: 6.45, N: 8.96. IR (KBr, cm^{-1}): $\tilde{\nu} = 3339/3305/3273/3242 \nu(\text{N-H}), 3052 \nu(\text{C-H}), 2999/2937/2880 \nu(\text{C-H}), 1603/1578 \delta(\text{N-H}), 1478/1431 \delta(\text{C-H}), 738/708 \delta(\text{C-H})$. UV/ vis (CH_3CN): $\lambda_{\text{max}}(\epsilon) = 300 (3671), 716 (82)$.

Blue crystals of **4** were obtained as a side product during the crystallization of **3**.

3 Ligand Influence of Copper(I) Schiff Base Macrocyclic Complexes

3.1 Ligand Influence Over the Formation of Dinuclear [2+2] versus Trinuclear [3+3] Cu^I Schiff Base Macrocyclic Complexes

This work was published previously in the Journal of "Inorganic Chemistry"

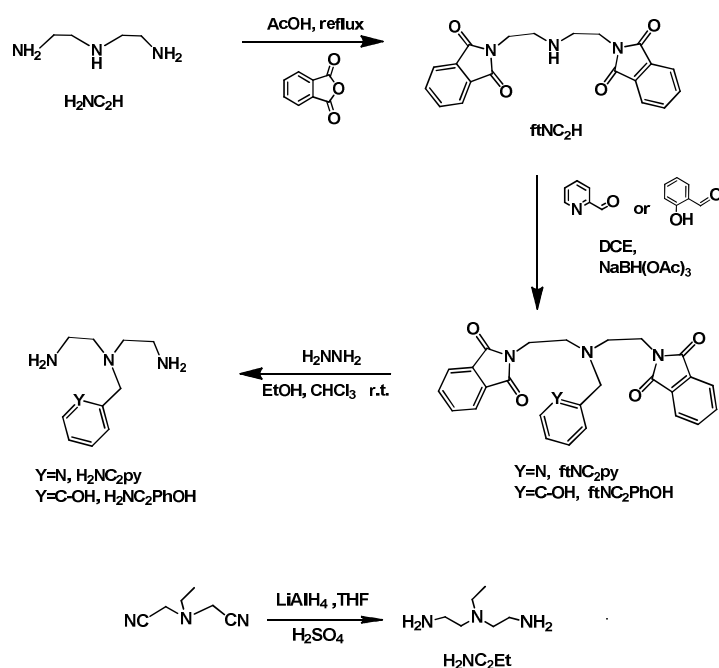
Arbuse, A., Mandal, S., Maji, S, Martínez, M. A., Fontrodona, X., D., Utz, D., Heine-
mann, F. W., Kisslinger, S., Schindler, S., Sala, X. and Llobet, A.. *Inorg. Chem.* **2011**,
50, 6878-6889 (doi: 10.1021/ic102185y).

Schiff bases and their related transition metal complexes have been extensively employed in many fields of science including biochemistry, material science, catalysis, supramolecular chemistry, transport and separation phenomena, medicine, etc. due to their synthetic versatility.¹²⁴⁻¹³⁰ A large variety of [1+1] and [2+2] macrocyclic ligands have been synthesized in order to understand the role of the different donor atoms, the influence of their relative position, the number and size of the chelating rings formed, the flexibility and the shape of the coordinating moiety on the selective binding of charged or neutral species.^{126, 131-134} In addition, Schiff base macrocyclic ligands can be used as starting materials to generate the corresponding secondary amines that in turn can be further functionalized generating the corresponding tertiary amines.¹³⁵ Furthermore higher condensations products such as [3+3] and [4+4] have also been reported although they are unusual.¹³⁶⁻¹⁴⁸ The combination of all these macrocycles provides a wide family of ligands, which allows an understanding at a molecular level of phenomena such as anion recognition.¹⁴⁹⁻¹⁵⁵ Furthermore these ligands can be coordinated to transition metal ions and thus generate a large family of complexes with subtle differences that allow understanding important phenomena related to complex-DNA interactions,¹³² activation of small molecules such as dioxygen,¹⁵⁶⁻¹⁵⁷ carbon dioxide etc.¹⁵⁸ Macrocyclic ligands with peripheral functionalities constitute a specific class within this type of ligands since they allow to have complementary

properties that can be used for multi-recognition processes, specific separation and transport processes across membranes or additional control of small molecule activation and catalysis.^{105, 159}

The use of metal ion template is a powerful synthetic tool to direct the Schiff base synthesis to a desired oligomer that allows controlling the size and shape of the resulting macrocycle.^{140, 142, 145-146} In general the synthetic routes reported thus far generate single oligomers although, a few exceptions have been described particularly for the discrimination of [2+2] vs. [4+4].^{136, 139, 141}

A



B

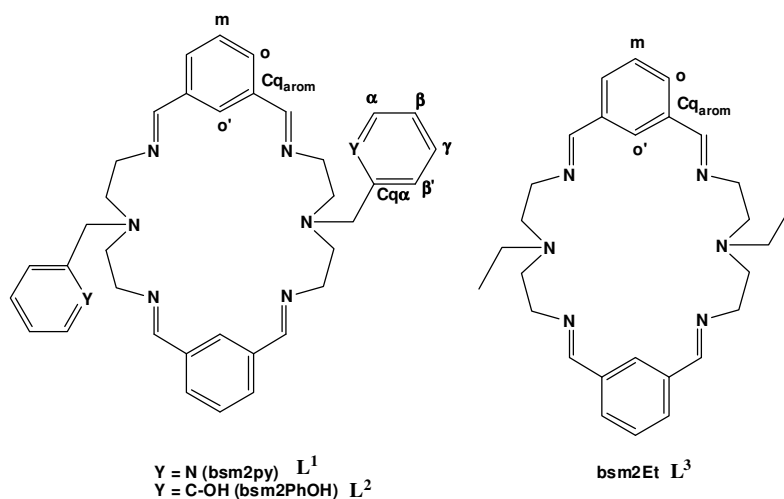


Figure 3-1: A) Synthetic strategy for the preparation of substituted N^2 -triamines: $\text{H}_2\text{NC}_2\text{py}$, $\text{H}_2\text{NC}_2\text{PhOH}$ and $\text{H}_2\text{NC}_2\text{Et}$. B) Macrocyclic ligands obtained from the [2+2] condensation of N^2 -triamines and isophthalaldehyde, including proton labeling used.

Hereon we report the synthesis of three new macrocyclic Schiff base ligands with different pendant arms (2-methylpyridyl, 2-methylphenol, and donor-free ethyl) obtained from the [2+2] condensation of isophthalaldehyde and N²-functionalized triamine. The new ligands are labeled, bsm2py (**L**¹), bsm2PhOH (**L**²) and bsm2Et (**L**³) where “bs” refers to Schiff Base, “m” is for the meta substitution at the aromatic ring, “2” for the number of methylenic units linking the aminic atoms and finally “py”, “PhOH” and “Et” refer to 2-methylpyridyl, 2-methylphenol, and ethyl groups respectively. The latter groups bonded at the central N-atom of triamine become the pendant arms of the macrocyclic ligand. Figure 3-1 presents a drawing of these ligands together with the synthetic strategy used to obtain them. The coordination chemistry of these ligands with Cu^I is also reported giving the formation of dinuclear [2+2] and trinuclear [3+3] Cu^I complexes. Their interconversion is studied by means of MS spectroscopy. Corresponding [3+3] Schiff Bases are denoted as **L**⁴, **L**⁵ and **L**⁶.

3.2 Results and Discussion

Dinuclear Cu^I complexes containing a macrocyclic ligand obtained from the condensation of isophthalaldehyde and a diethylenetriamine (R = H, see Figure 3-2, abbreviated as “mac” from now on) have been described previously.¹⁶⁰⁻¹⁶¹

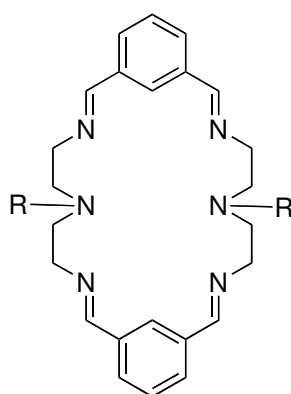


Figure 3-2: The ligand mac (R = H)

The derived Cu^I complex was especially interesting because it undergoes an intramolecular ligand hydroxylation reaction when reacts with dioxygen.¹⁶²⁻¹⁶⁵ This reaction can be regarded as a model

reaction for the enzymatic reaction of tyrosinase, a monooxygenase that is responsible for *o*-hydroxylation of the phenol entity.^{4, 6, 166-167}

To gain more insight into the interesting properties of this macrocyclic ligand type we now have investigated how the modification of the R group in $[\text{Cu}_2(\text{mac})(\text{CH}_3\text{CN})_2]^{2+}$ from H to an ethyl group, 2-methylpyridyl and 2-methylphenol would influence the coordination behavior of this systems.

3.2.1 Synthesis of macrocycle components.

For the preparation of the substituted triamines a multistep process, shown in the upper part of Figure 3-1, was followed, consisting on: a) the protection of the primary amines with phthalic anhydride to form the corresponding phthalimides; b) the addition of the pyridyl or phenol aldehyde or iodoethane to the central amine and c) deprotection of the phthalamides with hydrazine to yield the corresponding primary amines. The ethyl substituted central amine was also prepared by following a different synthetic strategy depicted at the bottom of Figure 3-1A. It describes the preparation of the dicyano derivative that is then reduced to the corresponding amine by LiAlH_4 .

The reaction of a dialdehyde and a diamine can yield a large range of condensation products both macrocyclic and acyclic, as shown in Figure 3-3, that can be in equilibrium. The relative amount of each product depends basically on entropic and geometric factors. From an enthalpic viewpoint it involves the formation and breaking of the same type of bond, and highly strained systems will be enthalpically disfavored. The relative formation of the products shown in Figure 3-3 is also influenced by solvent, reaction temperature, reaction time and very importantly their solubility. This wide range of condensation compounds has been previously described in the literature for related systems, e. g. for the pyridyldialdehyde system.^{134, 168-169} Another factor that strongly influences reactivity is the presence of a metal cation that can act as a templating agent, and thus stabilize the formation of a condensation product that possesses a cavity size and shape that is complementary to the templating cation.

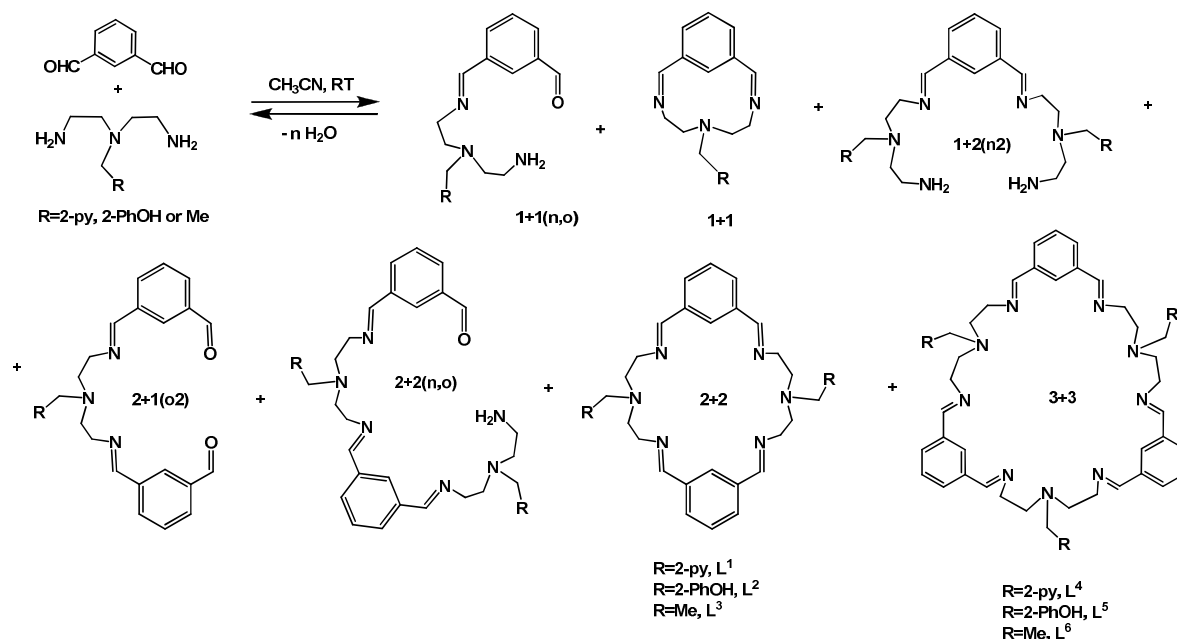


Figure 3-3: Potential condensation products from the reaction of isophthalaldehyde and N^2 -substituted triamine. For the labeling, the numerical values indicate the number of reacted units and in parenthesis the unreacted groups. For instance 1+1(n,o) means a condensation of one molecule of isophthalaldehyde and one of triamine. In parenthesis the (n) indicates an unreacted amine and (o) an unreacted aldehyde.

3.2.2 Synthesis Metal free [2+2] Macrocyclic Ligands.

The direct, metal-free, reaction of a dialdehyde and a diamine can yield a large range of condensation products both macrocyclic and acyclic, as shown in Figure 3-3, that can be in equilibrium. The relative amount of each product depends basically on entropic and geometric factors. From an enthalpic viewpoint it involves the formation and breaking of the same type of bond, and highly strained systems will be enthalpically disfavored. The relative formation of the products shown in in Figure 3-3 is also influenced by solvent, reaction temperature, reaction time and very importantly their solubility. This wide range of condensation compounds has been previously described in the literature for related systems, e. g. for the pyridyldialdehyde system.^{134, 168-169}

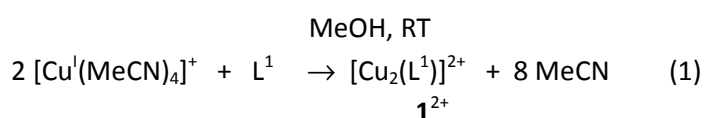
In our case the [2+2] macrocyclic ligands were prepared by a condensation of a 1:1 molar ratio of an adequately substituted triamine and isophthalaldehyde which was very slowly added to the respective triamine solution to favor both lower oligomeric compounds as well as macrocyclic type of products. The relatively low yields obtained indicate the formation of other products together with potentially unreacted starting materials. Once the [2+2] condensation product was formed it was

redissolved in either MeOH or MeCN and allowed to stir at RT for 24 h. MS analysis of the solution indicates the presence of the [2+2] condensation product only. Thus once it is formed and in the absence of a catalyst there is no equilibration process that could generate a mixture of oligomers at least on the time scale of days.

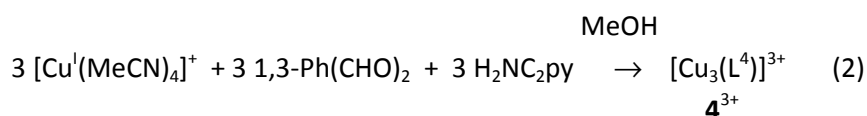
3.2.3 Synthesis of Cu^I complexes.

Another factor that strongly influences reactivity is the presence of a metal cation that can act as a templating agent, and thus stabilize the formation of a condensation product that possesses a cavity size and shape that is complementary to the templating cation.

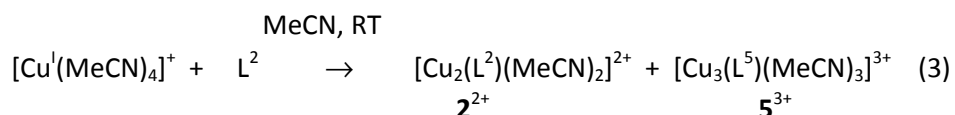
The synthesis of the Cu^I complexes was carried out by mixing two equivalents amount of a [Cu^I(MeCN)₄]⁺ salt, and the [2+2] free ligand or via a template procedure as indicated in the following equations. For the case of the L¹ ligand the solvent and the crystallization time has a strong influence over the complexes obtained. In MeOH the main product obtained in 80% yield is **1**²⁺ as indicated in the following equation.



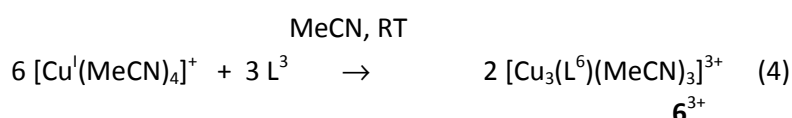
On the other hand, and in sharp contrast using MeCN as the solvent generates the analogous trinuclear complex **4**³⁺ in 70% yield. Given the fact that the L¹ ligand does not isomerize in solution it suggests the presence of a metal assisted transformation that generates L⁴ out of L¹ as will be discussed later. Further, a one pot synthesis using the triamine, dialdehyde and Cu^I as a template metal generates the **4**³⁺ complex in 68% yield, as shown in equation 2,



For the case of the L^2 ligand only the dinuclear complex, 2^{2+} , is obtained in either MeOH or MeCN in good yields (approx. 80%) after 1h of mixing the reactants at room temperature. However if the solution is allowed to stand for 12-15 days a mixture of dinuclear, 2^{2+} , and trinuclear, 5^{3+} , is obtained,



Finally for the case of the L^3 macrocyclic ligand only the trinuclear complex was obtained in 71% yield, indicating the formation of the L^6 ligand as shown in equation 4.



3.2.4 Solid State Characterization.

The crystal structure of the ligand L^2 consists of eight discrete L^2 molecules (see Table 3-1). The X-ray analysis shows four crystallographically independent but chemically identical L^2 units, which present very slight variations in bond distances and angles. It is interesting to note that, for each molecular structure, the two benzene rings are nearly parallel to one another with an angle of 1.76, 1.84, 6.27, or 6.96° and that the phenol groups are placed in mutually trans position in an inversion center arrangement around the tertiary amine, permitting the establishment of H-bonding with the nearby units. In Figure 3-3 ball and stick representations of the X-ray structures for the dinuclear complex, 2^{2+} , and the trinuclear complexes, 4^{3+} , 5^{3+} , and 6^{3+} , is depicted. For the dinuclear complex, 2^{2+} , the *meta* substitution of the aromatic ring places the two copper centers at a distance of 7.97 Å; whereas the two benzene rings are nearly parallel to one another with an angle of 29.1°. Each copper center has a distorted tetrahedral arrangement as a result of the constraints imposed by the triaza moiety of the macrocyclic ligand. This generates a long Cu-N (2.208 Å) distance with the central

amine group, two medium Cu-N (2.022 Å and 2.061 Å) distances with the imines, and a short distance with the MeCN monodentate ligand Cu-N (1.918 Å). The strain of the macrocyclic ligand also imposes two short N-Cu-N angles of 84.85° and 83.95°, with the rest of the N-Cu-N angles ranging 111-128°. Finally, the dangling phenol group is not coordinating the Cu metal center. The metric parameters described here are also in agreement with related Cu^I complexes that have been previously reported in the literature.^{154, 170} Table 3-2 lists selected bond distances and angles for the first coordination sphere of one of the Cu^I metal centers of complexes **4**, **2**, **5**, and **6**.

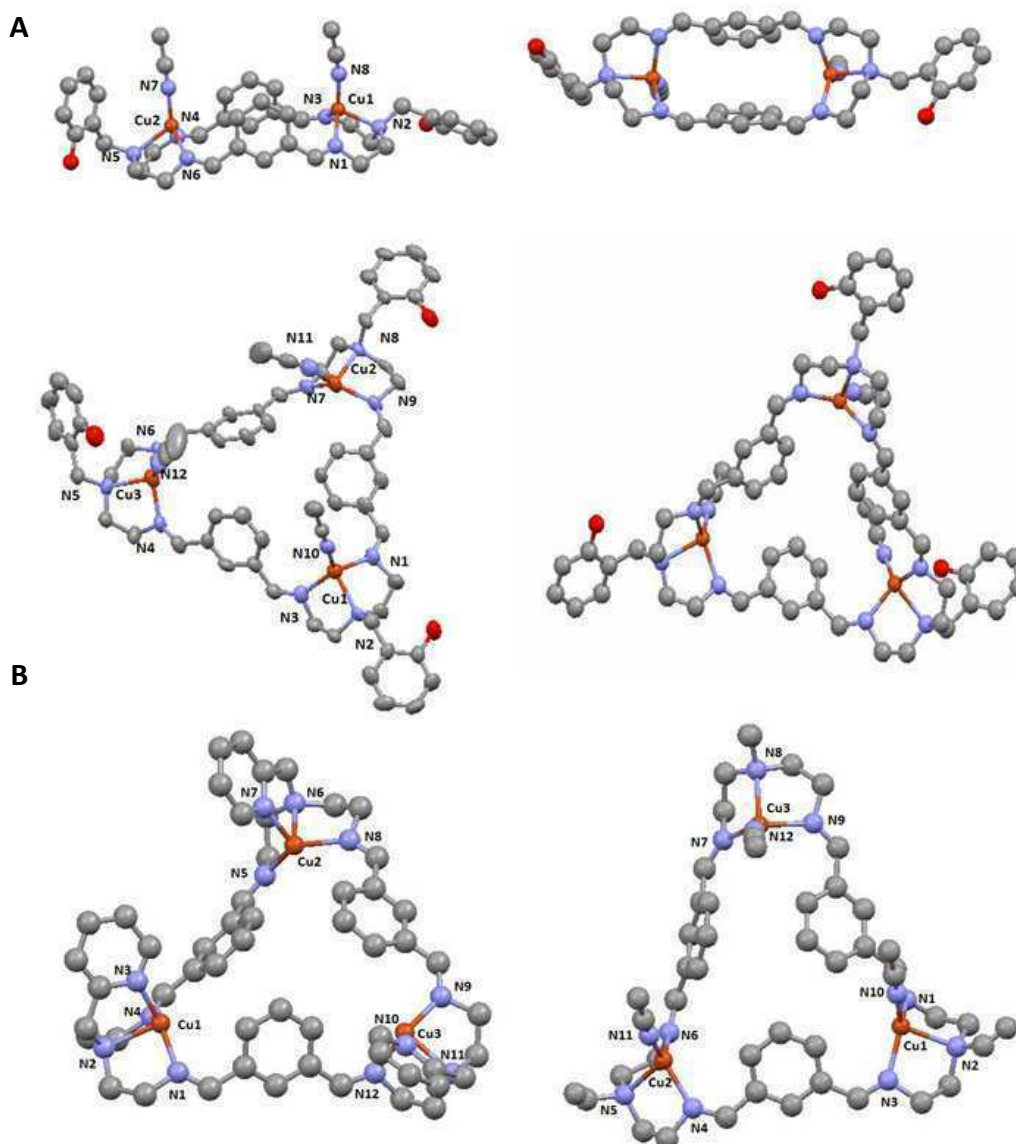


Figure 3-4: Ball and stick diagram for the X-ray crystal structure for Cu^I complexes. (A) top, two representations of **2**²⁺; bottom, two of **5**³⁺. (B) Left, **4**³⁺; Right, **6**³⁺. Color codes: Cu, orange; N, blue; C, gray; O, red. H atoms are not shown.

For the trinuclear complexes **5**³⁺ and **6**³⁺, the local Cu^I coordination is comparable to that of the dinuclear **2**²⁺ complex. Here, the metal centers are disposed in a triangular arrangement with Cu-Cu distances (ranging from 8.8 to 9.4 Å) that are a bit larger than those for the dinuclear complex, as discussed above, and thus manifest the relative flexibility of this family of [2+2] and [3+3] Schiff base ligands. Comparing the **5**³⁺ trinuclear complex and the **2**²⁺ dinuclear complex, the major difference is that the latter has slightly shorter N_{im}-Cu₍₁₎-N_{im} angles, 119-123° vs. 108-111.32°, while the Cu bonding distances are practically identical. For the trinuclear complex **4**³⁺, the dangling pyridyl group is coordinating the metal center, replacing the MeCN when compared to **5**³⁺. For the trinuclear complexes, it is also interesting to see that the three benzene rings altogether adopt a bowl shape arrangement. For the case of **4**³⁺, the closest H atoms among the three aromatic rings are situated at 2.52, 2.70, and 2.77 Å, forming an irregular triangle, and the angles between these aromatic rings are 56.7, 69.0, and 83.2°. With regard to the 3D packing of these molecules, it is interesting to realize that those containing the triflate anion have packing that is dominated by H-bonding with triflate oxygen atoms and the macrocycle. A similar situation is found for complex **4**³⁺ containing PF₆⁻ as counteranion that crystallizes with THF, H₂O, and MeOH. Here again, packing interactions are dominated by extensive hydrogen bonding between the solvate oxygen atoms and the macrocycle. However, complex **4**³⁺ containing SbF₆⁻ as counteranion crystallizes with no solvate molecules, and its packing structure is significantly different from the rest. In particular, it is interesting to see the presence of dimers of trinuclear units bonded by π - π and CH- π interactions between macrocyclic ligands.

3. Ligand Influence of Copper(I) Schiff Base Macrocyclic Complexes

Table 3-1: Crystallographic data for structures: **L²**, **4(SbF₆)₃**, **4(PF₆)₃**, **2(CF₃SO₃)₂**, **5(CF₃SO₃)₃** and **6(CF₃SO₃)₃**

Structure	L²	4(SbF₆)₃	4(PF₆)₃ 2.5THF·0.5H ₂ O·0.75 MeOH	2(CF₃SO₃)₂ MeCN	5(CF₃SO₃)₃ 2 H ₂ O	6(CF₃SO₃)₃ ·1EtOEt
Empirical formula	C ₃₈ H ₄₂ N ₆ O ₂	C ₅₄ H ₅₉ Cu ₃ F ₁₈ N ₁₂ Sb ₃	C _{64.75} H ₈₄ Cu ₃ F ₁₈ N ₁₂ O ₃ · 7.5P ₃	C ₄₈ H ₅₁ Cu ₂ N ₉ O ₈ F ₆ S ₂	C ₆₆ H ₇₆ Cu ₃ F ₉ N ₁₂ O ₁₄ S ₃	C ₅₅ H ₇₆ Cu ₃ N ₁₂ F ₉ O ₁₀ · S ₃
Formula Weight	614.52	1774.00	1715.97	1163.16	1719.19	1523.08
Temperature, K	300(2)	100(2)	100(2)	100(2)	300(2)	373(2)
Wavelength, Å	0.71073	0.71073	0.71073	0.71073	0.71073	0.71073
Crystal system	Monoclinic	Triclinic	Triclinic	Monoclinic	Triclinic	Triclinic
Space group	P2(1)	P-1	P-1	P21/n	P-1	P-1
a, Å	13.357(5)	12.008(18)	11.4563(3)	15.203(3)	15.72(2)	11.383(6)
α, deg	90.00	109.82(3)	80.620(2)	90	104.45(3)	84.485(10)
b, Å	35.402(13)	15.72(2)	17.6766(6)	18.211(3)	16.73(2)	14.732(8)
β, deg	101.776(7)	104.97(3)	81.518(2)	99.371(3)	111.79(3)	80.547(9)
c, Å	14.629(6)	20.01(3)	36.255(1)	19.084(3)	18.04(3)	20.652(11)
γ, deg	90.00	97.76(3)	82.902(2)	90	106.39(3)	86.199(10)
Vol., Å ³	6772(4)	3328(9)	7127.1(4)	5213.3(16)	3878(10)	3396(3)
Z	8	2	4	4	1	2
ρ(g/cm ³)	1.205	1.770	1.599	1.482	1.462	1.489
R [<i>I</i> > 2σ(<i>I</i>)] ^a	0.0563	0.1057	0.0755	0.0399	0.0818	0.0898
wR	0.1371	0.2698	0.1516	0.0617	0.2416	0.2699

$$R = \sum [F_o - F_c] / \sum F_o \quad wR = \left[\sum (w(F_o^2 - F_c^2))^2 / \sum (wF_o^4) \right]^{1/2}$$

Table 3-2: Selected bond distances and angles for the first coordination sphere of one of the Cu^I metal centers of complexes, **4³⁺**, **2²⁺**, **5³⁺** and **6³⁺**.

4(PF₆)₃		2(CF₃SO₃)₂		5(CF₃SO₃)₃		6(CF₃SO₃)₃	
Cu(1)-N _{py} (10)	2.034(5)	Cu(1)-N _{MeCN} (8)	1.918(2)	Cu(1)-N _{MeCN} (10)	1.97(7)	Cu(1)-N _{MeCN} (10)	1.917(10)
Cu(1)-N _{im} (1)	1.979(5)	Cu(1)-N _{im} (3)	2.0223(19)	Cu(1)-N _{im} (3)	2.04(5)	Cu(1)-N _{im} (1)	2.026(7)
Cu(1)-N _{im} (3)	2.009(5)	Cu(1)-N _{im} (1)	2.0610(18)	Cu(1)-N _{im} (1)	2.05(5)	Cu(1)-N _{im} (3)	2.036(8)
Cu(1)-N _{ter} (2)	2.189(5)	Cu(1)-N _{ter} (2)	2.2078(18)	Cu(1)-N _{ter} (2)	2.19(5)	Cu(1)-N _{ter} (2)	2.209(8)
N _{im} (3)-Cu(1)-N _{im} (1)	131.2(2)	N _{MeCN} (8)-Cu(1)-N _{im} (3)	128.82(8)	N _{MeCN} (10)-Cu(1)-N _{im} (3)	122(2)	N _{MeCN} (10)-Cu(1)-N _{im} (1)	113.7(3)
N _{im} (1)-Cu(1)-N _{py} (10)	115.6(2)	N _{MeCN} (8)-Cu(1)-N _{im} (1)	116.10(8)	N _{MeCN} (10)-Cu(1)-N _{im} (1)	111(2)	N _{MeCN} (10)-Cu(1)-N _{im} (3)	121.0(3)
N _{im} (3)-Cu(1)-N _{py} (10)	110.4(2)	N _{im} (3)-Cu(1)-N _{im} (1)	111.32(8)	N _{im} (3)-Cu(1)-N _{im} (1)	123(2)	N _{im} (1)-Cu(1)-N _{im} (3)	123.7(3)
N _{im} (1)-Cu(1)-N _{ter} (2)	86.1(2)	N _{MeCN} (8)-Cu(1)-N _{ter} (2)	117.68(8)	N _{MeCN} (10)-Cu(1)-N _{ter} (2)	120(2)	N _{MeCN} (10)-Cu(1)-N _{ter} (2)	115.5(3)
N _{im} (3)-Cu(1)-N _{ter} (2)	85.1(2)	N _{im} (3)-Cu(1)-N _{ter} (2)	83.96(7)	N _{im} (3)-Cu(1)-N _{ter} (2)	85(2)	N _{im} (1)-Cu(1)-N _{ter} (2)	83.7(3)
N _{py} (10)-Cu(1)-N _{ter} (2)	81.9(2)	N _{im} (1)-Cu(1)-N _{ter} (2)	84.85(7)	N _{im} (1)-Cu(1)-N _{ter} (2)	85(2)	N _{im} (3)-Cu(1)-N _{ter} (2)	84.4(3)

3.2.5 NMR spectroscopy.

The ^1H -NMR spectra of $\mathbf{1}^{2+}$ was recorded in $\text{CD}_3\text{CN}-d_3$ or in $\text{DMF}-d_7$ and is presented in Figure 3-4. At room temperature the spectra show very broad signals that indicate the presence of a dynamic behavior analogous to the previously described for $[\text{Cu}_2(\text{mac})(\text{CH}_3\text{CN})_2]^{2+}$.¹⁶³ Whereas the aliphatic part is unremarkable the aromatic part displays sharp resonances at -25°C and below. Together with these sharp resonances, lower intensity and wider peaks also appear that are presumably due to another highly symmetric stereoisomer of $\mathbf{1}^{2+}$, given the reduced number of resonances observed. It is also interesting to observe that resonance for H_a in $\mathbf{1}^{2+}$ appears at 10.22 ppm while for $[\text{Cu}_2(\text{mac})(\text{CH}_3\text{CN})_2]^{2+}$ is shifted to 8.74 ppm, manifesting how subtle differences in structure can produce large electronic perturbation at a specific site.

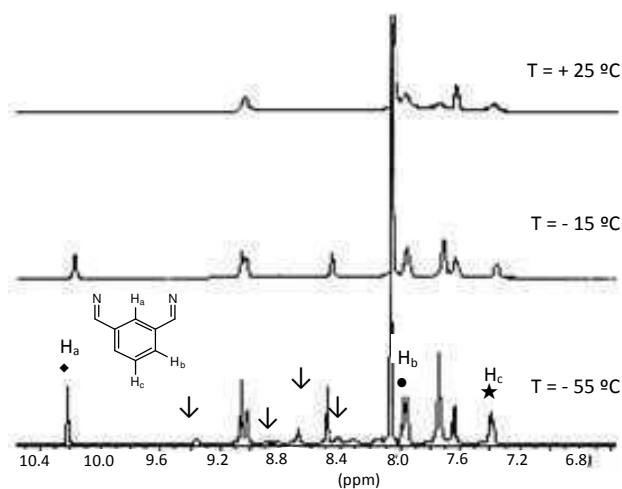


Figure 3-5: Variable Temperature ^1H NMR Spectra of $\mathbf{1}(\text{PF}_6)_2$ in d_7 -DMF at -55 , -15 and $+25^\circ\text{C}$ (arrows mark the peaks of the second isomer).

The Cu^{I} complexes described here in general react slowly (within the time scale of days) with molecular oxygen except for the ones containing the phenolic ligand $\mathbf{2}^{2+}$ and $\mathbf{5}^{3+}$ that react a bit faster, to form presumably the corresponding bis- μ -hydroxido derivatives “ $\text{Cu}(\mu\text{-OH})_2\text{Cu}$ ” as has been previously shown for related meta substituted macrocyclic complexes.¹³⁵ Unlike $[\text{Cu}_2(\text{mac})(\text{CH}_3\text{CN})_2]^{2+}$ no hydroxylation of the ligand occurs with the complexes described in the present work.

3.2.6 MS Spectroscopy and the [2+2] vs. [3+3] Evolution Process.

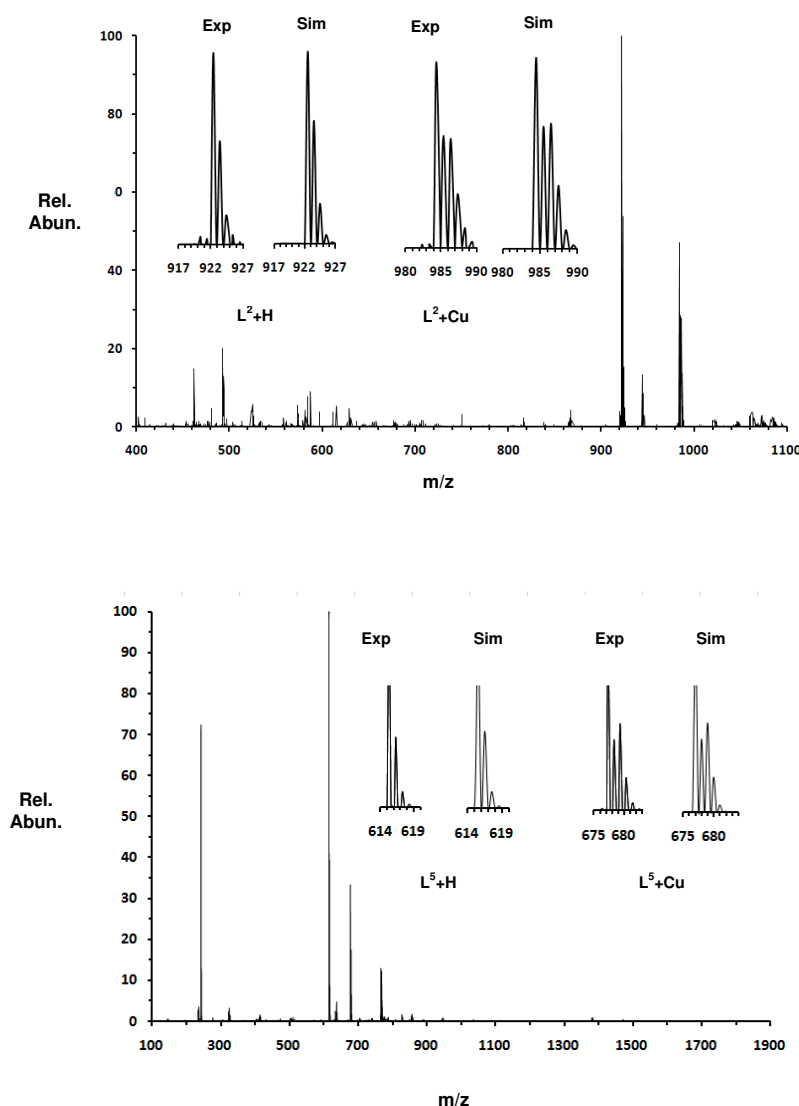
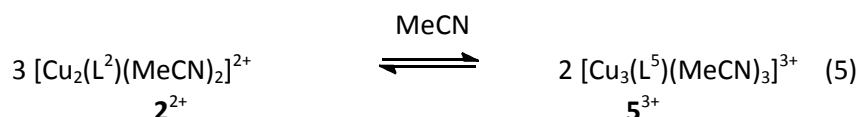


Figure 3-6: ESI-MS spectra obtained for **2**(CF_3SO_3)₂ (top) and **5**(CF_3SO_3)₃ (bottom) in MeCN.

Complexes **2**²⁺ and **5**³⁺ were analyzed by ESI-MS and their spectra are presented in Figure 3-6. In both cases their molecular peaks could not be identified but a series of fragments are found. For complex **2**²⁺ key monocharged peaks at 615 m/z (L^2+H ; highest intensity), 637 m/z (L^2+Na), 677 m/z (L^2+Cu), 739 (L^2+Cu_2-1), and 766 ($\text{L}^2+\text{Cu}_2\text{Na}-3$) could be identified. For complex **5**³⁺ key peaks are found at 922 m/z (L^5+H ; highest intensity), 984 m/z (L^5+Cu) and their corresponding doubly charged peaks at 461 m/z and 492 m/z respectively. For both complexes the relative intensities of their peaks

coincide perfectly with the simulated ones. As indicated in the previous section reaction of $[\text{Cu}^{\text{I}}(\text{MeCN})_4]^+$ in MeCN with the [2+2] condensation macrocyclic ligand L^2 , generates a mixture of the dinuclear and trinuclear complexes as indicated in equation 3. From this it can be inferred that an equilibrium between the dinuclear and trinuclear complex should exist,



This reaction was monitored by MS following the relative intensities of the peaks at 615 m/z for $\mathbf{2}^{2+}$ and 922 m/z for $\mathbf{5}^{3+}$, at room temperature under diluted conditions. Initially only complex $\mathbf{2}^{2+}$ exists in solution but as time elapses the formation of $\mathbf{5}^{3+}$ is clearly observed as depicted in Figure 3-7. After 1.5 months the system reaches equilibrium with a relative concentration $[\mathbf{5}^{3+}]/[\mathbf{2}^{2+}]$ of 0.65, that implies an equilibrium constant of 0.42 for equation 5. This value indicates that the [2+2] condensation complex $[\mathbf{2}^{2+}]$, is more energetically favored than the [3+3] complex $[\mathbf{5}^{3+}]$, probably due to entropic factors and also to a minor extend to the relative strain of their structures. It is important to bear in mind that these experiments have been carried out under high dilution conditions so that both complexes are completely soluble. Therefore these results can't be extrapolated at a synthetic level with regard to the relative amount of $[\mathbf{2}^{2+}]$ and $[\mathbf{5}^{3+}]$, since in that case we used a mixture of MeCN and ether.

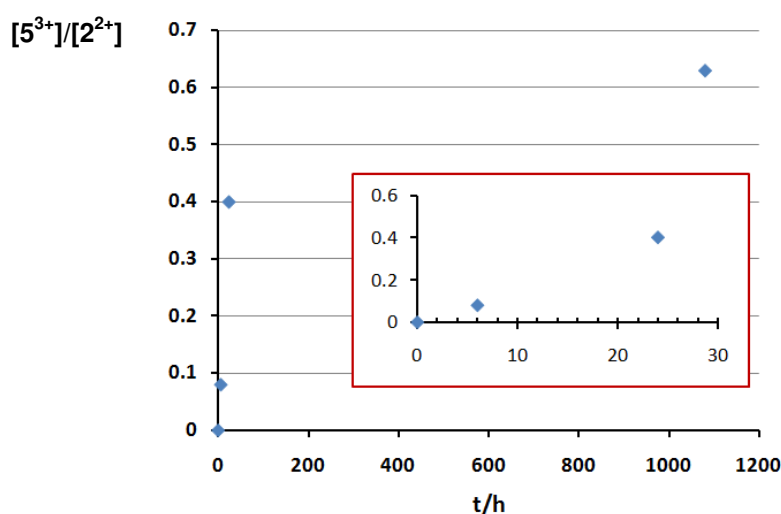
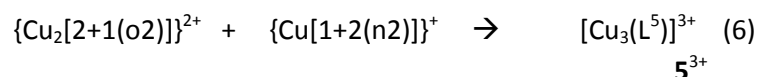
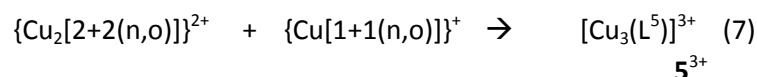


Figure 3-7: Graph of the $\mathbf{2}^{2+}$ to $\mathbf{5}^{3+}$ oligomerization evolution as a function of time monitored by MS spectroscopy. The inset shows the first 30 h. Units are the same as in the main graph.

The formation of the trinuclear complex from the dinuclear compound indicates that at least one of the imine C=N of the [2+2] Schiff Base ligand has to be broken and then the fragments have to react again so that the new [3+3] ligand can be formed. This process has not been observed for the free ligand, at least during the time scale of days. Thus it must be self-assisted by the Cu^I dinuclear complex. This is in sharp contrast with other macrocyclic ligands where this process is known to occur very fast as is the case for the systems derived from pyridine dialdehyde and diamine.^{134, 168-169} Figure 4-3 presents potential condensation products that can be obtained from the reaction of a 1:1 dialdehyde and triamine in order to illustrate the variety of compounds including macrocyclic and acyclic compounds. As mentioned earlier the L² does not undergo any reorganization process by itself but it does so when complexed to Cu^I ions. Thus potential fragments that can lead to the trinuclear complex are,



or the



The ligand nomenclature is described in Figure 3-3. For instance for the case of [2+1(o2)], the [2+1] indicates the condensation product of two dialdehydes and one triamine and in the parenthesis is indicated the number and nature of unreacted groups, “n” for a secondary amine and “o” for aldehyde.

3.3 Conclusions

In this paper we report the synthesis of three new [2+2] macrocyclic ligands, L¹, L² and L³, with pendant arms that consist on the condensation of phthalaldehyde and N²-substituted triamines with moderate to good yields. It is also shown that once these [2+2] compounds are formed they do not

undergo further rearrangement reactions in solution and thus the different compounds shown in Figure 3-3 are not in equilibrium in our case. Therefore the formation of the [1+1] condensation product, higher oligomers such as [3+3], [4+4], etc. and linear polymers represent very minor products, and thus the [2+2] condensation product is the favored one.

In contrast the reaction of the [2+2] condensation ligands, L^1 and L^2 , with Cu^I complexes generate a mixture of dinuclear (1^{2+} and 2^{2+}) and trinuclear (4^{3+} and 5^{3+}) complexes that are in equilibrium in solution. The unique reactivity of the present Cu^I complex puts forward the delicate balance between electronic and geometrical factors that allow to break and generate imine bonds and thus observing the [2+2] and [3+3] equilibrium reaction. Finally, all of the Cu^I complexes described here react only very slowly with molecular oxygen at room temperature and thus manifest the capacity of the Schiff base ligand to stabilize the Cu^I oxidation state in a MeCN solution.

3.4 Experimental Section

3.4.1 Physical Methods.

IR spectra of solid samples were taken in a Mattson-Galaxy Satellite FT-IR spectrophotometer using a MKII Golden Gate single reflection ATR system. HRMS analyses were recorded on Waters LCT Premier liquid chromatographcoupled time-of-flight mass spectrometer (HPLC/MS-TOF) with electrospray ionization (ESI). MS analyses were recorded on an esquire 6000 ESI ion Trap LC/MS (Bruker Daltonics) equipped with an electrospray ion source. NMR spectra were measured using a Bruker DPX 200 MHz, a Bruker DXP 300 MHz or a Bruker DRX 400 MHz. Elemental analysis were performed using a CHNS-O EA-1108 elemental analyzer from Fisons. UV-vis spectra were taken in a Cary 50 Scan spectrophotometer.

3.4.2 Materials and Synthesis.

All reagents used in the present work were obtained from Aldrich Chemical Co. and were used without further purification unless otherwise stated. ftNC₂H, ftNC₂py and H₂NC₂py (see Figure 3-3 for abbreviations; H₂NC₂py is also abbreviated as apme¹⁶⁰) were synthesized as described in the literature.¹⁷¹ H₂N-C₂NEt was synthesized by following two methods: (i) Method A as described by Song et al.¹⁷² and (ii) a newly developed Method B (see below). Solvents were purchased from SDS and purified and dried by passing them through an activated alumina purification system (MBraun SPS-800) or by conventional distillation techniques. Preparation and manipulation of Cu^I complexes were carried out in a Drybox (MBraun, N₂ or Ar) with O₂ and H₂O concentrations <1.0 ppm.

3.4.3 Ligand Synthesis.

3.4.3.1 bsm2py (L¹).

A solution of isophthalaldehyde (0.228 g, 1.70 mmol) in CH₃CN (40 mL) was slowly added (6.0 mL/h *via* syringe pump) to a solution of H₂NC₂py (0.330 g, 1.70 mmol) in acetonitrile (40 mL) at 0° C and allowed to react overnight at room temperature. It was then filtered to remove some solid particles and the filtrate was then concentrated in the rotary evaporator leading to a separation of an oil. The solvent was decanted and the oil dried under vacuum. Yield: 0.380 g (76 %). Anal. Calcd (%) for C₃₆H₄₀N₈ · 0.6H₂O · 0.4CH₃CN (MW = 611.99 g·mol⁻¹): C, 72.22; H, 6.98; N, 19.23. Found: C, 72.24; H, 6.45; N, 19.21. ¹H-NMR (400 MHz, CDCl₃) δ (ppm): 2.98 (t, *J* = 4 Hz, 8H, pyN-CH₂-CH₂-N=), 3.72 (t, *J* = 4 Hz, 8H, pyN-CH₂-CH₂-N=), 3.87 (s, 4H, NCH₂-py), 7.04-7.07 (m, 2H, H_β), 7.16 (s, 2H, H_{ortho}'), 7.29-7.33 (m, 2H, H_{meta}), 7.38-7.42 (m, 4H, H_β' + H_γ), 7.84-7.87 (m, 4H, H_{ortho}), 8.08 (s, 4H, -CH=N), 8.49 (d, *J* = 3.82 Hz, 2H, H_α). ¹³C-NMR (CDCl₃, 400 MHz) δ(ppm): 55.22 (pyN-CH₂-CH₂-N=), 59.72 (pyNCH₂-CH₂-N=), 61.38 (N-CH₂-py), 121.78 (C_β), 123.11 (C_β'), 128.70 (C_{ortho}), 128.90 (C_γ), 129.75 (C_{ortho}'), 136.12 (C_{meta}), 136.67 (C_{qarom}), 148.80 (C_α), 160.15 (C_{qα}), 161.09 (CH=N). FT-IR ν (cm⁻¹): 2838 (C-H), 1644 (C=N), 1588, 1568 (C-C py), 1473, 1433 (C-H), 797 (C-H ar), 756 (C-H py), 692 (C-H ar), 614 (C-H py). HRMS (*m/z*): [M⁺Na]⁺: 607.3279 (100%); Calcd. Mass: 607.3274.

3.4.3.2 ftNC₂PhOH.

Salicylaldehyde (3.0 mL, 28 mmol) was added to a mixture of ftNC₂H (10.000 g, 28 mmol) in 1,2-dichloroethane (150 mL). The crude product was stirred for several minutes. Afterwards NaBH(OAc)₃ (8.60 g, 0.039 mol) was slowly added and the mixture stirred at room temperature for 24 hours. The organic layer was extracted after adding 100 mL of water. The aqueous phase was washed with dichloromethane (2 x 100 mL). The organic fractions were dried over MgSO₄ and concentrated up to ~10 mL. 150 mL of methanol were then added while stirring, producing the precipitation of the product as a white solid, which was filtered and dried under vacuum. Yield: 11.21 g (87%).

Anal. Calcd (%) for C₂₇H₂₃N₃O₅·0.25 H₂O (MW= 473.99 g.mol⁻¹): C, 68.42; H, 5.00; N, 8.87. Found: C, 68.33; H, 5.02; N, 9.01. ¹HNMR (400 MHz, CDCl₃) δ (ppm): 2.95 (t, *J* = 6 Hz, 4H, ftN-CH₂-CH₂-N), 3.89 (m, 6H, ftN-CH₂-CH₂-N + N-CH₂-PhOH), 6.24-6.29 (m, 1H, H_α), 6.71-6.78 (m, 1H, H_β), 6.92-6.98 (m, 1H, H_{β'}), 7.01-7.08 (m, 1H, H_γ), 7.70-7.84 (m, 8H, H_{ar}), 9.07 (s, br, PhOH). ¹³C-NMR (100 MHz, CDCl₃) δ (ppm): 34.8 (ftN-CH₂-CH₂-N), 51.5 (ftN-CH₂-CH₂-N), 58.1 (N-CH₂-PhOH), 116.0 (C_αPhOH), 119.5 (C_γPhOH), 121.4 (C_{qα}PhOH), 123.2 (C_{prot1}) 129.0, 129.1 (C_βPhOH, C_{β'}PhOH), 132.2 (C_{qprot}), 133.8 (C_{prot2}), 156.8 (C-OH), 168.2 (C=O). FT-IR ν (cm⁻¹): 1700 (C=O), 1398 (CO-N), 754 (C-H PhOH), 708 (C-H ar), 532 (C-H ft). Anal. Calcd (%) for C₂₇H₂₃N₃O₅·0.25 H₂O (MW = 473.99 g.mol⁻¹): C, 68.42; N, 8.86; H, 5.00. Found: C, 68.17; N, 8.92; H, 5.05. MS (m/z): M-H⁺: 470.3 (100%). HRMS (m/z): [M+Na]⁺: 492.1526 (100%); Calcd. Mass: 492.1535.

3.4.3.3 H₂NC₂PhOH.

To a solution of ftNC₂PhOH (8.65 g, 18.42 mmol) in CHCl₃:Ethanol (60 mL:320 mL), hydrazine monohydrate (9.7 mL, 0.2 mol) was added. The mixture was stirred at room temperature for 24 hours and the obtained white precipitate filtered off as well as discarded. The resulting transparent solution was evaporated under reduced pressure. Chloroform (150 mL) was then added to the residue and the mixture stirred for another 24 hours and filtered again. Evaporation of the chloroform fraction afforded the desired product as an oil. Yield: 2.62 g (85%). Anal. Calcd (%) for C₁₁H₁₉N₃O·0.14CHCl₃ (MW = 226.00 g.mol⁻¹): C, 59.20; H, 8.54; N, 18.59. Found: C, 59.39; H, 8.81;

N, 18.21. $^1\text{H-NMR}$ (400 MHz, CDCl_3) δ (ppm): 2.59 (t, $J = 6$ Hz, 4H, $\text{H}_2\text{N-CH}_2\text{-CH}_2\text{-N}$), 2.86 (t, $J = 6$ Hz, 4H, $\text{H}_2\text{N-CH}_2\text{-CH}_2\text{-N}$), 3.73 (s, 2H, $\text{N-CH}_2\text{-PhOH}$), 6.6-7.2 (m, 4H, H_{PhOH}). $^{13}\text{C-NMR}$ (100 MHz, CDCl_3) δ (ppm): 39.3 ($-\text{CH}_2\text{-NH}_2$), 55.7 ($-\text{CH}_2\text{-CH}_2\text{-NH}_2$), 57.9 ($-\text{CH}_2\text{-PhOH}$), 116.4 ($\text{C}\alpha$), 119.1 ($\text{C}\gamma$), 122.7 ($\text{Cq}\alpha$), 128.8 ($\text{C}\beta$), 129.3 ($\text{C}\beta'$), 157.5 (C-OH). FT-IR ν (cm^{-1}): 1587 (C=C), 1472, 1446 ($-\text{CH}_2-$), 1269, 1256 (ArC-OH), 753 (C-H ar), 708 (C-H PhOH), 532 (C-H ar). MS (m/z): $[\text{M}+\text{H}]^+$: 210.1 (100%).

3.4.3.4 bsm2PhOH (L^2).

To a solution of $\text{H}_2\text{NC}_2\text{PhOH}$ (1.021 g, 4.88 mmol) in MeCN (50 mL) is slowly added (9 mL/h *via* syringe pump) under stirring a solution of isophthalaldehyde (0.655 g, 4.88 mmol) in MeCN (50 mL). After 24 hours of stirring a white solid was obtained and filtered and then dried under vacuum. Yield: 0.797 g (53%). Crystals for X-ray diffraction were obtained by dissolving 0.015 g of bsm2PhOH in 1 mL of chloroform and then diluting the solution with MeOH. Slow evaporation of the solvents afforded white crystals suitable for X-ray diffraction. Anal. Calcd (%) for $\text{C}_{38}\text{H}_{42}\text{N}_6\text{O}_2$ (MW = 614.78 $\text{g}\cdot\text{mol}^{-1}$): C, 74.24; H, 6.89; N, 13.67. Found: C, 73.88; H, 6.84; N, 13.67. $^1\text{H-NMR}$ (400 MHz, CDCl_3) δ (ppm): 2.98 (t, $J = 6$ Hz, 8H, $\text{CH=N-CH}_2\text{-CH}_2\text{-N}$), 3.68 (t, $J = 6$ Hz, 8H, $\text{CH=N-CH}_2\text{-CH}_2\text{-N}$), 3.88 (s, 4H, $\text{N-CH}_2\text{-PhOH}$), 6.75-6.85 (m, 2H, $\text{H}_{\gamma\text{PhOH}}$), 6.85-6.90 (m, 2H, $\text{H}_{\alpha\text{PhOH}}$), 7.0-7.1 (m, 2H, $\text{H}_{\beta'\text{PhOH}}$), 7.06 (s, 2H, $\text{H}_{\text{orto}', \text{arom}}$), 7.15-7.25 (m, 2H, $\text{H}_{\beta\text{PhOH}}$), 7.35-7.45 (m, 2H, $\text{H}_{\text{meta, arom}}$), 7.8-7.9 (m, 4H, $\text{H}_{\text{orto, arom}}$), 8.04 (s, 4H, CH=N), 10.22 (s, br, PhOH). $^{13}\text{C-NMR}$ (100 MHz, CDCl_3) δ (ppm): 55.6 ($\text{CH=N-CH}_2\text{-CH}_2\text{-N}$), 58.9 ($\text{N-CH}_2\text{-PhOH}$), 59.6 ($\text{CH=N-CH}_2\text{-CH}_2\text{-N}$), 116.6 ($\text{C}\alpha_{\text{PhOH}}$), 119.1 ($\text{C}\gamma_{\text{PhOH}}$), 123.0 ($\text{Cq}\alpha_{\text{PhOH}}$), 128.6, 128.7, 128.9, 129.0 ($\text{C}_{\text{orto, arom}}$, $\text{C}_{\text{meta, arom}}$, $\text{C}\beta_{\text{PhOH}}$, $\text{C}\beta'_{\text{PhOH}}$), 130.5 ($\text{C}_{\text{orto}', \text{arom}}$), 136.2 (Cq_{arom}), 157.8 (C-OH), 161.7 (CH=N). FT-IR ν (cm^{-1}): 3185 (OH), 2837, 2805 (C-H), 1642 (C=N), 799 (C-H ar), 746 (C-H PhOH), 691 (C-H ar). MS (m/z): M-H^+ : 615.3. HRMS (m/z): $[\text{M}+\text{H}]^+$: 615.3451 (100%); Calcd. Mass: 615.3448.

3.4.3.5 EtN(CH_2CN) $_2$.

In a round-bottom flask containing 70% ethylamine (2 mL, 25 mmol), water (15 mL) and HCl (6 mL), a 4.2 mL sample of 37% formaldehyde (55 mmol) was added and the mixture stirred for 30 min. The solution was then cooled at 0 $^\circ\text{C}$ and NaCN (2.94 g, 55 mmol) was added, allowing the mixture to

react at room temperature for 24 h. Then NaOH (1 g) and dichloromethane (15 mL) were added, the organic phase extracted and the aqueous phase washed with dichloromethane (2 x 15 mL). The combined organic fractions were dried over MgSO_4 and the solvent was removed in the rotary evaporator. The oil obtained was then purified via flash chromatography in silica gel using a hexane/ethyl acetate mixture (2:1) as eluent. Yield: 1.274 g (42%). Anal. Calcd (%) for $\text{C}_6\text{H}_9\text{N}_3 \cdot 0.25\text{H}_2\text{O}$ (MW = 127.66 $\text{g}\cdot\text{mol}^{-1}$): C, 56.45; H, 7.50; N, 32.92. Found: C, 56.37; H, 7.42; N, 32.71 ^1H -NMR (400 MHz, CDCl_3) δ (ppm): 1.17 (t, J = 7 Hz, 3H, N- CH_2 -**CH₃**), 2.72 (q, J = 7 Hz, 2H, N-**CH₂**-CH₃), 3.62 (s, 4H, N-**CH₂**-CN). ^{13}C -NMR (100 MHz, CDCl_3) δ (ppm): 12.4 (**-CH₃**), 41.7 (**-CH₂**-CH₃), 48.01 (**-CH₂**-CN), 114.35 (**-CN**). FT-IR $\nu(\text{cm}^{-1})$: 2978, 2944, 2834 (C-H), 1428 ($-\text{CH}_2-$), 1106, 868.

3.4.3.6 ftN-C2NEt.

A mixture of ftNC2H (5.000 g, 13.76 mmol), K_2CO_3 (2.850 g, 20.64 mmol) and iodoethane (2.2 mL, 27.52 mmol) in 150 mL acetonitrile were refluxed for 18 h. After cooling to room temperature it was filtered and solvent was evaporated to dryness. The residue was re-dissolved in 100 mL CHCl_3 and was washed with 3N aqueous NaCl solution and the watery phase extracted three times with 3 x 20 mL CHCl_3 . The combined organic phases were dried over Na_2SO_4 . Evaporation of the solvent gave yellow oil which turned solid under high vacuum. Yield: 5.10 g (95 %). Anal. Calcd (%) for $\text{C}_{22}\text{H}_{21}\text{N}_3\text{O}_4$ (MW = 391.42 $\text{g}\cdot\text{mol}^{-1}$): C, 67.51; H, 5.41; N, 10.74. Found: C, 67.20; H, 5.42; N, 10.85. ^1H -NMR (400 MHz, CDCl_3) δ (ppm): 0.95 (t, J = 6 Hz, 3H, N- CH_2 -**CH₃**), 2.65 (q, J = 6 Hz, 2H, N-**CH₂**-CH₃), 2.80 (t, J = 6 Hz, 4H, ftN- CH_2 -**CH₂**-N), 3.75 (t, J = 6 Hz, 4H, ftN-**CH₂**-CH₂-N), 7.67-7.78 (m, 8H, Har). ^{13}C -NMR (400 MHz, CDCl_3) δ (ppm): 11.91 (N-**CH₂**-CH₃), 35.92 (ftN-**CH₂**-CH₂-N), 47.24 (N-**CH₂**-CH₃), 51.21 (ftN- CH_2 -**CH₂**-N), 123.05 (C_{arom}), 132.22 (C_{qarom}), 133.68 (C_{arom}), 168.26 (**C=O**). HRMS (m/z): $[\text{M}^+\text{Na}]^+$: 414.1436 (100%); Calcd. Mass: 414.1430.

H₂N-C2NEt was synthesized by following two procedures:

Method A: A round bottom flask, kept under nitrogen, containing LiAlH_4 (3.737 g, 95 mmol) and dry THF (110 mL) was cooled to -10°C . Carefully, concentrated H_2SO_4 (5 mL) was added, the mixture stirred for 30 minutes at -10°C , and then allowed to warm to room temperature. $\text{EtN}(\text{CH}_2\text{CN})_2$

(1.274 g, 10.4 mmol) was dissolved in dry THF (10 mL), added carefully to the hydride mixture, and allowed to react overnight. Then water (7 mL) was added slowly, the mixture was stirred 24 hours and the solvent was evaporated through a N₂ stream. Afterwards, dichloromethane (50 mL) and methanol (50 mL) were added and the mixture was stirred again 24 hours. The solid found was then filtered off and discarded and the filtrate evaporated. The product was finally obtained through distillation under reduced pressure. Yield: 0.291 g (21%).

Method B: To a solution of ftN-C₂NEt (5.000 g, 12.77 mmol) in chloroform:ethanol (50 mL:280 mL), hydrazine monohydrate (6.98 mL, 0.14 mol) was added. The mixture was stirred at room temperature for 24 hours and the obtained white precipitate filtered off and discarded. The resulting transparent solution was evaporated under reduced pressure. Chloroform (150 mL) was then added to the residue and the mixture stirred for another 24 hours and filtered again. Evaporation of the chloroform fraction afforded oil which was purified by distillation at 150 °C in vacuum. Yield: 0.920 g (55%). Anal. Calcd (%) for C₆H₁₇N₃ · 0.15H₂O (MW = 133.92 g·mol⁻¹): C, 53.81; H, 13.02; N, 31.38. Found: C, 53.64; H, 13.53; N, 31.59. ¹H-NMR (400 MHz, CDCl₃) δ (ppm): 1.01 (t, *J* = 7 Hz, 3H, N-CH₂-CH₃), 1.31 (s, br, 4H, N-CH₂-CH₂-NH₂), 2.40-2.60 (m, 6H, N-CH₂-CH₃ + N-CH₂-CH₂-NH₂), 2.75 (t, *J* = 7 Hz, 4H, N-CH₂-CH₂-NH₂). ¹³C-NMR (400MHz, CDCl₃) δ(ppm): 11.77 (N-CH₂-CH₃), 39.86 (N-CH₂-CH₂-NH₂), 47.74 (N-CH₂-CH₃), 56.75 (N-CH₂-CH₂-NH₂). FT-IR ν(cm⁻¹): 3354, 3289 (NH₂), 2962, 2934, 2870, 2804 (C-H), 1460 (-CH₂-, CH₃), 918, 864 (NH₂).

3.4.3.7 bsm2Et (L³).

The procedure is the same as for bsm2py, starting with H₂N-C₂NEt (0.300 g, 2.29 mmol) in MeCN (40 mL) and isophthalaldehyde (0.308 g, 2.29 mmol) in MeCN (40 mL). The product is obtained as solid. Yield: 0.250 g (48%). Anal. Calcd (%) for C₂₈H₃₈N₆ (MW = 458.64 g·mol⁻¹): C, 73.33; H, 8.35; N, 18.32. Found: C, 73.29; H, 8.34; N, 18.24. ¹H-NMR (400 MHz, CDCl₃) δ (ppm): 0.96 (t, *J* = 7 Hz, 6H, N-CH₂-CH₃), 2.55 (q, *J* = 7 Hz, 4H, N-CH₂-CH₃), 2.85 (t, *J* = 6 Hz, 8H, N-CH₂-CH₂-Nbz), 3.66 (t, *J* = 6 Hz, 8H, N-CH₂-CH₂-Nbz), 7.07 (s, 2H, H_{ortho',arom}), 7.43 (t, *J* = 7 Hz, 2H, H_{ortho,arom}), 7.91-7.96 (m, 4H, H_{meta,arom}),

8.04 (s, 4H, CH=N). ¹³C-NMR (400 MHz, CDCl₃) δ (ppm): 12.37 (N-CH₂-CH₃), 48.57 (N-CH₂-CH₃), 54.35 (N-CH₂-CH₂-N=CH), 60.00 (N-CH₂-CH₂-N=CH), 128.32, 128.88, 129.72 (C_{orto}′, C_{meta}, C_{orto}), 136.72 (C_{qarom}), 161.10 (CH=N). HRMS (m/z): [M⁺Na]⁺: 481.3051 (100%); Calcd. Mass: 481.3056.

3.4.4 Synthesis of Cu^I complexes.

3.4.4.1 [Cu₂(L¹)](PF₆)₂, 1(PF₆)₂.

[Cu(CH₃CN)₄]PF₆ (0.373 g, 1 mmol) was added to a solution of bsm2py (0.292 g, 0.5 mmol) in MeOH (20 mL) and the mixture was stirred for one hour at room temperature. The resulting yellow-orange precipitate was filtered and washed with Et₂O. The solid was then redissolved in CH₂Cl₂, filtered, the obtained solid discarded and the solvent removed under vacuum to obtain the product. Yield: 0.400 g (0.40 mmol; 80%). Diffusion of a mixture of THF/Et₂O (1:1) into the mother solution yielded a dark yellow powder Anal. Calcd (%) for C₃₆H₄₀Cu₂F₁₂N₈P₂·0.5CH₂Cl₂ (MW = 1044.24 g·mol⁻¹): C: 41.98, H: 3.95, N: 10.73, Found: 41.87, H: 3.95, N: 10.77. FD-MS (70 eV, CH₃CN): m/z = 857 (71%) [Cu₂L¹(PF₆)]⁺, 791 (20%) [CuL¹(PF₆)]⁺, 647 (100%) [CuL¹]⁺, 356 (17%) [Cu₂L¹]²⁺. IR (KBr) ν (cm⁻¹): 2914/2857 (C-H), 1637 δ(C=N), 1440 δ(C-H_{aliphatic}), 842 (P-F), 764/689 δ(C-H_{arom}).

3.4.4.2 [Cu₃(L⁴)](PF₆)₃, 4(PF₆)₃.

[Cu(CH₃CN)₄]PF₆ (0.373 g, 1 mmol) was added to a solution of H₂NC₂py (0.194 g, 1 mmol) and isophthalaldehyde (0.134 g, 1.00 mmol) in MeOH (20 mL) and the mixture was stirred for two hours at room temperature. The resulting orange precipitate was filtered off, washed with a small amount of MeOH and Et₂O and dried under vacuum. Yield: 0.342 g (0.288 mmol; 68%). Recrystallisation of the crude product from CH₃CN and diffusion of a mixture of THF/Et₂O (1:1) into the mother solution for about 2 weeks yielded red crystals suitable for X-Ray diffraction analysis. Anal. Calcd (%) for C₅₄H₆₀Cu₃N₁₂F₁₈P₃ (MW = 1502.67 g·mol⁻¹): C, 43.16; H, 4.02; N, 11.19. Found: C, 43.34; H, 4.30; N, 11.06. IR (KBr)ν(cm⁻¹): 2916/ 2854 (C-H), 1633 (C=N), 1439 (C-H), 842 (P-F), 763/766 δ(C-H). FD-MS (70 eV, CH₃CN): m/z = 939 (95%) [CuL⁴]⁺, 876 (100%) [L⁴+H]⁺.

3.4.4.3 [Cu₃(L⁴)](SbF₆)₃, 4(SbF₆)₃.

To a suspension of L¹ (0.029g, 0.05 mmol) in CH₃CN (0.5 mL) a solution of [Cu(CH₃CN)₄]SbF₆ (0.048g, 0.10 mmol) in CH₃CN (0.5 mL) is added dropwise and the solution is stirred for 1 hour. Slow diethyl ether diffusion into the solution for about 2 weeks affords orange crystals, which have been characterized by X-ray diffraction analysis. Yield: 0.042g (69%). Anal. Calcd (%) for C₅₄H₆₀Cu₃N₁₂F₁₈Sb₃ (MW = 1775.02 g·mol⁻¹): C, 36.54; N, 9.47; H, 3.41. Found: C, 36.86; N, 9.70; H, 3.72. ¹H-NMR (400 MHz, CD₃COCD₃) δ (ppm): 2.8-3.3 (m, 4H, N-CH₂-CH₂-N=), 3.4-4.0 (m, 4H, N-CH₂-CH₂-N=), 4.19 (s, 2H, py-CH₂-N), 7.2-8.8 (m, 10H, Har + CH=N). FT-IR ν (cm⁻¹): 2916, 2853 (C-H), 1633 (C=N), 1603 (SbF₆), 1440 (def -CH₂-), 764 (def C-Har), 653 (SbF₆).

3.4.4.4 [Cu₂(L²)(CH₃CN)₂](CF₃SO₃)₂ 2MeCN·H₂O, 2(CF₃SO₃)₂·2MeCN·H₂O

A solution of [Cu(CH₃CN)₄][CF₃SO₃] (0.050 g, 0.128 mmol) in MeCN (2 mL) was added to a suspension of L² (0.040 g, 0.065 mmol) in MeCN (1 mL). The yellow solution was stirred for 1 h and then it was filtered. Addition of diethyl ether (50 mL) into the yellow solution generates a yellow powder. Yield: 0.060 g (80 %) ESI-MS (m/z): 615.3 [L²+H]⁺, 637.2 [L²+Na]⁺, 677.2 [L²+Cu]⁺. ¹H-NMR (200 MHz, CD₃COCD₃) δ(ppm): 2.9-3.3 (m, 4H, =N-CH₂-CH₂-N), 3.9-4.4 (m, 6H, =N-CH₂-CH₂-N + N-CH₂-PhOH), 6.8-7.4 (mm, 5H PhOH), 7.8-9.2 (mm, 6H, Har + CH=N). FT-IR ν (cm⁻¹): 3320 (OH), 2916, 2855 (C-H), 1628 (C=N), 1275, 1221, 1025 (CF₃SO₃), 758 (C-H PhOH), 634 (CF₃SO₃). Anal. Calcd (%) for C₆₀H₆₃Cu₃N₉F₉O₁₂S₃·2CH₃CN·H₂O (MW = 1660.1 g·mol⁻¹): C, 46.31; N, 9.28; H, 4.31; S, 5.79. Found: C, 46.12; N, 9.31; H, 4.29; S, 5.77.

The compound was also synthesized in MeOH as described initially and MS analysis indicates formation of 2²⁺ only. However, slow diethyl ether diffusion into the acetonitrile solution (first synthesis) of the compound affords a mixture of yellow and orange crystals, after 12-15 days, which have been both characterized by X-ray diffraction analysis and show the formation of [Cu₂(L²)(CH₃CN)₂](CF₃SO₃)₂, 2(CF₃SO₃)₂ and [Cu₃(L⁵)](CF₃SO₃)₃, 5(CF₃SO₃)₃. MS (m/z): 615 [L²+H]⁺, 922 [L⁵+H]⁺.

3.4.4.5 [Cu₃(L⁶)(CH₃CN)₃](CF₃SO₃)₃, 6(CF₃SO₃)₃.

A solution of [Cu(CH₃CN)₄]CF₃SO₃ (0.025 g, 0.064 mmol) in CH₃CN (2 mL) was added to a suspension of L³ (0.015 g, 0.032 mmol) in CH₃CN (0.5 mL) and the mixture was stirred for 1 hour. Slow diethyl ether diffusion into the solution for about 2 weeks affords yellow crystals, which have been characterized by X-ray diffraction analysis. Yield: 0.020 g (71%). Anal. Calcd. (%) for C₄₅H₅₇Cu₃N₉F₉O₁₂S₃·2.25 CH₃CN·0.75 C₄H₁₀O (MW = 1473.66 g.mol⁻¹): C, 42.79; N, 10.69; H, 4.87; S, 6.53. Found: C, 42.86; N, 10.58; H, 4.73; S, 6.38. ¹H-NMR (400MHz, CD₃COCD₃) δ (ppm): 1.1-1.3 (m, 3H, N-CH₂-CH₃), 2.6-3.1 (m, 6H, N_{ter}-CH₂-), 3.6-4.0 (m, 4H, CH=N-CH₂-CH₂-N_{ter}), 7.7-8.8 (m, 6H, Har + CH=N). FT-IR ν(cm⁻¹): 1631 (C=N), 1253, 1223 (CF₃SO₃), 1149 (def -CH₂-), 1027 (CF₃SO₃), 634 (CF₃SO₃).

3.4.5 X-ray diffraction studies.

The complexes were crystallized as described in the synthetic procedure. Crystals of L², 2(CF₃SO₃)₂, 4(SbF₆)₃, 5(CF₃SO₃)₃ and 6(CF₃SO₃)₃ were mounted on a nylon loop and used for X-ray structure determination. The measurements were carried out on a Bruker Smart Apex CCD diffractometer. Single crystals of 4(PF₆)₃ were coated with polyfluorether oil and mounted on a glass fiber. Data were collected on a Nonius Kappa diffractometer with a CCD array detector at 173(2) K Mo-Kα radiation was used in all measurements (λ = 71.073 pm). Space groups were determined from systematic absences and subsequent least-squares refinement. The structures were solved by direct methods and refined on F₂ using fullmatrix least-squares techniques.¹⁷³ The non-hydrogen atoms were refined anisotropically. The H-atoms were placed in geometrically optimized positions using a riding model on the atom to which they are attached except the O-H hydrogen atoms for the 2(CF₃SO₃)₃ which are refined without constraints. For the structure 5(CF₃SO₃)₃ a considerable amount of electron density attributable to partially disordered solvent water molecules was removed with the SQUEEZE option of PLATON.¹⁷⁴ Those solvent molecules are, however, included in the reported chemical formula and derived values (e.g. formula weight, F₀₀₀, etc). Structures 2 (CF₃SO₃)₃, 5(CF₃SO₃)₃ and 6(CF₃SO₃)₃

present disorder on one of the CF_3SO_3 counterions. For the structure **4**(PF_6)₃ SAME restraints were used to refine solvate molecules (THF and MeOH). Further crystallographic experimental details are given in Table 3-1 and 3-2.

4 Open-Chain Copper(I) Complexes

4.1 Syntheses, Characterization and Properties of Open-Chain Copper(I) Complexes

This work was published previously in the European Journal of Inorganic Chemistry

Utz, D.; Kisslinger, S.; Heinemann, F. W.; Hampel, F.; Schindler, S., *Chem. Eur. J.* **2011**, *2011*, 255–267 (doi: 10.1002/ejic.201190002).

Macrocyclic ligands are a special class of ligands that are important for many applications, especially due to their ability to strongly bind metal cations that fit the macrocyclic cavity. Early work from Nelson and co-workers followed up by Fenton and co-workers has shown the versatility of using dialdehydes together with amines to form an interesting group of macrocyclic ligands.^{126, 134} Martell and co-workers successfully showed the application of one of the systems to model the reactivity of the copper enzyme tyrosinase. Tyrosinases are monooxygenases that are responsible for the hydroxylation of the phenol residue in tyrosine – thus forming a catechol – and subsequent two electron oxidation to the according *o*-quinones.^{4-6, 59, 166, 175-180} For a better understanding of tyrosinase reactivity, low molecular weight copper complexes have been synthesized as model compounds for this enzyme and their reactivity towards dioxygen has been investigated.^{61, 115, 181-193} The model compound for tyrosinase containing a macrocyclic ligand used by Martell and co-workers was the dinuclear $[\text{Cu}_2(\text{mac})(\text{CH}_3\text{CN})_2](\text{ClO}_4)_2$, (mac = 3,6,9,17,20,23-hexaazatricyclo[23.3.1.1]trianta-1(29),2,9,11(30),12(13),14,16,23,25,27-decaene: Figure 4-1) which showed hydroxylation of the aromatic moiety of the ligand upon oxidation.^{162-165, 194}

No peroxido or bis- μ -oxido complex formation could be detected during the oxidation reaction using low temperature stopped-flow techniques.^{162, 165} Kinetic studies revealed that the reaction most likely proceeded through a peroxido complex as an intermediate.^{162, 165} Furthermore, related complexes of $[\text{Cu}_2(\text{mac})(\text{CH}_3\text{CN})_2](\text{ClO}_4)_2$ were investigated. Here, no intramolecular ligand hydroxylation

reactions were observed but bis- μ -oxido-complexes could be spectroscopically characterized.^{156, 195}

Theoretical calculations confirmed the formation of different peroxido and oxido complexes as active species for these macrocyclic systems.^{156, 195-196} However, so far the mechanism of how a dicopper site binds and/or activates O_2 , is far from being completely understood.¹⁹³

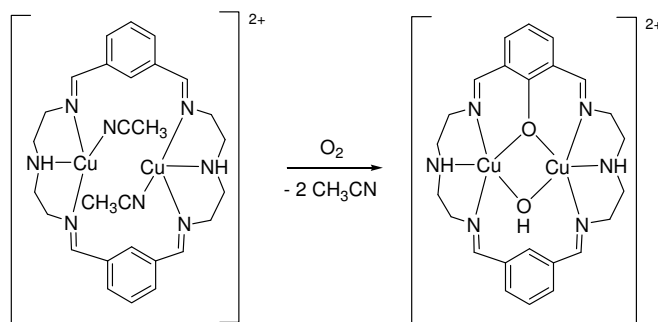


Figure 4-1: Oxidation and intramolecular ligand hydroxylation of $[Cu_2(mac)(CH_3CN)_2](ClO_4)_2$.

In order to investigate the question whether the dinuclearity of $[Cu_2(mac)(CH_3CN)_2](ClO_4)_2$ is crucial for the hydroxylation reaction, copper(I) complexes of the open-chain ligand (7E)- N^1 -benzylidene- N^2 -((E)-2-(benzylideneamino)ethyl)ethane-1,2-diamine (L^1) (which resembles half of the macrocyclic ligand mac) were synthesized and characterized. Furthermore, their reactivity towards dioxygen was investigated. Additionally, the chemically reduced form of L^1 , the amine N^1 -benzyl- N^2 -(2-(benzylamino)ethyl)ethane-1,2-diamine (L^2) was synthesized and characterized (Figure 4-2).

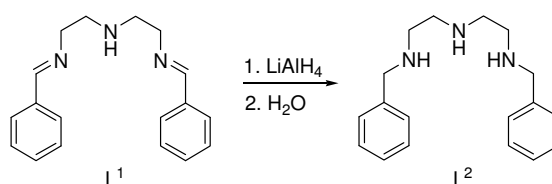


Figure 4-2: Reduction of (7E)- N^1 -benzylidene- N^2 -((E)-2-(benzylideneamino)ethyl)ethane-1,2-diamine (L^1) to N^1 -benzyl- N^2 -(2-(benzylamino)ethyl)ethane-1,2-diamine (L^2).

4.2 Results and discussion

4.2.1 Syntheses and Characterization of L^1 , $[Cu(L^1)(CH_3CN)]PF_6$ (1) and $[Cu_2(L^1)_2](ClO_4)_2$ (2).

The reaction of benzaldehyde with diethylenetriamine in a 2:1 ratio yielded the Schiff Base ligand L^1 . However, L^1 shows an imine-aminal equilibrium in solution similar to its macrocyclic analogue

mac.^{164-165, 194} Mac crystallizes in its mono aminal form.^{164, 194} Imine-aminal equilibria in solution, as well as the preference of the aminal form in solid state, are widely known for Schiff base ligands.^{164, 195, 197} The ^1H NMR spectrum in CDCl_3 clearly demonstrates that 61% of L^1 are present in the aminal and only 39% in the bisimine form (Figure 4-2).

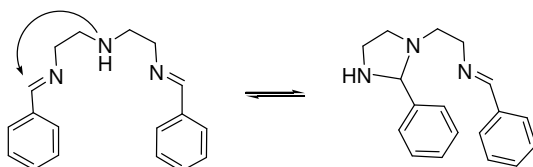


Figure 4-3: Imine-aminal equilibrium of L^1 .

In solid state only the aminal form is found, as indicated by IR spectroscopy and X-Ray analysis. The molecular structure of the aminal form of L^1 is shown in Figure 3-3. Within the crystal packing the molecules are stacked along the crystallographic b axis. Two stacks at a time are connected by intermolecular hydrogen bonds between the secondary amine groups $\text{N}(1) - \text{H}(1) \cdots \text{N}(1^{\#1})$ (with $\text{N}(1) - \text{H}(1) = 0.92(3) \text{ \AA}$, $\text{H}(1) \cdots \text{N}(1^{\#1}) = 2.55(3) \text{ \AA}$, $\text{N}(1) \cdots \text{N}(1^{\#1}) = 3.437(2) \text{ \AA}$ and $\text{N}(1) - \text{H}(1) \cdots \text{N}(1^{\#1}) = 164(2)^\circ$; $^{\#1} = x+1, y-0.5, -z+1$).

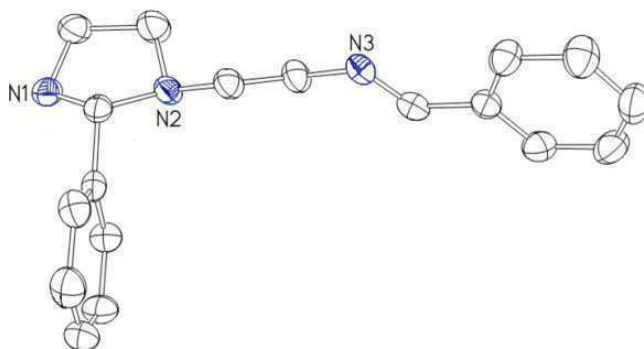


Figure 4-4: Thermal ellipsoid plot of the molecular structure of L^1 (50 % probability ellipsoids).

As expected, the reaction of L^1 with $[\text{Cu}(\text{CH}_3\text{CN})_4]\text{PF}_6$ yields the mononuclear complex $[\text{CuL}^1(\text{CH}_3\text{CN})]\text{PF}_6$ (**1**). The molecular structure of $[\text{Cu}(\text{L}^1)(\text{CH}_3\text{CN})]^+$ with the atomic numbering scheme is shown in Figure 4-5. The copper(I) center is coordinated in a distorted tetrahedral manner by two imine donors, an amine donor and an acetonitrile molecule with a $\text{Cu}(\text{N}-)$ -distance of $2.164(2) \text{ \AA}$, the $\text{Cu}(\text{N}=\text{C})$ -distances of $2.044(2)$ and $2.086(2)$ and the $\text{Cu}(\text{N}\equiv\text{C})$ -distances of $1.938(2)$. The coordination

sphere around the copper(I) center is similar to the one in $[\text{Cu}_2(\text{mac})(\text{CH}_3\text{CN})_2](\text{ClO}_4)_2$.^{163, 165} Therefore, **1** clearly resembles “one half” of $[\text{Cu}_2(\text{mac})(\text{CH}_3\text{CN})_2](\text{ClO}_4)_2$. However, the structure of **1** is less strained compared to its macrocyclic analogue. The N(2)-Cu(1)-N(3) angle is more than 15° and the N(1)-Cu(1)-N(100) angle more than 10° wider compared to $[\text{Cu}_2(\text{mac})(\text{CH}_3\text{CN})_2](\text{ClO}_4)_2$.

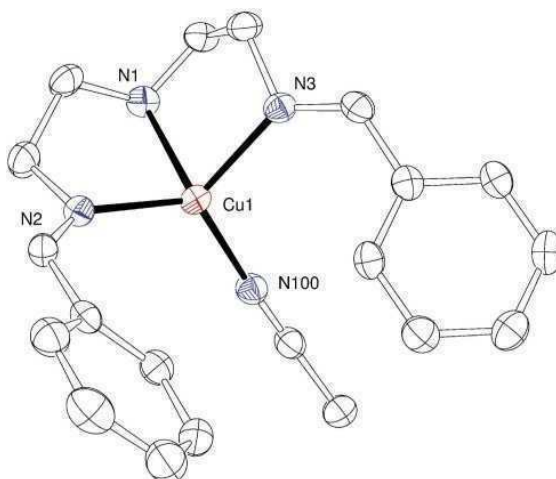


Figure 4-5: Molecular structure of the cation of $[\text{Cu}(\text{L}^1)(\text{CH}_3\text{CN})](\text{PF}_6)$ (**1**)

In contrast, and quite unexpectedly, we observed that if $[\text{Cu}(\text{CH}_3\text{CN})_4]\text{ClO}_4$ was used instead of $[\text{Cu}(\text{CH}_3\text{CN})_4]\text{PF}_6$ in the synthesis of the copper(I) complex, a helical dinuclear species, $[\text{Cu}_2\text{L}^1_2](\text{ClO}_4)_2$ (**2**), forms. The molecular structure of the cation of **2** with the atomic numbering scheme is presented in Figure 4-6.

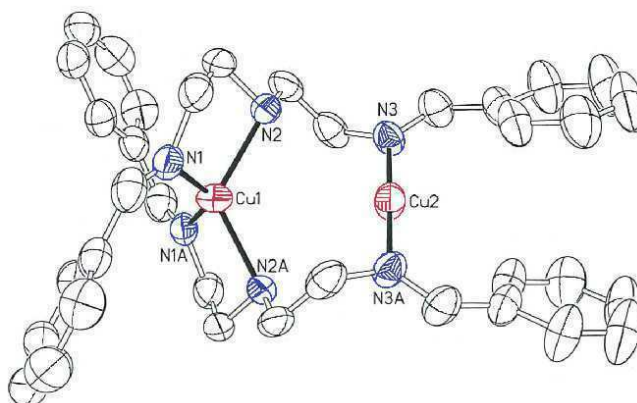


Figure 4-6: Thermal ellipsoid plot of the molecular structure of the cation of $[\text{Cu}_2(\text{L}^1)_2](\text{ClO}_4)_2$ (**2**) (40% probability ellipsoids, C bound hydrogen atoms omitted for clarity).

The helical complex exhibits a crystallographic C_2 -axis running through the two copper(I) centers. One copper(I) ion is coordinated in a distorted tetrahedral manner by two imine donors with a Cu-N-

distance of 2.030(3) Å and two amine donors with a Cu-N-distance of 2.134(2) Å. The second copper(I) center shows linear coordination by two imine donors with a Cu-N-distance of 1.886(2) Å, and weak interactions with two ClO_4^- counterions ($\text{Cu}(2) \cdots \text{O}(14) = 2.927(3)$ Å). The ClO_4^- counterions form hydrogen bonds to the N-H groups ($\text{N}(2)\text{-H}(2) \cdots \text{O}(14)$ with $\text{N}(2) - \text{H}(2) = 0.91$ Å, $\text{H}(2) \cdots \text{O}(14) = 2.26$ Å, $\text{N}(2) \cdots \text{O}(14) = 3.137(3)$ Å and $\text{N}(2) - \text{H}(2) \cdots \text{O}(14) = 161^\circ$). The separation of the two copper centers is 3.609(1) Å. Helical copper(I) complexes with Schiff base ligands are known^{155, 198-199} and even a system with a macrocyclic ligand similar to mac has been described.¹⁹⁹ However, most interesting is a comparison with a dicopper(I) helicate complex with a 2,6-bis(pyrazole-2-yl) pyridine derivative.²⁰⁰ This ligand while chemically totally different compared with L^1 shows some similarity if one overlaps their chemical formulas as shown in Figure 4-7.

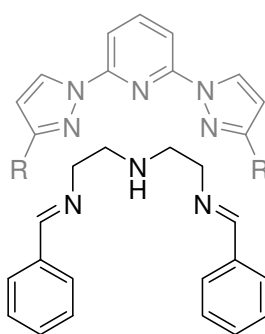


Figure 4-7: Comparison of L^1 with a 2,6-bis(pyrazole-2-yl)-pyridine derivative (R = H, Me, tBu).

That this comparison is not far fetched can be seen clearly in a comparison of **1** with the reported complex $[\{\text{Cu}(\mu\text{-L}^{\text{Mes}})\}_2]^{2+}$. In both complexes we have a similar structural unit with a four and two coordinated copper(I) ion.

4.2.2 Crystallographic Data.

Table 4-1: Crystal data and structure refinement for **L¹**, **1**, **2** and **3**.

Compound	L¹	[Cu(L¹)(CH₃CN)]PF₆ (1)	[Cu₂(L¹)₂](ClO₄)₂ (2)	[Cu(L¹)(PPh₃)](ClO₄) (3)
Empiric Formular	C ₁₈ H ₂₁ N ₃	C ₂₀ H ₂₄ N ₄ CuPF ₆	C ₃₆ H ₄₂ N ₆ Cu ₂ Cl ₂ O ₈	C _{37.5} H ₃₉ N ₃ CuCl _{1.33} PO _{4.33}
Molecular weight	279.38	528.94	884.74	742.83
Temperature [K]	210(2)	173(2)	295(2)	100(2)
Crystal System	monoclinic	triclinic	monoclinic	trigonal
	P2 ₁	P1	C2/c	R-3
a [Å]	8.947(1)	8.8145(2)	16.763(1)	35.126(1)
b [Å]	5.515(1)	11.2443(2)	15.213(1)	35.126(1)
c [Å]	16.088(2)	12.2806(2)	17.344(1)	15.4896(5)
α [°]	90	110.282(1)	90	90
β [°]	90.93(1)	91.682(1)	116.44(1)	90
γ [°]	90	95.242(1)	90	120
V [Å ³]	784.2(2)	1134.49(4)	3960.3(5)	16550.7(9)
Z	2	2	4	18
ρ _{calcd.} [mg·m ⁻³]	1.183	1.534	1.484	1.342
μ [mm ⁻¹]	0.071	1.548	1.266	0.778
Final R indices (all data)	R1 = 0.0629	R1 = 0.0337	R1 = 0.0462	R1 = 0.0553
	wR2 = 0.0892	wR2 = 0.0873	wR2 = 0.0796	wR2 = 0.1270
R indices [I > 2σ(I)]	R ₁ ^[a] = 0.0405	R ₁ ^[a] = 0.0468	R ₁ ^[a] = 0.1047	R ₁ ^[a] = 0.1070
	wR2 = 0.0805	wR2 = 0.0934	wR2 = 0.0956	wR2 = 0.1577

[a] $R_1(F_o) = \sum ||F_o| - |F_c|| / \sum |F_o|$; $wR_2(F_o^2) = (\sum [w(F_o^2 - F_c^2)^2] / \sum [w(F_o^2)^2])^{1/2}$

Table 4-2: Crystal data and structure refinement for **4**, **5** and **6**.

Compound	[Cu ₂ (L ¹) ₂ (OCH ₃) ₂](PF ₆) ₂ (4)	[Cu ₂ (L ¹) ₂ (OH) ₂](PF ₆) ₂ (5)	[Cu ₂ (L ²) ₂ Cl ₃](PF ₆) ₂ ·2MeOH (6)
Empiric Formular	C ₃₈ H ₄₈ N ₆ O ₂ Cu ₂ P ₂ F ₁₂	C ₄₂ H ₅₆ N ₆ O ₄ Cu ₂ P ₂ F ₁₂	C ₃₈ H ₅₀ Cl ₃ Cu ₂ F ₆ N ₆ O ₂ P
Molecular weight	1037.84	1125.95	1001.24
Temperature [K]	210(2)	100(2)	173(2)
Crystal System	monoclinic	triclinic	monoclinic
	<i>P</i> 2 ₁ / <i>n</i>	<i>P</i> -1	<i>C</i> 2/ <i>c</i>
<i>a</i> [Å]	9.074(1)	9.4575(4)	22.0450(4)
<i>b</i> [Å]	11.193(1)	10.6958(5)	7.3390(2)
<i>c</i> [Å]	21.017(3)	12.4593(7)	27.4254(5)
α [°]	90	101.657(4)	90
β [°]	92.75(1)	92.168(4)	102.720(2)
γ [°]	90	104.018(3)	90
<i>V</i> [Å ³]	2132.1(4)	1192.6(1)	4328.2(2)
<i>Z</i>	2	1	4
$\rho_{\text{calcd.}}$ [mg·m ⁻³]	2132.1(4)	1.568	1.537
μ [mm ⁻¹]	1.168	1.053	1.272
Final <i>R</i> indices (all data)	<i>R</i> 1 = 0.0615	<i>R</i> 1 = 0.0501;	<i>R</i> 1 = 0.0731
	<i>wR</i> 2 = 0.1201	<i>wR</i> 2 = 0.0834	<i>wR</i> 2 = 0.1333
<i>R</i> indices [<i>I</i> > 2 σ (<i>I</i>)]	<i>R</i> ₁ ^[a] = 0.1309	<i>R</i> ₁ ^[a] = 0.0933	<i>R</i> ₁ ^[a] = 0.0731
	<i>wR</i> 2 = 0.1478	<i>wR</i> 2 = 0.0954	<i>wR</i> 2 = 0.1465

$$[a] R_1(F_o) = \sum |F_o| - |F_c| / \sum |F_o|; wR_2(F_o^2) = (\sum [w(F_o^2 - F_c^2)^2] / \sum [w(F_o^2)^2])^{1/2}$$

Table 4-3: Selected bond lengths [Å] and angles [°] for the compounds **1-6**.

[Cu(L ¹)(CH ₃ CN)]PF ₆ (1)				[Cu ₂ (L ¹) ₂](ClO ₄) ₂ (2)			
Cu(1)-N(100)	1.938(2)	Cu(1)-N(1)	2.164(2)	Cu(1)-N(1)	2.030(3)	Cu(1)-N(1A) ^[a]	2.030(3)
Cu(1)-N(2)	2.044(2)	Cu(1)-N(3)	2.086(2)	Cu(1)-N(2)	2.132(2)	Cu(1)-N(2A) ^[a]	2.134(2)
N(100)-Cu(1)-N(2)	122.93(6)	N(100)-Cu(1)-N(2)	122.93(6)	Cu(2)-N(3)	1.886(2)	Cu(2)-N(3A) ^[a]	1.886(2)
N(100)-Cu(1)-N(3)	110.65(6)	N(100)-Cu(1)-N(3)	110.65(6)	N(1)-Cu(1)-N(1A) ^[a]	134.5(2)	N(1)-Cu(1)-N(1A) ^[a]	134.5(2)
N(2)-Cu(1)-N(3)	121.17(6)	N(2)-Cu(1)-N(3)	121.17(6)	N(1)-Cu(1)-N(2)	84.5(1)	N(1)-Cu(1)-N(2)	84.5(1)
N(100)-Cu(1)-N(1)	125.08(7)	N(100)-Cu(1)-N(1)	125.08(7)	N(1A)-Cu(1)-N(2)	117.8(1)	N(1A)-Cu(1)-N(2)	117.8(1)
N(2)-Cu(1)-N(1)	84.72(6)	N(2)-Cu(1)-N(1)	84.72(6)	N(1)-Cu(1)-N(2A) ^[a]	117.8(1)	N(1)-Cu(1)-N(2A) ^[a]	117.8(1)
N(3)-Cu(1)-N(1)	83.51(6)	N(3)-Cu(1)-N(1)	83.51(6)	N(1A) ^[a] -Cu(1)-N(2A) ^[a]	84.5(1)	N(1A) ^[a] -Cu(1)-N(2A) ^[a]	84.5(1)
C(100)-N(100)-Cu(1)	163.2(2)	C(100)-N(100)-Cu(1)	163.2(2)	N(2)-Cu(1)-N(2A) ^[a]	122.9(2)	N(2)-Cu(1)-N(2A) ^[a]	122.9(2)
				N(3A) ^[a] -Cu(2)-N(3)	179.2(2)	N(3A) ^[a] -Cu(2)-N(3)	179.2(2)

[Cu(L ¹)(PPh ₃)](ClO ₄) (3)				[Cu ₂ (L ¹) ₂ (OCH ₃) ₂](PF ₆) ₂ (4)			
Cu(1)-N(1)	2.112(3)	Cu(1)-N(2)	2.161(3)	Cu(1)-N(1)	2.019(5)	Cu(1)-O(1)	1.936(4)
Cu(1)-N(3)	2.092(3)	Cu(1)-P(1)	2.205(1)	Cu(1)-N(2)	2.073(4)	Cu(1)-O(1A) ^[b]	1.940(4)
N(3)-Cu(1)-N(1)	109.6(2)	N(3)-Cu(1)-N(1)	109.6(2)	Cu(1)-N(3)	2.365(5)	Cu(1)-Cu(1A) ^[b]	3.013(2)
N(3)-Cu(1)-N(2)	82.8(2)	N(3)-Cu(1)-N(2)	82.8(2)	O(1)-Cu(1)-O(1A) ^[b]	78.0(2)	O(1)-Cu(1)-O(1A) ^[a]	78.0(2)
N(1)-Cu(1)-N(2)	83.8(2)	N(1)-Cu(1)-N(2)	83.8(2)	O(1)-Cu(1)-N(1)	99.3(2)	O(1)-Cu(1)-N(1)	99.3(2)
N(3)-Cu(1)-P(1)	114.12(8)	N(3)-Cu(1)-P(1)	114.12(8)	O(1A) ^[b] -Cu(1)-N(1)	164.8(2)	O(1A) ^[b] -Cu(1)-N(1)	164.8(2)
N(1)-Cu(1)-P(1)	132.06(8)	N(1)-Cu(1)-P(1)	132.06(8)	O(1)-Cu(1)-N(2)	158.7(2)	O(1)-Cu(1)-N(2)	158.7(2)
N(2)-Cu(1)-P(1)	119.64(9)	N(2)-Cu(1)-P(1)	119.64(9)	O(1A) ^[b] -Cu(1)-N(2)	95.1(2)	O(1A) ^[b] -Cu(1)-N(2)	95.1(2)
N(3)-Cu(1)-N(1)	109.6(2)	N(3)-Cu(1)-N(1)	109.6(2)	N(1)-Cu(1)-N(2)	82.0(2)	N(1)-Cu(1)-N(2)	82.0(2)
				O(1)-Cu(1)-N(3)	120.0(2)	O(1)-Cu(1)-N(3)	120.0(2)
[Cu ₂ (L ¹) ₂ (OH) ₂](PF ₆) ₂ (5)				[Cu ₂ (L ²) ₂ Cl ₃](PF ₆ ·2MeOH) (6)			
Cu(1)-N(1)	2.320(3)	Cu(1)-O(1)	1.928(3)	Cu(1)-N(2)	2.021(3)	N(2)-Cu(1)-Cl(2)	166.85(8)
Cu(1)-N(2)	2.038(3)	Cu(1)-O(1A) ^[c]	1.957(3)	Cu(1)-N(3)	2.052(3)	N(3)-Cu(1)-Cl(2)	93.47(8)
Cu(1)-N(3)	2.020(3)	Cu(1)-Cu(1A) ^[c]	2.9846(9)	Cu(1)-N(1)	2.060(3)	N(1)-Cu(1)-Cl(2)	95.26(8)
O(1)-Cu(1)-O(1A) ^[c]	79.6(2)	O(1)-Cu(1)-O(1A) ^[a]	79.6(2)	Cu(1)-Cl(2)	2.2700(9)	N(2)-Cu(1)-Cl(1)	88.59(8)
O(1)-Cu(1)-N(3)	99.2(2)	O(1)-Cu(1)-N(3)	99.2(2)	Cu(1)-Cl(1)	2.5874(8)	N(3)-Cu(1)-Cl(1)	98.19(8)
O(1A) ^[c] -Cu(1)-N(3)	162.5(2)	O(1A) ^[c] -Cu(1)-N(3)	162.5(2)	N(2)-Cu(1)-N(3)	83.2(1)	N(1)-Cu(1)-Cl(1)	95.58(7)
O(1)-Cu(1)-N(2)	159.7(2)	O(1)-Cu(1)-N(2)	159.7(2)	N(2)-Cu(1)-N(1)	84.6(1)	Cl(2)-Cu(1)-Cl(1)	104.49(3)
O(1A) ^[c] -Cu(1)-N(2)	92.3(2)	O(1A) ^[c] -Cu(1)-N(2)	92.3(2)	N(3)-Cu(1)-N(1)	161.3(1)		
N(3)-Cu(1)-N(2)	82.9(2)	N(3)-Cu(1)-N(2)	82.9(2)	Cu(1) ^[d] -Cl(1)-Cu(1)	110.62(5)		
O(1)-Cu(1)-N(1)	116.7(2)	O(1)-Cu(1)-N(1)	116.7(2)				

^[a] Symmetry code: -x+2, y, -z+1.5; ^[b] Symmetry code: -x+1, -y, -z+1; ^[c] Symmetry code: -x+1, -y+1, -z+1; ^[d] -x+1, y, -z+1/2

4.2.3 Discussion of the structure dependence on the counterion.

The fact that the nature of the counterion has an important impact on the molecular structure is often observed in crystal engineered coordination polymers, where the anion is part of the polymeric array.²⁰¹⁻²⁰³ Furthermore, counterions can have a strong influence on supramolecular structures. For example, Lehn showed that in some circular double helices (where the counterion occupies the center of the arrangement) the nature of the anion is responsible for the formation of either a cubic, or a

pentagonal or a hexagonal architecture, respectively.²⁰⁴ Non-covalent interactions between cation and counterion might be crucial for the formation of various structure types. Silver-terpyridyl and silver-pyridyl-thioether complexes form different aggregates, with the structure depending on the counterions and the solvents used.²⁰⁵ It is suggested that weak interactions such as hydrogen bonding and X...H-C contacts play an important role in complex formation. Interestingly and most recently zwitterionic dicopper helicates with a salicylaldiminato unit as ligand were used for anion encapsulation studies.¹⁵⁵

Effects of counterions on the solid state structure of metal complexes, e. g. on a platinum(II) thio-urea complex²⁰⁶ have been observed previously, however, from our knowledge, **1** and **2** are the first “simple” complexes where the nature of the non- or weakly coordinating counterions determines the complex structure in such a way. In general, non-covalent intramolecular and intermolecular interactions stabilize different species and are probably crucial for the formation of different complex structures. In **1**, one F...H-C-interaction $< 2.55 \text{ \AA}$ and one weak intermolecular hydrogen bond with $F(6)\cdots H(1_2) = 2.442 \text{ \AA}$ were observed per PF_6^- counterion. The helical complex **2** is stabilized by one hydrogen bond per ClO_4^- counterion to the N-H group with a hydrogen acceptor distance of 2.26 \AA . Furthermore, two O...H-C interactions $< 2.60 \text{ \AA}$ are apparent per ClO_4^- anion. The aromatic rings with C(6)-C(11) and C(6A)-C(11A) are not coplanar to each other, and with the closest distance of 3.774 \AA between C(6) and C(11_2) of the next neighbor molecule not suitable for providing effective π - π interactions. Compounds **1** and **2** exhibit no striking differences concerning weak interactions with exception of the stronger hydrogen bond in **2**. Therefore, crystallization and crystal packing effects might play a crucial role in structure formation. Figures of crystal packing are presented in Figure 4-8.

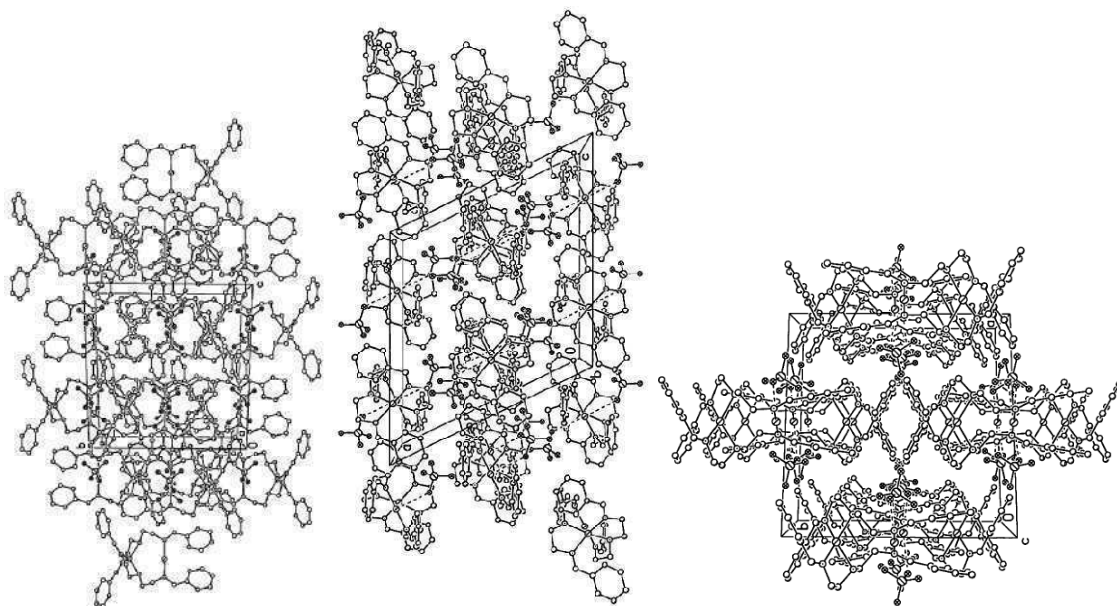


Figure 4-8: Packing diagram of complex **2**, view along the crystallographic a-axis (left), b-axis (middle) and c-axis (right) (hydrogen atoms omitted for clarity).

4.2.4 Further variation of the counterions.

To further investigate the influence of the counterion on the structure of the corresponding complexes, the copper(I) compounds with the counterions BF_4^- and SbF_6^- were synthesized in a similar way to **1**. Unfortunately, single crystals suitable for X-ray analyses could not be obtained. However, mononuclear and dinuclear coordination types can be differentiated by spectroscopic methods apart from X-Ray analyses. For example, the band for N-H vibration of **1** appears at 3350 cm^{-1} in the IR(KBr) spectrum, while in **2** the wavenumber decreases to 3259 cm^{-1} probably due to N-H \cdots O hydrogen bonds between the N-H groups and ClO_4^- . Moreover, the presence or absence of MeCN signals in ^1H and ^{13}C NMR spectra establishes the formation of both, the mononuclear and the dinuclear species.

For copper(I) complexes with the BF_4^- counterion, a band for N-H vibration appears similar to **2** at 3268 cm^{-1} in the IR(KBr) spectrum, while in the ^1H and ^{13}C NMR spectra (measured in DMSO-d_6) no signals for CH_3CN could be found. These results indicate that $[\text{Cu}_2\text{L}^1_2](\text{BF}_4)_2$ was obtained during the reaction. For the copper(I) complex with the SbF_6^- counterion, however, the IR(KBr) spectrum exhibited two bands for N-H vibrations at 3286 and 3342 cm^{-1} , indicating the presence of both $[\text{Cu}_2\text{L}^1_2](\text{SbF}_6)_2$ and $[\text{CuL}^1(\text{CH}_3\text{CN})]\text{SbF}_6$ in the solid state. Integration of the MeCN signal in the ^1H NMR

spectrum (measured in DMSO- d_6) gave evidence that a mixture of $[\text{Cu}_2\text{L}^1_2](\text{SbF}_6)_2$ and $[\text{CuL}^1(\text{CH}_3\text{CN})]\text{SbF}_6$ in a 4.6 to 1 ratio was formed.

Thus, tetrahedral counterions such as ClO_4^- or BF_4^- prefer the formation of dinuclear species. Octahedral PF_6^- forms the mononuclear compound, and with SbF_6^- a mixture of mononuclear and dinuclear species is obtained. The dependence of the molecular structure on the counterion might be the result of packing effects in the solid state.

4.2.5 Investigation of the solution behavior of **1** and **2**.

In order to investigate the solution behavior of **1** and **2**, various experiments were carried out. To study potential equilibria between **1** and **2**, low temperature NMR techniques were applied. Temperature dependent ^1H NMR spectra of **1** and **2** in CD_3CN and $\text{DMF-}d_7$ were recorded down to -40°C and -55°C , respectively. The NMR spectra for both compounds were similar and differed only in the presence of the CH_3CN peak for **1**. Figure 4-9 shows the ^1H NMR spectra of **1** in CD_3CN at -40 , -20 , -10 und $+25^\circ\text{C}$. From the NMR patterns it is clear that for **1** and **2** only the mononuclear species is present in solution. Therefore, **2** decomposes into the mononuclear component in coordinating solvents.

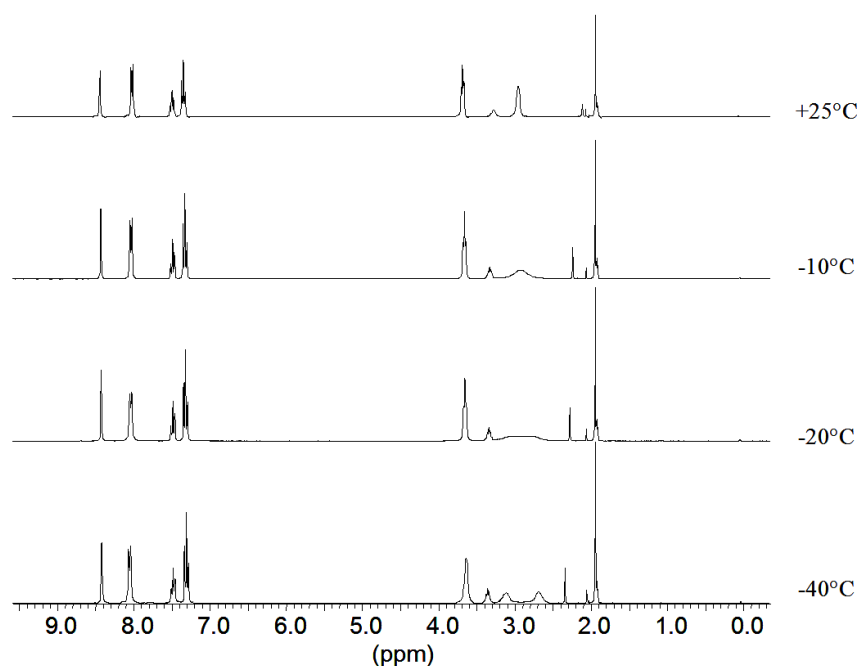


Figure 4-9: ^1H NMR spectra of $[\text{Cu}(\text{L}^1)(\text{CH}_3\text{CN})]\text{PF}_6$ in CD_3CN at -40 , -20 , -10 and $+25^\circ\text{C}$.

^1H NMR spectra did not give any indication about equilibria between dinuclear and mononuclear species, as no significant line broadening could be observed. Only the signal for the N-CH_2 -protons splitted at about $-20\text{ }^\circ\text{C}$ into two broad signals at 2.69 and 3.11 ppm which show coalescence at about $-10\text{ }^\circ\text{C}$. The signal splitting derives from the diastereotopy of the hydrogen atoms in the N-CH_2 groups, resulting in different chemical shifts. By raising the temperature, dissociation and subsequent association of the amine protons makes the diastereotopic hydrogen atoms chemically equivalent.

Low temperature ^1H NMR spectroscopy of **1** and **2** in CD_3OD down to $-80\text{ }^\circ\text{C}$ gave different spectra for both complexes. For **1**, NMR spectra were very similar to those obtained in coordinating solvents. For **2**, however, ^1H -NMR spectra showed line broadening from $-20\text{ }^\circ\text{C}$ on. Due to the limited solubility of **2** in weakly coordinating solvents, no deeper insight could be gained.

UV-Vis spectroscopy of **1** and **2** in CH_3CN also reveals that **2** forms a mononuclear species in coordinating solvents, as **2** yields an identical UV-Vis spectrum with ϵ values about twice as high as for the mononuclear compound **1**. Further evidence for the decomposition of the dinuclear species by coordinating agents is given by formation of $[\text{Cu}(\text{L}^1)(\text{PPh}_3)]\text{ClO}_4$ (**3**) from the reaction of **2** with PPh_3 . The molecular structure of $[\text{Cu}(\text{L}^1)(\text{PPh}_3)]^+$ is shown in Figure 4-10. The copper(I) center is coordinated in a distorted tetrahedral manner by two imine donors, an amine donor and the phosphine ligand. The Cu-(N)-distance of $2.161(3)\text{ \AA}$ is practically identical to that in **1** with $2.164(2)\text{ \AA}$, while the Cu-(N=) -distances of $2.092(3)$ and $2.112(3)\text{ \AA}$ are longer compared to $2.044(2)$ and $2.086(2)\text{ \AA}$ in **1**, which is probably due to the steric strain caused by the phosphine ligand. The Cu-P-distance of $2.205(1)$ falls within the usually observed range. The steric demand of the phosphine ligand is also apparent in the shortage of bond angles (N(1)-Cu(1)-N(2) : $83.8(2)^\circ$; N(3)-Cu(1)-N(1) : $109.6(2)^\circ$; N(3)-Cu(1)-N(2) : $82.8(2)^\circ$).

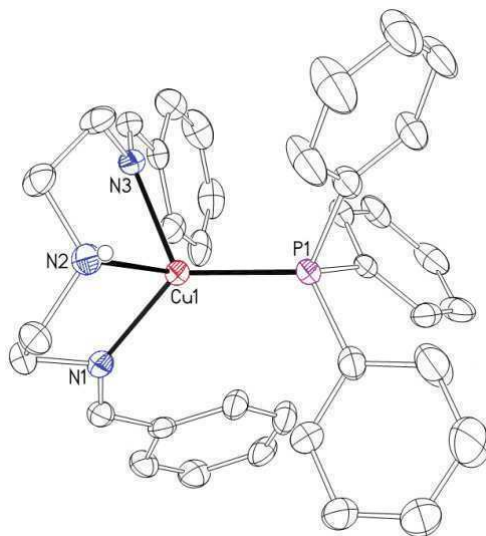


Figure 4-10: Thermal ellipsoid plot of the molecular structure of the cation of **3**, $[\text{Cu}(\text{L}^1)(\text{PPh}_3)]^+$ (50 % probability ellipsoids, C bound H atoms omitted for clarity).

From these experiments we conclude that in coordinating solvents **1** and **2** form similar mononuclear copper(I) complexes. Related observations that a helical complex with a terpy derivative as a ligand shows different coordination behavior in solution compared with the solid state were reported previously by Potts et al.²⁰⁷

4.2.6 Electrochemistry.

Cyclic voltammetry of **1** and **2** was performed with a scan rate of 100 mV/s in CH_3CN . Both compounds exhibited the same electrochemical behavior. CV spectra showed irreversible electrochemical behavior for the Cu(I)/Cu(II) redox couple with $E_{1/2} = +0.12 \text{ V}$ ($E_{\text{pa}} = +0.19 \text{ V}$, $E_{\text{pc}} = +0.04 \text{ V}$, $j_{\text{pa/pc}} = 0.46$). An additional irreversible reduction peak with $E_{\text{pc}} = -0.16 \text{ V}$ was observed. This peak could be assigned to the reduction of a decomposition product of the copper(II) species. In contrast, $[\text{Cu}_2(\text{mac})(\text{CH}_3\text{CN})_2](\text{ClO}_4)_2$ only exhibited one irreversible oxidation peak with $E_{\text{pa}} = 0.12 \text{ V}$. E_{pa} in $[\text{Cu}_2(\text{mac})(\text{CH}_3\text{CN})_2](\text{ClO}_4)_2$ is shifted by 70 mV to more negative potentials compared to **1**, although both complexes exhibit a very similar coordination sphere. The E_{pa} shift could be explained by differences in the wider chemical environment of the copper(I) centers in both complexes.

4.2.7 Copper(II) complexes.

In order to compare the oxidation behavior of **1** and $[\text{Cu}_2(\text{mac})(\text{CH}_3\text{CN})_2](\text{ClO}_4)_2$, **1** was reacted with dioxygen in different solvents. Oxidation of **1** in CH_3OH yielded the bis-methoxido bridged species $[\text{Cu}_2(\text{L}^1)_2(\text{OCH}_3)_2](\text{PF}_6)_2$ (**4**), while in CH_2Cl_2 $[\text{Cu}_2(\text{L}^1)_2(\text{OH})_2](\text{PF}_6)_2$ (**5**) was formed. The molecular structure of $[\text{Cu}_2(\text{L}^1)_2(\text{OCH}_3)_2]^{2+}$ with the atomic numbering scheme is shown in Figure 4-11.

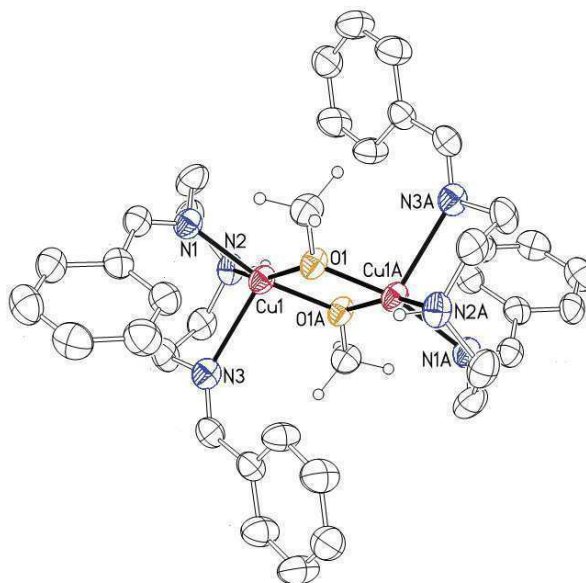


Figure 4-11: Thermal ellipsoid plot of the molecular structure of the cation of **4**, $[\text{Cu}_2(\text{L}^1)_2(\text{OCH}_3)_2]^{2+}$ (50 % probability ellipsoids, C bound H atoms of the ligand omitted for clarity).

In dinuclear for each copper(II) ion is coordinated in a distorted square pyramidal manner with $\tau = 0.108$ ($\tau = 0$ for a square pyramidal, $\tau = 1$ for a trigonal bipyramidal complex).¹⁰⁸ The copper centers are related to one another by a center of inversion. The base of the pyramid is formed by N(1), N(2), O(1) and O(1A), while N(3) forms the top of the pyramid. Compared to **1**, the Cu(1)-N(1) and the Cu(1)-N(2) distances are shorter with 2.019(5) (2.044(2) in **1**) and 2.073(4) (2.164(2) in **1**) Å, while the Cu(1)-N(3) distance is significantly enlarged with 2.365(5) Å (2.086(2) in **1**). Cu(1)-O(1) and Cu(1)-O(1A) distances are relatively short with 1.936(4) and 1.940(4) Å, respectively. The Cu(1)-Cu(1A) distance of 3.013(2) Å shows no peculiarity compared to related complexes. The PF_6^- counterions are involved in hydrogen bonding with the N-H groups (N(2)-H(2)⋯F(14^{#1})) with N(2) – H(2) = 0.92 Å, H(2)⋯F(14^{#1}) = 2.28 Å, N(2) – H(2)⋯F(14^{#1}) = 3.199(7) Å and N(2) – H(2)⋯F(14^{#1}) = 176°.

^{#1} $-x+1, -y, -z+1$). The molecular structure is related to the analogous bis-methoxido bridged species obtained during the oxidation of $[\text{Cu}_2(\text{mac})(\text{CH}_3\text{CN})_2](\text{ClO}_4)_2$ in a mixture of solvents containing acetonitrile.¹⁶³ Here Rieger and co-workers had demonstrated that $[\text{Cu}_2(\text{mac})(\text{CH}_3\text{CN})_2](\text{ClO}_4)_2$ not always undergoes intramolecular ligand hydroxylation and thus they obtained the first bis-methoxido bridged copper(II) complex as oxidation product.

The molecular structure of $[\text{Cu}_2(\text{L}^1)_2(\text{OH})_2]^{2+}$ with the atomic numbering scheme can be seen in Figure 4-12. In the dinuclear complex each copper(II) ion is coordinated in a square pyramidal geometry with $\tau = 0.046$.

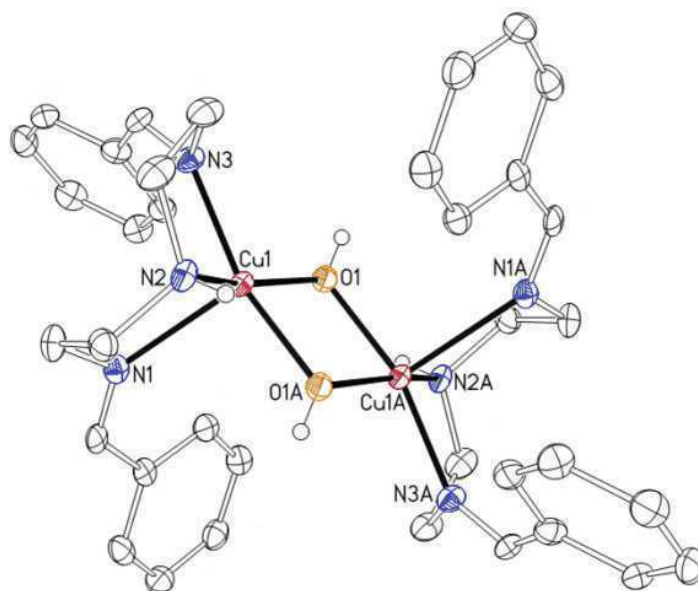


Figure 4-12: Thermal ellipsoid plot of the molecular structure of the cation of **5**, $[\text{Cu}_2(\text{L}^1)_2(\text{OH})_2]^{2+}$, (50 % probability ellipsoids, C bound H atoms omitted for clarity).

The copper(II) centers are related to each other by a center of inversion on the Cu(1)-Cu(1A) axis. Both pyramids share the O(1)-O(1A) edge analogous to **4**. The base of the pyramid is formed by N(2), N(3), O(1) and O(1A), while N(1) forms the top of the pyramid. Compared to **4**, Cu(1)-N(1), Cu(1)-O(1) and Cu(1)-N(2) distances are slightly shorter with 2.320(3), 1.928(3) and 2.038(3) Å. The Cu(1)-N(3) distance is similar with 2.020(3) Å, and the Cu(1)-O(1A) distance is slightly enlarged with 1.957(2) Å. Similar to **4**, the formation of hydrogen bonds between the N-H group of the ligand and the PF_6^- anion is observed (N(2)-H(2)⋯F(12) with N(2) – H(2) = 0.93 Å, H(2)⋯F(12) = 2.18 Å,

$N(2) \cdots F(12) = 3.058(4) \text{ \AA}$ and $N(2) - H(2) \cdots F(12) = 158^\circ$ and with the alternative position of the distorted PF_6^- anion $N(2) - H(2) \cdots F(15A)$ with $N(2) - H(2) = 0.93 \text{ \AA}$, $H(2) \cdots F(15A) = 2.60 \text{ \AA}$, $N(2) \cdots F(15) = 3.23(2) \text{ \AA}$ and $N(2) - H(2) \cdots F(15A) = 126^\circ$.

4.2.8 Investigation of the oxidation reaction.

Due to the molecular structures of the copper(II) compounds, no hydroxylation of the ligand was observed during the oxidation of **1** in MeOH and CH_2Cl_2 . But as yields for **4** and **5** were quite low with 73% and 58%, a further experiment was performed to investigate potential ligand hydroxylation. **1** was reacted with dioxygen in CH_2Cl_2 , and the copper(II) ions were removed with NH_3 . However, the organic residue, consisted of L^1 and its decomposition product benzaldehyde. No hydroxylation of L^1 was observed in any reaction.

In order to detect "dioxygen adduct" of these complexes such as peroxido or superoxido species during the oxidation of **1** in CH_2Cl_2 , the reaction was investigated by low temperature stopped-flow investigations. This technique has been quite useful in the past to observe such reactive intermediates.^{51-52, 92-93, 115, 188} In up to 41 s total time, time resolved spectra did not show any changes in absorption at temperatures between $-88^\circ C$ and $-3^\circ C$. The oxidation reaction proceeded very slowly, and no spectroscopic detection of any reactive "dioxygen complex" adduct was possible.

In order to draw conclusions about the intermediates formed during the oxidation reaction, a chemical approach was chosen. Nucleophilic peroxido compounds can be protonated by acids at the peroxido moiety to give H_2O_2 . In reverse, the detection of H_2O_2 should indicate previous formation of a peroxido species. If **1** is oxidized in CH_2Cl_2 at $-40^\circ C$ and quenched with HPF_6 , an average amount of 7.8% H_2O_2 was found by iodometric titration. Formation of H_2O_2 could also be verified by using H_2O_2 test strips. The amounts of H_2O_2 found in the reaction mixture varied strongly due to the fact that the time of quenching the peroxido compound with acid was chosen arbitrarily.

During investigations of the oxidation reaction we found that the absorption spectrum of a freshly oxidized solution of **1** in CH_2Cl_2 clearly differs from the spectrum of $[\text{Cu}_2(\text{L}^1)_2(\text{OH})_2](\text{PF}_6)_2$. Therefore, a compound other than **5** was the first "stable" product formed in the oxidation reaction. IR spectra of the oxidized solution did not show any bands belonging to an OH vibration, and in the FD-mass spectrum a peak at $m/e = 357$ for the $[\text{Cu}(\text{L}^1)\text{O}]^+$ fragment was observed. Thus, we assume that the oxido compound $[\text{Cu}_2(\text{L}^1)_2\text{O}]^{2+}$ was formed. Further evidence was given by monitoring the reaction of a freshly oxidized solution of **1** in CH_2Cl_2 with one equivalent of H_2O by UV-Vis spectroscopy. Absorption spectra clearly indicated the formation of **5** (shoulder, $\lambda_{\text{max}} = 582 \text{ nm}$ (473)) from $[\text{Cu}_2(\text{L}^1)_2\text{O}]^{2+}$ ($\lambda_{\text{max}} = 594 \text{ nm}$ (185)) as shown in Figure 4-13. Copper-oxido complexes have been recently described to be most likely an active species in the selective oxidation of methane to methanol catalyzed by methane monooxygenase.²⁰⁸⁻²¹⁰

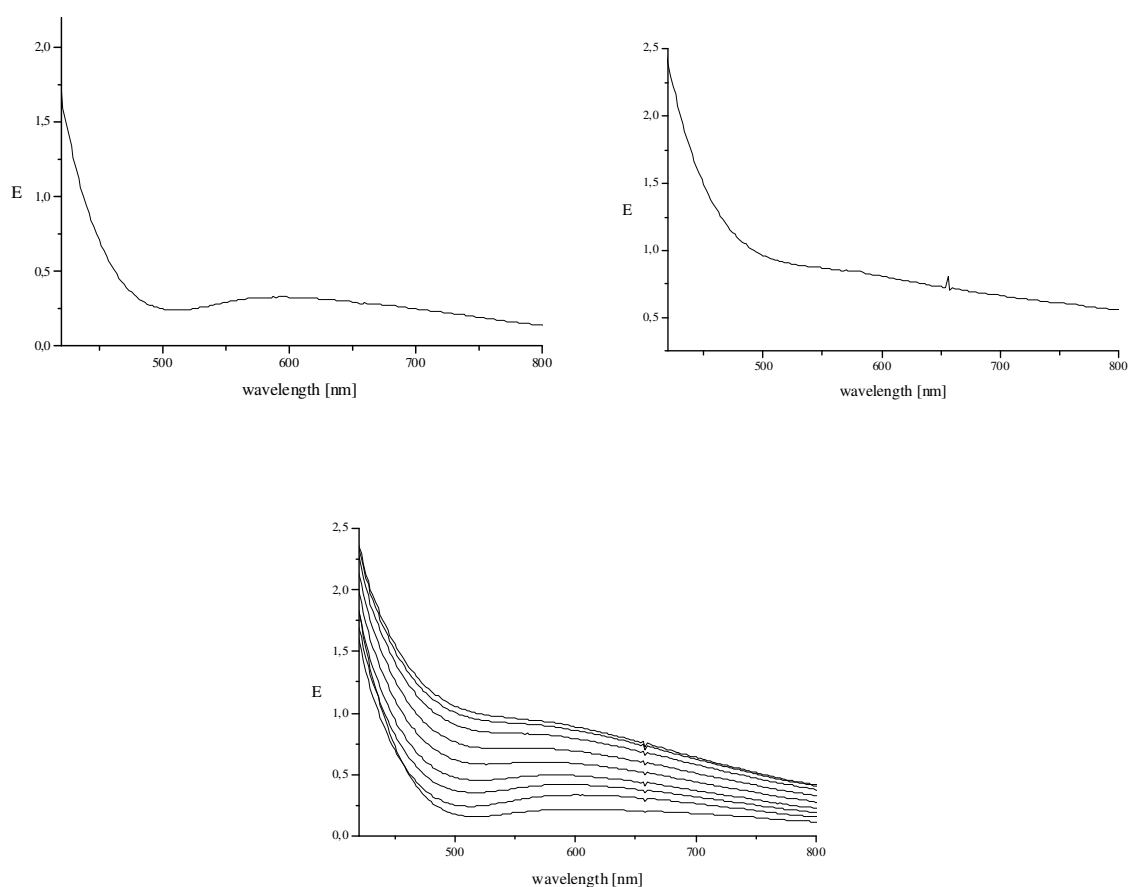


Figure 4-13: Top left: UV-Vis spectrum of an oxidized solution of **1** in CH_2Cl_2 ; top right: UV-Vis spectrum of **5** in CH_2Cl_2 ; bottom: Time resolved UV-Vis spectra of an oxidized solution of **1** in CH_2Cl_2 , quenched with one equivalent water.

1 reacts slowly with dioxygen, probably forming a peroxido species and the oxido compound $[\text{Cu}_2(\text{L}^1)_2\text{O}]^{2+}$ prior to the bis-hydroxido bridged complex **5**. In contrast, macrocyclic $[\text{Cu}_2(\text{mac})(\text{CH}_3\text{CN})_2](\text{ClO}_4)_2$ reacts much faster with dioxygen to give a peroxido intermediate. The peroxido intermediate decays under hydroxylation of the ligand.^{162, 165} The higher reactivity of $[\text{Cu}_2(\text{mac})(\text{CH}_3\text{CN})_2](\text{ClO}_4)_2$ towards dioxygen might be attributed to the more negative redox potential, as well as its highly preorganized structure. Dioxygen might fit very well between the two copper(I) centers, and because of the proximity to the aromatic spacer, hydroxylation of the ligand is possible. In **1** there is no preorganization present, and the aromatic moieties of the ligand are much more flexible. These differences might be responsible for the very different oxidation behavior. These findings are not completely unexpected because similar observations were made previously for an important model compound, $[\text{Cu}_2(\text{XYL-H})]^{2+}$. This dinuclear copper(I) complex shows hydroxylation of the aromatic spacer group upon reaction with dioxygen.^{115, 184, 187-188, 191} Kinetic studies of the oxidation process revealed that the reaction probably proceeds through a peroxido intermediate.^{115, 188} In contrast here as well the mononuclear copper(I) compound containing "half" of the XYL-H ligand did not show any hydroxylation of the ligand upon oxidation.^{187, 211} However, other mononuclear copper(I) complexes exhibit aromatic as well as aliphatic ligand hydroxylation when reacted with dioxygen.²¹²⁻²¹⁴

4.2.9 Copper complexes with the ligand L^2 .

From our previous work we know that it can be difficult to observe copper "dioxygen adduct" complexes as reactive intermediates if Schiff bases are used as ligands.^{93, 163, 165, 215} Therefore we also synthesized the ligand L^2 , the amine derivative of the imine ligand L^1 . The ligand L^2 has been described previously as a hydrochloride salt.²¹⁶ We used LiAlH_4 instead of NaBH_4 for the reduction of L^1 to L^2 , to avoid a workup with acids.

It is quite difficult - mainly due to disproportionation reactions – for many copper(I) amine complexes, to isolate these compounds as solids and/or to structurally characterize them. Therefore, we

were not surprised that similar to our recent work on related ligands to L^2 ,^{54, 217} only dilute solutions of copper(I) L^2 complexes could be prepared in situ by mixing the amine with $[Cu(CH_3CN)_4]PF_6$ in different solvents.

1H -NMR spectroscopy in $DMSO-d_6$ supports the presumption of the presence of a highly symmetrical copper(I) complex in solution. For the methyl protons of CH_3CN (present due to the $[Cu(CH_3CN)_4]PF_6$ added) only a singlet at 2.07 ppm is observed. This could be either caused by a fast exchange between coordinated and "free" acetonitrile or it could mean that CH_3CN is not coordinated at all. Unfortunately, it is not possible from these measurements to distinguish between these two possibilities, because the downfield shift of the signal for the methyl protons compared to "free" CH_3CN is too small to be significant. However, we assume from previous studies that acetonitrile is coordinated in solution and the complex should be formulated as $[Cu(L^2)(CH_3CN)]PF_6$. The coordination of L^2 to the copper ion mainly affects the chemical shift of the NH protons. These appear with a downfield shift of about 1.5 ppm at 3.49 ppm compared to L^2 . The CH_2 groups of the ethyl bridges show a singlet at 2.64 ppm, the benzyl groups show a singlet at 3.73 ppm. The aromatic protons show a multiplet at 7.27-7.37 ppm. ^{13}C -NMR spectroscopy exhibits only one signal for CH_3CN , at 0.00 and 116.92 respectively, which is shifted only about 0.5 ppm upfield compared with "free" CH_3CN . Again, this shift is not significant enough to prove or to exclude a coordination of CH_3CN . The additional signals at 45.88 and 47.70 ppm for the CH_2 groups of the ethyl bridges, 53.20 for the benzylic CH_2 groups and at 126.09, 127.20, 127.51 and 138.06 for the aromatic C atoms support the C_5 symmetry of the complex. Furthermore, coordination of L^2 to the copper(I) ion is characterized with the observation of a peak at $m/z = 346$ (100 %) for the fragment $[Cu(L^2)]^+$ by FD-MS measurements in CH_3CN . An additional peak at $m/z = 284$ (20%) for L^2 can be seen. UV-Vis spectroscopy of an in situ synthesized complex measured in CH_3CN solution revealed two bands at 214 nm ($\lambda = 17.301 M^{-1}cm^{-1}$) and 242 nm (shoulder, $\lambda = 6.863 M^{-1}cm^{-1}$). These bands can be assigned to intra-ligand transitions.

4.2.10 Electrochemistry of $[\text{Cu}(\text{L}^2)(\text{CH}_3\text{CN})]\text{PF}_6$.

Furthermore, we performed electrochemical measurements with equimolar solutions of $[\text{Cu}(\text{CH}_3\text{CN})_4]\text{PF}_6$ and L^2 (1:1) in CH_3CN . In Figure 4-14 the cyclic voltammogram of this solution with $v = 50, 100$ and 200 mV/s is presented. The $\text{Cu(I)}/\text{Cu(II)}$ redox behavior of this complex is quasi-reversible with $E_{1/2} = +0.02 \text{ V}$ for $v = 100 \text{ mV/s}$ ($E_{\text{pa}} = +0.10 \text{ V}$, $E_{\text{pc}} = -0.07 \text{ V}$) and $j_{\text{pa/pc}} = 1.04$. Compared with $[\text{Cu}(\text{L}^1)(\text{CH}_3\text{CN})]\text{PF}_6$ described above the redox potential has shifted to an about 0.5 V more negative value. Thus, $[\text{Cu}(\text{L}^2)(\text{CH}_3\text{CN})]\text{PF}_6$ is thermodynamically less stable and can be oxidized more easily.

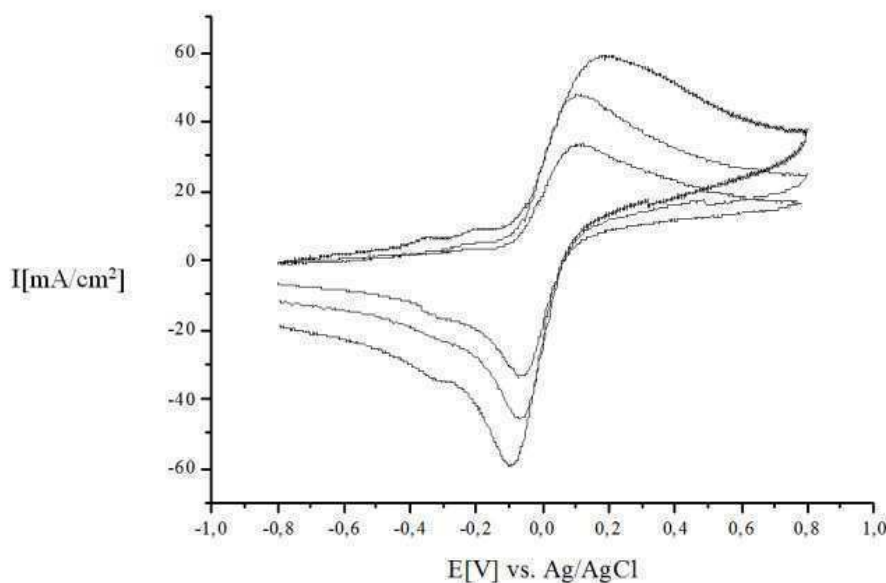


Figure 4-14: Cyclic Voltammetry of a 1:1 mixture of $[\text{Cu}(\text{CH}_3\text{CN})_4]\text{PF}_6$ and L^2 in CH_3CN ($v = 50, 100, 200 \text{ mV/s}$).

Previously, correlations have been made for some copper(I)-compounds in regard to the basicity of the ligands and the resulting redox potentials of the complexes.⁹² An increase in ligand basicity caused by a shift of the redox potentials towards more negative values was observed. Assuming that $[\text{Cu}(\text{L}^2)(\text{CH}_3\text{CN})]\text{PF}_6$ has the same coordination geometry as $[\text{Cu}(\text{L}^1)(\text{CH}_3\text{CN})]\text{PF}_6$, we can explain the shift of the redox potential towards more negative values with the higher basicity of L^2 .

4.2.11 Investigation of the oxidation reaction of $[\text{Cu}(\text{L}^2)(\text{CH}_3\text{CN})]\text{PF}_6$.

The reaction of the in situ synthesized $[\text{Cu}(\text{L}^2)(\text{CH}_3\text{CN})]\text{PF}_6$ with dioxygen was investigated in CH_2Cl_2 at $-88\text{ }^\circ\text{C}$, $-41\text{ }^\circ\text{C}$ and $-3\text{ }^\circ\text{C}$, using stopped-flow techniques as described above. No "dioxygen adduct" complex could be detected spectroscopically under these conditions. Again this was not really surprising because we had observed previously for copper(I) complexes with related tridentate ligands that only in very few cases these reactive intermediates can be detected.²¹⁷ Therefore, no further detailed kinetic measurements were performed on this system.

4.2.12 $[\text{Cu}_2(\text{L}^2)_2\text{Cl}_3]\text{PF}_6 \times 2\text{ MeOH}$ (**6**).

To get an idea of how a copper "dioxygen adduct" complex might look like it has been shown in the past that a copper(II) chlorido complex is an acceptable analogue.⁹³ Therefore, a copper(II) chlorido complex with L^2 as ligand was prepared and structurally characterized. The crystal structure of the cation of $[\text{Cu}_2(\text{L}^2)_2\text{Cl}_3]\text{PF}_6 \times 2\text{ MeOH}$ (**6**) is presented in Figure 4-15. Both copper(II) ions in the dinuclear complex show distorted square pyramidal geometry (with a τ -value of 0.09) and are coordinated by three amine- and two chloride donors. Both pyramids are linked by the axial chloride anion Cl (1) with $\text{Cu}(1)\text{-Cl}(1) = 2.5874(8)\text{ \AA}$, $\text{Cl}(1)\text{-Cu}(1)\text{-Cl}(2) = 104.49(3)^\circ$ and $\text{Cu}(1)\text{-Cl}(1)\text{-Cu}(1\text{A}) = 110.62(5)^\circ$. The base of both pyramids is formed by N(1), N(2), N(3) and Cl(2) with $\text{N}(1)\text{-Cu}(1)\text{-N}(2) = 84.57(11)^\circ$, $\text{N}(2)\text{-Cu}(1)\text{-N}(3) = 83.20(11)^\circ$, $\text{N}(3)\text{-Cu}(1)\text{-Cl}(2) = 93.47(8)^\circ$ and $\text{N}(1)\text{-Cu}(1)\text{-Cl}(2) = 95.26(8)^\circ$. The Cu Cu distance is relatively short with 4.255 \AA , whereas the copper amine donor distances between $2.021(3)$ and $2.060(3)\text{ \AA}$ compare well with similar copper complexes.^{62, 218-220} From the molecular structure it is obvious that a dinuclear peroxido or oxido complex can (and most likely) will form during the reaction of $[\text{Cu}(\text{L}^2)(\text{CH}_3\text{CN})]\text{PF}_6$ with dioxygen. However, due to kinetic reasons as discussed in detail previously, we couldn't detect such an intermediate spectroscopically.^{162, 165, 215, 217}

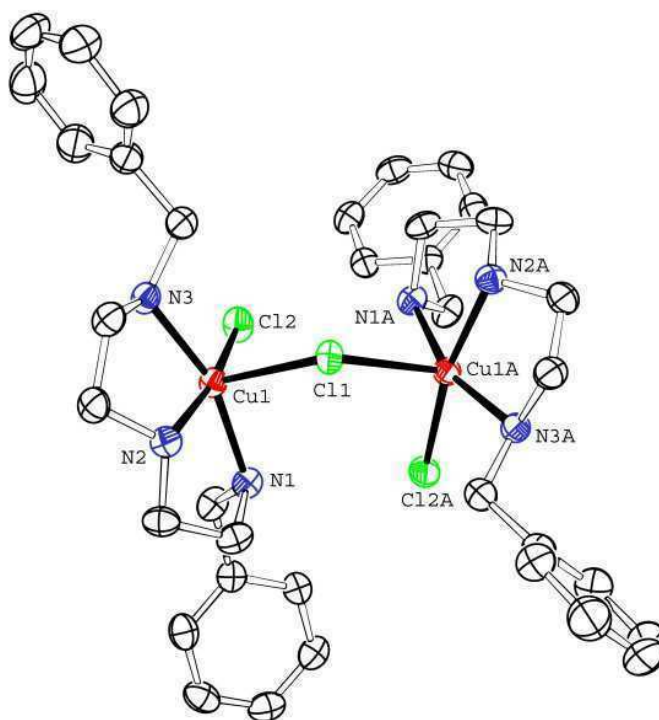


Figure 4-15: Molecular structure of the cation of $[\text{Cu}_2(\text{L}^1)_2\text{Cl}_3]^+$.

4.3 Conclusions

The new tridentate ligand L^1 provides a wide range of copper(I) and copper(II) complexes. Copper(I) complexes of L^1 display an unusual anion effect. With the counterion PF_6^- , the mononuclear copper(I) complex $[\text{Cu}(\text{L}^1)(\text{CH}_3\text{CN})]\text{PF}_6$ (**1**) was formed, while in the reaction of L^1 with $[\text{Cu}(\text{CH}_3\text{CN})_4]\text{ClO}_4$ the dinuclear helical compound $[\text{Cu}_2(\text{L}^1)_2](\text{ClO}_4)_2$ (**2**) resulted. The formation of different molecular structures was probably caused by crystallization effects as well as the stronger hydrogen bond in **2**. No other striking differences concerning weak interactions were found for either of the complexes.

In coordinating solvents, the dinuclear compound changed into the mononuclear species. This finding was supported by the formation of $[\text{Cu}(\text{L}^1)(\text{PPh}_3)]\text{ClO}_4$ (**3**) in the reaction of **2** with PPh_3 .

Oxidation of **1** with dioxygen in CH_3OH and CH_2Cl_2 yielded the dinuclear complexes $[\text{Cu}_2(\text{L}^1)_2(\text{OCH}_3)_2](\text{PF}_6)_2$ (**4**) and $[\text{Cu}_2(\text{L}^1)_2(\text{OH})_2](\text{PF}_6)_2$ (**5**). No hydroxylation of the ligand was observed upon oxidation. The oxidation behavior differs from that of the dinuclear compound

$[\text{Cu}_2(\text{mac})(\text{CH}_3\text{CN})_2](\text{ClO}_4)_2$. Reasons for the different reactivity could be seen in the higher redox potential of **1** and the absence of a dinuclear copper core providing a highly preorganized system. Investigation of reaction intermediates during the oxidation reaction showed that a peroxido species as well as the oxido compound $[\text{Cu}_2(\text{L}^1)_2\text{O}](\text{PF}_6)_2$ were formed during the reaction. However, detection of the peroxido species by UV-Vis spectroscopy was not possible. Furthermore, the reaction of $[\text{Cu}(\text{L}^2)(\text{CH}_3\text{CN})]\text{PF}_6$ with dioxygen was investigated (L^2 is the corresponding amine analogue of the imine L^1). Again, spectroscopically we could not detect a "dioxygen adduct" complex as a reactive intermediate. A dinuclear copper(II) complex, $[\text{Cu}_2(\text{L}^2)_2\text{Cl}_3]\text{PF}_6$, was prepared and structurally characterized.

4.4 Experimental Section

4.4.1 Materials and Methods

Reagents and solvents used were of commercially available reagent quality. Organic solvents used in the syntheses of the copper(I) complexes were dried in the usual way. Diethylenetriamine and benzaldehyde were distilled prior to use. $[\text{Cu}(\text{CH}_3\text{CN})_4]\text{X}$ ($\text{X} = \text{ClO}_4, \text{PF}_6, \text{BF}_4, \text{SbF}_6$) salts were synthesized according to the literature.¹²¹ Preparation and handling of air-sensitive compounds were carried out in a glove box filled with argon (MBraun, Germany; water and dioxygen less than 1 ppm).

^1H and ^{13}C NMR spectra were recorded by a DXP 300 AVANCE spectrometer. For low temperature measurements of **1** and **2** in DMF-d_7 , a Bruker DRX 400 AVANCE spectrometer was used. IR spectra were recorded in solution or as KBr pellets by a ATJ Mattson Infinity 60 AR-FT-IR instrument. Elemental analyses were carried out on a Carlo Erba Element Analyser Model 1106 and FD mass spectra were measured by a JEOL JMS 700 instrument at 70 eV and a source temperature of 200 °C. For standard UV-Vis spectroscopic investigations and for the investigation of the reaction of an oxidized solution of **1** with H_2O , a Hewlett Packard 8452A diode array spectrophotometer was used. Time-resolved UV-Vis spectra of the reaction of **1** with dioxygen were recorded with a modified

Hi-Tech SF-3L low-temperature stopped-flow unit (Salisbury, U.K.) equipped with a J&M TIDAS 16-500 photodiode array spectrophotometer (J&M, Aalen, Germany).⁵¹ Using syringes, an in situ prepared 4×10^{-4} M solution of **1** was transferred to the low-temperature stopped-flow instrument. A dioxygen saturated solution was prepared by bubbling dioxygen through CH_2Cl_2 in a syringe (solubility of dioxygen at 25 °C in CH_2Cl_2 : 3.8×10^{-3} M).³⁹ Cyclic voltammetry was carried out using an EG&G Model 263 potentiostat. The measurements were performed at 25 °C under nitrogen in CH_3CN or DMSO solutions containing 0.1 M $n\text{-Bu}_4\text{NPF}_6$ and $1 \times 10^{-3} - 10^{-4}$ M copper(I) complex. The experiments utilized a two-chambered electrochemical H-cell in which the working solution compartment was separated from the other by a fine glass frit. The reference electrode for the electrochemical measurements was an Ag/AgCl electrode (BAS MF-1052). As the working electrode glassy carbon disk and as a reference electrode a coiled platinum wire was used. Potentials are reported relative to the ferrocene/ferrocenium couple (+ 0.42 V vs. Ag/AgCl reference) which was used as an external reference.

4.4.2 X-ray Structure Determination of **L**¹ and **1** to **6**.

Single crystals were coated with protective perfluoropolyether oil and mounted on a glass fiber. Data for **L**¹, **2** and **4** were collected by a Siemens P4 diffractometer at 210(2), 295(2), 210(2) K and for **1**, **3**, **5** and **6** by a Nonius Kappa CCD diffractometer at 173(2), 100(2), 100(2) K, respectively ($\text{MoK}\alpha$, $\lambda = 0.71073$ Å, graphite-monochromator each). Space groups were determined from systematic absences. All structures were solved by direct methods and refined on F^2 using full-matrix least-squares techniques.¹²² All non-hydrogen atoms were refined with anisotropic thermal parameters.

For all compounds, data were corrected for Lorentz and polarization effects. An empirical absorption correction using SCALEPACK was carried out for **1**. Pure organic **L**¹ absorption effects were neglected. Semiempirical absorption corrections on the basis of Psi-scans were performed for **2** and **4**, a semiempirical absorption correction on the basis of multiple scans using SORTAV²²¹ was carried out for **3**. A numerical absorption correction based on the indexing of crystal faces was performed for **5**.

Hydrogen atoms of **6** were treated using the "Riding Model". Hydrogen atoms of **L**¹ were located from a difference Fourier map and refined with individual isotropic displacement parameters. With the exception of oxygen O¹ bound hydrogen atom H¹ of **5**, whose position was derived from a difference Fourier map all hydrogen atoms of compounds **2**, **3**, **4** and **5** were placed in positions of optimized geometry. Their displacement parameters were tied to the equivalent isotropic displacement parameters of the corresponding carrier atoms by a factor of 1.2 or 1.5.

Due to the absence of heavy atoms, the absolute structure of **L**¹ was not determined. Hydrogen atoms of **1** were located from a difference Fourier map and refined with isotropic displacement parameters. Positional parameters were refined while one mutual isotropic displacement parameter was kept fixed during refinement. In the crystal structure of **3**, solvent molecules (best described as CH₂Cl₂ and THF) were distorted around the crystallographic C₃ axis. For these molecules, no hydrogen atoms were taken into account during refinement. The PF₆⁻ counterion of **4** in the equatorial plane and the PF₆⁻ counterions of **5** were distorted. Two alternative positions were refined with occupancies of 87.1(6)% for F(11) to F(14) and 12.9(6)% for F(11A) to F(14A) in the case of **4** and of 75.9(4)% for F(13) to F(16) and 24.1(4)% for F(13A) to F(16A) in the case of **5**. The structure **5** included two acetone molecules per copper(II) complex unit. Complex **6** included two MeOH molecules per copper(II) complex unit.

4.4.3 Syntheses of Ligands and Complexes.

Caution! Perchlorate salts are potentially explosive and should be handled with great care!

4.4.3.1 (7E)-N¹-benzylidene-N²-((E)-2-(benzylideneamino)ethyl)ethane-1,2-diamine (**L**¹).

L¹ was synthesized by a modified literature procedure.²¹⁶ A solution of 4.25 g (40.0 mmol) benzaldehyde and 2.06 g (20.0 mmol) diethylenetriamine in 300 mL CHCl₃ was heated under reflux for 3 h. The resulting yellow solution was washed with 50 mL H₂O, and the organic layer was dried over Na₂SO₄. Evaporation of the solvent yielded a yellow oil that was crystallized from hot CH₃CN contain-

ing charcoal. The product was obtained as a white solid in 63% yield (3.50 g). Colorless single crystals suitable for X-ray diffraction studies were obtained from recrystallisation of the crude product from CH₃CN at –20 °C. Anal. Calcd. for C₁₈H₂₁N₃: C: 77.38, H: 7.57, N: 15.04, Found: C: 77.48, H: 8.22, N: 15.07. ¹H-NMR (300 MHz, CDCl₃): δ = 1.91 (s, 1 H, N-H), 2.52-2.59 (m, 2 H, CH₂-N_{tert} in the amina), 2.91-3.01 (m, 2 and 4 H, CH₂-N- in the amina and the bisimine), 3.23-3.46 (m, 2 H, CH₂-N_{sec} in the amina), 3.76 (m, 2 and 4 H, CH₂-N= in the amina and the bisimine), 4.16 (s, 1 H, C-H in the amina), 7.26-7.67 (m, 10 H, C-H aromatic), 8.22 (s, 1 H, N=C-H in the amina), 8.31 (s, 2 H, N=C-H in the bisimine). ¹³C{¹H}-NMR (300 MHz, CDCl₃): δ = 44.99 (CH₂-N_{tert} in the amina), 49.78 (CH₂-N_{sec} in the amina), 53.38, 53.44 (CH₂-N- in the amina and in the bisimine), 60.92, 61.09 (CH₂-N= in the amina and in the bisimine), 83.59 (C-H in the amina), 127.81, 128.08, 128.38, 128.55, 130.58, 136.07, 136.24, 140.62 (C aromatic), 161.73, 162.18 (N=C in the amina and in the bisimine). FD-MS (CH₃CN), m/e: 560 (43%) [2L¹]⁺, 280 (100%) [L¹]⁺. IR (KBr, cm⁻¹): 3244 ν(N-H), 2925/2878/2839/2797 ν(C-H), 1645 ν(C=N), 758/696 δ(C-H).

4.4.3.2 (N¹-benzyl-N²-(2-(benzylamino)ethyl)ethane-1,2-diamine (L²).

This ligand has been described in the literature previously as the trihydrochloride salt.²¹⁶ To a solution of 4.00 g (14.3 mmol) L¹ in 100 mL absolute THF under N₂ 2.72 g (71.0 mmol) LiAlH₄ was added in small portions and stirred under reflux for 4 h. After cooling 30 mL H₂O were added cautiously to the suspension which was further stirred for 45 minutes at room temperature. The resulting white precipitate was filtered off and washed with 25 mL THF and CH₂Cl₂. The filtrate was evaporated to dryness and the yellow residue was redissolved in 50 mL CH₂Cl₂ and washed three times with 25 mL 1N NaOH. The organic phase was dried over Na₂SO₄. Evaporation of the solvent gave a yellow residue which was purified by Kugelrohr distillation at 250 °C in vacuo to yield 2.88 g (10.4 mmol; 71% d. Th.) of a yellow oil. FD-MS (CHCl₃): m/z = 283 (30%) [L²]⁺, 567 (100%) [2 L²]⁺; IR (KBr, cm⁻¹): $\tilde{\nu}$ = 3303 ν(N-H), 3061/3027 ν(C-H aromatic), 2893/2818 ν(C-H aliphatic), 1453 δ(C-H aliphatic), 1115 ν(C-N), 738/700 δ(C-H aromatic); ¹H-NMR (CDCl₃, ppm): δ = 1.60 (s, 3 H, NH), 2.71 (s, 8 H, CH₂), 3.77 (s, 4 H, CH₂-Ar),

7.22-7.30 (m, 10 H, H aromatic); $^{13}\text{C}\{^1\text{H}\}$ -NMR (CDCl_3 , ppm): δ = 48.87, 49.32 (CH_2), 53.93 ($\text{CH}_2\text{-Ar}$), 126.83, 128.07, 128.32, 140.49 (C aromatic); UV-Vis (CH_3CN , λ_{max} [nm] (ϵ [$\text{M}^{-1}\text{cm}^{-1}$])): 214 (19.062), 258 (shoulder, 1.142).

4.4.3.3 $[\text{Cu}(\text{L}^1)(\text{CH}_3\text{CN})]\text{PF}_6$ (**1**).

To a solution of 0.419 g (1.50 mmol) L^1 in 20 mL MeOH 0.560 g (1.50 mmol) $[\text{Cu}(\text{CH}_3\text{CN})_4]\text{PF}_6$ were added and stirred for 3 h at room temperature. The resulting yellow precipitate was filtered off, washed with diethylether and dried in vacuo to yield 0.289 g (0.59 mmol, 40%) of **1**. Yellow single crystals suitable for X-ray diffraction studies were obtained by diffusion of Et_2O into the filtrate of **1**. Anal. Calcd. for $\text{C}_{20}\text{H}_{24}\text{N}_4\text{CuPF}_6$: C: 45.42, H: 4.57, N: 10.59, Found: C: 45.49, H: 4.85, N: 10.53. ^1H -NMR (300 MHz, DMSO-d_6): δ = 2.08 (s, 3 H), 2.97 (m, 4 H), 3.77 (m, 4 H), 4.51 (s, 1 H), 7.36 (dd, 4 H), 7.56 (dd, 2 H), 8.09 (d, 4 H), 8.71 (s, 2 H). $^{13}\text{C}\{^1\text{H}\}$ -NMR (300 MHz, DMSO-d_6): δ = 0.00, 45.62, 59.37, 116.92, 127.27, 127.67, 131.04, 132.62, 163.92. FD-MS (MeOH), m/e : 622 (42%) $[\text{Cu}(\text{L}^1)_2]^+$, 343 (100%) $[\text{Cu}(\text{L}^1)]^+$, 281 (21%) $[\text{L}^1]^+$. IR (KBr, cm^{-1}): 3350 $\nu(\text{N-H})$, 2962/2920/2868 $\nu(\text{C-H})$, 1632 $\nu(\text{C=N})$, 836 $\nu(\text{P-F})$, 760/697 $\delta(\text{C-H})$. UV/Vis (CH_3CN): λ_{max} [nm] (ϵ [$\text{M}^{-1}\text{cm}^{-1}$])) = 206 (52.381), 242 (29.766), 284 (4.584), 334 (3.119).

4.4.3.4 $[\text{Cu}_2(\text{L}^1)_2](\text{ClO}_4)_2$ (**2**).

The dinuclear compound was synthesized in a similar manner to **1** in 80% yield. Red single crystals suitable for X-ray diffraction studies were obtained by diffusion of THF into the filtrate of **2**. Anal. Calcd. for $\text{C}_{36}\text{H}_{42}\text{N}_6\text{Cu}_2\text{Cl}_2\text{O}_8$: C: 48.87, H: 4.78, N: 9.50, Found: C: 48.85, H: 4.85, N: 9.33. ^1H -NMR (300 MHz, DMSO-d_6): δ = 2.98 (m, 8 H), 3.77 (m, 8 H), 4.51 (s, 2 H), 7.36 (dd, 8 H), 7.56 (dd, 4 H), 8.09 (d, 8 H), 8.71 (s, 4 H). $^{13}\text{C}\{^1\text{H}\}$ -NMR (300 MHz, DMSO-d_6): δ = 46.98, 66.73, 128.63, 129.03, 132.41, 133.98, 165.31. FD-MS (MeOH), m/e : 622 (11%) $[\text{Cu}(\text{L}^1)_2]^+$, 442 (61%) $[[\text{Cu}(\text{L}^1)](\text{ClO}_4)]^+$, 343 (100%) $[\text{Cu}(\text{L}^1)]^+$. IR (KBr, cm^{-1}): 3259 $\nu(\text{N-H})$, 2909/2861 $\nu(\text{C-H})$, 1627 $\nu(\text{C=N})$, 1102 $\nu(\text{Cl-O})$, 757/692 $\delta(\text{C-H})$. UV/Vis (CH_3CN): λ_{max} [nm] (ϵ [$\text{M}^{-1}\text{cm}^{-1}$])) = 206 (99.393), 242 (60.722), 284 nm (8.853), 334 (5.902).

4.4.3.5 [Cu₂(L¹)₂](BF₄)₂ and [Cu(L¹)(CH₃CN)]SbF₆/[Cu₂(L¹)₂](SbF₆)₂.

These compounds were synthesized analogously to **1** in 76% and 80% yield, respectively. Satisfying ¹H, ¹³C NMR and IR spectra and elemental analyses were obtained.

4.4.3.6 [Cu(L¹)(PPh₃)](ClO₄) (3**).**

To a suspension of 0.442 g (0.50 mmol) [Cu₂(L¹)₂](ClO₄)₂ in 50 mL MeOH 0.262 g (1.00 mmol) PPh₃ were added and stirred for 3 h at room temperature. The volume of the yellow solution was reduced to about 5 mL. The resulting yellow precipitate was filtered off, washed with diethylether and dried in vacuo to yield 0.58 g (0.82 mmol; 82%) of **3**. Yellow single crystals suitable for X-ray diffraction studies were obtained by diffusion of THF/Et₂O (1:1) into a solution of **3** in CH₂Cl₂. Anal. Calcd. for C₃₆H₃₆N₃CuPClO₄: C: 61.37, H: 5.14, N: 5.96, Found: C: 61.45, H: 5.44, N: 5.68. ¹H-NMR (300 MHz, CDCl₃): δ = 2.92 (s(br), 2 H), 3.47 (s(br), 2 H), 3.59 (s(br), 1 H), 3.75 (s(br), 4 H), 6.83 (dd, 4 H), 7.11-7.37 (m, 17 H), 7.94 (d, 4 H), 8.61 (s, 2 H). ¹³C{¹H}-NMR (300 MHz, CDCl₃): δ = 48.28, 61.94, 128.63, 128.95 (d, ³J=9.45 Hz), 129.18, 130.15, 132.17, 132.18 (d, ¹J=36.33 Hz), 133.13 (d, ²J=15.98 Hz), 133.27, 165.31. ³¹P{¹H, ¹³C}-NMR (300 MHz, CDCl₃): δ = 2.38 (s). FD-MS (CH₂Cl₂), m/e: 604 (23%) [Cu(L¹)(PPh₃)]⁺, 441 (12%) [Cu(L¹)(ClO₄)]⁺, 342 (100%) [Cu(L¹)]⁺, 262 (9%) [PPh₃]⁺. IR (KBr, cm⁻¹): 3317 ν(N-H), 3055 ν(C-H), 2918/2862 ν(C-H), 1632 ν(C=N), 1436 δ(C-H), 1092 ν(Cl-O), 751/696 δ(C-H). UV/Vis (CH₃CN): λ_{max} [nm] (ε [M⁻¹cm⁻¹]) = 210 (7.565), 236 (3.688), 278 (1.705), 362 (592).

4.4.3.7 [Cu₂L¹₂(OCH₃)₂](PF₆)₂ (4**).**

To a solution of 0.698 g (2.50 mmol) L¹ in 20 mL MeOH 0.933 g (2.50 mmol) [Cu(CH₃CN)₄]PF₆ were added and stirred under aerobic conditions for 3 h at room temperature. The resulting green precipitate was filtered off, washed with diethylether and dried in vacuo to yield 0.939 g (0.91 mmol, 73%) of **4**. Green single crystals suitable for X-ray diffraction studies were obtained by slow evaporation of the filtrate exposed to air. Anal. Calcd. for C₃₈H₄₈N₆Cu₂O₂P₂F₁₂: C: 43.98, H: 4.66, N: 8.10, Found: C: 44.11, H: 5.03, N: 7.81. FD-MS (MeOH), m/e: 342 (100%) [Cu(L¹)]⁺, 279/280 (10%) [L¹]⁺.

IR (KBr, cm^{-1}): 3326 $\nu(\text{N-H})$, 2929/2891/2820 $\nu(\text{C-H})$, 1645 $\nu(\text{C=N})$, 840 $\nu(\text{P-F})$, 757/694 $\delta(\text{C-H})$. UV-Vis (MeOH): λ_{max} [nm] (ϵ [$\text{M}^{-1}\text{cm}^{-1}$]) = 296 (8.185), 384 (734), 656 (238). $\mu_{\text{eff}} = 0$ B. M..

4.4.3.8 $[\text{Cu}_2(\text{L}^1)_2(\text{OH})_2](\text{PF}_6)_2$ (5).

A solution of 0.40 g (0.757 mmol) $[\text{Cu}(\text{L}^1)(\text{CH}_3\text{CN})]\text{PF}_6$ in 15 mL CH_2Cl_2 was cooled to -40°C and bubbled with O_2 for 15 min. After stirring the suspension for 1.5 h at room temperature, the green precipitate was filtered off, washed with CH_2Cl_2 and dried at 100°C in vacuo to yield 0.22 g (0.218 mmol; 58%) of **5**. Green single crystals suitable for X-ray diffraction studies were obtained by recrystallisation of the green precipitate from acetone at -20°C . Anal. Calcd. for $\text{C}_{36}\text{H}_{44}\text{N}_6\text{Cu}_2\text{P}_2\text{F}_{12}\text{O}_2$: C: 42.82, H: 4.21, N: 8.17, Found: C: 42.84, H: 4.42, N: 8.50. FD-MS (MeOH), m/e : 343 (100%) $[\text{Cu}(\text{L}^1)]^+$, 357 (10%) $[\text{Cu}(\text{L}^1)\text{O}]^+$. IR (KBr, cm^{-1}): 3600 $\nu(\text{O-H})$, 3330 $\nu(\text{N-H})$, 3065 $\nu(\text{C-H})$, 2941 $\nu(\text{C-H})$, 1643 $\nu(\text{C=N})$, 1453 $\delta(\text{C-H})$, 842 $\nu(\text{P-F})$, 758/694 $\delta(\text{C-H})$. UV-Vis (MeCN): λ_{max} [nm] (ϵ [$\text{M}^{-1}\text{cm}^{-1}$]): 236 (11.874), 262 (11.526), 334 (2293), 626 (80). $\mu_{\text{eff}} = 0$ B. M.

4.4.3.9 $[\text{Cu}_2(\text{L}^2)_2\text{Cl}_3]\text{PF}_6 \cdot 2\text{MeOH}$ (6).

To a solution of 0.170 g (1.00 mmol) $\text{CuCl}_2 \cdot 2\text{H}_2\text{O}$ and 0.082 g (0.50 mmol) NH_4PF_6 in 20 mL CH_3CN 0.283 g L^2 in 10 mL MeOH were added. The mixture was stirred for 30 min at room temperature. The resulting blue precipitate was filtered off and recrystallised from a mixture of CHCl_3 and MeOH to yield 0.160 g (0.162 mmol; 32%) of the desired product which was suitable for X-Ray diffraction analysis. Anal. Calcd. For $\text{C}_{36}\text{H}_{50}\text{N}_6\text{Cu}_2\text{Cl}_3\text{PF}_6$ ($M = 977.21$ g/mol): C: 45.75, H: 5.33, N: 8.89, Found: C: 45.80, H: 6.07, N: 9.01. FD-MS (CH_3CN): $m/z = 799$ (53%) $[\text{Cu}_2(\text{L}^2)_2\text{Cl}_3]^+$, 381 (100%) $[\text{Cu}(\text{L}^2)\text{Cl}]^+$, 284 (43%) $[\text{L}^2]^+$. IR (KBr, cm^{-1}): $\tilde{\nu} = 3278/3256/3183$ $\nu(\text{N-H})$, 2953/2890 $\nu(\text{C-H aliphatic})$, 1454 $\delta(\text{C-H aliphatic})$, 840 $\nu(\text{P-F})$, 751/703 $\delta(\text{C-H aromatic})$. UV-Vis (MeOH, λ_{max} [nm] (ϵ [$\text{M}^{-1}\text{cm}^{-1}$])): 298 (9.537), 660 (173). μ_{eff} (298 K) = 1.82 B. M.

4.4.4 Investigation of the potential hydroxylation reaction of the ligand.

A solution of 0.793 g (1.50 mmol) $[\text{Cu}(\text{L}^1)(\text{CH}_3\text{CN})]\text{PF}_6$ in 20 mL CH_2Cl_2 was bubbled at -40°C with O_2 for 20 min and allowed to warm to room temperature. After stirring the green suspension for 1.5 h, it was extracted five times with 30 mL of a 2:1 mixture of NH_3 (25%) and brine. The combined aqueous phases were then washed with 50 mL CH_2Cl_2 . The combined organic phases were dried over Na_2SO_4 and evaporated to dryness. The resulting brown oil was dried in vacuo to yield 65% of a mixture of L and the decomposition product benzaldehyde. This was ascertained by ^1H and ^{13}C NMR spectroscopy and mass spectrometry. In the IR spectrum, no absorption band for a potential O-H vibration could be observed.

4.4.5 Quantitative investigation of H_2O_2 formation upon oxidation.

A solution of 0.559 g (2.00 mmol) L^1 and 0.745 g (2.00 mmol) $[\text{Cu}(\text{CH}_3\text{CN})_4]\text{PF}_6$ in 50 mL CH_2Cl_2 was bubbled with O_2 for 5 min at -40°C . The resulting green solution was allowed to warm to -30°C and quenched with 4.84 g (20.00 mmol) HPF_6 (60%) in 10 mL Et_2O . After warming to room temperature, the suspension was stirred for 10 min. The brown precipitate was filtered off, washed with 10 mL Et_2O , and to the filtrate a solution of 1.0 g KI in 25 mL H_2O /10 mL concentrated acetic acid was added. After stirring the solution for 20 min it was titrated with 0.1 N $\text{Na}_2\text{S}_2\text{O}_3$ solution using a freshly prepared starch solution as indicator to yield 7.8% H_2O_2 (referring to 100% formation of the peroxido species) on average.

5 Iron(II) complexes of apme-derivates

5.1 Synthesis, characterization and properties of iron(II) complexes with a series of tripodal ligands based on the parent ligand tris(2-pyridylmethyl)amine

This work was published previously in the Journal "Inorganica Chimica Acta"

Kisslinger, S., Kelm, H., Beitat, A., Würtele, C., Krüger, H.-J. and Schindler, S.. *Inorg. Chim. Acta* **2011**, 374, 540-545 (doi:10.1016/j.ica.2011.02.062).

In the last 20 years spin-crossover (SCO) properties have been studied extensively using iron(II)-complexes because of their possible future applications in molecular electronics.^{34-35, 222-223} Especially iron(II) complexes have been used in these studies. It is well known that high-spin (HS, 5T_2) - low-spin (LS, 1A_1) transitions in iron(II) complexes can be induced by changes in pressure or temperature and by light irradiation.^{29, 31-32, 42, 68, 71-72, 77-78, 224-232} Observations that the spin state is quite sensitive to small changes of the ligand field, caused intensive research work on modifications of the ligands surrounding the metal ion. Iron(II) complexes of the tripodal ligand tris(2-pyridylmethyl)amine (tpa, Figure 6-1; abbreviated as tmpa in the literature as well) as a ligand proved as being quite interesting and useful in these studies (in addition with coligands such as thiocyanate).²³³ However, only most recently the crystal structure of $[\text{Fe}(\text{tpa})(\text{NCS})_2]$ has been reported.^{78, 234} Here it could be demonstrated furthermore, that solvent effects are quite important in regard to the SCO behavior of the complex.

Increasing the chelate ring size of one of the chelate rings from 5 to 6 leads to the ligand N^2, N^2 -bis[(2-pyridyl)methyl]-2-(2-pyridyl)ethylamine (pmea, Figure 5-1). $[\text{Fe}(\text{pmea})(\text{NCS})_2]$ also showed SCO behavior that has been studied previously by some of us.⁷⁵ Furthermore, Matouzenko et al. replaced one aromatic donor group in tpa with an aliphatic amine arm to obtain (2-aminoethyl)bis(2-pyridylmethyl)amine (uns-penp, Figure 5-1; alternatively abbreviated as DPEA in the literature).⁶⁸

[Fe(uns-penp)(NCS)₂] exhibited a gradual SCO between 130 and 150 K. Furthermore, this group used (3-aminopropyl)bis(2-pyridylmethyl)amine (DPPA) as a ligand.⁷² Compared with uns-penp/DPEA the chelate ring size of the aliphatic amine arm in the according iron(II) complex was increased from 5 to 6. The resulting complex [Fe(DPPA)(NCS)₂] crystallized in three polymorphs, where two of them exhibited SCO (a gradual SCO at about 150 K for one of the polymorphs and a very abrupt SCO at 114 K for the other one).

Following up on these results we decided to investigate whether replacing one further pyridyl group through an aliphatic arm in the ligand could improve SCO properties in this type of iron(II) complexes. Thus we prepared and investigated iron(II) complexes with the ligand apme and its derivatives (Figure 5-1).

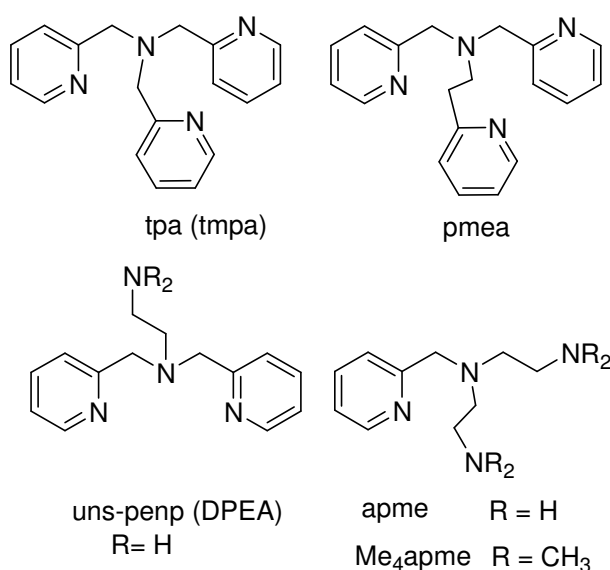


Figure 5-1: Abbreviations used for tripodal ligands: tris(2-pyridylmethyl)amine (tpa), N²,N²-bis[(2-pyridyl)methyl]-2-(2-pyridyl)ethylamine (pmea), (2-aminoethyl)bis(2-pyridyl-methyl)amine (uns-penp, R = H), N¹-(2-aminoethyl)-N¹-(2-pyridyl-methyl)-1,2-ethandiamine (apme, R = H) as well as bis[2-dimethylamino)ethyl]-(2-pyridylmethyl)amin (Me₄apme, R = CH₃).

5.2 Results and Discussion

Complexes [Fe(L)(NCS)₂] with L = tripodal ligand such as tpa or pmea can be prepared by reacting the ligands with the precursor complex [Fe(py)₄(NCS)₂] in methanol.⁷⁵ Yellow to orange powders were obtained and crystals for X-ray analysis could be obtained by slow diffusion of diethyl ether into

the solution of the complexes. However, using this method for apme so far was not successful, no solid material was obtained this way. Therefore, the reaction was performed in acetone.

5.2.1 [Fe(imine₂-apme)(NCS)₂] (**1**)

In contrast to our previous investigation on copper complexes with apme¹⁷¹ here an imine formation with the solvent acetone occurred instead and N¹-(propane-2-ylidene)-N²-(2-(propane-2-ylideneamino)ethyl)-N²-((pyridin-2-yl)methyl)ethane-1,2-diamine (imine₂-apme) coordinated to iron(II) was obtained. This complex, [Fe(imine₂-apme)(NCS)₂] (**1**), could be isolated and was structurally characterized. The molecular structure of **1** is presented in Figure 5-2. Crystallographic data and selected bond lengths and angles are given in Tables 5-1 and 5-2.

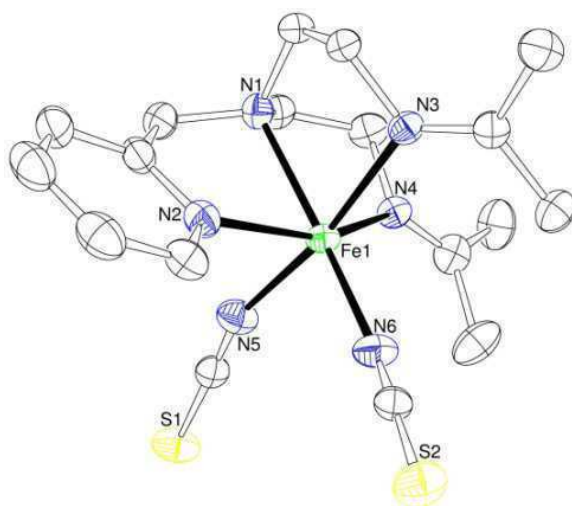


Figure 5-2: Molecular structure of [Fe(imine₂-apme)(NCS)₂] (**1**).

1 crystallizes in a Pna2₁ orthorhombic space group. The iron(II) cation in **1** is coordinated by six nitrogen donor atoms. Two of them belong to the two thiocyanate ligands that are and four of them to the tripodal ligand. The iron-nitrogen bond distances adjoining to the thiocyanate anions are shorter than those adjoining to the pyridines and the aliphatic amino groups (see Table 5-2). This may be due to electrostatic attraction in the case of the thiocyanate anion as well as due to different hybridizations and π -acceptor abilities of the pyridine and the aliphatic amino groups. The coordination sphere of the iron center is best described as distorted octahedron, because N-Fe-N angles between *cis* and *trans* nitrogen atoms deviate strongly from the values 90° and 180° as expected for an ideal

octahedral environment (see Table 5-3). N-Fe-N bond angles of **1** are between 75.73° and 114.66° for *cis* nitrogen donors, whereas bond angles of *trans* nitrogen donors are between 154.39° and 170.00°. Further three five-membered chelate rings are formed in **1**, as shown in Figure 5-2. A facial coordination is observed (the amine N together with the two imine atoms being one donor set) in contrast to **3** and **4** described below. No thiocyanate group is coordinated *trans* to the aromatic donor arm (Table 5-4).

5.2.2 [Fe(apme)(NCS)₂] (**2**)

Due to the fact that it was not possible to obtain [Fe(apme)(NCS)₂] (**2**) this way acetonitrile was used as an alternative solvent. Here crystals were obtained (a few crystals were selected from the product mixture) and crystallographic characterization showed that the target complex **2** was finally obtained. The molecular structure of **2** is presented in Figure 5-3. Crystallographic data and selected bond lengths and angles are given in Tables 5-1 and 5-2.

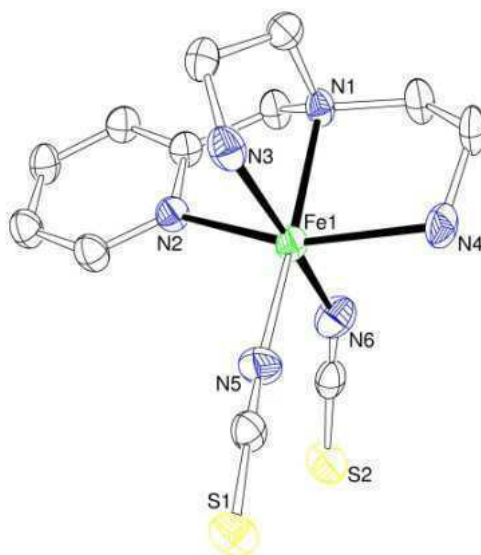


Figure 5-3: Molecular structure of [Fe(apme)(NCS)₂] (**2**).

As already described for **1**, **2** is coordinated by six nitrogen donor atoms, whereas two of them belong to the two thiocyanate ligands and four of them to the tripodal ligand. The iron-nitrogen bonds adjoining to the thiocyanate anions are shorter than those adjoining to the pyridines and the aliphatic amino groups. N-Fe-N angles between *cis* and *trans* nitrogen atoms deviate strongly from the

values of 90° and 180°, thus complex **2** adopts a distorted octahedral geometry too. Three five membered chelate rings are formed in **2**, as shown in Figure 5-3. Nitrogen-iron-nitrogen bond angles of **1** are between 84.87° and 106.92° for *cis*-standing nitrogen donors, whereas bond angles of *trans*-standing nitrogen donors are between 153.85° and 171.19°. The order of bond lengths is 2.080 Å/ 2.162 Å for NCS-ligands, followed by the nearly equally long bond lengths to the aromatic (2.205 Å) and aliphatic (2.205/ 2.213/ 2.233 Å) donor atoms. As observed for **1**, only the *fac* isomer of **2** had crystallized.

Analysis of the bulk compound unfortunately revealed that the sample is impure. One of the impurities was identified as starting material, [Fe(py)₄(NCS)₂]. Since the isolated material is impure no Mößbauer spectroscopy measurements were performed with this compound. Using other solvents such as dichloromethane did not improve the purity of the sample and here we only were able to recover crystalline starting material, [Fe(py)₄(NCS)₂].

5.2.3 [Fe(HMe₄apme)(NCS)₃] (**3**)

To avoid this problem, the tetra methylated derivative of apme, Me₄apme (Figure 5-1, R = Me), was used as a ligand. However, as described previously for related copper complexes with uns-penp, the amine arm of the ligand was protonated in methanol and therefore did not coordinate to the metal ion.²³⁵ Thus the complex with the protonated ligand and an additional thiocyanate anion as co-ligand, [Fe(HMe₄apme)(NCS)₃] (**3**), was obtained instead. The molecular structure of **3** is presented in Figure 5-4. Crystallographic data and selected bond lengths and angles are given in Tables 5-1 and 5-2.

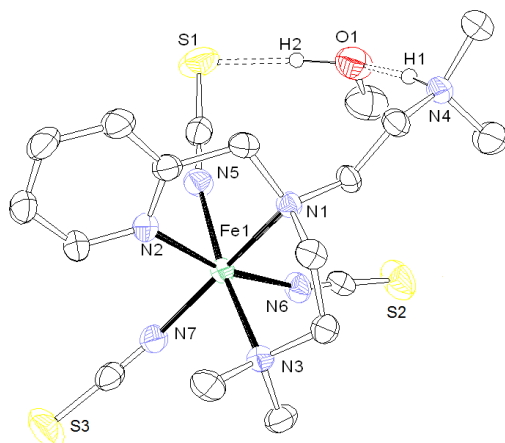


Figure 5-4: Molecular structure of $[\text{Fe}(\text{HMe}_4\text{apme})(\text{NCS})_3]$ (**3**).

The refinement furthermore shows that the complex molecule contains a methanol solvent molecule in the independent unit of the elementary cell with hydrogen bonding to the protonated amine group. The NH and the OH hydrogen atoms were found and isotropically refined. All other hydrogen atoms were positioned geometrically and all non-hydrogen atoms were refined anisotropically.

N-Fe-N bond angles of **3** are between 74.54° and 101.30° for *cis* nitrogen donor atoms, whereas bond angles of *trans* nitrogen donor atoms are between 162.78° and 170.76° . The coordination sphere of the iron center again is best described as distorted octahedron. **3** forms two five membered chelate rings.

5.2.4 $[\text{Fe}(\text{Me}_4\text{apme})(\text{NCS})_2]$ (**4**)

The protonation of the ligand Me_4apme described above was a consequence of using methanol as a solvent. Therefore, again a different solvent was used for the attempted synthesis of the complex $[\text{Fe}(\text{Me}_4\text{apme})(\text{NCS})_2]$. In contrast to the ligand apme acetone could be used because imine formation is not possible with Me_4apme . Thus it was possible to obtain $[\text{Fe}(\text{Me}_4\text{apme})(\text{NCS})_2]$ (**4**) in analytically pure form and the molecular structure of this complex is presented in Figure 5-5. Crystallographic data and selected bond lengths and angles are given in Tables 5-1 and 5-2.

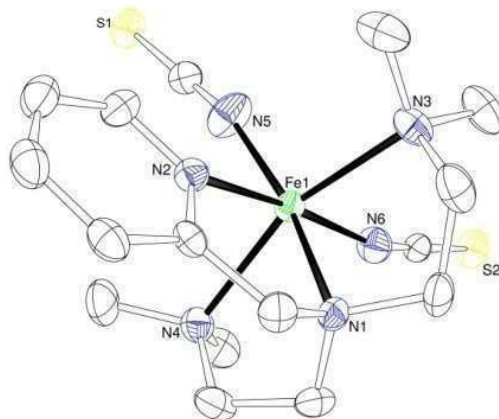


Figure 5-5: Molecular structure of $[\text{Fe}(\text{Me}_4\text{apme})(\text{NCS})_3]$ (**4**).

N-Fe-N bond angles in **4** are between 76.70° and 104.08° for *cis* nitrogen donor atoms, whereas bond angles of trans-standing nitrogen donor atoms are between 166.86° and 173.70° . As observed for the other complexes described above, steric strain impedes the angles of 90° and 180° respectively of a perfect octahedron. In contrast to **2**, only the meridional form could be crystallized of **4**. Most likely the steric strain of the methylene groups impedes crystallization of the *fac* isomer here. Only for the complexes **3** and **4** we found thiocyanate groups in *trans* position to a pyridine ring, as shown in Table 5-4.

5.2.5 Mößbauer spectroscopy of $[\text{Fe}(\text{Me}_4\text{apme})(\text{NCS})_2]$ (**4**)

The spin state of complex **4** was investigated in more detail by ^{57}Fe Mößbauer spectroscopy at different temperatures. Figure 5-6 shows Mößbauer spectra at 40 K and 298 K. The spectrum obtained at room temperature reveals a doublet with an isomer shift δ_s of 1.01 mm s^{-1} relative to an α -iron foil at room temperature and a quadrupole splitting ΔE_Q of 1.65 mm s^{-1} . These values agree with those obtained for other high-spin iron(II) complexes and support the earlier assignment of the spin state of the iron(II) ion in complex **4** based on the Fe-N bond lengths determined by X-ray structure analysis. Lowering the measurement temperature to 40 K resulted only in a moderate increase of the isomer shift δ_s and the quadrupole splitting ΔE_Q to 1.12 mm s^{-1} and 2.23 mm s^{-1} , respectively. This increase of the values upon lowering the temperatures follows the usually observed temperature

dependency of Mößbauer parameters. There are no indications for the presence of a low-spin component at 40 K and therefore for an occurrence of a spin crossover behavior. Thus, the iron ion in complex **4** remains in its high-spin state over the entire temperature range.

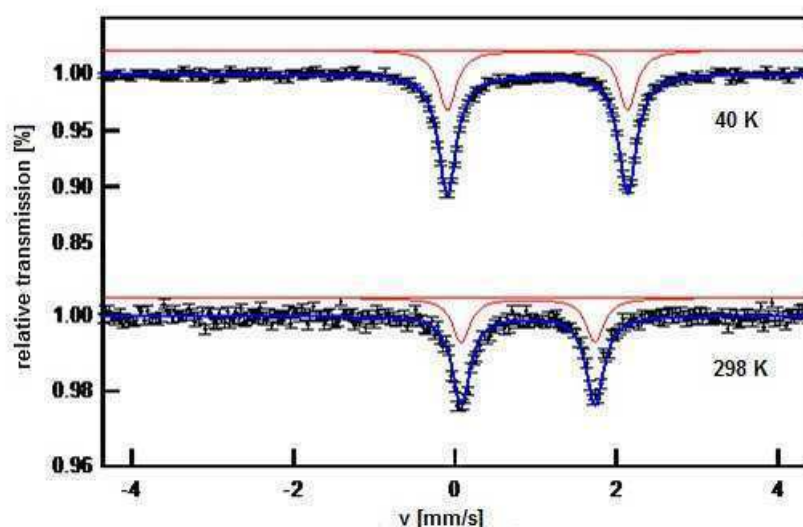


Figure 5-6: Mößbauer spectra of $[\text{Fe}(\text{Me}_4\text{apme})(\text{NCS})_2]$ (**4**) between 40 and 298 K.

5.2.6 Unpublished results: Magnetic susceptibility measurements of $[\text{Fe}(\text{imine}_2\text{-apme})(\text{NCS})_2]$ (**1**)

Powder and recrystallized samples of the compound $[\text{Fe}(\text{imine}_2\text{-apme})(\text{NCS})_2]$ were subjected to magnetic susceptibility measurements using a squid magnetometer. Figure 5-7 shows the χT vs. T plots for those samples at 0.1 Tesla measured between 300 K and 5 K in the cooling mode and between 5 K and 300 K in the heating mode, where χ is the molar magnetic susceptibility and T the temperature. No spin transition was detected for neither crystal, nor powder sample of $[\text{Fe}(\text{imine}_2\text{-apme})(\text{NCS})_2]$, and a part from the expected lowering of the χT value at low temperatures due to zero-field splitting the magnetic susceptibility data indicate that the iron(II) center remains in the HS state at all temperatures above 5 K. The slightly positive value of the powder sample might be caused by acetone solvent molecules within the complex powder as found in the elemental analysis.

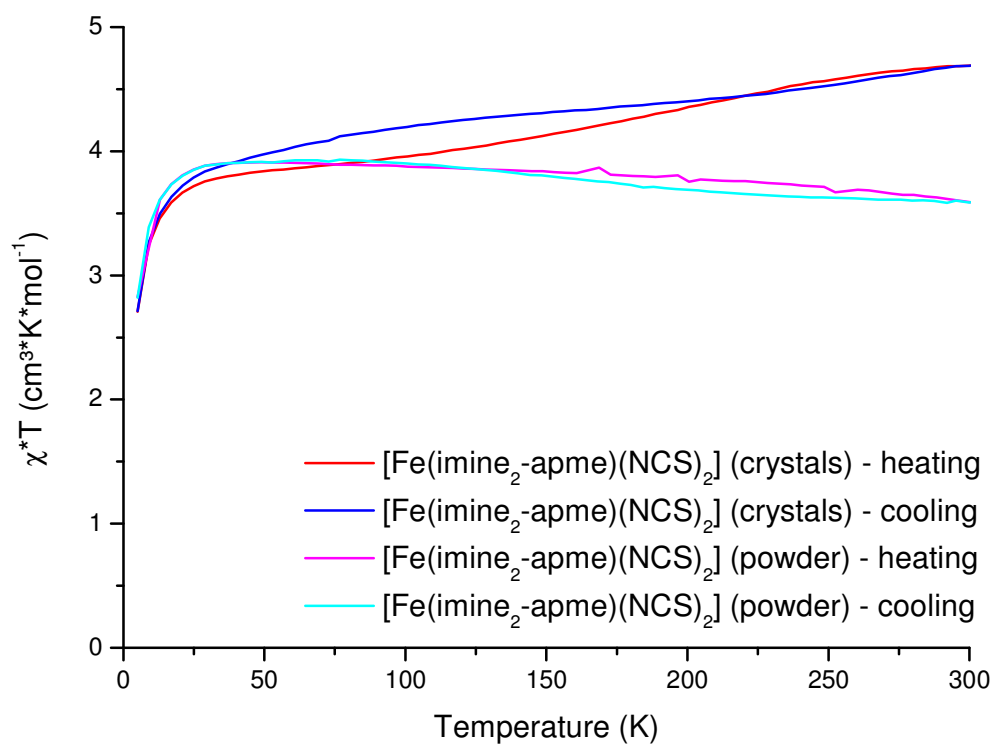


Figure 5-7: Magnetic susceptibility measurements using a SQUID magnetometer of $[\text{Fe}(\text{imine}_2\text{-apme})(\text{NCS})_2]$ (1) between 300 and 5 K (cooling mode) and 5 K and 300 K (heating mode).

5.2.7 Crystallographic Data.

Table 5-1: Selected crystallographic data unit cell parameters, and values of **1**, **2**, **3** and **4**.

Compound	[Fe(imine ₂ -apme)(NCS) ₂] (1)	[Fe(apme)(NCS) ₂] (2)	[Fe(HMe ₄ apme)(NCS) ₃] (3)	[Fe(Me ₄ apme)(NCS) ₂] (4)
Empiric Formular	C ₁₈ H ₂₆ FeN ₆ S ₂	C ₁₂ H ₁₈ FeN ₆ S ₂	C ₁₈ H ₃₁ FeN ₇ OS ₃	C ₁₆ H ₂₆ FeN ₆ S ₂
Molecular weight	446.44	366.29	513.53	422.40
Temperature [K]	150(2)	150(2)	193(2)	193(2)
Crystal size [mm]	0.48x0.24x0.22	0.39 x 0.37 x 0.20	0.16 x 0.08 x 0.08	0.52 x 0.48 x 0.24
Crystal System	orthorhombic	monoclinic	monoclinic	monoclinic
	Pna2 ₁	P2 ₁ /c	P2 ₁ /c	P2 ₁ /n
a [Å]	15.1739(2)	7.9242(3)	10.461(1)	9.769
b [Å]	8.9232(1)	13.2741(4)	16.932(2)	15.934
c [Å]	32.3826(6)	15.4981(5)	14.220(2)	13.057
α [°]	90	90	90	90
β [°]	90	92.338(3)	100.28(1)	93.23(3)
γ [°]	90	90	90	90
V [Å ³]	4384.60(11)	1628.84(9)	2478.4(4)	2029.3(7)
Z	8	4	4	4
ρ _{calcd.} [mg·m ⁻³]	1.353	1.494	1.376	1.383
μ [mm ⁻¹]	7.410	9.840	0.885	0.960
F(000)	1872.25	760	1080	888
Scan range θ [°]	5.14 to 62.57	4.39 to 62.65	2.54 to 28.08	2.45 to 28.15
Index ranges	-11 ≤ h ≤ 17;	-9 ≤ h ≤ 7	-13 ≤ h ≤ 13	-21 ≤ h ≤ 20
	-10 ≤ k ≤ 10;	-15 ≤ k ≤ 12	-22 ≤ k ≤ 22	-22 ≤ k ≤ 22
	-37 ≤ l ≤ 31	-17 ≤ l ≤ 17	-18 ≤ l ≤ 18	-17 ≤ l ≤ 17
Reflections collected	16260	5520	21813	18253
Unique reflections	5618	2583	5620	4870
R _{int}	0.0350	0.0476	0.0900	0.0632
Data/restraints/parameters	5618 / 1 / 495	2583 / 4 / 202	5620 / 0 / 285	4870 / 0 / 230
Goodness of fit F ²	0.898	0.996	0.922	0.905
Final R indices (all data)	R1 = 0.0313	R1 = 0.0612	R1 = 0.1134	R1 = 0.0546
	wR2 = 0.0496	wR2 = 0.1358	wR2 = 0.1381	wR2 = 0.0841
R indices [I > 2σ(I)]	R1 = 0.0252	R1 = 0.0528	R1 = 0.0529	R1 = 0.0340
	wR2 = 0.0487	wR2 = 0.1312	wR2 = 0.1133	wR2 = 0.0788
Largest diff. peak/hole [e·Å ⁻³]	0.170 and -0.216	0.838 and -0.995	0.643 and -0.766	0.358 and -0.457

Table 5-2: Selected bond lengths [Å] and angles [°] for compounds 1-4.

[Fe(imine ₂ -apme)(NCS) ₂] (1)				[Fe(apme)(NCS) ₂] (2)			
Fe(1)-N(6)	2.069(3)	N(6)-Fe(1)-N(1)	164.11(10)	Fe(1)-N(5)	2.080(3)	N(5)-Fe(1)-N(4)	98.7(3)
Fe(1)-N(5)	2.142(3)	N(5)-Fe(1)-N(1)	92.52(10)	Fe(1)-N(6)	2.162(4)	N(6)-Fe(1)-N(4)	88.5(4)
Fe(1)-N(4)	2.221(2)	N(4)-Fe(1)-N(1)	79.52(9)	Fe(1)-N(2)	2.205(3)	N(2)-Fe(1)-N(4)	153.8(3)
Fe(1)-N(2)	2.236(3)	N(2)-Fe(1)-N(1)	75.73(9)	Fe(1)-N(3)	2.205(4)	N(3)-Fe(1)-N(4)	97.6(4)
Fe(1)-N(1)	2.242(2)	N(6)-Fe(1)-N(3)	94.1(1)	Fe(1)-N(4)	2.213(3)	N(5)-Fe(1)-N(1)	170.1(3)
Fe(1)-N(3)	2.252(3)	N(5)-Fe(1)-N(3)	170.0(1)	Fe(1)-N(1)	2.233(3)	N(6)-Fe(1)-N(1)	95.9(3)
N(6)-Fe(1)-N(5)	95.4(1)	N(4)-Fe(1)-N(3)	92.16(9)	N(5)-Fe(1)-N(6)	93.6(4)	N(2)-Fe(1)-N(1)	76.1(1)
N(6)-Fe(1)-N(4)	114.6(1)	N(2)-Fe(1)-N(3)	88.90(9)	N(5)-Fe(1)-N(2)	106.9(3)	N(3)-Fe(1)-N(1)	79.1(2)
N(5)-Fe(1)-N(4)	86.14(10)	N(1)-Fe(1)-N(3)	77.49(10)	N(6)-Fe(1)-N(2)	84.8(3)	N(4)-Fe(1)-N(1)	79.4(2)
N(6)-Fe(1)-N(2)	90.7(1)			N(5)-Fe(1)-N(3)	91.6(3)		
N(5)-Fe(1)-N(2)	88.42(10)			N(6)-Fe(1)-N(3)	171.1(3)		
N(4)-Fe(1)-N(2)	154.39(9)			N(2)-Fe(1)-N(3)	86.8(2)		
[Fe(HMe ₄ apme)(NCS) ₃] (3)				[Fe(Me ₄ apme)(NCS) ₂] (4)			
Fe(1)-N(6)	2.091(4)	N(6)-Fe(1)-N(2)	167.5(3)	Fe(1)-N(5)	2.041(2)	N(1)-Fe(1)-N(2)	76.70(7)
Fe(1)-N(7)	2.108(3)	N(7)-Fe(1)-N(2)	93.8(3)	Fe(1)-N(6)	2.107(9)	N(5)-Fe(1)-N(3)	104.08(9)
Fe(1)-N(5)	2.162(3)	N(5)-Fe(1)-N(2)	83.8(3)	Fe(1)-N(1)	2.213(6)	N(6)-Fe(1)-N(3)	88.24(7)
Fe(1)-N(2)	2.231(3)	N(6)-Fe(1)-N(3)	92.3(3)	Fe(1)-N(2)	2.215(8)	N(1)-Fe(1)-N(3)	80.39(6)
Fe(1)-N(3)	2.274(3)	N(7)-Fe(1)-N(3)	87.7(2)	Fe(1)-N(3)	2.300(8)	N(2)-Fe(1)-N(3)	92.36(6)
Fe(1)-N(1)	2.297(3)	N(5)-Fe(1)-N(3)	170.7(2)	Fe(1)-N(4)	2.349(8)	N(5)-Fe(1)-N(4)	97.32(9)
N(2)-C(6)	1.339(5)	N(2)-Fe(1)-N(3)	93.9(2)	N(5)-Fe(1)-N(6)	95.27(8)	N(6)-Fe(1)-N(4)	89.22(7)
N(3)-C(8)	1.472(5)	N(6)-Fe(1)-N(1)	95.9(3)	N(5)-Fe(1)-N(1)	166.86(7)	N(1)-Fe(1)-N(4)	78.85(6)
N(4)-C(13)	1.495(5)	N(7)-Fe(1)-N(1)	162.7(3)	N(6)-Fe(1)-N(1)	97.23(7)	N(2)-Fe(1)-N(4)	87.94(6)
N(6)-Fe(1)-N(7)	97.1(4)	N(5)-Fe(1)-N(1)	90.2(2)	N(5)-Fe(1)-N(2)	90.68(8)		
N(6)-Fe(1)-N(5)	88.2(4)	N(2)-Fe(1)-N(1)	74.5(1)	N(6)-Fe(1)-N(2)	173.70(7)		
N(7)-Fe(1)-N(5)	101.3(3)	N(3)-Fe(1)-N(1)	80.5(1)				

Table 5-3: Range of N-Fe-N angles between *cis* and *trans* nitrogen atoms

Complex	range of N-Fe-N angles between <i>cis</i> nitrogen atoms	range of N-Fe-N angles between <i>trans</i> nitrogen atoms
[Fe(imine ₂ -apme)(NCS) ₂]	75.73(9) - 114.7(1)	154.39(9) - 170.0(1)
[Fe(apme)(NCS) ₂]	84.9(1) - 106.9(1)	153.85(13) - 171.2(1)
[Fe(HMe ₄ apme)(NCS) ₃]	74.54(11) - 101.3(1)	162.8(1) - 170.8(1)
[Fe(Me ₄ apme)(NCS) ₂]	76.70(7) - 104.08(9)	166.86(7) - 173.70(7)

Table 5-4: Fe-C-N angles thiocyanate trans to aliphatic amino and pyridine group

Complex	Fe-C-N angle (thiocyanate trans to aliphatic amino group)	Fe-C-N angle (thiocyanate trans to pyridine group)
[Fe(imine ₂ -apme)(NCS) ₂]	164.1(1); 170.0(1)	none
[Fe(apme)(NCS) ₂]	170.2(1); 171.2(1)	none
[Fe(HMe ₄ apme)(NCS) ₃]	162.8(1); 170.8(1)	167.6(1)
[Fe(Me ₄ apme)(NCS) ₂]	166.86(7)	173.70(7)

5.2.8 IR-Spectroscopy of [Fe(apme)(NCS)₂], [Fe(imine₂-apme)(NCS)₂], [Fe(Me₄apme)(NCS)₂] and [Fe(TMG₂apme)(NCS)₂]

It is well known in the literature, that infrared spectra can give information about spin crossover behavior.²³⁶⁻²⁴¹ HS-state can be found about 2050-2070 cm⁻¹, whereas a possible LS-state can be seen at about 2100 cm⁻¹.²³⁷ Figure 5-8 shows infra red measurements at room temperature for [Fe(apme)(NCS)₂], [Fe(Me₄apme)(NCS)₂], [Fe(imine₂-apme)(NCS)₂] and [Fe(TMG₂-apme)(NCS)₂]. The NCS-bonds are found at 2064.9 cm⁻¹ for [Fe(apme)(NCS)₂], 2077.9/ 2055.2 cm⁻¹ for [Fe(Me₄apme)(NCS)₂], 2071.4/ 2061.9 cm⁻¹ for [Fe(imine₂-apme)(NCS)₂] and 2061.5/ 2061.9 cm⁻¹ for [Fe(TMG₂apme)(NCS)₂] respectively. These values are characteristically for HS-complexes.

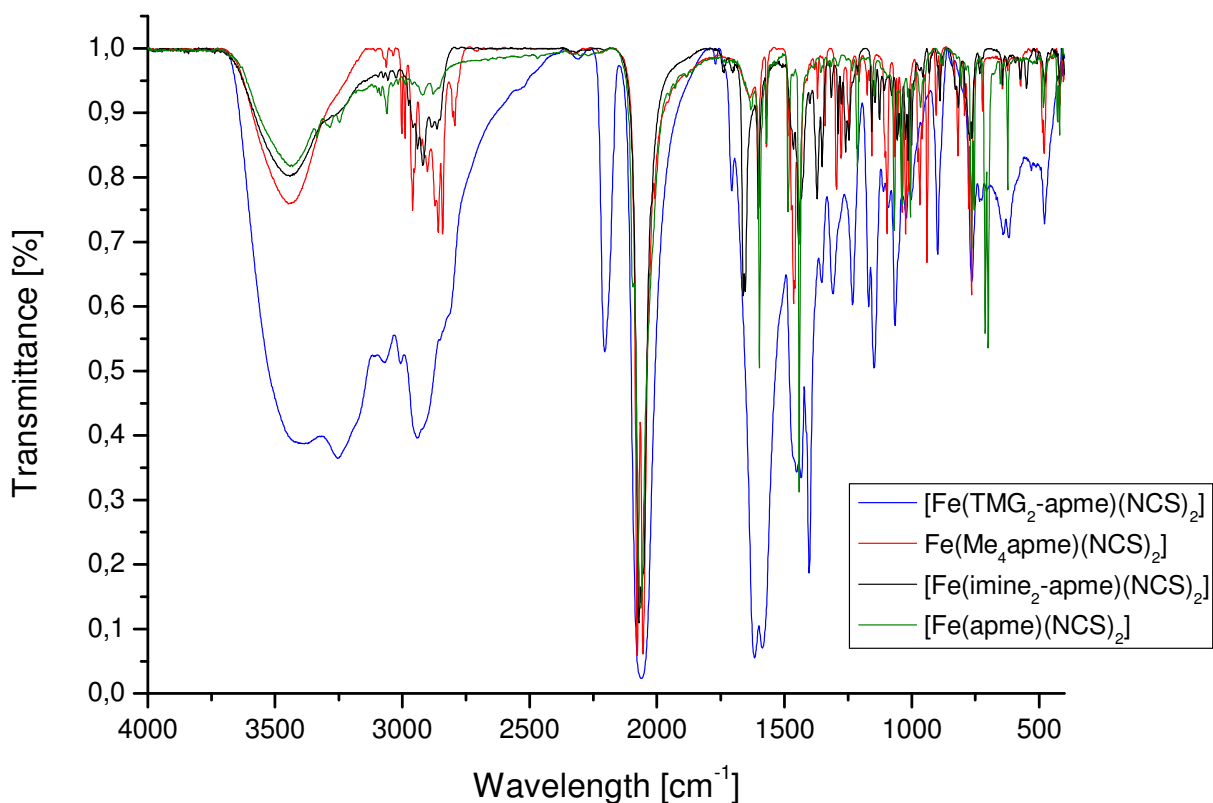


Figure 5-8: IR-spectra of $[\text{Fe}(\text{apme})(\text{NCS})_2]$, $[\text{Fe}(\text{imine}_2\text{-apme})(\text{NCS})_2]$, $[\text{Fe}(\text{Me}_4\text{apme})(\text{NCS})_2]$ and $[\text{Fe}(\text{TMG}_2\text{-apme})(\text{NCS})_2]$.

5.3 Conclusions

During our efforts to investigate if the replacement of two pyridyl donor arms with aliphatic amine groups in the tripodal ligand tpa would improve the SCO properties of the according iron(II) complexes $[\text{Fe}(\text{L})(\text{NCS})_2]$ we could synthesize and structurally characterize $[\text{Fe}(\text{imine}_2\text{-apme})(\text{NCS})_2]$, $[\text{Fe}(\text{apme})(\text{NCS})_2]$, $[\text{Fe}(\text{HMe}_4\text{apme})(\text{NCS})_3]$ and $[\text{Fe}(\text{Me}_4\text{apme})(\text{NCS})_2]$. All complexes are best described adopting a distorted octahedral coordination geometry. Bond lengths from the molecular structures clearly show that all complexes are high-spin. Due to the impurity of the bulk material of $[\text{Fe}(\text{apme})(\text{NCS})_2]$ it was not possible to investigate this complex in more detail. However, Mößbauer spectroscopic investigations of $[\text{Fe}(\text{Me}_4\text{apme})(\text{NCS})_2]$, where Me_4apme is the tetra methylated derivative of apme, indicated that variation of the tripodal ligand system from tpa to apme does not improve SCO properties at all for this type of complexes.

5.4 Experimental Section

5.4.1 Materials and Methods

Reagents and solvents used were of commercially available reagent grade quality. The complex $[\text{Fe}(\text{py})_4(\text{NCS})_2]$ was synthesized and characterized according to literature methods.²⁴²

Preparation and handling of air-sensitive compounds was carried out in a glove box filled with argon (Braun, Garching, Germany; water and dioxygen less than 1 ppm) and common Schlenck techniques. Solvents used here were always bought anhydrous and freed from oxygen through distillation. Elemental analyses have been performed at the Institute for Organic Chemistry, University of Gießen.

5.4.2 Ligand synthesis.

The ligands were prepared and characterized according to the literature.^{104, 171, 243}

5.4.3 Procedures for the synthesis of iron(II) complexes with the ligands imine₂-apme, apme, HMe₄apme and Me₄apme.

The complexes were prepared according to a similar procedure.⁶⁸

5.4.3.1 $[\text{Fe}(\text{imine}_2\text{-apme})(\text{NCS})_2]$.

A suspension of $[\text{Fe}(\text{py})_4(\text{NCS})_2]$ (244 mg; 0.4 mmol) in acetone (5 mL) was added dropwise to a solution of the ligand apme (77 mg; 0.4 mmol) in acetone (5 mL) and stirred for 30 minutes. No precipitate was formed immediately, so the solution was added to 50 mL diethyl ether. A yellow-green powder was obtained, containing 1/3 acetone per molecule according to the elemental analysis. The precipitate was filtered, washed with ether and dried under vacuum. Yellow crystals suitable for X-ray characterization were obtained by slow diffusion of ether in a solution of acetone.

Yield: 82 mg (46%). Anal. Calcd for $\text{FeC}_{18.9}\text{H}_{27.8}\text{N}_6\text{O}_{0.3}\text{S}_2$: C, 48.94; H, 6.04; N, 18.12. Found: C, 49.42; H, 6.15; N, 18.73. IR (KBr, cm^{-1}): 3440.6, 2919.7; 2071.4 (NCS); 2061.9 (NCS); 1661.5 (imine); 1653.5 (imine); 1601.3; 1571.9; 1444.2.

5.4.3.2 [Fe(apme)(NCS)₂].

A suspension of [Fe(py)₄(NCS)₂] (251 mg; 0.5 mmol) in CH₃CN (5 mL) was added dropwise to a solution of the ligand apme (97 mg; 0.5 mmol) in CH₃CN (5 mL) and stirred for 15 minutes. No precipitate was formed immediately from the green solution, so the solution was added to 50 mL diethyl ether and an impure yellow and green powder was obtained. The precipitate was filtered, washed with ether and dried under vacuum. Crystals formed from re-crystallization from acetonitrile. A yellow-green powder was obtained, but the precipitate was impure.

Yield: 76 mg (39%). Anal. IR (KBr, cm⁻¹): 3431.3, 3060.8; 2064.9 (NCS); 1632.2; 1570.7; 1484.9; 1441.7.

5.4.3.3 [Fe(HMe₄apme)(NCS)₃].

A solution of [Fe(py)₄(NCS)₂] (244 mg; 0.4 mmol) in CH₃OH (5 mL) was added dropwise to a solution of the ligand Me₄apme (100 mg; 0.4 mmol) in CH₃OH (5 mL) and stirred for 30 minutes. After a few minutes yellow powder was obtained. The precipitate was filtered, washed with ether and dried under vacuum. Crystals were obtained after re-crystallization from acetone.

5.4.3.4 [Fe(Me₄apme)(NCS)₂].

A suspension of [Fe(py)₄(NCS)₂] (251 mg; 0.5 mmol) in acetone (5 mL) was added dropwise to a solution the ligand Me₄apme (125 mg; 0.5 mmol) in acetone (5 mL) and stirred for 30 minutes. No precipitate from the orange solution was formed immediately, so the solution was added to 30 mL diethyl ether and yellow powder was obtained. The precipitate was filtered, washed with ether and dried under vacuum. Yellow crystals suitable for X-ray characterization were obtained by slow diffusion of ether in a solution of acetone.

Yield: 124 mg (59%). Anal. Calcd for FeC₁₆H₂₆N₆S₂: C, 45.90; H, 6.20; N, 19.90. Found: C, 45.97; H, 6.39; N, 19.96. IR (KBr, cm⁻¹): 3447.2, 2959.4, 2859.1, 2841.9, 2077.9 (NCS), 2055.2 (NCS), 1603.3; 1570.3; 1463.9; 1437.0.

5.4.3.5 Unpublished complex [Fe(TMG₂-apme)(NCS)₂].

A suspension of [Fe(py)₄](NCS)₂] (251 mg; 0.5 mmol) in acetone (5 mL) was added dropwise to a solution of the ligand TMG₂apme (125 mg; 0.5 mmol) in acetone (5 mL) and stirred for 30 minutes. No precipitate from the brown solution was formed immediately, so the solution was added to 30 mL diethyl ether and a yellow powder formed. Trying to dry the powder led to a brown colored oil.

The elemental analysis indicates a protonation of at least one aliphatic donor group of the ligand TMG₂apme resulting in the complex [H_{1.8}Fe(TMG₂-apme)(NCS)_{3.8}]. Yield: 115 mg (47%). Anal. Calcd for FeC₂₂H₄₀N_{11.8}S_{3.8}: C, 42.72; H, 6.03; N, 24.70. Found: C, 42.78; H, 5.99; N, 24.12. IR (KBr, cm⁻¹): 3253.3, 2942.6; 2205.5; 2061.5 (NCS); 2061.9 (NCS); 1706.7; 1617.1; 1586.2; 1434.2; 1402.6.

No crystals suitable for X-ray characterization were obtained.

5.4.4 X-Ray

The X-ray crystallographic data of compounds **1-2** were collected on a Gemini S-Ultra single crystal CCD diffractometer from Oxford Diffraction equipped with a CryojetHT-temperature system. An Enhance Ultra Cu-X-ray source ($\lambda = 1.54184 \text{ \AA}$) was used. The crystallographic data of complexes **3-4** were collected on a STOE IPDS-diffractometer equipped with a low temperature system (Karlsruher Glastechnisches Werk). Mo-K α radiation ($\lambda = 0.71069 \text{ \AA}$) and a graphite monochromator was used. Table 5-1 summarizes the crystal parameters as well as some details of the data collections and the structure refinements of all crystals. Semiempirical absorption corrections from equivalents (Multiscan) were carried out with the data of **1** and **2** using the program SCALE 3 ABSPACK from the CrysAlisPro program suite²⁴⁴; no absorption corrections were applied to the data sets of **3** and **4**. The structures were solved by direct methods in SHELXS97 and refined by using full-matrix least squares in SHELXL97.²⁴⁵⁻²⁴⁶ All non-hydrogen atoms were refined anisotropically. The NH and OH hydrogen atoms in **2** and **3** were found by Fourier difference maps and refined isotropically. The positions of all other hydrogen atoms were calculated using a riding model with isotropic thermal parameters. The

structure analyses show two independent complex molecules in the asymmetric unit of the elementary cell in **1** and a methanol solvent molecule in addition to the complex molecule in **3**, respectively.

Crystallographic data for the structures reported in this paper have been deposited with the Cambridge Crystallographic Data Center as supplementary publication no. CCDC- 813778 for **1**, CCDC- 813779 for **2**, CCDC-813780 for **3** and CCDC-813781 for **4**. Copies of the data can be obtained, free of charge from The Cambridge Crystallographic Data Center via www.ccdc.cam.ac.uk/data_request/cif.

5.4.5 Mößbauer Spectroscopy

Mößbauer spectra were recorded using a conventional spectrometer of the Fa. Wissel GmbH in the constant acceleration mode. The temperature can be maintained between 6K and 400 K by a closed-cycle cryostat unit of Advanced Research Systems Inc. The sample holder is mounted on the tip of the second stage heat station of the expander unit DE204SF inside a radiation shield and a vacuum shroud. The expander unit is decoupled from the vibrations of the compressor ARS-4HW by a DMX20-41 interface. The temperature is controlled by a Lakeshore 331S unit. The windows of the vacuum shroud are made of mylar foils. The spectra were analyzed by least-square fits using a Lorentzian line shape with the program WinNormus-for-Igor Version 2.0. The isomer shifts are given relative to an α -iron at room temperature.

5.4.6 Magnetic susceptibility measurements

Magnetic susceptibility measurements were performed using a Quantum Design MPMS-5S squid magnetometer. All samples were stored under argon to prevent oxidation of Fe(II) before the measurements. Each sample (~ 7-8 mg) was mounted on a plastic straw before introduction into the squid magnetometer. DC magnetization measurements were performed in a field of 0.1 T, from 5 to 300 K (heating mode) and from 300 to 5 K (cooling mode). Corrections for the diamagnetism of the sample were calculated using Pascal's constants.

6 Tmpa related iron(II) complexes with methylene, imine and guanidine groups

This work is submitted to in the Journal “Zeitschrift für anorganische und allgemeine Chemie”

Kisslinger, S., Kelm, H., Zheng, S., Beitat, A., Würtele, C., Wortmann, R., Bonnet, S., Herres-Pawlis, S., Krüger, H.-J.*, Schindler, S.*, *Z. anorg. allg. Chem.*, submitted.

6.1 Synthesis and Characterization of Iron(II) Thiocyanate Complexes with Derivatives of the Tris(2-pyridylmethyl) amine (tmpa) Ligand

Since about 1965 spin-crossover (SCO) behavior has been studied by various groups focussing mainly on iron(II)-complexes,^{29, 236-241, 247-251} after this phenomenon was initially discovered by Cambi et al. in 1931.²³⁻²⁴ These compounds are interesting due to their potential use in future molecular electronic devices.^{34-35, 222-223, 252-257} Quite frequently, thiocyanate or selenocyanate anions have been employed as co-ligands in these studies. As previously described, low-spin – high-spin transitions in these complexes ($LS, {}^1A_1 \rightleftharpoons HS, {}^5T_2$) can be induced by changing pressure or temperature as well as by light irradiation.^{29, 31-32, 42, 68, 71-72, 77-78, 224-232} In this regard $[Fe(tmpa)(NCS)_2]$ (Figure 6-1: tmpa = tris(2-pyridylmethyl)amine; tmpa is alternatively abbreviated in the literature as tpa) proved to be interesting.²²⁹ Quite surprisingly, however, only recently were crystal structures of this complex reported.⁷⁸⁻⁷⁹ There it could be demonstrated that inclusion of solvent molecules into the crystal lattice of $[Fe(tmpa)(NCS)_2]$ has a profound effect on the SCO properties of this compound.

In previous studies, two strategies were employed to modify and affect the ligand field strength of tripodal ligands and thereby to influence the SCO behavior of the resulting iron(II) dithiocyanate complexes. One strategy consists of combining pyridine nitrogen donors with aliphatic amine donors as already suggested by Toftlund. The other focuses on increasing the lengths of the individual

tripodal arms and thus yielding six-membered instead the five-membered chelate rings upon coordination of the metal ion.

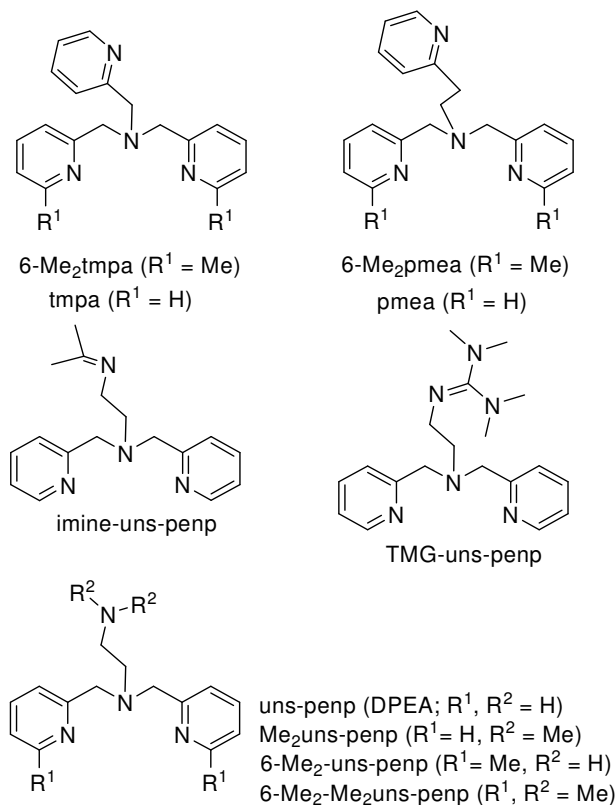


Figure 6-1: Abbreviations used for tripodal ligands.

Modifying the parent ligand tmpa by increasing one of the chelate rings in the resulting complex leads to the synthesis of [Fe(pmea)(NCS)₂] (pmea = N²,N²-bis[(2-pyridyl)methyl]-2-(2-pyridyl)ethylamine), Figure 6-1). In contrast to earlier investigations with this ligand, it could be demonstrated that this complex showed SCO behavior as well.^{75, 247}

Collet and co-workers tried to “fine-tune” the tripodal ligands for better SCO properties by mixing aliphatic and aromatic nitrogen donor groups in the ligand.^{68, 232} Therefore, this group investigated the use of the ligand N¹,N¹-bis(pyridin-2-ylmethyl)ethane-1,2-diamine (uns-penp, Figure 6-1; alternatively abbreviated as DPEA in the literature), in which one of the pyridine donor groups in tmpa is replaced by an aliphatic amine arm. The resulting complex [Fe(uns-penp)(NCS)₂] exhibited an abrupt SCO transition between 150 and 130 K.⁶⁸ In addition, this group used (3-aminopropyl)bis(2-pyridylmethyl)amine (DPPA) as a ligand. This ligand affords two five-membered and one

six-membered chelate rings upon coordination of a metal ion.⁷² Here, three crystalline polymorphs were found. One of these exhibited a very abrupt SCO at 114 K, the second showed a gradual SCO at about 150 K and the third displayed no SCO behavior at all.

In more recent work we introduced a second aliphatic group into the tmpa ligand system, leading to apme (apme = N'-(2-aminoethyl)-N'-(2-pyridyl-methyl)-1,2-ethanediamine)).²⁵⁸ Miyazaki et al. investigated an iron(II) complex with the related ligand DAPP (DAPP = bis(3-aminopropyl)(2-pyridylmethyl)amine) and observed SCO behavior for [Fe(DAPP)(abpt)](ClO)₄ (abpt = 4-amino-3,5-bis(pyridin-2-yl)-1,2,4-triazole).²⁵⁹ In contrast, the corresponding iron(II) dithiocyanate complexes with apme and derivatives of this ligand did not show any SCO behavior. All these complexes remained high spin over the entire range of investigated temperatures.²⁵⁸

Following up on these results, we decided to investigate a further strategy to modify the ligand field strength of tripodal ligands. The introduction of methyl groups in the *ortho*-position of the pyridine nitrogen atom or as amine substituents should reduce the ligand field strength of the respective ligand due to increased steric interactions upon coordination of the metal ion. Therefore, these ligands might lead to iron(II) dithiocyanate complexes displaying SCO transitions at a more desirable room-temperature range. Therefore, we prepared [Fe(L)(NCS)₂] complexes with the ligands shown in Figure 6-1: L = N,N-bis(6-methylpyridin-2-yl)methyl(pyridine-2-yl)methanamine (6-Me₂tmpa, also abbreviated as 6-Me₂tpa in the literature⁶⁹), N,N-bis((6-methylpyridin-2-yl)methyl)-2-(pyridin-2-yl)ethanamine (6-Me₂pmea), N¹,N¹-bis((6-methylpyridin-2-yl)methyl)ethane-1,2-diamine (6-Me₂uns-penp) and N¹,N¹-dimethyl-N²,N²-bis((6-methylpyridin-2-yl)methyl)ethane-1,2-diamine (6-Me₂-Me₂uns-penp). All these ligands have in common that two of the pyridyl groups in the ligand system have methyl substituents at the 6-position. Further, in order to study the effect of methyl substituents at the amine arm, derived from uns-penp, we used the ligand L = N¹,N¹-dimethyl-N²,N²-bis(pyridin-2-ylmethyl)ethane-1,2-diamine (Me₂uns-penp) to prepare the corresponding iron(II) dithiocyanate complex. In addition, the influence of replacing the amine donor function in uns-penp with an imine donor group has been investigated in the corresponding complexes of the tripodal

ligands N^1 -(propan-2-ylidene)- N^2,N^2 -bis((pyridin-2-yl)methyl)ethane-1,2-diamine (imine-uns-penp) and 2-(2-(bis((pyridin-2-yl)methyl)amino)ethyl)-1,1,3,3-tetramethyl-guanidine (TMG-uns-penp).

6.2 Results and Discussion

6.2.1 Syntheses of ligands and complexes.

The complexes were obtained as yellow, orange or yellow-green powders after mixing solutions of stoichiometric amounts of the corresponding ligands L (L = 6-Me₂tmpa, 6-Me₂pmea, 6-Me₂-uns-penp, 6-Me₂-Me₂uns-penp, Me₂uns-penp, and TMG-uns-penp) and the precursor complex [Fe(py)₄(NCS)₂] dissolved either in alcohol or acetone. Recently, we observed imine formation in the reaction of apme with [Fe(py)₄(NCS)₂] in acetone, yielding the complex [Fe(imine₂-apme)(NCS)₂] containing the new ligand imine₂-apme.²⁵⁸ The same reactivity was also observed using uns-penp as a ligand in acetone. Thus, the reaction with [Fe(py)₄(NCS)₂] led to the formation of [Fe(imine-uns-penp)(NCS)₂] (**4**). Slow diffusion of diethylether into solutions of [Fe(6-Me₂pmea)(NCS)₂], [Fe(6-Me₂-Me₂uns-penp)(NCS)₂], [Fe(Me₂uns-penp)(NCS)₂], [Fe(imine-uns-penp)(NCS)₂] and [Fe(TMg-uns-penp)(NCS)₂] resulted in the formation of yellow or green crystals suitable for X-ray diffraction studies. The yellow crystals of [Fe(6-Me₂tmpa)(NCS)₂] and [Fe(6-Me₂-uns-penp)(NCS)₂], obtained by the same crystallisation method were unfortunately not suitable for X-ray diffraction studies.

6.2.2 Structural properties of the complexes.

The molecular structures of [Fe(6-Me₂pmea)(NCS)₂] (**1**), [Fe(6-Me₂-Me₂uns-penp)(NCS)₂] (**2**), [Fe(Me₂uns-penp)(NCS)₂] (**3**), [Fe(imine-uns-penp)(NCS)₂] (**4**), and [Fe(TMg-uns-penp)(NCS)₂] (**5**) are presented in the Figures 6-2 – 6-6, respectively. Crystallographic data and selected bond lengths and angles are given in Tables 6-1 and 6-2.

In all five complexes the iron(II) centers are coordinated by six nitrogen donor atoms, two of them belonging to the two thiocyanate ligands and four of them to the corresponding tripodal ligand. With the exception of complex **1**, in each complex the tripodal ligand forms only five-membered chelate

The coordination environment of the complexes **1**, **2** and **3** vary from that of complexes **4** and **5** due to the fact that, in the former complexes, the bis(picoly)amine unit is meridionally arranged. In contrast, complexes **4** and **5**, which possess one arm containing an imine instead of the amine donor group, crystallize with a facial arrangement of the bis(picoly)amine unit. Both arrangements for tripodal ligands have been previously demonstrated in iron(II) dithiocyanate complexes. For example, only the *mer* isomer has also been observed in crystals of $[\text{Fe}(\text{uns-penp})(\text{NCS})_2]$,⁶⁸ while only the *fac*

isomer has been reported for crystalline $[\text{Fe}(\text{DPPA})(\text{NCS})_2]$.⁷² As mentioned in the Introduction, these two complexes differ only by the presence of an additional methylene group in the aliphatic amine arm of the tripodal ligand DPPA. The same is true for **1** compared with $[\text{Fe}(\text{pmea})(\text{NCS})_2]$. While only the *mer* isomer is found for **1**, $[\text{Fe}(\text{pmea})(\text{NCS})_2]$ crystallizes in *fac* geometry.⁷⁷ Therefore, we can conclude, that small changes in ligand field strength or steric aspects at one of the arms of the tripodal ligand can lead to the realization of different stereoisomers.

It is interesting to compare the effect of introducing different methyl groups on the Fe-N bond lengths of the tripodal ligands. Thus, the introduction of methyl substituents into the *ortho* position of two of the pyridine rings leads to a noticeable increase of the Fe-N_{py} bond lengths (2.278 and 2.293 Å) compared to the unsubstituted pyridine moiety (2.256 Å) in complex **1**.

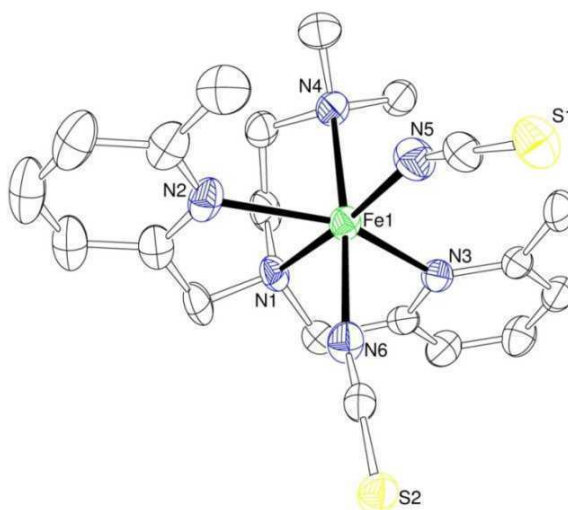


Figure 6-3: ORTEP plot of the molecular structure of $[\text{Fe}(6\text{-Me}_2\text{-Me}_2\text{uns-penp})(\text{NCS})_2]$ (**2**).

In the three structurally related complexes $[\text{Fe}(\text{uns-penp})(\text{NCS})_2]$, **3**, and **2**, the steric stress of the coordinated tripodal ligand is successively increased first by the presence of the sterically more-demanding methyl substituents at the amine donor atom in **3** and, then, by the additional incorporation of methyl substituents at the pyridine rings in **2**. Thus a close comparison of the distances between the iron ion and the nitrogen donor atoms of the tripodal ligands in $[\text{Fe}(\text{uns-penp})(\text{NCS})_2]$ and **3** reveals that only the Fe-N bond adjoining the aliphatic amine arm increases substantially by 0.136 Å, while all the other Fe-N bond lengths of the tripodal ligands are essentially the same in both

complexes. (Table 6-3) Adding further strain by introducing methyl substituents at the pyridine rings in **2** now leads to an elongation of the Fe-N_{py} bonds by more than 0.09 Å, as compared to **3**. While the Fe-N_{amine} bond length only marginally changes in **2**, the bond to the central nitrogen atom is slightly shortened, probably in order to better accommodate the other long Fe-N of the tripodal ligand.

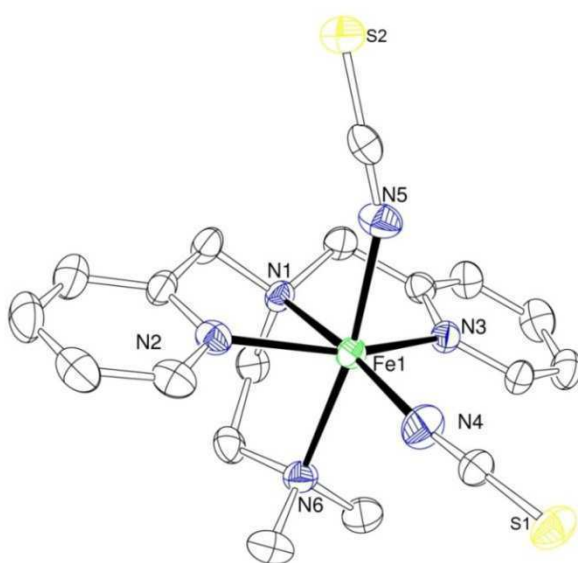


Figure 6-4: ORTEP plot of the molecular structure of [Fe(Me₂uns-penp)(NCS)₂] (**3**).

Recently, we observed that imine formation between acetone and apme was supported using [Fe(py)₄(NCS)₂] and the complex [Fe(imine₂-apme)(NCS)₂] with the new ligand imine₂-apme was obtained.²⁵⁸ The same reactivity was observed using uns-penp as a ligand in acetone. Reaction with [Fe(py)₄(NCS)₂] led to the formation of [Fe(imine-uns-penp)(NCS)₂] (**4**). The molecular structure of **4** is shown in Figure 6-5; crystallographic data and selected bond lengths and angles are given in Tables 6-1 and 6-2.

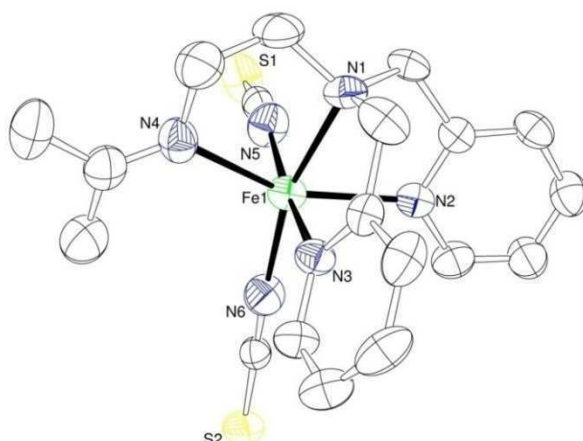


Figure 6-5: ORTEP plot of the molecular structure of $[\text{Fe}(\text{imine-uns-penp})(\text{NCS})_2]$ (**4**).

Related to the imine ligand of **4** is the guanidine derivative of uns-penp, TMG-uns-penp. The guanidine group inserts no extra steric strain into the molecule. On the contrary, the $\text{Fe-N}_{\text{imine}}$ bond length in **5** is reduced by 0.1 Å relative to that in **4**, indicating the better π -acceptor capabilities of the guanidine group.

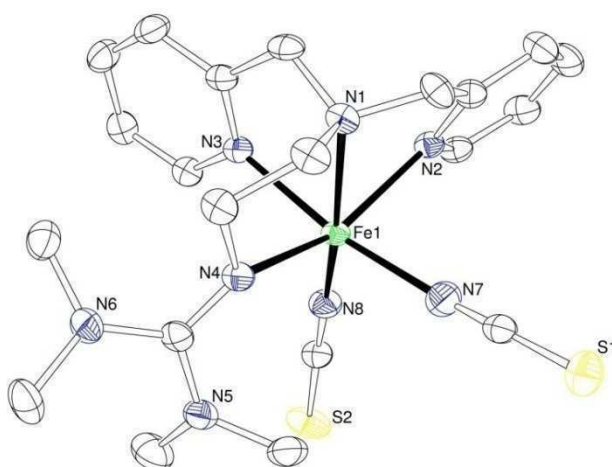


Figure 6-6: ORTEP plot of the molecular structure of $[\text{Fe}(\text{TMG-uns-penp})(\text{NCS})_2]$ (**5**).

Complexes **1** – **5** display Fe-N bond lengths (larger than 2 Å) (Table 6-2) that clearly indicate high-spin states at the temperatures of the crystallographic measurement.^{68, 72, 260-265} This spin state at room temperature was confirmed for all compounds by infra red spectroscopy and even at lower temperatures by SQUID and Mößbauer measurements (see below).

6.2.3 Crystallographic Data.

Table 6-1: Selected crystallographic data unit cell parameters, and values of [Fe(Me₂pmea)(NCS)₂] (1), [Fe(6-Me₂-Me₂uns-penp)(NCS)₂] (2), [Fe(Me₂uns-penp)(NCS)₂] (3) [Fe(imine-uns-penp)(NCS)₂] (4) and [Fe(TMGunspenp)(NCS)₂] (5).

Compound	[Fe(6-Me ₂ pmea)(NCS) ₂] (1)	[Fe(6-Me ₂ -Me ₂ uns-penp)(NCS) ₂] (2)	[Fe(Me ₂ uns-penp) (3)]	[Fe(imine-uns-penp) (4)]	[Fe(TMGunspenp) (5)]
Empiric Formular	C ₂₃ H ₂₃ FeN ₆ S ₂	C ₂₀ H ₂₆ FeN ₆ S ₂	C ₁₈ H ₂₂ FeN ₆ S ₂	C ₁₉ H ₂₂ FeN ₆ S ₂	C ₂₁ H ₂₈ FeN ₈ S ₂
Molecular weight	503.44	470.44	442.39	454.40	512.48
Temperature [K]	150(2)	113(2)	173 (2)	193(2)	193(2)
Crystal size [mm]	0.38 x 0.26 x 0.26	0.27 x 0.14 x 0.08	0.36 x 0.16 x 0.12	0.44 x 0.08 x 0.08	0.24 x 0.12 x 0.04
Crystal System	monoclinic	monoclinic	monoclinic	orthorhombic	triclinic
	P 2 ₁ /n	P 2 ₁ /c	P2 ₁ /n	Pna2 ₁	P-1
a [Å]	10.5625(3)	21.0056(8)	8.240(2)	15.295(3)	8.6066(17)
b [Å]	14.9136(4)	12.1951(5)	13.467(3)	10.669(2)	10.094(2)
c [Å]	15.1715(4)	17.4014(7)	18.397(4)	13.387(3)	15.492(3)
α [°]	90	90	90	90	86.01(3)
β [°]	96.938(3)	93.406(4)	94.07(3)	90	82.98(3)
γ [°]	90	90	90	90	66.28(3)
V [Å ³]	2372.39(11)	4449.8(3)	2036.4(7)	2184.5(8)	1222.6(4)
Z	4	8	4	4	2
ρ _{calcd.} [mg·m ⁻³]	1.410	1.404	1.443	1.382	1.392
μ [mm ⁻¹]	6.923	7.334	0.961	0.898	0.813
F(000)	1044	1968	920	944	536
Scan range θ [°]	4.17 to 62.61	4.19 to 62.77	2.64 to 28.03	2.66 to 28.16	2.66 to 28.10
Index ranges	-10 ≤ h ≤ 12	-24 ≤ h ≤ 15	-10 ≤ h ≤ 10;	-20 ≤ h ≤ 20	-11 ≤ h ≤ 11
	-16 ≤ k ≤ 17	-13 ≤ k ≤ 14	-17 ≤ k ≤ 17;	-13 ≤ k ≤ 13	-13 ≤ k ≤ 13
	-17 ≤ l ≤ 16	-19 ≤ l ≤ 20	-22 ≤ l ≤ 24	-17 ≤ l ≤ 17	-19 ≤ l ≤ 19
Reflections collected	9449	20147	18124	18777	11222
Unique reflections	3769	7068	4849	5142	5487
R _{int}	0.0268	0.0754	0.0424	0.0833	0.1017
Data/restraints/parameters	3769 / 0 / 291	7068 / 15 / 571	4849 / 0 / 249	5142 / 1 / 255	5487 / 0 / 295
Goodness of fit F ²	1.053	0.992	0.823	0.852	0.861
Final R indices (all data)	R1 = 0.0455	R1 = 0.1027	R1 = 0.0552;	R1 = 0.0917	R1 = 0.1287
	wR2 = 0.0918	wR2 = 0.1562	wR2 = 0.1179	wR2 = 0.0991	wR2 = 0.1452
R indices [I > 2σ(I)]	R1 = 0.0366	R1 = 0.0619	R1 = 0.0358	R1 = 0.0430	R1 = 0.0564
	wR2 = 0.0892	wR2 = 0.1394	wR2 = 0.1026	wR2 = 0.0882	wR2 = 0.1196
Largest diff. peak/hole [e·Å ⁻³]	0.506 and -0.335	0.940 and -0.357	0.595 and -0.791	0.407 and -0.248	0.649 and -0.748

6. Tmpa related iron(II) complexes with methylene, imine and guanidine groups

Table 6-2: Selected bond lengths [Å] and angles [°] for the compounds **1-5**.

[Fe(6-Me ₂ pmea)(NCS) ₂] (1)				[Fe(6-Me ₂ -Me ₂ uns-penp)(NCS) ₂] (2)			
Fe(1)-N(6)	2.075(2)	N(6)-Fe(1)-N(3)	103.10(9)	Fe(1)-N(5)	2.059(4)	N(1)-Fe(1)-N(3)	75.8(3)
Fe(1)-N(5)	2.141(2)	N(5)-Fe(1)-N(3)	90.67(8)	Fe(1)-N(6)	2.116(4)	N(5)-Fe(1)-N(2)	101.8(6)
Fe(1)-N(1)	2.204(2)	N(1)-Fe(1)-N(3)	76.19(8)	Fe(1)-N(1)	2.209(3)	N(6)-Fe(1)-N(2)	90.2(5)
Fe(1)-N(4)	2.256(2)	N(4)-Fe(1)-N(3)	84.14(8)	Fe(1)-N(3)	2.278(4)	N(1)-Fe(1)-N(2)	76.7(4)
Fe(1)-N(3)	2.278(2)	N(6)-Fe(1)-N(2)	104.96(9)	Fe(1)-N(2)	2.331(4)	N(3)-Fe(1)-N(2)	152.3(4)
Fe(1)-N(2)	2.293(2)	N(5)-Fe(1)-N(2)	91.17(8)	Fe(1)-N(4)	2.357(6)	N(5)-Fe(1)-N(4)	93.6(9)
N(6)-Fe(1)-N(5)	87.59(9)	N(1)-Fe(1)-N(2)	75.92(8)	N(5)-Fe(1)-N(6)	94.6(7)	N(6)-Fe(1)-N(4)	171.7(9)
N(6)-Fe(1)-N(1)	174.86(9)	N(4)-Fe(1)-N(2)	92.45(7)	N(5)-Fe(1)-N(1)	174.2(4)	N(1)-Fe(1)-N(4)	80.8(6)
N(5)-Fe(1)-N(1)	87.33(9)	N(3)-Fe(1)-N(2)	151.92(8)	N(6)-Fe(1)-N(1)	90.9(3)	N(3)-Fe(1)-N(4)	91.3(9)
N(6)-Fe(1)-N(4)	95.57(9)			N(5)-Fe(1)-N(3)	105.8(5)	N(2)-Fe(1)-N(4)	87.4(1)
N(5)-Fe(1)-N(4)	174.42(9)			N(6)-Fe(1)-N(3)	87.0(4)		
N(1)-Fe(1)-N(4)	89.43(8)						
[Fe(Me ₂ uns-penp)(NCS) ₂] (3)				[Fe(imine-uns-penp)(NCS) ₂] (4)			
Fe(1)-N(4)	2.024(2)	N(4)-Fe(1)-N(1)	171.37(9)	Fe(1)-N(6)	2.059(4)	N(1)-Fe(1)-N(2)	74.4(4)
Fe(1)-N(5)	2.146(2)	N(5)-Fe(1)-N(1)	90.13(9)	Fe(1)-N(5)	2.095(3)	N(6)-Fe(1)-N(4)	114.1(8)
Fe(1)-N(3)	2.179(2)	N(3)-Fe(1)-N(1)	75.92(8)	Fe(1)-N(3)	2.190(3)	N(5)-Fe(1)-N(4)	92.7(6)
Fe(1)-N(2)	2.201(2)	N(2)-Fe(1)-N(1)	76.49(8)	Fe(1)-N(1)	2.234(4)	N(3)-Fe(1)-N(4)	84.6(6)
Fe(1)-N(1)	2.239(2)	N(4)-Fe(1)-N(6)	92.92(9)	Fe(1)-N(2)	2.245(4)	N(1)-Fe(1)-N(4)	77.8(6)
Fe(1)-N(6)	2.351(2)	N(5)-Fe(1)-N(6)	168.78(9)	Fe(1)-N(4)	2.249(4)	N(2)-Fe(1)-N(4)	152.2(5)
N(4)-Fe(1)-N(5)	98.04(10)	N(3)-Fe(1)-N(6)	89.95(7)	N(6)-Fe(1)-N(5)	95.1(6)	C(15)-N(4)-Fe(1)	129.8(4)
N(4)-Fe(1)-N(3)	101.12(10)	N(2)-Fe(1)-N(6)	86.73(8)	N(6)-Fe(1)-N(3)	92.9(5)	C(14)-N(4)-Fe(1)	111.4(3)
N(5)-Fe(1)-N(3)	90.33(8)	N(1)-Fe(1)-N(6)	79.06(7)	N(5)-Fe(1)-N(3)	171.8(7)	C(7)-N(1)-Fe(1)	104.6(2)
N(4)-Fe(1)-N(2)	106.47(10)	C(1)-N(1)-Fe(1)	107.7(4)	N(6)-Fe(1)-N(1)	164.2(5)	C(13)-N(1)-Fe(1)	103.5(3)
N(5)-Fe(1)-N(2)	87.83(9)	C(7)-N(1)-Fe(1)	105.6(5)	N(5)-Fe(1)-N(1)	94.3(5)	C(7)-N(1)-Fe(1)	111.5(3)
N(3)-Fe(1)-N(2)	152.34(8)			N(3)-Fe(1)-N(1)	77.5(3)	C(8)-N(3)-C(12)	118.6(3)
				N(6)-Fe(1)-N(2)	92.6(6)	C(8)-N(3)-Fe(1)	116.1(3)
				N(5)-Fe(1)-N(2)	91.7(5)	C(12)-N(3)-Fe(1)	124.8(3)
				N(3)-Fe(1)-N(2)	87.0(5)		
[Fe(TMg-uns-penp)(NCS) ₂] (5)							
Fe(1)-N(8)	2.060(4)	N(8)-Fe(1)-N(7)	98.5(8)				
Fe(1)-N(7)	2.111(5)	N(8)-Fe(1)-N(4)	108.4(5)				
Fe(1)-N(4)	2.140(4)	N(7)-Fe(1)-N(3)	169.6(5)				
Fe(1)-N(3)	2.202(4)	N(4)-Fe(1)-N(3)	85.4(5)				
Fe(1)-N(1)	2.236(4)	N(8)-Fe(1)-N(1)	164.7(7)				
Fe(1)-N(2)	2.240(4)	N(7)-Fe(1)-N(1)	92.7(7)				
C(14)-N(4)	1.474(6)	N(4)-Fe(1)-N(1)	80.2(4)				
C(12)-N(3)	1.356(6)	N(3)-Fe(1)-N(1)	77.3(4)				
C(6)-N(2)	1.322(6)	N(8)-Fe(1)-N(2)	97.0 (5)				
C(13)-N(1)-C(1)	112.6(4)	N(7)-Fe(1)-N(4)	96.0 (7)				
C(13)-N(1)-C(7)	112.0(4)	N(8)-Fe(1)-N(3)	90.6(6)				
C(1)-N(1)-C(7)	110.8(4)	N(7)-Fe(1)-N(2)	86.0(5)				
C(13)-N(1)-Fe(1)	103.1(2)	N(3)-Fe(1)-N(2)	88.1(4)				
C(1)-N(1)-Fe(1)	106.6(3)	N(4)-Fe(1)-N(2)	153.7(4)				
C(7)-N(1)-Fe(1)	111.3(3)	N(1)-Fe(1)-N(2)	73.4(3)				

Table 6-3: Comparison of bond lengths (Å) between the iron ion and the nitrogen donor atoms of the tripodal ligand in [Fe(uns-penp)(NCS)₂], [Fe(Me₂uns-penp)(NCS)₂] (**3**), [Fe(6-Me₂-Me₂uns-penp)(NCS)₂] (**2**).

Bond	[Fe(uns-penp)(NCS) ₂]	3	2
Fe-N _{amine}	2.215	2.351	2.357
Fe-N _{py}	2.177	2.179	2.278
Fe-N _{py}	2.186	2.201	2.331
Fe-N _c ^[a]	2.231	2.239	2.209
Fe-N _{amine}	2.215	2.351	2.357

[a] N_c = tertiary amine nitrogen atom interconnecting the three arms of the tripodal ligand

6.2.4 IR-Spectroscopy.

It is generally possible to distinguish high-spin and low-spin states in iron(II) dithiocyanate complexes via IR-spectroscopy. The CN stretching vibrations in a low-spin state can be found at slightly higher wave numbers (about 2100 cm⁻¹) than those in a high-spin state (about 2050-2080 cm⁻¹).²³⁶⁻²⁴¹ Therefore, IR-measurements at room temperature were performed on compounds **1-5**, as well as on [Fe(6-Me₂tmpa)(NCS)₂] and [Fe(6-Me₂uns-penp)(NCS)₂] as shown on Figure 6-7 and Figure 6-8. For *cis* [Fe(L)(NCS)₂] complexes, two absorptions for the corresponding CN stretching vibrations are expected. Thus, two features were found at 2072.0 and 2062.3 cm⁻¹ for [Fe(6-Me₂tmpa)(NCS)₂], 2073.3 and 2061.3 cm⁻¹ for **1**, 2081.1 and 2069.0 cm⁻¹ for [Fe(6-Me₂uns-penp)(NCS)₂], 2072.6 and 2053.9 cm⁻¹ for **2** and at 2071.2/ 2068.3 cm⁻¹ for **4**. For compounds **3** and **5** the two absorptions could not be resolved, instead a broad feature was observed at 2061.4 cm⁻¹ and at 2062.6 cm⁻¹ respectively. The IR spectroscopic results clearly assign a high-spin state to all investigated compounds at room temperature.

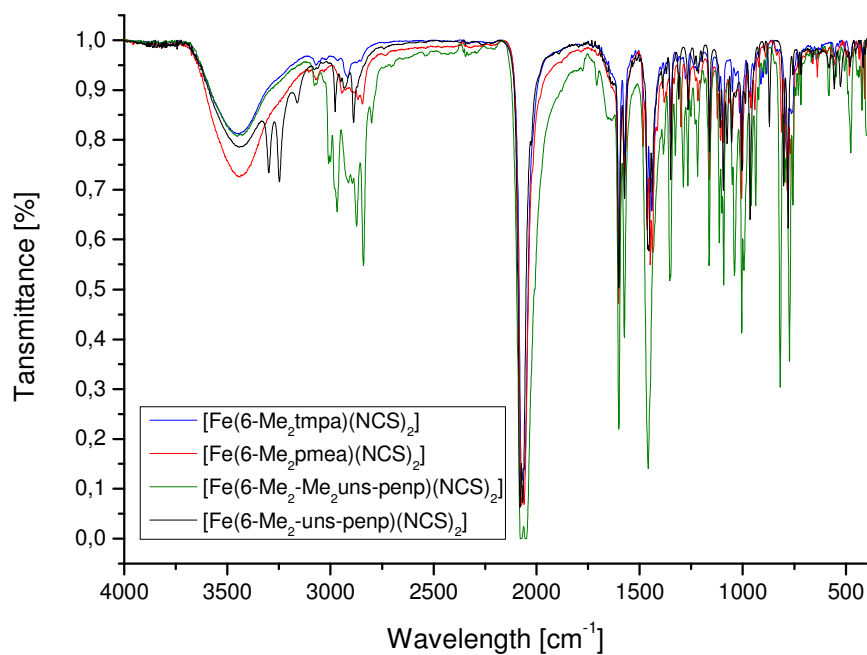


Figure 6-7: IR-Spectrum of [Fe(6-Me₂tmpa)(NCS)₂], [Fe(6-Me₂pmea)(NCS)₂], [Fe(6-Me₂-uns-penp)(NCS)₂] and [Fe(6-Me₂-Me₂uns-penp)(NCS)₂] in KBr pellets at 298 K.

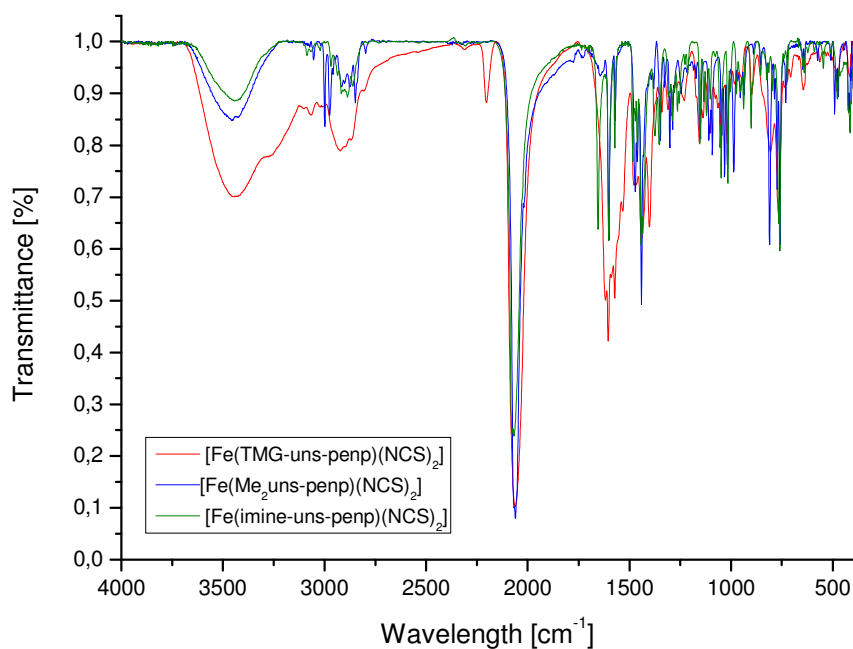


Figure 6-8: IR-spectra of [Fe(Me₂uns-penp)(NCS)₂], [Fe(imine-uns-penp)(NCS)₂] and [Fe(TMg-uns-penp)(NCS)₂] in KBr pellets at 298 K.

6.2.5 Magnetic susceptibility measurements.

Powder samples of compounds **3**, **5**, and $[\text{Fe}(\text{6-Me}_2\text{tmpa})(\text{NCS})_2]$, as well as recrystallized samples of compounds **4**, **1**, $[\text{Fe}(\text{6-Me}_2\text{-uns-penp})(\text{NCS})_2]$, and **2**, were subjected to magnetic susceptibility measurements using a squid magnetometer. Figure 6-9 and 6-10 show the χT vs. T plots for those complexes at 0.1 Tesla measured between 300 K and 5 K in cooling and heating modes, where χ is the molar magnetic susceptibility and T the temperature. For all measured samples the room temperature χT value was found to be close to $3.0 - 3.5 \text{ cm}^3 \text{ mol}^{-1} \text{ K}$, which is a typical value for a high-spin iron(II) compound with an octahedral coordination environment. No spin transition was detected for any of the compounds in this study. Except for the expected lowering of the χT value at temperatures below 25 K due to zero-field splitting, the χT value remains almost constant over the entire range of temperatures providing strong evidence that the iron(II) center remains in the high-spin state at all temperatures.

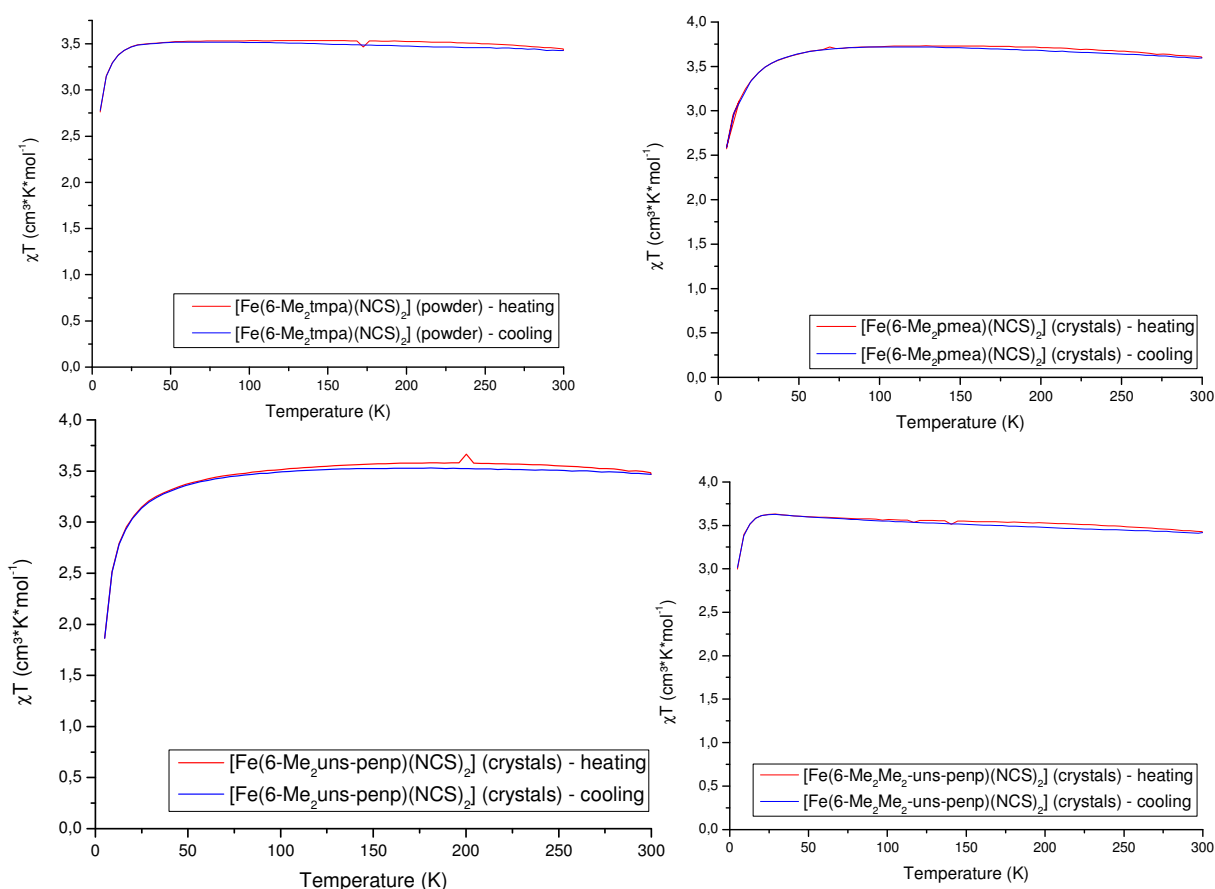


Figure 6-9: Magnetic susceptibility measurements of top: $[\text{Fe}(\text{6-Me}_2\text{tmpa})(\text{NCS})_2]$ (left), $[\text{Fe}(\text{6-Me}_2\text{pmea})(\text{NCS})_2]$ (right), bottom: $[\text{Fe}(\text{6-Me}_2\text{-uns-penp})(\text{NCS})_2]$ (left) $[\text{Fe}(\text{6-Me}_2\text{-Me}_2\text{uns-penp})(\text{NCS})_2]$ (right) between 5 K and 300 K.

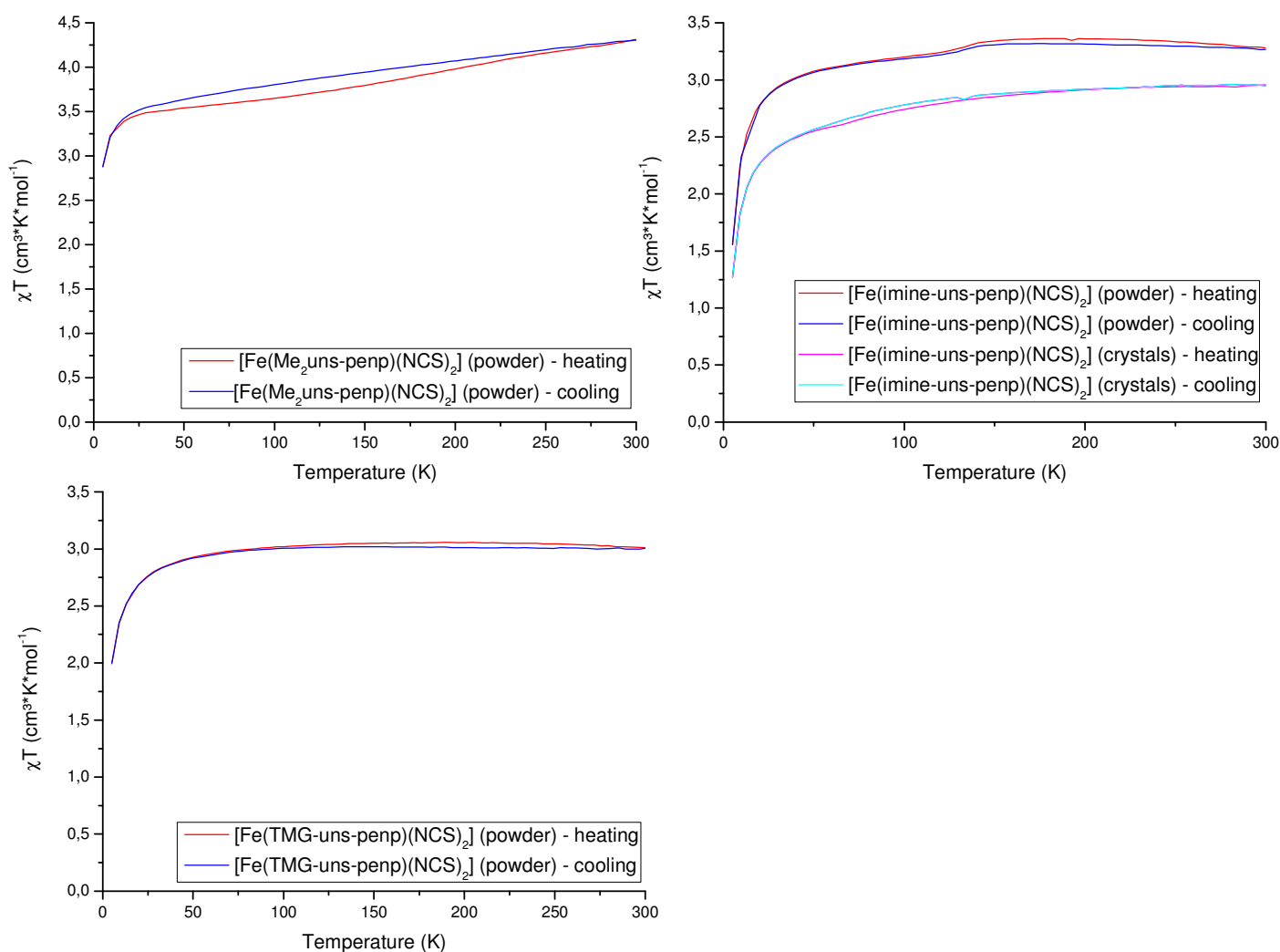


Figure 6-10: Magnetic susceptibility measurements of top: $[\text{Fe}(\text{Me}_2\text{uns-penp})(\text{NCS})_2]$ (left), $[\text{Fe}(\text{imine-uns-penp})(\text{NCS})_2]$ (right) and bottom: $[\text{Fe}(\text{TMG-uns-penp})(\text{NCS})_2]$ between 5 K and 300 K.

6.2.6 Mößbauer spectroscopy.

In addition to crystallographic and SQUID measurements a ^{57}Fe Mößbauer spectroscopic investigation of the compounds **1-4** as well as $[\text{Fe}(6\text{-Me}_2\text{tmpa})(\text{NCS})_2]$ and $[\text{Fe}(6\text{-Me}_2\text{uns-penp})(\text{NCS})_2]$ was performed at different temperatures. Figure 6-11 shows the Mößbauer spectra of each compound at 298 K and 40 K. The respective isomer shifts δ_s relative to an α -iron foil and the quadrupole splittings ΔE_Q of each compound are collected in Table 6-4. For all compounds doublets were observed with values for the isomer shift δ_s and the quadrupole splitting ΔE_Q which are consistent with those obtained for other high-spin iron(II) complexes mentioned in the literature, like for example $[\text{Fe}(\text{uns-penp})(\text{NCS})_2]$ ⁶⁸. The increase of values upon lowering the temperatures is in line of the

usually observed temperature dependency of Mößbauer parameters. There are no indications for the presence of a low-spin component at 40 K for any measured complex and, thus, no sign of SCO behavior. Therefore, Mössbauer data support the SQUID results (see above) showing that all investigated complexes exist in their high-spin states at room temperature as well as at 40 K.

Table 6-4: Isomer shifts δ_S relative to an α -iron foil and quadrupole splittings ΔE_Q of the complexes at room temperature and at 40 K.

Complex	$\delta_S(\text{mm s}^{-1})$		$\Delta E_Q(\text{mm s}^{-1})$	
	298	40 K	298 K	40 K
[Fe(6-Me ₂ tmpa)(NCS) ₂]	0.89	1.00	0.89	1.00
1	0.93	1.05	0.93	1.05
[Fe(6-Me ₂ -uns-penp)(NCS) ₂]	0.92	1.01	0.92	1.01
2	0.88	0.96	0.88	0.96
3	0.88	0.97	0.88	0.97
4	0.89	0.99	1.95	2.55

6. Tmpa related iron(II) complexes with methylene, imine and guanidine groups

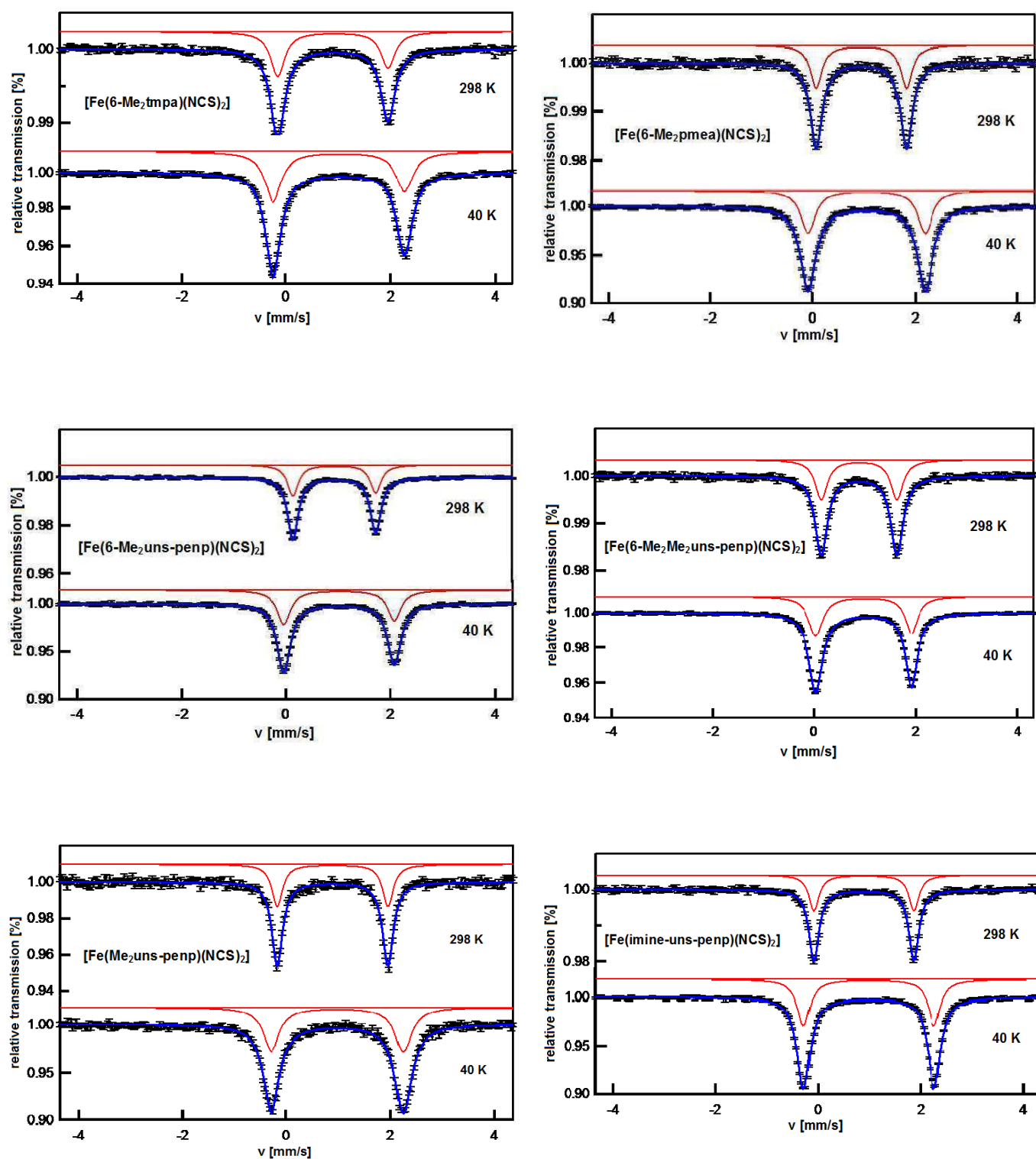


Figure 6-11: Mößbauer spectra of top: $[\text{Fe}(6\text{-Me}_2\text{tmpa})(\text{NCS})_2]$ and **1**; middle: $[\text{Fe}(6\text{-Me}_2\text{uns-penp})(\text{NCS})_2]$ and **2** and bottom: **3** and **4** between 298 and 40 K. (Note): The isomer shifts in this Figure are given relative to the cobalt source, while the isomer shifts in Table 6-4 are referenced versus an α -iron foil.)

6.3 Summary

We could successfully synthesize and structurally characterize $[\text{Fe}(\text{6-Me}_2\text{tmpa})(\text{NCS})_2]$, $[\text{Fe}(\text{6-Me}_2\text{pmea})(\text{NCS})_2]$ (**1**), $[\text{Fe}(\text{6-Me}_2\text{-uns-penp})(\text{NCS})_2]$, $[\text{Fe}(\text{6-Me}_2\text{-Me}_2\text{uns-penp})(\text{NCS})_2]$ (**2**), $[\text{Fe}(\text{Me}_2\text{uns-penp})(\text{NCS})_2]$ (**3**), $[\text{Fe}(\text{imine-uns-penp})(\text{NCS})_2]$ (**4**) and $[\text{Fe}(\text{TMG-uns-penp})(\text{NCS})_2]$ (**5**). The coordination environment of the iron(II) center in all complexes is best described as a distorted octahedron. Structural analysis as well as infrared, magnetic susceptibility and Mößbauer measurements clearly show that these complexes all maintain their high spin states between 5 and 300 K. Thus, varying the tripodal ligand by introducing sterically more demanding methyl groups decreases the ligand field strength of the tripodal ligand to such an extent that the resulting iron(II) dithiocyanate complexes cannot undergo any temperature-induced spin crossover transition at ambient pressures.

6.4 Experimental Section

6.4.1 Materials and Methods.

Reagents and solvents used in the preparation of compounds were of commercially available reagent quality. Organic solvents used in the syntheses of the iron(II) complexes were dried in the usual way. The $[\text{Fe}(\text{py})_4(\text{NCS})_2]$ salt as well as the ligands $\text{Me}_2\text{uns-penp}$ and TMG-uns-penp were synthesised according to literature methods.^{104, 242-243} Preparation and handling of air-sensitive compounds were carried out in a glove box filled with argon (MBraun, Germany; water and dioxygen less than 1 ppm).

6.4.1.1 Synthesis of the ligand N,N-Bis((6-methylpyridin-2-yl)methyl)(pyridine-2-yl)methanamine (6-Me₂tmpa).

This synthesis is a modification of a literature method.¹⁰⁴ 6-methyl-2-pyridinecarboxaldehyde (2.50 g, 20 mmol) was added to a mixture of 2-(aminomethyl)pyridine (1.08 g, 10 mmol) dissolved in dichloromethane (100 mL) and $\text{NaBH}(\text{OAc})_3$ (5.98 g, 28 mmol) in a 250 mL round-bottom flask. The solution was stirred at room temperature for 24 hours. The reaction was quenched by the addition of

a saturated solution of NaHCO_3 (40 mL). The organic layer was separated and the aqueous layer was extracted with ethylacetate (3×15 mL). The organic fractions were combined and dried over anhydrous Na_2SO_4 . Filtration and removal of the solvent by rotary evaporation yielded the title compound as a light-yellow-colored solid (3.09 g, 9.7 mmol, 97 %).

^1H NMR (CDCl_3 , 400 MHz) δ / ppm: 8.44 (d, 1H, py-H), 7.53 (m, 2H, py-H), 7.48 (t, 2H, py-H), 7.36 (d, 2H, py-H), 7.04 (t, 1H, py-H), 6.90 (d, 2H, py-H), 3.79 (d, 6H, py- CH_2), 2.43 (s, 6H, NCH_2).
 ^{13}C NMR (CDCl_3 , 400 MHz) δ / ppm: 159.5, 158.8, 157.5, 148.9, 136.8, 136.5, 122.7, 121.5, 121.3, 119.4, 76.9 (CDCl_3), 60.2, 60.0, 24.3.

6.4.1.2 Synthesis of the ligand *N,N*-Bis((6-methylpyridin-2-yl)methyl)-2-(pyridin-2-yl)ethanamine (6-Me₂pmea).

This synthesis is a modification of a literature method.²⁶⁶ 6-Methyl-2-pyridinecarboxaldehyde (2.50 g, 20 mmol) was added to a mixture of 2-(aminoethyl)pyridine (1.22 g, 10 mmol) dissolved in dichloromethane (100 mL) and $\text{NaBH}(\text{OAc})_3$ (5.98 g, 28 mmol) in a 250 mL round-bottom flask. The solution was stirred at room temperature for 24 hours. The reaction was quenched by the addition of a saturated solution of NaHCO_3 (40 mL). The organic layer was separated and the aqueous layer was extracted with ethylacetate (3×15 mL). The organic fractions were combined and dried over anhydrous Na_2SO_4 . Filtration and removal of the solvent by rotary evaporation yielded the title compound as a yellow-colored oil (3.21 g, 9.6 mmol, 96 %).

^1H NMR (CDCl_3 , 400 MHz) δ / ppm: 8.46 (d, 1H, py-H), 7.53 (t, 1H, py-H), 7.47 (t, 2H, py-H), 7.16 (d, 2H, py-H), 7.09 (d, 2H, py-H), 6.96 (d, 2H, py-H), 3.88 (s, 4H, py- CH_2), 2.98 (q, 4H, py- CH_3), 2.54 (s, 6H, NCH_2). **^{13}C NMR (CDCl_3 , 400 MHz) δ / ppm:** 160.6, 158.7, 157.4, 149.5, 136.6, 136.1, 122.4, 121.6, 119.7, 77.3 (CDCl_3), 60.4, 54.8, 36.0, 24.2.

6.4.1.3 Synthesis of the ligand *N*¹,*N*¹-bis((6-methylpyridin-2-yl)methyl)ethane-1,2-diamine (6-Me₂-uns-penp).

Synthesis of N-(2-(bis((6-methylpyridin-2-yl)methyl)amino)ethyl)acetamide (N-acetyl-6-Me₂-uns-penp): N-Acetyleneethylenediamine (1.02 g, 10 mmol) and 6-methyl-2-pyridinecarboxaldehyde (2.50 g,

20 mmol) were placed in dichloromethane (50 mL) in a 250 mL round-bottom flask. $\text{NaBH}(\text{OAc})_3$ (5.98 g, 28 mmol) was added and the mixture was allowed to stir for 24 hours at room temperature. The reaction was quenched by adding a saturated solution of NaHCO_3 (40 mL). The organic layer was separated and the aqueous layer was extracted with ethylacetate (3×20 mL). The organic fraction was dried over anhydrous Na_2SO_4 . Filtration and removal of the solvent by rotary evaporation yielded the title compound as an ochre-colored oil, that crystallized to a solid in the refrigerator within 24 h (2.97 g, 9.5 mmol, 95 %).

^1H NMR (CDCl_3 , 400 MHz) δ / ppm: 7.52 (t; 2H py-H), 7.15 (d, 2 H, py-H), 7.04 (d, 2H, py-H), 3.80 (s, 4H, CH_2), 3.30 (q, 2H, $\text{CH}_2\text{-NH}$), 2.68 (t, 2H, $\text{CH}_2\text{-N}(\text{CH}_2)_2$), 2.55 (s, 6H, $\text{CH}_3\text{-py}$), 2.00 (s, 3H, $\text{CH}_3\text{-CO}$). ^{13}C NMR (CDCl_3 , 400 MHz) δ / ppm: 170.0, 158.3, 157.8, 136.6, 121.6, 120.2, 77.3 (CDCl_3), 60.4, 52.9, 37.4, 24.4, 23.2.

Synthesis of N^1,N^1 -bis((6-methylpyridin-2-yl)methyl)ethane-1,2-diamine (6-Me₂-uns-penp):
N-acetyl-6-Me₂-uns-penp (2.93 g, 9.3 mmol) was added to half-concentrated HCl (50 mL) and was heated under reflux for 24 hours. After cooling the mixture was washed with dichloromethane (50 mL) and the organic phase were separated. The aqueous solution was carefully brought to pH 12 and extracted with dichloromethane (4 x 25 mL). The organic fraction was combined and dried over anhydrous Na_2SO_4 . Filtration and removal of the solvent by rotary evaporation yielded the title compound as a light-yellow colored oil that crystallized to a solid in the refrigerator within 24h (2.40 g, 8.9 mmol, 96 %).

^1H NMR (CDCl_3 , 400 MHz) δ / ppm: 7.53 (t; 2H py-H), 7.33 (d, 2H py-H), 7.00 (d, 2H, py-H), 3.81 (s, 4H, $\text{CH}_2\text{-N-CH}_2$), 2.77 (t, 2H, $\text{CH}_2\text{-NH}_2$), 2.65 (t, 2H, $\text{CH}_2\text{-N}(\text{CH}_2)_2$), 2.50 (s, 6H, $\text{CH}_3\text{-py}$), 2.00 (s, 2H, NH_2). ^{13}C NMR (CDCl_3 , 400 MHz) δ / ppm: 159.3, 157.4, 136.3, 121.2, 119.6, 77.4 (CDCl_3), 60.8, 57.2, 39.5, 24.4.

6.4.1.4 Synthesis of the ligand N^1,N^1 -Dimethyl- N^2,N^2 -bis((6-methylpyridin-2-yl)methyl)-ethane-1,2-diamine(6-Me₂-Me₂uns-penp).

N,N-dimethylethylenediamine (0.88 g, 10 mmol) and 6-methyl-2-pyridinecarboxaldehyde (2.50 g, 20 mmol) were placed in dichloromethane (50 mL) in a 250 mL round-bottom flask. NaBH(OAc)₃ (5.98 g, 28 mmol) was added and the solution was stirred at room temperature for 24 hours. The reaction was quenched by the addition of a saturated solution of NaHCO₃ (40 mL). The organic layer was separated and the aqueous layer was extracted with ethylacetate (3 × 20 mL). The organic fractions were combined and dried over anhydrous Na₂SO₄. Filtration and removal of the solvent by rotary evaporation yielded the title compound as a light-yellow-colored oil that crystallized to a solid in the refrigerator within 24h (2.86 g, 9.6 mmol, 96 %).

¹H NMR (CDCl₃, 400 MHz) δ / ppm: 7.54 (t, 2H, py-H), 7.31 (d, 2H, py-H), 6.99 (d, 2H, py-H), 3.81 (s, 4H, CH₂-N-CH₂), 2.76 (m, 2H, (CH₂)₂-N-CH₂), 2.71 (m, 2H, CH₂-N-(CH₃)₂), 2.52 (s, 6H, py-CH₃), 2.31 (s, 6H, -NCH₃). ¹³C NMR (CDCl₃, 400 MHz) δ / ppm: 159.3, 157.1, 136.7, 121.5, 119.9, 77.3 (CDCl₃), 60.5, 55.9, 50.6, 44.2, 24.3.

6.4.1.5 Synthesis of the ligand N^1 -(Propane-2-ylidene)- N^2,N^2 -bis((pyridin-2-yl)methyl)-ethane-1,2-diamine (Imine-uns-penp).

The ligand imine-uns-penp was prepared in a similar template reaction as described below for compound **4**. The starting ligand uns-penp was prepared according to published procedures and purified using Kugelrohr distillation.⁵⁵

6.4.2 Complex Synthesis

6.4.2.1 Synthesis of the complex [Fe(6-Me₂tmpa)(NCS)₂].

An ethanol solution (5 mL) of 6-Me₂tmpa (159 mg; 0.5 mmol) was added to a solution of [Fe(py)₄(NCS)₂] (244 mg; 0.5 mmol) in methanol (10 mL). A yellow precipitate soon formed which was collected by filtration, washed with ethanol and dried under vacuum.

Yield: 193 mg (79%). Anal. Calcd for $\text{FeC}_{22}\text{H}_{22}\text{N}_6\text{S}_2$: C, 53.88; H, 4.52; N, 17.14. Found: C, 53.33; H, 4.43; N, 17.25. IR (KBr, cm^{-1}): 3451.6; 2915.9, 2072.0 (NCS); 2062.3 (NCS); 1601.9; 1463.6.

6.4.2.2 Synthesis of the complex $[\text{Fe}(\text{6-Me}_2\text{pmea})(\text{NCS})_2]$ (1).

An ethanol solution (5 mL) of 6-Me₂pmea (166 mg; 0.5 mmol) was added to a solution of $[\text{Fe}(\text{py})_4(\text{NCS})_2]$ (244 mg; 0.5 mmol) in methanol (10 mL). An orange precipitate soon formed, which was collected by filtration, washed with ethanol and dried under vacuum.

Yield: 189 mg (75%). Anal. Calcd for $\text{FeC}_{23}\text{H}_{24}\text{N}_6\text{S}_2$: C, 54.76; H, 4.80; N, 16.66. Found: C, 54.57; H, 4.74; N, 16.84. IR (KBr, cm^{-1}): 3438.6; 2045.4, 2073.3 (NCS), 2061.3 (NCS); 1603.1; 1448.2.

6.4.2.3 Synthesis of the complex $[\text{Fe}(\text{6-Me}_2\text{-uns-penp})(\text{NCS})_2]$

An ethanol solution (5 mL) of 6-Me₂-uns-penp (68 mg; 0.25 mmol) was added to a solution of $[\text{Fe}(\text{py})_4(\text{NCS})_2]$ (122 mg; 0.25 mmol) in methanol (10 mL). The orange solution was allowed to stand overnight and dark yellow crystals were obtained, which were not suitable for X-ray diffraction studies. The crystalline material was collected by filtration, washed with ethanol and dried under vacuum.

Yield: 86 mg (78%). Anal. Calcd for $\text{FeC}_{18}\text{H}_{22}\text{N}_6\text{S}_2$: C, 48.87; H, 5.01; N, 19.00. Found: C, 48.77; H, 4.99; N, 19.99. IR (KBr, cm^{-1}): 3297.5; 2932.7, 2081.0 (NCS); 2069.0 (NCS); 1601.6; 1455.1.

6.4.2.4 Synthesis of the complex $[\text{Fe}(\text{6-Me}_2\text{-Me}_2\text{uns-penp})(\text{NCS})_2]$ (2).

A suspension of $[\text{Fe}(\text{py})_4(\text{NCS})_2]$ (183 mg; 0.3 mmol) in acetone (5 mL) was added dropwise to a solution of the ligand 6-Me₂-Me₂uns-penp (100 mg; 0.3 mmol) in acetone (5 mL). The resulting clear solution was stirred for 50 minutes. No precipitate formed immediately, so the red solution was added to 50 mL diethyl ether and a brown-yellow powder was obtained. The precipitate was filtered, washed with ether and dried under vacuum. An orange powder was obtained. Yellow crystals suitable for X-ray characterization were obtained by slow diffusion of ether into a solution of acetone.

Yield: 113 mg (31%). Anal. Calcd for $\text{FeC}_{20}\text{H}_{26}\text{N}_6\text{S}_2$: C, 51.06; H, 5.57; N, 17.86. Found: C, 50.16; H, 5.48; N, 18.51%. IR (KBr, cm^{-1}): 3451.2, 3008.1; 2839.6; 2072.6 (NCS); 2053.9 (NCS); 1601.5; 1575.0; 1458.3.

6.4.2.5 [Fe(Me₂uns-penp)(NCS)₂] (3).

A solution of $[\text{Fe}(\text{py})_4(\text{NCS})_2]$ (307 mg; 0.63 mmol) in methanol (10 mL) was added dropwise to a solution of the ligand Me₂uns-penp (170 mg; 0.63 mmol) in methanol (10 mL) and stirred for 1.5 hours. After a few minutes a yellow precipitate began to form and a yellow powder was obtained. The precipitate was filtered, washed with methanol and dried under vacuum. Yellow crystals suitable for X-ray characterization were obtained by slow diffusion of ether into a solution of methanol.

Yield: 196 mg (71%). Anal. Calcd for $\text{FeC}_{18}\text{H}_{22}\text{N}_6\text{S}_2$: C, 48.87; H, 5.01; N, 19.00. Found: C, 47.41; H, 4.85; N, 19.66%. IR (KBr, cm^{-1}): 3451.3, 2990.0; 2847.7; 2061.4 (NCS); 1600.1; 1570.1; 1440.2.

6.4.2.6 [Fe(imine-uns-penp)(NCS)₂] (4).

A suspension of $[\text{Fe}(\text{py})_4(\text{NCS})_2]$ (266 mg; 0.75 mmol) in acetone (5 mL) was added dropwise to a solution of the ligand uns-penp (219 mg; 0.78 mmol) in acetone (5 mL) and stirred for 7 hours. This variation of the usual 1:1 ratio was chosen to avoid recrystallization of the precursor complex. Slowly a green-yellow powder formed. The precipitate was filtered, washed with ether and dried under vacuum. Yellow crystals suitable for X-ray characterization were obtained by slow diffusion of ether in a solution of acetone.

Yield: 183 mg (54%). Anal. Calcd for $\text{FeC}_{19}\text{H}_{22}\text{N}_6\text{S}_2$: C, 50.22; H, 4.88; N, 18.50. Found: C, 50.37; H, 4.90; N, 18.59%. IR (KBr, cm^{-1}): 3442.4, 2887.8; 2861.8; 2071.2 (NCS); 2068.3 (NCS); 1654.3 (imine); 1601.3; 1571.5; 1441.8; 1434.1.

6.4.2.7 [Fe(TMGS-uns-penp)(NCS)₂] (5).

A suspension of [Fe(py)₄(NCS)₂] (300 mg; 0.66 mmol) in acetone (5 mL) was added dropwise to a solution of the ligand TMGS-uns-penp (200 mg; 0.66 mmol) in acetone (5 mL) and stirred for 1 hour. No precipitate from the brown solution formed immediately, so the solution was added to 40 mL diethyl ether and a brown-yellow powder was obtained. The precipitate was filtered, washed with ether and dried under vacuum. Dark-yellow crystals suitable for X-ray characterization were obtained by slow diffusion of ether in a solution of acetone.

Yield: 89 mg (43%). Anal. Calcd for FeC₂₁H₂₈N₈S₂: C, 49.22; H, 5.51; N, 21.87. Found: C, 46.20; H, 5.03; N, 21.65%. IR (KBr, cm⁻¹): 3451.1, 2922.3; 2062.6 (NCS); 1618.6; 1603.5; 1571.9; 1440.0.

6.4.3 X-Ray

The X-ray crystallographic data of complexes **1** and **2** were collected on a Gemini S-Ultra single crystal CCD diffractometer from Oxford Diffraction equipped with a CryojetHT-temperature system. Cu-K_α radiation ($\lambda = 1.54184 \text{ \AA}$) and a graphite monochromator were used. The crystallographic data of complexes **3**, **4** and **5** were collected on a STOE IPDS-diffractometer equipped with a low temperature system (Karlsruher Glastechnisches Werk). Mo-K_α radiation ($\lambda = 0.71073 \text{ \AA}$) and a graphite monochromator. Table 6-1 summarizes the crystal parameters as well as some details of the data collections and the structure refinements of all crystals. Semiempirical absorption corrections from equivalents (Multiscan) were carried out with the data of **1** and **2** using the program SCALE 3 ABSPACK from the CrysAlisPro program suite²⁴⁴; no absorption corrections were applied to the data sets of **3**, **4** and **5**. The structures were solved by direct methods with SHELXS97 and refined by using full-matrix least squares methods with SHELXL97.²⁴⁵⁻²⁴⁶ All non-hydrogen atoms were refined anisotropically.

Crystallographic data for the structures reported in this paper have been deposited with the Cambridge Crystallographic Data Center as supplementary publication no. CCDC-870725 for **1**, CCDC-870726 for **2**, CCDC-870727 for **3**, CCDC-870728 for **4** and CCDC-870729 for **5**. Copies of the data can

be obtained, free of charge from The Cambridge Crystallographic Data Center via www.ccdc.cam.ac.uk/data_request/cif.

6.4.4 *Magnetic susceptibility measurements*

Magnetic susceptibility measurements were performed using a Quantum Design MPMS-5S squid magnetometer. Each sample (~10-20 mg) was mounted on a plastic straw before being introduced into the squid magnetometer. DC magnetization measurements were performed in a field of 0.1 T, from 5 to 300 K (heating mode) and from 300 to 5 K (cooling mode). For each sample the total measuring time was 20 h. Corrections for the diamagnetism of the sample were calculated using Pascal's constants.

6.4.5 *Mössbauer Spectroscopy*

Mössbauer spectra were recorded using a conventional spectrometer of the Fa. Wissel GmbH in the constant acceleration mode. The temperature could be maintained between 6K and 400 K by a closed-cycle cryostat unit of Advanced Research Systems Inc. The sample holder was mounted on the tip of the second stage heat station of the expander unit DE204SF inside a radiation shield and a vacuum shroud. The expander unit was decoupled from the vibrations of the compressor ARS-4HW by a DMX20-41 interface. The temperature was controlled by a Lakeshore 331S unit. The windows of the vacuum shroud were made of mylar foils. The spectra were analyzed by least-square fits using a Lorentzian line shape with the program WinNormus-for-Igor Version 2.0. The isomer shifts are given relative to an α -iron at room temperature.

7 Chelate ring size and spin-crossover in iron(II) complexes

7.1 Effect of chelate ring size in iron(II) thiocyanate complexes with tetradentate tripyridyl-alkylamine tripodal ligands

This work will be submitted in the Journal of Inorganic Chemistry

Leibold, M., Kisslinger, S., Heinemann, F. W., Hampel, F., Ichiyanagi, Y., Klein, M., Renz, F., Toftlund, H., Brehm, G., Schneider, S., Reiher, M. and Schindler, S.. *Inorg. Chem.* **2011**, ready for submission.

The spin crossover phenomenon in iron(II)-compounds is well known and has been extensively studied during the last twenty years to gain better understanding of the electronic structure and properties of such transition metal complexes and due to their possible applications in molecular electronics.^{34-35, 222-223} The high-spin (HS, 5T_2) to low-spin (LS, 1A_1) transitions in iron(II) complexes can be induced by changes in temperature or pressure and by light irradiation. This effect is well documented and summarized in several articles.^{29-32, 42, 68, 71-72, 78, 224-232} Further some of the studied iron(II) complexes displayed a LIESST effect (light-induced excited spin state trapping effect), published in several works.³⁰⁻³²

Observations, that the spin state is quite sensitive to small changes of the ligand field, caused intensive research work on modifications of the ligands surrounding the metal. Iron(II) complexes with tris(2-pyridylmethyl)amine (tmpa, Figure 7-1; abbreviated as tpa in the literature as well) as a ligand proved as being quite interesting and useful in these studies (in addition with coligands such as thiocyanate).²³³ Modifications of the iron/tmpa system produced ligands such as N,N-bis[(2-pyridyl)methyl]-2-(2-pyridyl)ethylamine (pmea, Figure 7-1). In this ligand one of the chelate ring sizes in the complex has been changed.

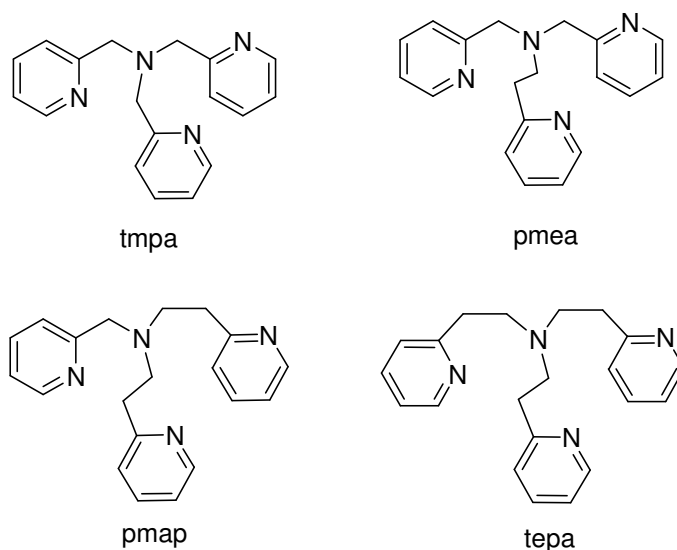


Figure 7-1: Abbreviations used for tripodal ligands: tris(2-pyridylmethyl)amine (tmpa), N²,N²-bis[(2-pyridyl)methyl]-2-(2-pyridyl)ethylamine (pmea), N²,N²-bis[2-(2-pyridyl)ethyl]-(2-pyridyl)methylamine (pmap) and tris[2-(2-pyridyl)ethyl]amine (tepa).

7.2 Results and Discussion

7.2.1 Synthesis of Ligands and complexes.

The ligands were synthesized according to published procedures.^{53, 67, 247, 267-269} The iron(II) complexes [FeL(NCS)₂] (L = pmea, pmap, tepa and tmpa) were obtained as yellow to brown powders after mixing the corresponding ligand with [Fe(py)₄(NCS)₂] dissolved in acetonitrile in a stoichiometric ratio. Crystals suitable for X-ray structural characterization were obtained for [Fe(pmea)(NCS)₂] (**2**), [Fe(pmap)(NCS)₂] (**3**) and [Fe(tepa)(NCS)₂] (**4**) by re-crystallization of the powders using the diffusion method described in the experimental section. In contrast to the crystals mentioned above [Fe(tmpa)(NCS)₂] (**1**) was obtained by slow diffusion of ether into a mixed solution of water and ethanol. However, only enough material was obtained to allow the crystallographic characterization of this complex. As discussed above, detailed studies on the iron(II) iso-thiocyanate complexes of tmpa are reported in the literature and more recently the crystal structures of a series of these complexes were described by Toftlund and coworkers and by Li et al.^{78, 232, 260} However, for completion and due to the fact that the structure of **1** reported herein does not contain additional solvent molecules we include this result in our work presented here. The molecular structure of [Fe(tmpa)(NCS)₂]

is presented in Figure 7-2. Crystallographic data and selected bond lengths and angles are given in Tables 7-1 and 7-2. On coordination of tmpa to iron ions, three fused five-membered chelate rings are formed.

If the carbon chain length of tmpa is increased by an insertion of pyridineethyl instead of pyridinemethyl groups, the ligands N,N-bis[(2-pyridyl)methyl]-2-(2-pyridyl)ethylamine (pmea), N,N-bis[2-(2-pyridyl)ethyl]-(2-pyridyl)methylamine (pmap) and tris[2-(2-pyridyl)ethyl]amine (tepa) are obtained (Figure 7-1). The molecular structure of **2**, **3** and **4** are presented in Figures 7-3, 7-4 and 7-5 respectively. Crystallographic data and selected bond lengths as well as angles are given in Tables 7-1 and 7-2.

The iron(II) cations in all four complexes are coordinated by six nitrogen donor atoms. Two of them belong to the two iso-thiocyanate ligands and four of them to the tripodal ligand. The iron-nitrogen bond distances adjoining to the iso-thiocyanates are shorter than those adjoining to the pyridines and the aliphatic amino groups (see Table 7-2). This may be due to electrostatic attraction in the case of thiocyanate as well as due to different hybridizations and π -acceptor abilities of the pyridine and aliphatic amino groups. The coordination geometry of the iron center is described best as distorted octahedral, because N-Fe-N angles between *cis* and *trans* nitrogen atoms deviate strongly from the values 90° and 180° as expected for an ideal octahedron (see Table 7-3). The reason for this distortion is a steric strain, which is a consequence of the coordination to the tripodal ligand; especially a meridional strain exists, which occurs, if two chelate rings have to be in the same plane, as already described in the literature.^{30, 270} The strain is stronger, if two six-membered chelate rings are in the same plane, because of the difficulty to combine the donor atoms of the five-membered rings in *trans* position to each other, considering the limited length of the methyl group between the aliphatic amine and the pyridine.

Models show a *cis* arrangement of the two thiocyanate groups as the only possibility in an octahedral complex with a tripodal ligand. *Cis*-diiso-thiocyanato iron(II) complexes with pmea and pmap as ligands feature chelate rings of different sizes.

Models show a *cis* arrangement of the two thiocyanate groups as the only possibility in an octahedral complex with a tripodal ligand. *Cis*-diiso-thiocyanato iron(II) complexes with pmea and pmap as ligands feature chelate rings of different sizes.

Table 7-2 shows iron-nitrogen bond distances. Throughout all examined examples the bonds to six membered chelate rings are shorter than five-membered rings. This can clearly be seen in the case of **1**. This fact is still true for **2** and **3**, but in these cases all the bond distances increase strongly, again because of the steric strain. The more pyridineethyl groups are integrated in the ligand, the more the steric strain. Thiocyanate groups of the complexes are nearly linear, while the Fe-N-C group is considerably bent (see Table 7-2). This effect increases in the series of **1**, **2** and **3**. Furthermore a Fe-N-C group involving the thiocyanate standing *trans* to a pyridine group is more bent than the same group involving the thiocyanate standing *trans* to the aliphatic group as found for every complex (see Table 7-4).

7. Chelate ring size and spin-crossover in iron(II) complexes

Table 7-1: Selected crystallographic data, unit cell parameters, and values of [Fe(tpma)(NCS)₂] (**1**), [Fe(pmea)(NCS)₂] (**2**), [Fe(pmap)(NCS)₂] (**3**) and [Fe(tepa)(NCS)₂] (**4**).

Compound	(1)	(2a)	(2b)	(2c)	(3)	(4)
Empiric Formular	C ₂₀ H ₁₈ FeN ₆ S ₂	C ₂₁ H ₂₀ FeN ₆ S ₂	C ₂₁ H ₂₀ FeN ₆ S ₂	C ₂₁ H ₂₀ FeN ₆ S ₂	C ₂₂ H ₂₂ FeN ₆ S ₂	C ₂₃ H ₂₄ FeN ₆ S ₂
Molar mass	462.37	476.40	476.40	476.40	490.43	504.45
Temperature [K]	173(2) K	125(2)	205(2)	295(2)	173(2)	173(2)
Crystal size [mm]	0.30 x 0.30 x 0.20	0.86 x 0.26 x 0.12	0.50 x 0.42 x 0.35	0.50 x 0.42 x 0.35	0.30 x 0.20 x 0.20	0.35 x 0.30 x 0.30
Crystal System	monoclinic	orthorhombic	orthorhombic	orthorhombic	orthorhombic	monoclinic
	P2 ₁ /c	Pna2 ₁	Pna2 ₁	Pna2 ₁	Pna2 ₁	P2 ₁
a [Å]	13.5652 (2)	14.989(2)	15.115(2)	15.237(2)	15.5048(5)	8.1210(2)
b [Å]	20.7575(4)	10.438(1)	10.751(2)	10.817(1)	10.8670(3)	15.1714(3)
c [Å]	15.1192(3)	13.341(3)	13.592(2)	13.678(2)	13.4399(4)	18.8912(6)
α [°]	90	90	90	90	90	90
β [°]	96.9300(10)	90	90	90	90	90.5520(9)
γ [°]	90	90	90	90	90	90
V [Å ³]	4226.16(13)	2087.3(6)	2208.7(6)	2544.2(5)	2264.50(12)	2327.42(10)
Z	8	4	4	4	4	4
ρ _{calcd.} [mg·m ⁻³]	1.453	1.516	1.433	1.404	1.439	1.440
μ [mm ⁻¹]	0.930	0.944	0.892	0.874	0.872	0.851
F(000)	1904	984	984	984	1016	1048
Scan range θ [°]	1.51 to 27.48	2.38 to 26.98	2.32 to 27.00	2.31 to 26.99	2.41 to 27.50	1.72 to 27
Index ranges	-17≤h≤17	-19 ≤ h ≤ 19	-19 ≤ h ≤ 19	-19 ≤ h ≤ 19	-20≤ h≤ 20	-10sh≤10
	-25≤k≤26	-13 ≤ k ≤ 13	-13 ≤ k ≤ 13	-13 ≤ k ≤ 13	-14≤ k≤ 14	-19≤k≤16
	-19≤l≤19	-17 ≤ l ≤ 17	-17 ≤ l ≤ 17	-17 ≤ l ≤ 17	-17≤ l≤ 17	-24≤l≤24
Reflections collected	17685	5429	5740	5126	4939	9150
Unique reflections	9672	4540	4817	4918	4939	5312
Reflections / > 2σ(I)	5581	0.0544	0.0231	0.0332	3684	4029
R _{int}	0.0473	0.0533	0.0231	0.0332	0.0000	0.0230
Data /restraints/parameters	9672 / 0 / 523	4540/1/272	4817/1/272	4918/1/348	4939 / 1 / 281	5312 / 0 / 289
Goodness of fit F ²	0.977	1.052	1.033	1.024	0.986	1.038
Final R indices (all data)	R1 = 0.0423	R1 = 0.0458	R1 = 0.0445	R1 = 0.0524	R1 = 0.0429	R1 = 0.0568
	wR2 = 0.0927	wR2 = 0.0987	wR2 = 0.0768	wR2 = 0.1035	WR2 = 0.0872	R2 = 0.0816
R indices [I > 2σ(I)]	R1 = 0.1084	R1 = 0.0644	R1 = 0.0727	R1 = 0.0913	R1 = 0.0760	R1 = 0.0568
	wR2 = 0.1210	wR2 = 0.1080	wR2 = 0.0848	wR2 = 0.1204	WR2 = 0.0984	wR2 = 0.0914
Largest diff. peak/hole [e·Å ⁻³]	0.979/-0.402	0.778/-0.510	0.245/-0.235	0.244/-0.277	0.418 /-0.300	0.461 /-0.594

Table 7-2: Selected bond lengths [Å] and angles [°] for compounds **1-4**.

[Fe(tmpa)(NCS)₂] (1)				[Fe(pmea)(NCS)₂] (2a)			
	2.099(3)	N(10)-Fe(1)-N(62)	94.6(1)	Fe(1)-N(5)	1.933(4)	N(5)-Fe(1)-N(1)	92.5(5)
Fe(1)-N(10)	2.110(3)	N(32)-Fe(1)-N(62)	170.2(1)	Fe(1)-N(6)	1.966(3)	N(2)-Fe(1)-N(1)	92.5(4)
Fe(1)-N(32)	2.210(3)	N(20)-Fe(1)-N(82)	176.2(2)	Fe(1)-N(3)	2.005(4)	N(5)-Fe(1)-N(2)	92.6 (7)
Fe(1)-N(62)	2.222(3)	N(10)-Fe(1)-N(82)	89.4(1)	Fe(1)-N(1)	1.991(3)	N(6)-Fe(1)-N(3)	89.3(6)
Fe(1)-N(82)	2.227(2)	N(32)-Fe(1)-N(82)	88.1(1)	Fe(1)-N(2)	1.975(3)	N(3)-Fe(1)-N(2)	86.9(8)
Fe(1)-N(1)	2.292(3)	N(62)-Fe(1)-N(82)	86.0(1)	Fe(1)-N(4)	2.044(4)	N(1)-Fe(1)-N(3)	173.3(5)
N(1)-C(1)	1.469(5)	N(20)-Fe(1)-N(1)	101.5(1)	N(1)-C(11)	1.358(6)	N(5)-Fe(1)-N(4)	171.8(6)
N(1)-C(4)	1.496(5)	N(10)-Fe(1)-N(1)	164.6(1)	N(1)-C(21)	1.348(5)	N(6)-Fe(1)-N(4)	96.6(5)
N(20)-Fe(1)-N(10)	93.3(2)	N(32)-Fe(1)-N(1)	81.5(1)	N(5)-Fe(1)-N(6)	87.6(5)	N(2)-Fe(1)-N(6)	179.6(7)
N(20)-Fe(1)-N(32)	94.4(1)	N(62)-Fe(1)-N(1)	89.5(1)	N(5)-Fe(1)-N(3)	93.4(4)	N(1)-Fe(1)-N(4)	80.7(5)
N(10)-Fe(1)-N(32)	93.1(1)	N(82)-Fe(1)-N(1)	76.0(1)	N(2)-Fe(1)-N(4)	83.3(4)	N(1)-Fe(1)-N(6)	87.6(5)
N(20)-Fe(1)-N(62)	91.1(1)			N(3)-Fe(1)-N(4)	93.7(6)		
[Fe(pmea)(NCS)₂] (2c)				[Fe(pmap)(NCS)₂] (3)			
Fe(1)-N(5)	2.067(5)	N(6)-Fe(1)-N(1)	89.4(6)	Fe(1)-N(20)	2.099(3)	N(20)-Fe(1)-N(62)	91.2(1)
Fe(1)-N(6)	2.118(4)	N(3)-Fe(1)-N(1)	163.5(6)	Fe(1)-N(10)	2.110(3)	N(10)-Fe(1)-N(62)	94.6(1)
Fe(1)-N(3)	2.187(5)	N(5)-Fe(1)-N(2)	91.9(7)	Fe(1)-N(32)	2.210(3)	N(32)-Fe(1)-N(62)	170.2(1)
Fe(1)-N(1)	2.190(4)	N(6)-Fe(1)-N(2)	173.4(9)	Fe(1)-N(62)	2.222(3)	N(20)-Fe(1)-N(82)	176.2(2)
Fe(1)-N(2)	2.201(4)	N(3)-Fe(1)-N(2)	86.9(8)	Fe(1)-N(82)	2.227(2)	N(10)-Fe(1)-N(82)	89.5(1)
Fe(1)-N(4)	2.264(4)	N(1)-Fe(1)-N(2)	91.5(5)	Fe(1)-N(1)	2.292(3)	N(32)-Fe(1)-N(1)	81.5(1)
N(1)-C(15)	1.339(6)	N(5)-Fe(1)-N(4)	164.6(7)	N(1)-C(1)	1.469(5)	N(62)-Fe(1)-N(1)	89.5(1)
N(1)-C(11)	1.349(7)	N(6)-Fe(1)-N(4)	98.0(7)	N(1)-C(4)	1.496(5)	N(82)-Fe(1)-N(1)	76.0(1)
N(5)-Fe(1)-N(6)	94.4(8)	N(3)-Fe(1)-N(4)	88.7(7)	N(20)-Fe(1)-N(10)	93.3(2)	N(10)-Fe(1)-N(32)	93.1(2)
N(5)-Fe(1)-N(3)	100.4(8)	N(1)-Fe(1)-N(4)	74.9(5)	N(32)-Fe(1)-N(82)	88.1(1)	N(20)-Fe(1)-N(1)	101.5(1)
N(6)-Fe(1)-N(3)	90.4(6)	N(2)-Fe(1)-N(4)	76.0(5)	N(62)-Fe(1)-N(82)	86.0(1)	N(10)-Fe(1)-N(1)	164.6(1)
N(5)-Fe(1)-N(1)	96.1(7)			N(20)-Fe(1)-N(32)	94.4(1)		

[Fe(tepa)(NCS)₂] (4)			
Fe(1)-N(2)	2.1193(16)	N(3)-Fe(1)-N(30)	85.26(6)
Fe(1)-N(3)	2.1330(16)	N(10)-Fe(1)-N(30)	96.81(6)
Fe(1)-N(10)	2.2324(15)	N(2)-Fe(1)-N(20)	89.80(6)
Fe(1)-N(30)	2.2359(16)	N(3)-Fe(1)-N(20)	87.86(6)
Fe(1)-N(20)	2.2364(17)	N(10)-Fe(1)-N(20)	90.19(6)
Fe(1)-N(1)	2.2704(15)	N(30)-Fe(1)-N(20)	172.55(6)
N(1)-C(27)	1.488(3)	N(2)-Fe(1)-N(1)	171.59(6)
N(1)-C(37)	1.492(2)	N(3)-Fe(1)-N(1)	98.55(6)
N(2)-Fe(1)-N(3)	89.76(7)	N(10)-Fe(1)-N(1)	84.14(6)
N(2)-Fe(1)-N(10)	87.60(6)	N(30)-Fe(1)-N(1)	86.45(6)
N(3)-Fe(1)-N(10)	176.72(6)	N(20)-Fe(1)-N(1)	91.76(6)
N(2)-Fe(1)-N(30)	93.02(6)		

Table 7-3: Range of N-Fe-N angles between cis and trans nitrogen atoms.

complex	range of N-Fe-N angles between cis nitrogen atoms	range of N-Fe-N angles between trans nitrogen atoms
[Fe(tmpa)(NCS) ₂] (1) HS-LS	82.5(1) - 97.7(1)	165.5(1) - 178.6(10)
	77.20(9)-107.3(1)	167.07(10)-168.6(1)
[Fe(pmea)(NCS) ₂] (2a) LS	80.7(5)-96.6(5)	171.8(6)-173.3(5)
[Fe(pmea)(NCS) ₂] (2c) HS	75.8(3) – 100.3(3)	164.1(3) – 173.3(3)
[Fe(pmap)(NCS) ₂] (3) HS	76.0(1) – 101.5(1)	164.6(1) – 176.2(2)
[Fe(tepa)(NCS) ₂] (4) HS	84.14(6) – 98.55(6)	171.59 – 176.72(6)

Table 7-4: Fe-C-N angles thiocyanate trans to aliphatic amino and pyridine group.

complex	Fe-C-N angle (thiocyanate trans to aliphatic amino group)	Fe-C-N angle (thiocyanate trans to pyridine group)
[Fe(tmpa)(NCS) ₂] (1) HS-LS	168.6(1)	167.1(1)
	178.1(1)	175.3(1)
[Fe(pmea)(NCS) ₂] (2a) LS	179.6(7)	171.8(6)
[Fe(pmea)(NCS) ₂] (2c) HS	173.4(9)	164.6(7)
[Fe(pmap)(NCS) ₂] (3) HS	172.1(3)	164.6(3)
[Fe(tepa)(NCS) ₂] (4) HS	166.3(6)	150.5(5)

7.2.1.1 [Fe(tmpa)(NCS)₂] (**1**).

1, measured at 173 K, crystallizes in a monoclinic P2₁/c structure is pictured on Figure 7-2. **1** forms three five-membered chelate rings and the iron center is surrounded by three pyridine and two isothiocyanate groups forming a distorted octahedral structure. The complex has an average Fe1-N

bond length of 1.97 Å and an average Fe2-N bond length of 2.16 Å. The bond lengths were 1.98/ 1.97/ 1.98 Å (Fe1-N_{py} groups) and 2.001 Å (Fe1-N_{amine} group), respectively, the bond lengths of the SCN-Fe1 groups are 1.936/ 1.944 Å. The bond lengths were 2.21/ 2.19/ 2.17 Å (Fe2-N_{py} groups) and 2.23 Å (Fe2-N_{amine} group), the bond lengths of the SCN-Fe2 groups are 2.03/ 2.09 Å. Bond angles of N_{amine}-Fe-N_{pyridine} groups found in the literature is average 77° for HS- and 84° for LS- complexes.^{68, 72, 260-265} Thus 83.12°/ 82.53° / 84.77° found for the angles of the three N_{amine}-Fe1-N_{pyridine} groups clearly indicate LS-state, whereas the 77.69°/ 78.76°/ 77.20° found for the three N_{amine}-Fe2-N_{pyridine} groups clearly indicate HS-state. The SCN-Fe1-NCS bond angle is 90.18° and is in agreement with the average LS- bond angle of 89° of the literature, whereas the SCN-Fe2-NCS bond angle is 97.95° and corresponds with the average HS-bond angle of 95° of the literature.²⁶⁰ Overall the different bond lengths and angles of Fe1 and Fe2 leave the conclusion of a LS-HS state at 173 K.

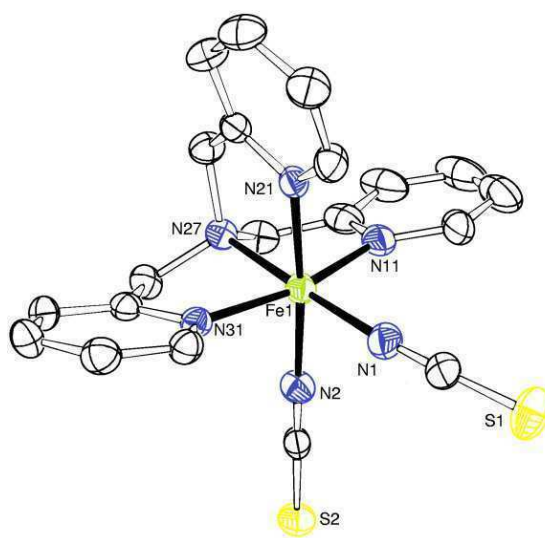


Figure 7-2: Molecular structure of [Fe(tpma)(NCS)₂] (**1**).

Toftlund and co-workers found two new phases of **1**, including solvent molecules of acetonitrile or ethanol within the molecular structure, resulting in a total of five known phases of this system.²⁶⁰ Toftlunds two new phases showed similar coordination geometries, as already described in the literature, but the Fe-N bond length differed significantly with temperature, reflecting a difference of spin-state.^{65, 68, 262-263, 271-272} Structural studies resulted in different types of intermolecular interactions within these phases. Toftlund and co-workers identified them as a hydrogen bond to the iso-

thiocyanate sulfur and π -stacking between pyridine groups. The bond length in both phases at room temperature were very similar namely 2.18 / 2.17 Å (Fe-N_{py} group) and 2.24/2.23 Å (Fe-N_{amine} group).²⁶⁰ Compared to the bond length mentioned above, a bond length of 2.06/ 2.10 Å (Fe-N_{py} group) and 2.12/2.16 Å (Fe-N_{amine} group) at 120 K differed highly. Furthermore Zheng and co-workers more recently investigated solvate effects with methanol in the tmpa system as well.⁷⁸ In contrary to **1** without solvate molecules, the solvate including complex crystallizes in a triclinic P-1 space group with average Fe-N bond lengths of 2.164/ 2.013 Å bond length at 298 K. If N_{amine}-Fe-N_{pyridine} bond angles of the Toftlund and Zheng group are compared with each other, the bond lengths and angles differ only marginal from each other for the same temperatures. Further Zheng and co-workers found a structure of **1** without solvent molecules. **1** there crystallizes in a monoclinic structure with the space group P2₁/c and an average Fe-N bond length of 1.963/ 1.957 Å at 120 K. Fe-NCS bond angles are at 92.8°, N_{amine}-Fe-N_{pyridine} bond lengths are at 81.3°/ 79.6°/ 78.9°. At 260 K a significant change in lengths and angles occurs. Bond lengths and angles as well as found LS- and HS- state correspond with our results and corresponds with the results for solvent including molecules, Toftlund and co-workers found.²⁶⁰

7.2.1.2 [Fe(pmea)(NCS)₂] (**2**).

Crystals of the complex with pmea as a ligand are measured at 125 K, 205 K and 225 K. **2** has two five-membered and one six-membered chelate ring and crystallizes in an orthorhombic Pna2₁ structure at all measured temperatures. **2** crystallizes in a facial arrangement of the bis(picoly)amine unit. The molecular structure **2** is shown in Figure 7-3. For **2** measured at 125 K we found an average Fe-N bond length of 1.985 Å. The N-Fe-N angles at 205 K depart from the optimal angles of 90° und 180° (see Table 7-2) with a range of 83.3 – 93.4 Å and 171.8 – 173.3 respectively. The crystals measured at 295 K show an average Fe-N bond length of 2.171. The N-Fe-N angles differ with a range of 74.9-100.4 Å and 163.5 – 179.6 Å respectively strongly from the optimal angle. In the literature the NCS-bond lengths for Fe(II) HS- complexes are reported between 2.04 and 2.14 Å.²⁶⁰ Fe-N bond lengths found for **2** lay between 2.067 Å and 2.118 Å at 295 K as can be seen in Table 7-2 and match

with other HS-complexes of the literature. Further bond angles of $N_{\text{amine}}\text{-Fe-}N_{\text{pyridine}}$ atoms indicate HS- or LS-status. In the literature 77° for HS-compounds and 84° for LS-compounds of Fe(II) five-membered ring complexes were reported.²⁶⁰ At 295 K the $N_{\text{amine}}\text{-Fe-}N_{\text{pyridine}}$ bond angles are found at 74.9° and 76.0° for the five-membered rings as well as 88.7° for the six-membered one. The first two are in accord to other publications for HS-complexes.²⁶⁰ The third difference to identify HS- and LS-components via crystal structure is to compare N-Fe-N angles between the two thiocyanate ligands. 95° indicates HS-state, as found in the literature, is very close to our angle (94.4°).

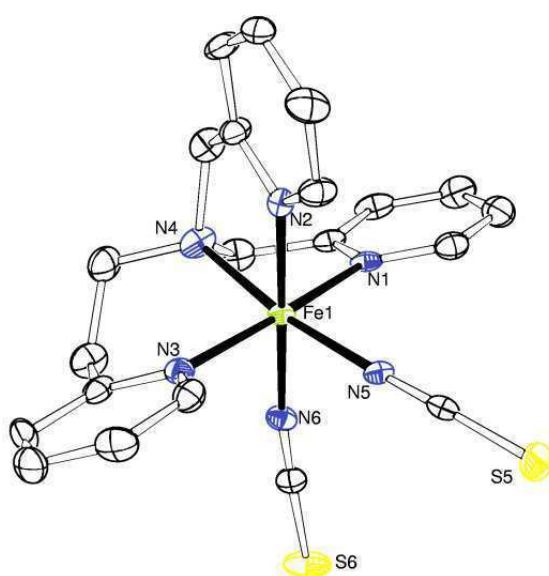


Figure 7-3: Molecular structure of $[\text{Fe}(\text{pmea})(\text{NCS})_2]$ (2).

At 205 K N-Fe bond lengths of the thiocyanate groups are found between 1.933 \AA and 1.966 \AA and are in agreement of literature data for Fe(II) LS-complexes (1.94 \AA to 1.96 \AA).²⁶⁰ Further, as mentioned above, the $N_{\text{amine}}\text{-Fe-}N_{\text{pyridine}}$ bond angle suggests HS- or LS- state. 80.7° and 83.3° were found for the five-membered ring parts, 88.7° for the six-membered one and at least one of the first two is very near to the 84° for LS- complexes found in the literature. The N-Fe-N angle of the thiocyanate groups lays at 87.6° and corresponds with the 89° found in the literature.²⁶⁰

New results of Zheng and co-workers show an orthorhombic structure with the space group $\text{Pc}2_1/n$ with average Fe-N bond length of 1.986 \AA with NCS-Fe bond lengths of 1.938 \AA and 1.971 \AA respectively at 120 K and a 2.174 \AA bond length with 2.060 \AA and 2.125 \AA for NCS-Fe bond lengths at 260 K.⁷⁸ $N_{\text{amine}}\text{-Fe-}N_{\text{pyridine}}$ bond lengths are found between 80.3° and 83.4° for five-membered rings and 94.1°

for the six-membered one at 120 K and 74.5°, 75.8° as well as 89.3° for 260 K. Bond lengths and angles as well as found LS- and HS- state correspond with our results; including the large angle and bond length for the six-membered ring. Interestingly a very short angle of one N_{amine}-Fe-N_{pyridine} group is found in both works for HS- (74.9° and 74.5°) and LS-form (80.7° and 80.3°). The thiocyanate N-Fe-N bond angles of the Zheng group are found at 87.9° (LS) and 94.3° (HS), which is nearly identical to our results and corresponds with other literature bond angles as well, although Li et al. found with the orthorhombic Pca2₁/n a different space group to our orthorhombic Pna2₁.

7.2.1.3 [Fe(pmap)(NCS)₂] (**3**).

3, pictured on Figure 7-4 and composed of two five-membered and one six-membered chelate ring, was measured at 173 K. **3** crystallizes in an orthorhombic Pna2₁ structure, shows an average bond length 2.15 Å and clearly predicates a HS-state.^{263, 265} N-Fe-N angles depart from the optimal angles of 90° und 180° (see Table 7-2) with a range of 81.5 – 94.6 Å and 170.2 – 176.2 respectively. NCS-bond lengths are found at 2.110 Å and 2.099 Å, K the N_{amine}-Fe-N_{pyridine} bond angles are found at 76.0° for the five-membered ring as well as 81.5° and 89.5° for the two six-membered chelate rings. One of the six-membered chelate rings has a very small angle compared to other six-membered rings found in the literature and in this work.^{72, 78} N-Fe-N angles between the two thiocyanate ligands lay at 93.3° and are in agreement with HS-states found in the literature.

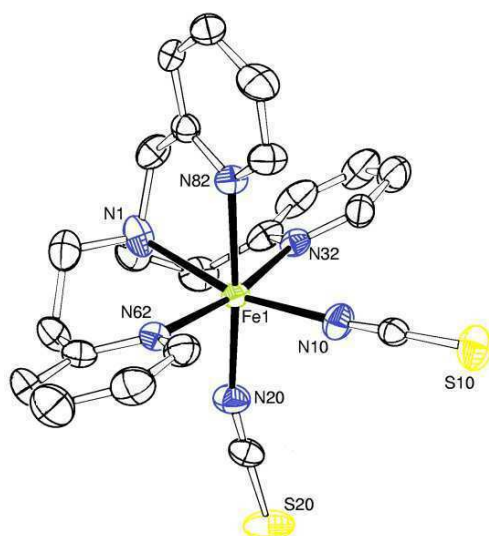


Figure 7-4: Racemic twin of [Fe(pmap)(NCS)₂] (**3**).

3 is meridionally arranged, in relation to the two six-membered rings, because of the force to reduce the meridional strain. The racemic twin of $[\text{Fe}(\text{pmap})(\text{NCS})_2]$ could be solved and refined for the molecular structure. According to this refinement there is a ratio of 40:60 for the two enantiomers. Measurements at lower temperatures show very similar results and no spin transition could be found. Mößbauer and magnetic measurements verified this result (see below).

7.2.1.4 $[\text{Fe}(\text{tepa})(\text{NCS})_2]$ (**4**).

4 is the last extension to the complexes **2** and **3** and forms three six-membered chelate rings (see Figure 7-5). This complex, as the other complexes of this series, shows a distorted octahedral coordination. **4** crystallizes in a monoclinic $P2_1$ structure. Average Fe-N bond lengths of the complex are at 2.171 Å and thus suggest a HS-state.^{263, 265} The N-Fe-N angles depart strongly from the optimal angles of 90° und 180° with a range of 84.14 – 96.81 Å and 171.59 – 172.55 Å respectively. The NCS-bond lengths are found at 2.1193 Å and 2.1330 Å and are in range of an iron(II) HS-complex (2.04 to 2.14 Å).²⁶⁰ The $\text{N}_{\text{amine}}\text{-Fe-N}_{\text{pyridine}}$ bond angles are found at 84.14°, 86.45° and 91.76° for the three six-membered chelate rings. N-Fe-N angles between the two thiocyanate ligands lay at 89.76° and are in agreement with HS-states found in the literature.

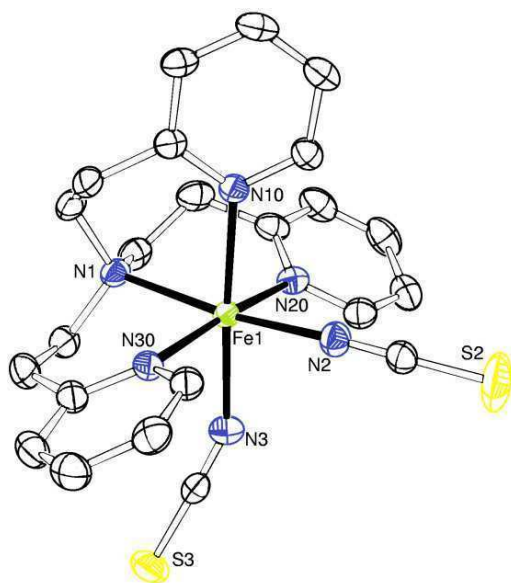


Figure 7-5: Molecular structure of $[\text{Fe}(\text{tepa})(\text{NCS})_2]$ (**4**).

Measurements at lower temperatures show very similar results and no spin transition could be found. Mößbauer and magnetic measurements verified this result (see below). In contrary to other complexes the NCS- groups are arranged in the most bended form, whereas the NCS- groups become almost linear with the decrease of six-membered chelate rings. (see Figures 7-1 - 7-4 and Table 7-4). The bond lengths of all three pyridine rings are a bit longer than those of the comparable **4** complex, which forms three five-membered chelate rings (see Table 7-2).

7.2.2 Mößbauer spectroscopy for [Fe(pmea)(NCS)₂] (**2**)

As described above, the spin crossover behavior of **1** has been discussed previously in the literature and will not be repeated herein.^{233, 247, 273-275} Spin crossover behavior was investigated for the complexes **2**, **3** and **4** instead. Whereas the complex compound **2** clearly exhibits spin crossover behavior, the complexes **3** and **4** do not (see results below). The Figures 7-6 to 7-10 and Table 7-5 show the results of the ⁵⁷Fe Mößbauer study on **2**. These results are in contrast to earlier results described in the literature, where only a temperature-constant intermediate spin was observed during magnetic measurements and no spin cross-over was suggested.²⁷⁶ Most likely this could have been caused by a decomposed ligand pmea. The new Mößbauer experiments were supported by IR measurements, published by Brehm et al. in 2006 and magnetic susceptibility measurements published by Zheng et al. 2010.^{75, 77} Brehm et al. found a spin cross-over from LS- to HS- states after temperature increase as evidenced by a reduction of the symmetric and antisymmetric N=CS-stretching frequencies from 2104/2117 cm⁻¹ (LS) to 2065/2075 cm⁻¹(HS). Further Brehm found a detectible shift due to motion of the pyridine skeleton. The two C=C stretching modes gave rise to two well-separated, moderately intense bands at 1571/1603 cm⁻¹ (HS) and 1572/ 1604 cm⁻¹. Within the Raman spectrum five bands in the range 50-100 cm⁻¹ could be seen from the LS complex, while the HS complex exhibited only one band. This facts repeated for wavenumbers up to about 500 cm⁻¹. Zheng et al. found a changing spin transition of **2** controlled by pressure.⁷⁷ The group found out, that spin transition moves progressively to a higher temperature range and the transition changes from a hysteresis to more and more gradual during external pressure increase.

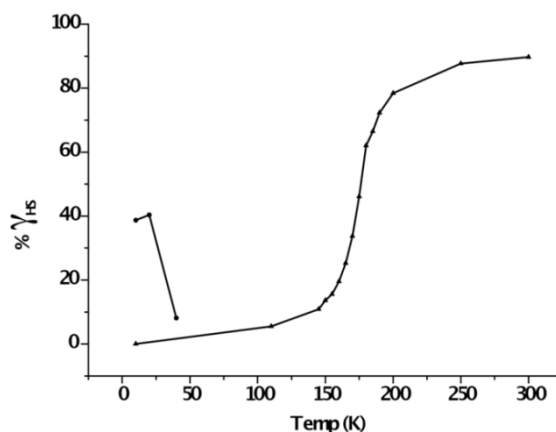


Figure 7-6: Temperature dependence of the HS and LS fits derived from ^{57}Fe Mößbauer spectra on $[\text{Fe}(\text{pmea})(\text{NCS})_2]$ (**2**) between 10 and 300 K.

Our new Mößbauer measurements show a doublet with isomer shift of 0.409 mm/s with a quadrupol split of 0.237 mm/s at 10 K. At 300 K a LS-doublet (IS = 0.290 mm/s; QS = 0.341 mm/s) is present with an area fraction of 10.2 %. In addition a doublet (IS = 0.880 mm/s; QS = 1.567 mm/s) is observed which is characteristic for an iron(II) in the high spin state. The Figures 7-7 to 7-10 and Table 7-5 show the thermal development of the two electronic HS- and LS- state. The thermal dependence of the HS fraction clearly indicates a thermally induced spin transition (see Figure 7-9). Below 100 K the compound is 100% in the LS state. Above 100 K a growing HS-fraction rises to a plateau around 250 K. This is supported by the magnetic measurement (see Figure 7-6). The compound shows at least one step in the transition. The fits in Figure 7-7 are derived from Mößbauer spectra observed between 10 and 300 K.

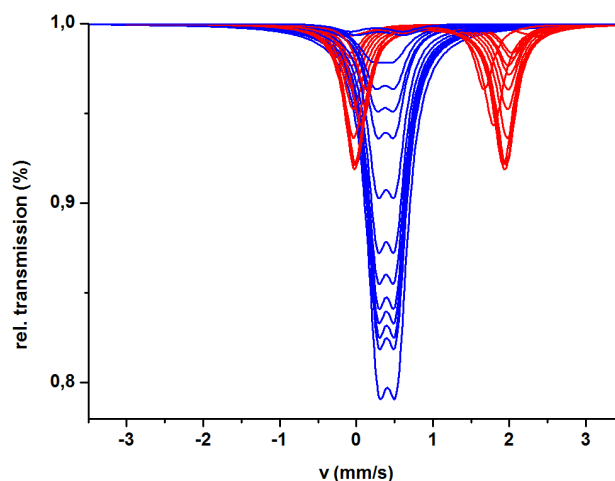


Figure 7-7: Temperature dependence of molar high spin ratio derived from ^{57}Fe Mößbauer spectra of $[\text{Fe}(\text{pmea})(\text{NCS})_2]$ (**2**) between 10 and 300 K and under continuous green light irradiation (514.5 nm; 20 mW/cm²) between 10 and 40 K indicating the presence of the LIESST effect.

As already described in the literature, a LIESST effect (light-induced excited spin state trapping effect) for the complex **1** was found.^{29, 231, 276} Yu et al. found a relaxation of HS(5T_2) \rightarrow LS(1A_1) occurring after warming the absorber to 50 K, after LIESST experimentation at 10 K. These results inspired experiments for LIESST effect for the related complex [Fe(pmea)(NCS)₂]. Those experiments reinforced this supposition. After radiating light into the complex at $T < 20$ K, a metastable HS state (5T_2) with nearly endless lifetime could be obtained. Irradiation into the absorption band of the LS-state of **2** executes the spin-permitted transition $^1A_1 \rightarrow ^1T_1$. A model of the LIESST effect is shown in Figure 7-8.

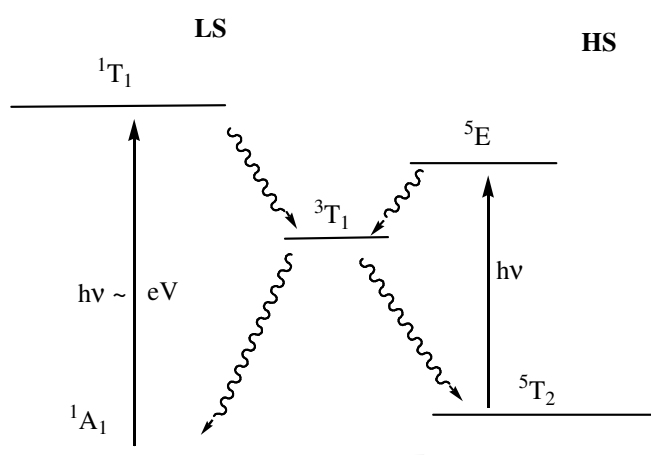


Figure 7-8: Model of the LIESST effect.

From this state two consecutive radiationless intersystem-crossing transitions occur, each with $\Delta S = 1$: $^1T_1 \rightarrow ^3T_1 \rightarrow ^5T_2$. The last state corresponds with a HS state. Here an optic pumping from LS- to HS- state can be seen. Important here is the fact, that the intersystem-crossing occurs faster than the relaxation of HS- to LS-state. Additionally the 3T_1 state is energetically lower, than the 1T_1 state, so a transition from $^3T_1 \rightarrow ^1A_1$ (LS-) state is possible. This branching ratio from 3T_1 to either 1A_1 ground-state or to the metastable 5T_2 state is ca. 1:4. Because the 3T_1 state is energetically lower than the 1T_1 state and lower than the 5E state, a rapid depopulation of the 5T_2 is possible only via photon absorption transferring first the system from the meta-stable 5T_2 state to the 5E state. Then two intersystem crossing transitions occur, each with $\Delta S = 1$: $^5E \rightarrow ^3T_1 \rightarrow ^1A_1$. The whole process can be considered as light-induced re-conversion to the LS state. If the intersystem crossing $\Delta S = 1$: $^5E \rightarrow ^3T_1 \rightarrow ^1A_1$ is faster than the relaxation of the LS state into the meta-stable HS state, 5T_2 , the LIESST effect is reversible. A theoretical study regarding the LIESST effect was also published by Kondo et al..²⁷⁷

Table 7-5: Temperature dependence of ^{57}Fe Mößbauer parameter **2** between 10 and 300 K (see pmea) and under continuous irradiation (see pmea*). The green light irradiation (514.5 nm; 20 mW/cm²) was performed at 10 K, 20K and 40K, while the effect of the red light irradiation (820 nm; 40 mW/cm²) was observed at 170 K, 175 K, 195 K, and 200 K.

pmea	Fe(II)-HS				Fe(II)-LS			
Temp.	IS	QS	A	W _s	IS	QS	A	W _s
K	mm/s	mm/s	%	mm/s	mm/s	mm/s	%	mm/s
300	0.8801	1.567	89.7	0.1664	0.2901	0.341	10.2	0.201
250	0.9251	1.738	87.7	0.1577	0.3162	0.34	12.3	0.240
200	0.9578	1.925	78.5	0.1601	0.3523	0.291	21.6	0.220
190	0.9603	1.964	72.3	0.1582	0.3729	0.2742	27.7	0.1749
185	0.9637	1.976	66.5	0.1632	0.3819	0.260	33.5	0.173
180	0.9676	1.980	62.0	0.1591	0.3861	0.244	38.0	0.156
175	0.9697	2.008	46.1	0.1569	0.3895	0.2433	53.9	0.1571
170	0.9695	2.016	33.7	0.1627	0.3904	0.2413	66.3	0.1563
165	0.9690	2.030	25.3	0.1635	0.3900	0.2421	74.7	0.1633
160	0.9761	2.048	19.5	0.1662	0.3934	0.2440	80.5	0.1619
155	0.9641	2.049	15.6	0.1641	0.3941	0.2485	84.4	0.1654
150	0.9893	2.092	13.6	0.1771	0.3974	0.2468	86.4	0.1646
145	0.9852	2.101	10.9	0.1703	0.3977	0.2462	89.1	0.1665
100	-	-	-	-	0.3967	0.2387	100	0.1564
10	-	-	-	-	0.4093	0.2369	100	0.1404
pmea*	Fe(II)-HS				Fe(II)-LS			
Temp.	IS	QS	A	W _s	IS	QS	A	W _s
K	mm/s	mm/s	%	mm/s	mm/s	mm/s	%	mm/s
200	0.9574	1.9275	78.14	0.1572	0.3579	0.288	21.86	0.205
195	0.9610	1.9526	75.2	0.1557	0.369	0.246	24.8	0.190
175	0.9653	1.9776	56.5	0.1590	0.3830	0.2454	54.51	0.1637
170	0.9670	2.016	28.9	0.155	0.3935	0.2429	71.1	0.1530
040	1.051	2.414	8.1	0.133	0.385	0.230	91.9	0.143
020	1.0475	2.409	40.4	0.151	0.392	0.223	59.6	0.133
010	1.042	2.443	38.7	0.121	0.382	0.220	61.3	0.151

The ^{57}Fe Mößbauer spectra of **2** before, during, and after irradiation is shown in Figure 7-9. At 10 K the spectra indicates 100% in the LS state. At 20 K under green light irradiation (514.5 nm ; 20 mW/cm^2) clearly in addition to the LS state a HS state is observed. This indicates the light induced excited spin state trapping (LIESST) effect. After irradiation at 100 K, 100 % LS state is observed. Hence the photo-induced state is fully reversible and a photo-induced decomposition is excluded while at 175 K the thermal spin transition is still observed.

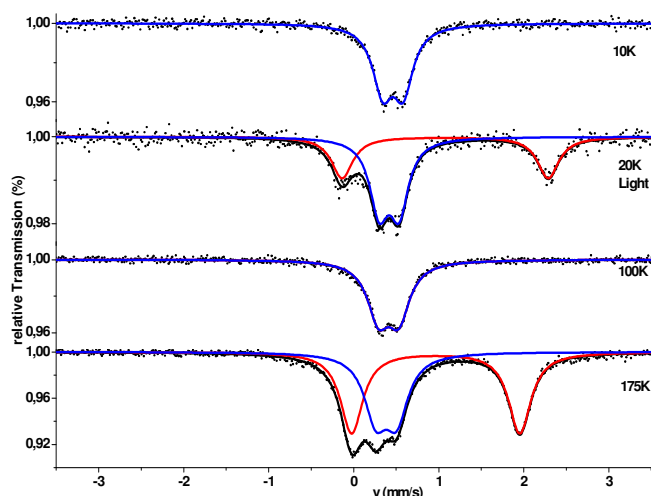


Figure 7-9: ^{57}Fe Mößbauer spectra of $[\text{Fe}(\text{pmea})(\text{NCS})_2]$ (**2**) before irradiation at 10 K shows 100% LS. At 20 K under green light irradiation (514.5 nm ; 20 mW/cm^2) clearly shows a light-induced excited spin state trapping (LIESST) effect. At 100 K after irradiation reversibility is indicated. While at 175 K still the thermal spin transition is reproduced.

Figure 7-10 shows the ^{57}Fe Mößbauer spectra of **2** under continuous red light irradiation (820 nm ; 40 mW/cm^2). The molar ratio clearly alters under red light irradiation. The effect of the light perturbed the thermal spin transition, this is called the LiPTH effect.²⁷⁸ At 170 and 200 K the steady state alters towards the LS state and in between at 175 K it shifts around 10 % towards the HS state. This excludes a possible local heating effect due to continuous irradiation. The LiPTH curve is clearly steeper in its transition which indicates a higher cooperativity among the centers.

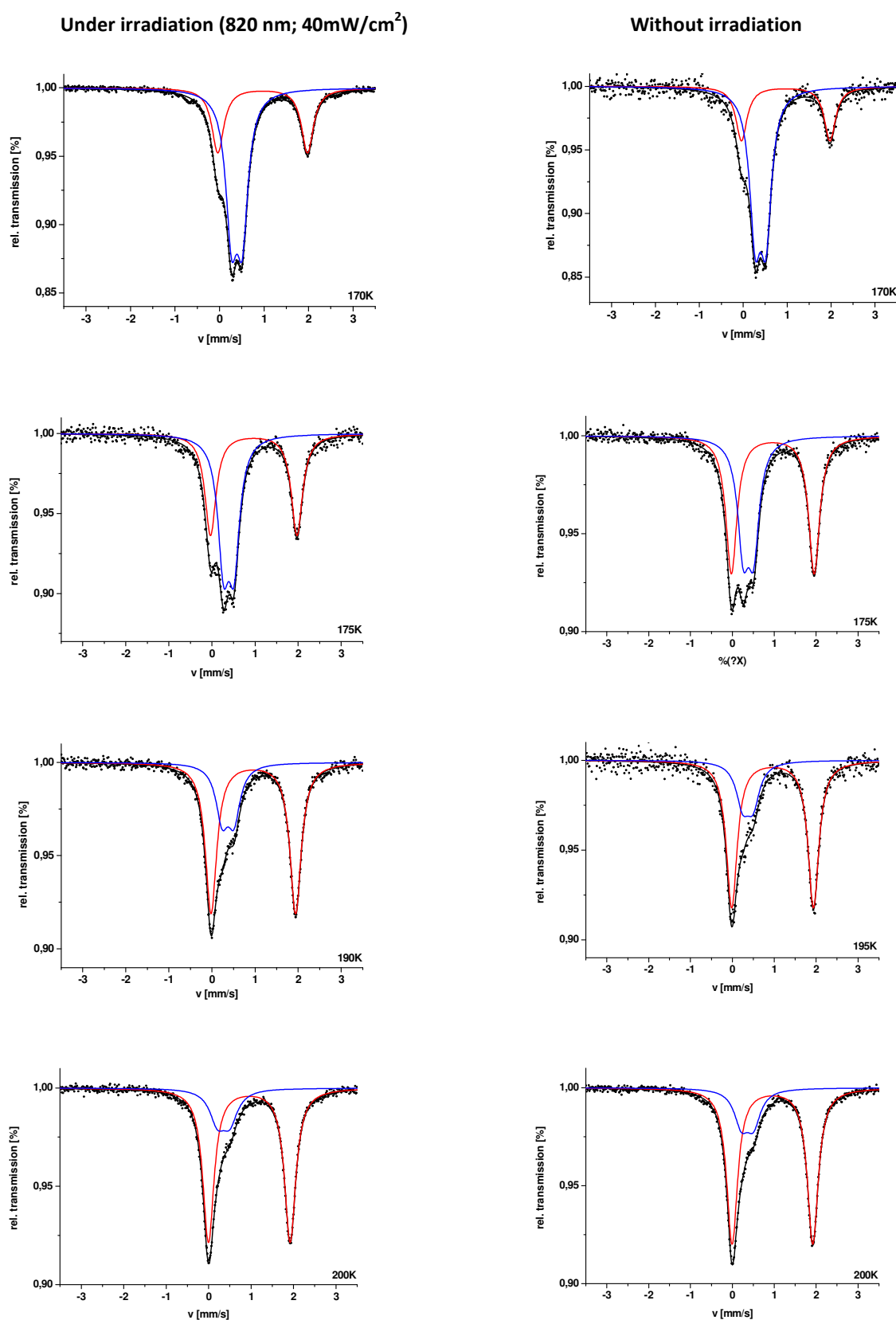


Figure 7-10: ⁵⁷Fe Mößbauer spectra of [Fe(pmea)(NCS)₂] (**2**) under continuous red light irradiation (820 nm; 40 mW/cm²) indicate a LiPTH effect of the thermal spin transition seen in comparison to the thermal transition between 170 and 200 K. The LiPTH transition indicates a higher cooperativity among the centers.

7.2.3 Magnetic susceptibility measurements for (1), (2), (3) and (4)

In addition to the Mößbauer measurements magnetic susceptibility experiments of the tmpa, pmea, pmap and tepa containing complexes were carried out. Figure 7-11 shows the χT vs. T plot for **1**, **2**, **3** and **4** at 1 Tesla in a SQUID magnetometer between 6 and 400 K, where χT is the magnetic susceptibility times temperature.

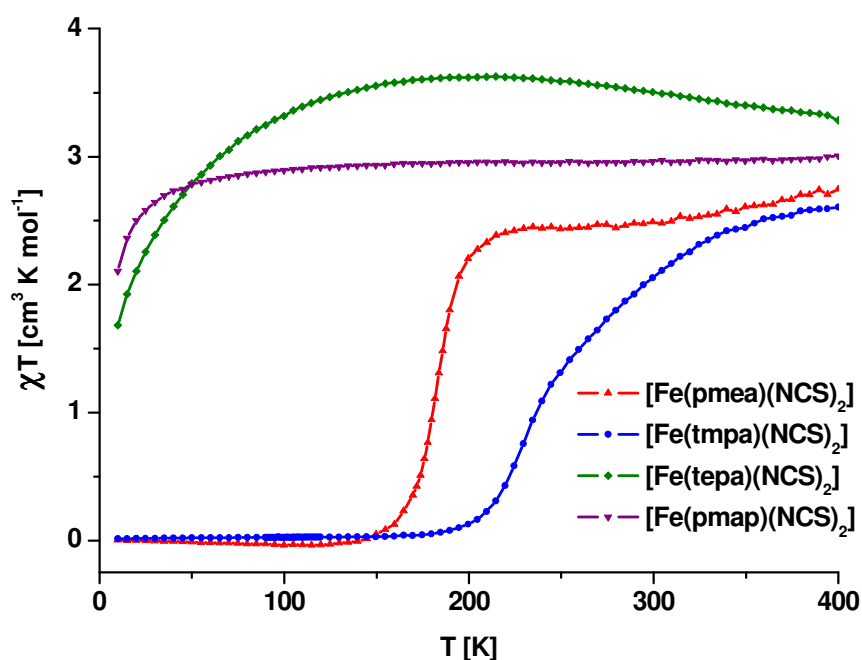


Figure 7-11: Magnetic susceptibility χT vs T plot for $[\text{Fe}(\text{tmpa})(\text{NCS})_2]$ (**1**), $[\text{Fe}(\text{pmea})(\text{NCS})_2]$ (**2**), $[\text{Fe}(\text{pmap})(\text{NCS})_2]$ (**3**) and $[\text{Fe}(\text{tepa})(\text{NCS})_2]$ (**4**) measured at 1 Tesla in a SQUID magnetometer between 6 and 400 K.

The results for **2** indicate an iron(II) in the LS configuration at low temperature. Heating up from around 140 K a steep transition from LS to HS takes place to a plateau at $2.5 \text{ cm}^3 \text{K}$ reached at 210 K, followed by a gradual growing transition to the HS state monitored up to 400 K. Together with the Mößbauer results this clearly indicates a multistep spin transition.

The results for **1** indicate an iron(II) in the LS state at low temperature. Above 180 K on heating a transition to the HS state occurs, which is not completed at 400 K. Together with the Mößbauer results this clearly indicates a spin transition.

The results for **3** indicate an iron(II) in the HS state at all temperatures. This is confirmed by the Mößbauer spectra.

The results for **4** indicate an iron in the HS state with short-range magnetic interactions among the different centers. The Mößbauer spectra indicates an iron(II) in the HS state and excludes the presence of an LS state.

7.2.4 IR-Spectroscopy of **1**, **2** and **3**.

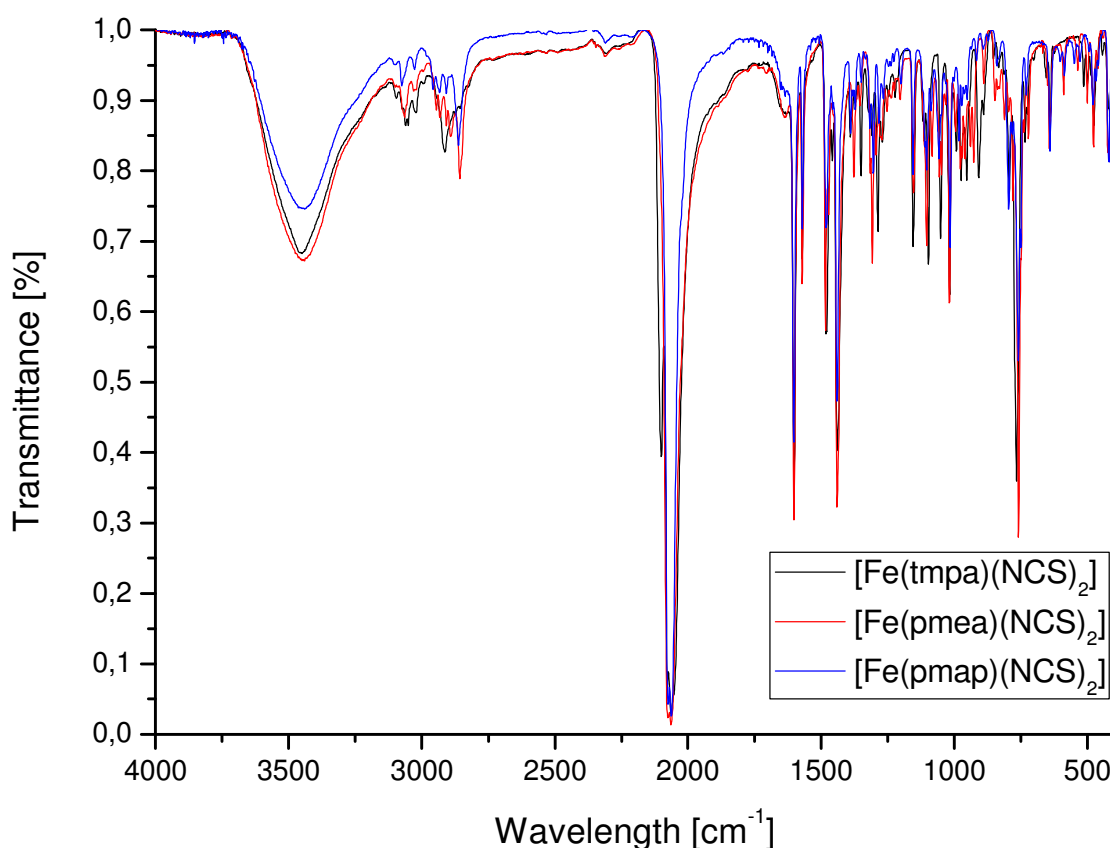


Figure 7-12: IR-Spectra of $[\text{Fe}(\text{tmpa})(\text{NCS})_2]$ (**1**), $[\text{Fe}(\text{pmea})(\text{NCS})_2]$ (**2**) and $[\text{Fe}(\text{pmap})(\text{NCS})_2]$ (**3**) at RT.

IR-measurements at room temperature of the compounds $[\text{Fe}(\text{tmpa})(\text{NCS})_2]$ (**1**), $[\text{Fe}(\text{pmea})(\text{NCS})_2]$ (**2**) and $[\text{Fe}(\text{pmap})(\text{NCS})_2]$ (**3**) were performed, as shown on Figure 7-12. The NCS-stretch shows always a doublet. For **1** this doublet is found at $2077.9/2064.4\text{ cm}^{-1}$, $2075.0/2064.1\text{ cm}^{-1}$ for **2**, and $2075.0/2062.5\text{ cm}^{-1}$ for **3** respectively. **1** shows additionally a singulet at 2100.1 cm^{-1} and as already verified by Mößbauer and SQUID measurements, **1** is partially existent in LS-state at room temperature. All other compounds are found in HS-state only at room temperature.

7.3 Conclusions

This paper compares iron(II) complexes with two thiocyanate molecules and the ligands N^2,N^2 -bis[(2-pyridyl)methyl]-2-(2-pyridyl)ethylamine (pmea), N^2,N^2 -bis[2-(2-pyridyl)ethyl]-(2-pyridyl)methylamine (pmap) as well as tris[2-(2-pyridyl)ethyl]amine (tepa) with the well studied parent iron(II) complex with tris(2-pyridylmethyl)amine (tmpa) as a ligand and two thiocyanates. All complexes could be synthesized and structurally characterized. Further SQUID and Mößbauer measurements could be obtained from all four complexes. $[\text{Fe}(\text{pmea})(\text{NCS})_2]$ (**2**) clearly shows a multistep spin transition. $[\text{Fe}(\text{tmpa})(\text{NCS})_2]$ (**1**) shows a LS state at low temperatures and upon heating changes to an incomplete HS state until 400 K. The complexes $[\text{Fe}(\text{pmap})(\text{NCS})_2]$ (**3**) and $[\text{Fe}(\text{tepa})(\text{NCS})_2]$ (**4**) do not show spin crossover at all as can be seen in Figure 7-11. For **2** we could find a LIESST effect as well.

7.4 Experimental Section

Materials and Methods. Reagents and solvents used were of commercially available reagent grade quality. The ligands pmea, pmap, tepa and the complex $[\text{Fe}(\text{py})_4(\text{NCS})_2]$ were synthesized and characterized according to literature methods.^{53, 242, 247, 267-268}

Preparation and handling of air-sensitive compounds was carried out in a glove box filled with argon (Braun, Garching, Germany; water and dioxygen less than 1ppm) and common Schlenck techniques. Elemental analyses have been performed at the Institute for Inorganic Chemistry, University of Erlangen-Nürnberg.

7.4.1 Mößbauer Spectroscopy.

Mößbauer absorption spectra were obtained with a conventional spectrometer operated in constant acceleration mode. The principle of the resonance detector is based on the registration of electrons of internal conversion, appearing during the decay of excited resonance nuclear levels. Due to the great difference in efficiency of conversion electron registration on the one hand and γ and

X-rays on the other, the resonance detector counts practically only the conversion electrons, emitted after resonance absorption of recoilless γ -radiation. The resonance counter is very suitable for transitions with a high degree of conversion, which in the case of ^{57}Fe is 8.2. The generally high value of the signal/noise ratio is an important feature of the resonance detector. In our experiment the gas-filled counter with internal one-line-converter made of ^{57}Fe enriched stainless steel was used. This construction provides the signal/noise ratio of ca. 10:1. The absorber was encapsulated in a Plexiglas container and mounted in a cryostat for variable temperatures down to ca. 4 K. A homemade so-called resonance detector was employed, which operates as a conversion electron detector, whereby an unusually high counting efficiency is obtained by placing a ^{57}Fe enriched stainless steel absorber inside the detector chamber. Counting efficiency is 10-20 times higher than with conventional detectors. Both, the Mößbauer absorption and emission spectra were fitted. All the isomer-shift values in this report are given with respect to stainless steel at room temperature.²⁷⁹ Mößbauer analyses have been performed at the Institute for Inorganic and Analytic Chemistry, University of Mainz.

7.4.2 Magnetic susceptibility.

Magnetic susceptibility data were collected in the temperature range 6.0-400 K and in an applied field of 1 Tesla of a Quantum Design model MPMS SQUID magnetometer. Pascal's constants were used to determine the diamagnetic corrections.²⁷⁹⁻²⁸⁰ Magnetism analyses have been performed at the Institute for Anorganic and Analytic Chemistry, University of Mainz.

7.4.3 Raman and IR spectroscopy.

IR spectra of pellets with 5 mg sample/200 mg matrix were recorded on a Bruker Equinox 55 spectrometer (resolution 2 cm^{-1} in FIR and 1 cm^{-1} in MIR). IR analyses have been performed at the Institute for Physical and Theoretical Chemistry, University of Erlangen-Nürnberg.

Raman spectra with 1064 nm excitation were recorded with a Bruker RFS100 FT-Raman spectrometer ($I = 25\text{ mW}$, $\phi \sim 1\text{ mm}$). Raman spectra with 785 nm excitation ($I = 300\text{ mW}$, $\phi \sim 0, 1\text{ mm}$) were

collected employing a homebuilt Ti-Sapphire laser pumped by an Argon laser (Coherent, Innova 90-6). After dispersion in a double grating spectrograph (Spex, model 1402), the Raman scattered light was detected by a liquid nitrogen-cooled CCD camera (ISA, model Spectrum One) with a spectral resolution of 2 cm^{-1} . The wavenumber reading of the dispersive Raman apparatus may differ by up to 4 cm^{-1} from that of the NIR-FT Raman spectrometer.⁷⁵ Raman spectra have been performed at the Institute for Physical and Theoretical Chemistry, University of Erlangen-Nürnberg.

7.4.4 Ligand synthesis.

The ligands were prepared according to the following procedure.^{53, 247, 267-268} The $[\text{Fe}(\text{py})_4(\text{NCS})_2]$ salt was synthesized according to the literature.²⁴²

7.4.5 Complex Synthesis

7.4.5.1 Synthesis of the complex $[\text{Fe}(\text{tmpa})(\text{NCS})_2]$ (1).

To 50 mL of a solution of $[\text{Fe}(\text{py})_4(\text{NCS})_2]$ (244 mg; 0.5 mmol) in methanol was added 25 mL of an ethanol solution of tmpa (145 mg; 0.5 mmol). A shining yellow precipitate soon formed, which was collected by filtration, washed with ethanol and dried under vacuum. A yellow powder was obtained. Yield: 150 mg (65%). Anal. Calcd for $\text{FeC}_{20}\text{H}_{18}\text{N}_6\text{S}_2$: C, 51.95; H 3.92; N 18.18; S 13.87; Fe 12.08. Found: C, 50.03; H, 3.90; N 17.42; S 13.21; Fe 12.30-13.06.

The complex was re-crystallised by diffusion of ether in a solution of acetonitrile. Yellow crystals were obtained.

7.4.5.2 Synthesis of the complex $[\text{Fe}(\text{pmea})(\text{NCS})_2]$ (2).

To 50 mL of a solution of $[\text{Fe}(\text{py})_4(\text{NCS})_2]$ (244 mg; 0.5 mmol) in methanol was added 25 mL of an ethanol solution of pmea (152 mg; 0.5 mmol). A yellow precipitate formed, which was collected by filtration, washed with ethanol and dried under vacuum. A yellow powder was obtained. Yield: 120 mg (50%). Anal. Calcd for $\text{FeC}_{21}\text{H}_{20}\text{N}_6\text{S}_2$: C, 52.95; H 4.23; N 17.64; S 13.46; Fe 11.72. Found: C, 50.01; H, 4.08; N 16.67; S 12.61; Fe 11.48-12.19.

The complex was re-crystallized by diffusion of ether in a solution of acetonitrile. Yellow-brown crystals were obtained. Crystals suitable for X-ray characterization were obtained by slow diffusion of ether in a solution of acetonitrile.

7.4.5.3 Synthesis of the complex [Fe(pmap)(NCS)₂] (3).

To 50 mL of a solution of [Fe(py)₄(NCS)₂] (244 mg; 0.5 mmol) in methanol was added 25 mL of an ethanol solution of pmea (159 mg; 0.5 mmol). A yellow precipitate formed, which was collected by filtration, washed with ethanol and dried under vacuum. A yellow powder was obtained. Yield: 190 mg (78%). Anal. Calcd for FeC₂₂H₂₂N₆S₂: C, 53.88; H, 4.52; N, 17.14; S, 13.08. Found: C, 53.92; H, 4.75; N, 17.31; S, 12.96.

Yellow crystals suitable for X-ray characterization were obtained by slow diffusion of methanol in a solution of DMSO.

7.4.5.4 Synthesis of the complex [Fe(tepa)(NCS)₂] (4).

To 50 mL of a solution of [Fe(py)₄(NCS)₂] (244 mg; 0.5 mmol) in methanol was added 25 mL of an ethanol solution of pmea (166 mg; 0.5 mmol). A brown precipitate soon formed, which was collected by filtration, washed with ethanol and dried under vacuum. A brown powder was obtained. Yield: 220 mg (87%). Anal. Calcd for FeC₂₃H₂₄N₆S₂: C, 54.76; H, 4.80; N, 16.66; S, 12.71. Found: C, 55.42; H, 5.28; N, 16.75; S, 12.07.

Yellow-brown crystals suitable for X-ray characterization were obtained by slow diffusion of ether in a solution of acetonitrile.

7.4.6 X-Ray.

X-ray measurements were collected with a Siemens P4 diffractometer using graphite-monochromated Mo K α radiation ($\lambda = 0.71073\text{\AA}$) by the ω -scan technique. Single crystals were coated with polyfluoroether oil and mounted on a glass fiber. Data have been corrected for Lorentz and polarization effects. Non-hydrogen atoms were refined with anisotropic thermal parameters.

Absorption effects have been corrected by semi-empirical methods using Psi-scans on 20 reflections ($12.2 \leq 2\theta \leq 38.8^\circ$, $T_{\min} = 0.296$, $T_{\max} = 0.353$).²⁸¹ The structure was solved by direct methods, full-matrix least-squares-refinement was carried out on F^2 values (SHELXTL NT 5.10).¹²² Crystal data and information on data collection are given in Table 7-1.

8 Iron (II) Complexes with the ligand *o*-bipy

8.1 Synthesis and Characterization of $[\text{Fe}(\textit{o}\text{-bipy})(\text{NCS})_2]$

As described in the previous chapters SCO of iron(II) complexes already was discovered by Cambi et al. in 1931²³⁻²⁴, but was not studied further for about 30 years.²¹ In that regard a large series of iron(II) complexes with thiocyanate ions as co-ligands have been investigated.^{29-32, 42, 78-79, 225, 229, 232, 247, 273-274} Most of those complexes have the thiocyanate co-ligands coordinated in the *cis*- position, as described in the previous chapters. Far less is known about iron(II) complexes with *trans*-coordination of the thiocyanate groups that exhibit spin crossover; only rigid ligands will lead to *trans*- geometries – more flexible ones will cause α - or β -*cis* geometries.²⁸² A possible *cis*-/*trans*- isomerism leads to changes of magnetic properties that have been described for example for $[\text{Fe}(\text{bpy})_2(\text{NCS})_2]$.²⁸³ This complex exhibits SCO, however it only crystallizes in the *cis*-form. The influence of axial ligands on magnetic properties was studied by Costa et al.²⁸⁴

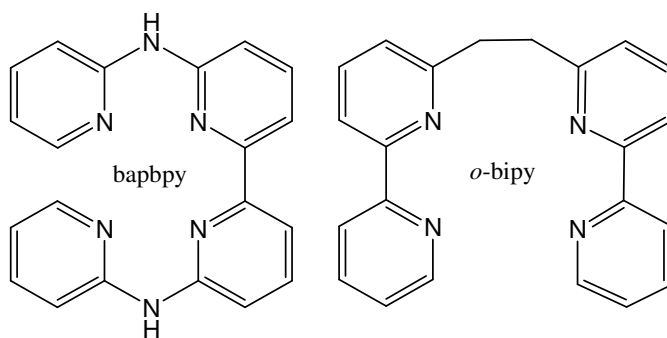


Figure 8-1: The ligand bapbpy²⁸⁵ compared to the ligand *o*-bipy⁸¹.

An example of a *trans*-complex that shows a two-step spin transition with a [HS – LS – LS] intermediate phase has been recently described by Bonnet et al.²⁸⁵ They had investigated the iron(II) complex $[\text{Fe}(\text{bapbpy})(\text{NCS})_2]$ (bapbpy = N-(6-(6-(pyridin-2-ylamino)pyridin-2-yl)pyridin-2-yl)pyridin-2-amine, Figure 8-1).

A related ligand to bapbpy is *o*-bipy (*o*-bipy = 1,2-bis(2,2'-bipyridyl-6-yl)ethane, Figure 8-1) that has been used previously by Garber et al. to investigate copper(II) complexes in their aim for fabricating

closed-ended macrocyclic ligands based on 2,2'-bipyridine, that may behave as porphyrine analogues. This ligand is a rigid system that couples two bipyridine components and should support formation of a *trans*-complex.⁸¹

8.2 Results and Discussion

The ligand *o*-bipy was synthesized according to the published procedure.⁸¹ It was possible to obtain crystals of the ligand and the molecular structure of *o*-bipy is shown in Figure 8-2.

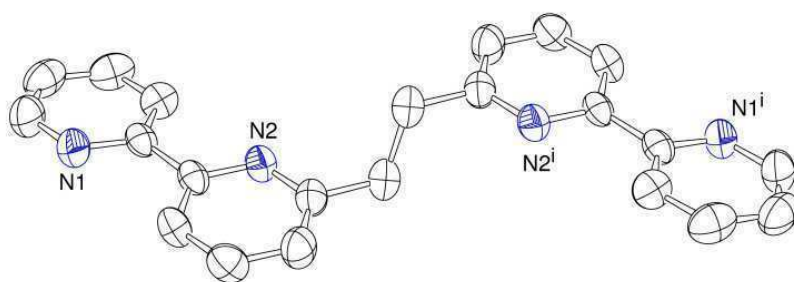


Figure 8-2: Molecular structure of the ligand *o*-bipy.

The complex $[\text{Fe}(\text{o-bipy})(\text{NCS})_2]$ was prepared in the usual way by adding the ligand *o*-bipy dissolved in acetone with the precursor complex $[\text{Fe}(\text{py})_4(\text{NCS})_2]$ dissolved in methanol. A pink-orange colored powder was obtained and crystals for x-ray analysis could be obtained by slow diffusion of diethyl ether into a solution of the powder in dmf. The molecular structure of $[\text{Fe}(\text{o-bipy})(\text{NCS})_2]$ is presented in Figure 8-2. Crystallographic data and selected bond lengths and angles are given in Tables 8-1 and 8-2.

$[\text{Fe}(\text{o-bipy})(\text{NCS})_2]$ crystallizes in a P-1 triclinic space group. The iron(II) center is coordinated by six nitrogen donor atoms. Four of these belong to the ligand and two additional belong to the two thiocyanate anions. The iron-nitrogen bond distances adjoining to the thiocyanate anions are shorter than those adjoining to the two bridged biphenyl groups (see Table 8-2). This may be a consequence of different hybridizations and π -acceptor abilities of the biphenyls and thiocyanate groups. The description of the coordination sphere of the iron(II) center is a distorted octahedron. The N-Fe-N angles differ slightly from the values 90° and 180° as expected for an ideal octahedral environment

(see Table 8-3). For *cis* nitrogen donors N-Fe-N bond angles are between 73.47° and 108.49°, whereas trans bond angles are between 176.3° and 177.86°. Because of the steric strain caused by the ethyl bridge, the ligand leaves place for the thiocyanate ions only in *trans* position. The bond lengths of the NCS groups is with 2.109/2.134 Å slightly shorter than those of the two bipyridine moieties with 2.203/ 2.234 Å and 2.234/2.227 Å. The N-Fe-N bond lengths are typical for a HS-state.^{263, 265}

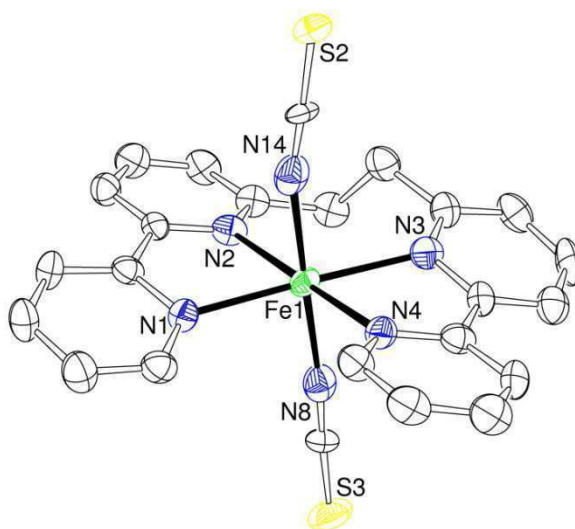


Figure 8-3: Molecular structure of [Fe(*o*-bipy)(NCS)₂].

8.2.1 Crystallographic Data.

Table 8-1: Selected crystallographic data unit cell parameters, and values of L^1 and **1**

Compound	<i>o</i> -bipy (L^1)	[Fe(<i>o</i> -bipy)(NCS) ₂] (1)
Empiric Formular	C ₂₂ H ₁₈ N ₄	C ₂₄ H ₁₈ FeN ₆ S ₂
Molecular weight	338.40	510.41
Temperature [K]	300(2)	193(2)
Crystal size [mm]	0.80 x 0.70 x 0.65	0.32 x 0.24 x 0.08
Crystal System	monoclinic	triclinic
	P2 ₁ /n	P-1
a [Å]	6.6144(11)	9.0837(18)
b [Å]	12.1565(19)	9.3456(19)
c [Å]	11.0404(16)	13.728(3)
α [°]	90	98.33(3)
β [°]	90.043(6)	101.07(3)
γ [°]	90	100.85(3)
V [Å ³]	887.7(2)	1103.3(4)
Z	2	2
ρ _{calcd.} [mg·m ⁻³]	1.266	1.536
μ [mm ⁻¹]	0.077	0.899
F(000)	356	524
Scan range θ [°]	2.49 to 21.80	2.48 to 28.13
Index ranges	-6 ≤ h ≤ 6	-11 ≤ h ≤ 12
	-12 ≤ k ≤ 12	-12 ≤ k ≤ 12
	-11 ≤ l ≤ 11	-16 ≤ l ≤ 17
Reflections collected	4234	9070
Unique reflections	1060	4922
R _{int}	0.3814	0.0684
Data/restraints/parameters	1060 / 0 / 118	4922 / 0 / 365
Goodness of fit F ²	0.963	0.822
Final R indices (all data)	R1 = 0.1063	R1 = 0.1379
	wR2 = 0.2231	wR2 = 0.1957
R indices [I > 2σ(I)]	R1 = 0.0818	R1 = 0.0724
	wR2 = 0.1972	wR2 = 0.1671
Largest diff. peak/hole [e·Å ⁻³]	0.293 and -0.362	2.259 and -0.890

Table 8-2: Selected bond lengths [Å] and angles [°] for compound **1**.

[Fe(<i>o</i>-bipy)(NCS)₂] (1)			
Fe(1)-N(8)	2.109(7)	N(8)-Fe(1)-N(3)	87.5(2)
Fe(1)-N(14)	2.134(7)	N(14)-Fe(1)-N(3)	91.5(2)
Fe(1)-N(1)	2.203(5)	N(1)-Fe(1)-N(3)	177.86(18)
Fe(1)-N(4)	2.227(4)	N(4)-Fe(1)-N(3)	73.37(17)
Fe(1)-N(3)	2.234(5)	N(8)-Fe(1)-N(2)	93.48(19)
Fe(1)-N(2)	2.242(4)	N(14)-Fe(1)-N(2)	87.52(19)
N(8)-Fe(1)-N(14)	178.8(2)	N(1)-Fe(1)-N(2)	73.47(17)
N(8)-Fe(1)-N(1)	91.6(2)	N(4)-Fe(1)-N(2)	176.3(2)
N(14)-Fe(1)-N(1)	89.4(2)	N(3)-Fe(1)-N(2)	108.49(17)
N(8)-Fe(1)-N(4)	89.84(19)		
N(14)-Fe(1)-N(4)	89.19(19)		
N(1)-Fe(1)-N(4)	104.72(17)		

Table 8-3: Range of N-Fe-N angles between *cis* and *trans* nitrogen atoms.

Complex	range of N-Fe-N angles between <i>cis</i> nitrogen atoms	range of N-Fe-N angles between <i>trans</i> nitrogen atoms
[Fe(<i>o</i>-bipy)(NCS)₂] (1)	73.47(17) – 108.49(17)	176.3(2) – 177.86(18)

8.2.2 Electrochemistry.

Cyclic voltammetry of [Fe(*o*-bipy)(NCS)₂] was performed with a scan rate of 100 mV/s in DMF. Cyclic voltammograms showed several redox processes (including the Fe(II)/Fe(III) potential) with three oxidation and reduction waves with the heights of the first and third redox wave signals significantly smaller than the second one. Figure 8-4 shows the cyclic voltammogram of [Fe(*o*-bipy)(NCS)₂]. Ferrocene was used as an internal standard.

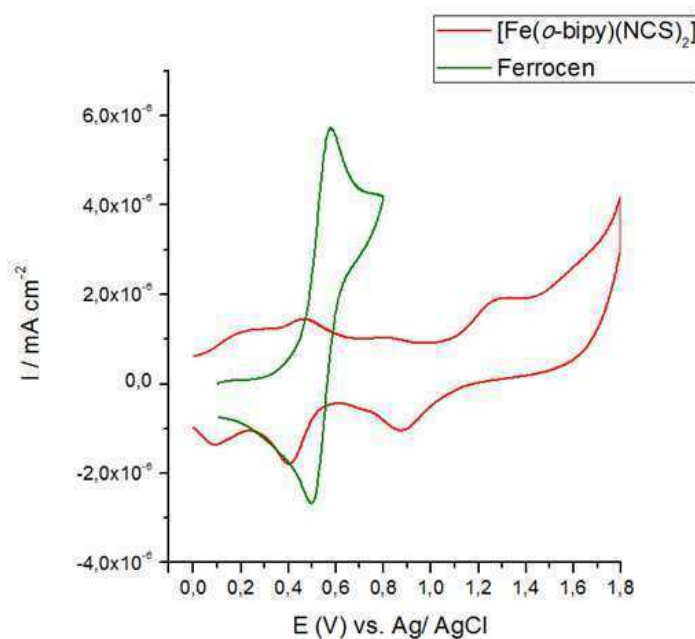


Figure 8-4: Electrochemistry of $[\text{Fe}(\text{o-bipy})(\text{NCS})_2]$ in DMF (RT) from 0 to 1.8 V.

8.2.3 Magnetic susceptibility measurements.

Powder samples of $[\text{Fe}(\text{o-bipy})(\text{NCS})_2]$ were used for SQUID measurements (Superconducting QUantum Interference Device). Figure 8-5 shows the χT vs. T plot for $[\text{Fe}(\text{o-bipy})(\text{NCS})_2]$ at 1 Tesla in a SQUID magnetometer between 30 K and 300 K, where χT is the magnetic susceptibility times temperature. No spin transition for $[\text{Fe}(\text{o-bipy})(\text{NCS})_2]$ could be detected. The SQUID measurements clearly show that $[\text{Fe}(\text{o-bipy})(\text{NCS})_2]$ is in the HS state at all temperatures above 30 K.

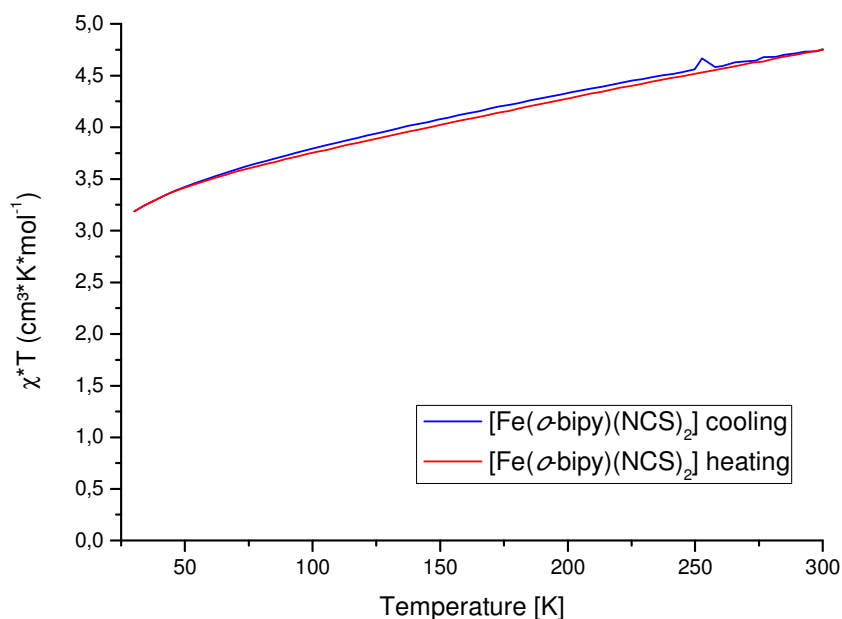


Figure 8-5: SQUID measurements of $[\text{Fe}(\text{o-bipy})(\text{NCS})_2]$ between 30 K and 300 K.

8.2.4 IR-Spectroscopy of $[\text{Fe}(\text{o-bipy})(\text{NCS})_2]$

As already discussed in the literature, with infrared spectroscopy it is possible to distinguish HS- (about 2050-2070 cm^{-1}) from LS- (about 2100 cm^{-1}) state.²³⁶⁻²⁴¹ Therefore IR-measurements at room temperature were performed and an IR spectrum of $[\text{Fe}(\text{o-bipy})(\text{NCS})_2]$ is shown in Figure 8-6. The NCS-stretch of $[\text{Fe}(\text{o-bipy})(\text{NCS})_2]$ shows a doublet at 2069.0/ 2057.7 cm^{-1} that is characteristic for a HS-state.

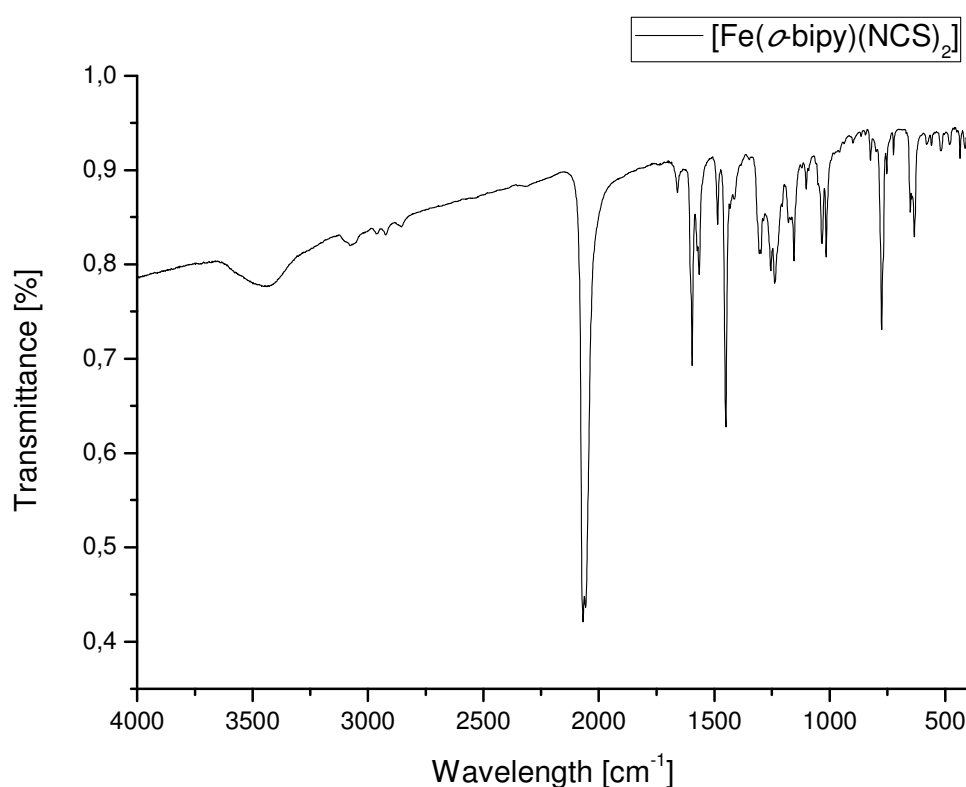


Figure 8-6: IR-Spectrum for $[\text{Fe}(\text{o-bipy})(\text{NCS})_2]$.

8.3 Conclusions

It was possible to synthesize and fully characterize the new trans complex $[\text{Fe}(\text{o-bipy})(\text{NCS})_2]$. However, in contrast to our expectations the results of our investigations clearly demonstrate that this complex does not show SCO properties in contrast to the related compound $[\text{Fe}(\text{bapbpy})(\text{NCS})_2]$.²⁸⁵ $[\text{Fe}(\text{o-bipy})(\text{NCS})_2]$ is in the HS-state in the temperature range from 300 K to 30 K. The reason for this is not quite clear, however DFT calculations on this complex might provide an answer to this question.

8.4 Experimental Section

8.4.1 Materials and Methods.

Reagents and solvents used were of commercially available reagent quality. Organic solvents used in the syntheses of the Iron(II) complexes were dried in the usual way. The ligand was synthesized

according to the literature⁸¹, but lithium diisopropylamide was dissolved in Et₂O instead of hexane. The [Fe(py)₄(NCS)₂] salt was synthesized according to the literature.²⁴² Preparation and handling of air-sensitive compounds were carried out in a glove box filled with argon (MBraun, Germany; water and dioxygen less than 1 ppm).

8.4.2 Synthesis of the complex [Fe(*o*-bipy)(NCS)₂]

A solution of *o*-bipy (284 mg; 0.8 mmol) in acetone (5 mL) was added dropwise to a solution of [Fe(py)₄(NCS)₂] (392 mg; 0.8 mmol) in methanol (5 mL) and stirred for 10 minutes. An orange-red precipitate formed after a few minutes. The precipitate was filtered, washed with acetone and dried under vacuum. Red crystals suitable for X-ray characterization were obtained by slow diffusion of ether in a solution of dimethylformamide. The elemental analysis indicates an extra 1.5 molecules of pyridine within the powder of the complex.

Yield: 373 mg (91%). Anal. Calcd for FeC_{31.5}H_{25.5}N_{7.5}S₂: C, 60.14; H, 4.09; N, 16.70. Found: C, 60.16; H, 4.14; N, 16.45. IR (KBr, cm⁻¹): 3426.9; 2069.0 (NCS); 2057.7 (NCS); 1595.6; 1450.3.

8.4.3 Cyclic voltametry

Cyclic voltametry was performed at room temperature using an eDAC potentiostat with a scan rate of 100 mV/s. The solution used for measuring contained 0.1 mol/L of the conducting salt tetrabutylammoniumtetrafluoroborate and 10⁻³ mol/L of the complex [Fe(*o*-bipy)(NCS)₂] in a 1:1 ratio using DMF as a solvent.

8.4.4 X-Ray

The X-ray crystallographic data of [Fe(*o*-bipy)(NCS)₂] were collected on a STOE IPDS-diffractometer equipped with a low temperature system (Karlsruher Glastechnisches Werk). Mo-K_α radiation (λ = 0.71069 Å) and a graphite monochromator was used. Single crystals of the ligand *o*-bipy were measured on a Bruker Smart X2S diffractometer operating with Mo-K_α radiation (λ = 0.71073 Å).

Table 8-1 summarizes the crystal parameters as well as some details of the data collections and the structure refinements of all crystals. No absorption corrections were applied to the data set. The structures were solved by direct methods in SHELXS97 and refined by using full-matrix least squares in SHELXL97.²⁴⁵⁻²⁴⁶ All non-hydrogen atoms were refined anisotropically. The positions of all hydrogen atoms of [Fe(*o*-bipy)(NCS)₂] were calculated using a riding model with isotropic thermal parameters, the hydrogen atoms of the ligand *o*-bipy were calculated geometrically and a riding model was applied during the refinement process.

8.4.5 *Magnetic susceptibility measurements*

SQUID measurements were performed in collaboration with the group of Sylvestre Bonnet using a Quantum Design MPMS-5S squid magnetometer at Leiden. Each sample was mounted on a plastic straw before introducing it into the squid magnetometer. DC magnetization measurements were performed in a field of 1 T, from 30 to 300 K (heating mode) and from 300 to 30 K (cooling mode). For each sample the total measuring time was 20 h. Corrections for the diamagnetism of the sample were calculated using Pascal's constants.

9 Summary

This work includes investigations on iron and copper complexes with tripodal and related ligands, based on (2-aminoethyl)bis(2-pyridyl-methyl)amine (tmpa). The Chapters 2-4 of this work concentrate on the synthesis, characterization and reactivity of copper complexes with these ligands, the Chapters 5-8 attend to iron(II) complexes, their characterization and behavior in regard to a possible spin crossover.

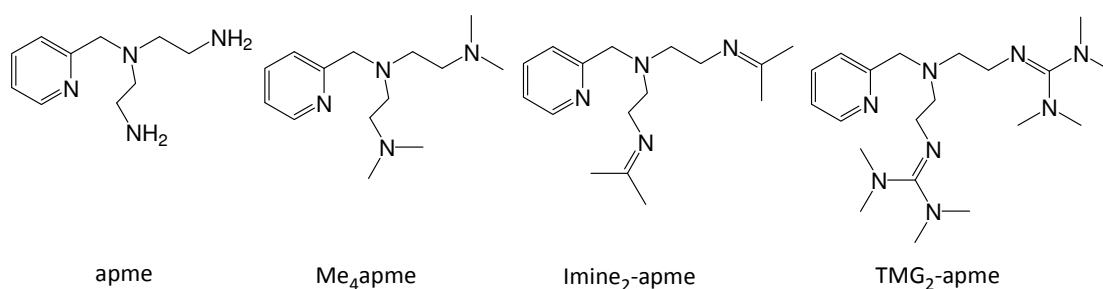


Figure 9-1: Abbreviations used for tripodal ligands: from left: N^1 -(2-aminoethyl)- N^1 -(2-pyridyl-methyl)-1,2-ethandiamine (apme); Bis[2-Dimethylaminoethyl]-(2-pyridylmethyl)amine (Me₄apme); N^1 -(propan-2-ylidene)- N^2 -(2-(propan-2-ylideneamino)ethyl)- N^2 -(pyridin-2-yl)methyl)ethane-1,2-diamine (Imine₂-apme); 2-(2-(bis((pyridin-2-yl)methyl)amino)ethyl)-1,1,3,3-tetramethylguanidine (TMG₂apme)

Chapter 2 describes an alternative way for the synthesis of the ligand apme (see Figure 9-1) Further the complexes $[\text{Cu}_2(\text{apme})_2](\text{ClO}_4)_2$, $[\text{Cu}_2(\text{apme})_2](\text{CF}_3\text{SO}_3)_2$, $[\text{Cu}(\text{apme})\text{Cl}]\text{BPh}_4$ and $[\text{Cu}(\text{apme})(\text{DMF})]\text{BPh}_4$ could be synthesized and structurally characterized. The solution behavior of $[\text{Cu}_2(\text{apme})_2](\text{ClO}_4)_2$ and $[\text{Cu}_2(\text{apme})_2](\text{CF}_3\text{SO}_3)_2$ was investigated by NMR spectroscopy. Figure 9-2 (left) shows ^1H NMR spectra of $[\text{Cu}_2(\text{apme})_2](\text{CF}_3\text{SO}_3)_2$ in CD_3CN at -35 , -5 , $+5$ and $+25^\circ\text{C}$. The results indicate that in solution monomeric species are present.

Furthermore, time resolved UV-vis spectra collected in acetone were carried out (Figure 9-2). They show an absorbance maximum at 539 nm ($\epsilon = 4400 \pm 200 \text{ M}^{-1}\text{cm}^{-1}$) that can be assigned to $[(\text{apme})\text{Cu}(\text{O}_2)\text{Cu}(\text{apme})]^{2+}$, a dinuclear copper peroxido complex, similar to the fully characterized complexes with related tren or tmpa based ligands.

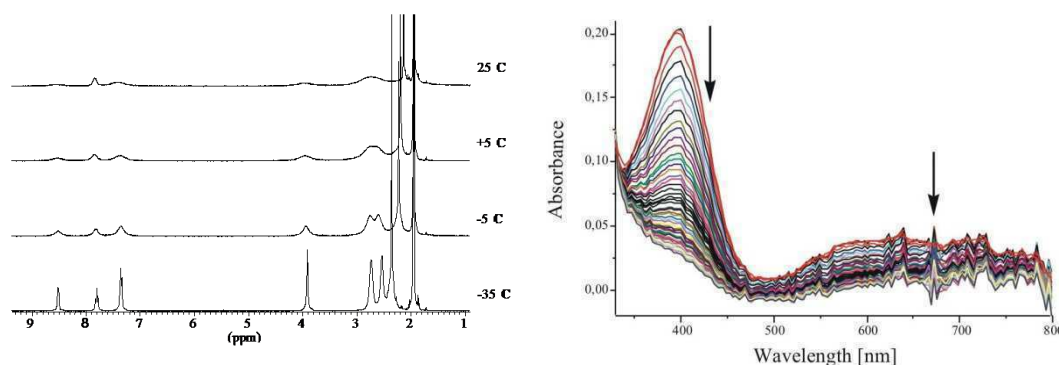


Figure 9-2: From left: Low temperature NMR spectra of $[\text{Cu}_2(\text{apme})_2](\text{CF}_3\text{SO}_3)_2$ in CD_3CN at -35°C , -5°C , $+5^\circ\text{C}$ and $+25^\circ\text{C}$; right: Time resolved UV/vis spectra for the reaction of an in situ reaction of apme $[\text{Cu}(\text{CH}_3\text{CN})_4]\text{ClO}_4$ and O_2 in CH_2Cl_2 at -87°C ; $[\text{complex}] = 5 \times 10^{-5} \text{ mol/L}$, $[\text{O}_2] = 5.1 \times 10^{-3} \text{ mol/L}$ in acetone, $t = 1.47 \text{ s}$ in CH_2Cl_2 ; $t = 0.76 \text{ s}$ in acetone.

In chapter 3 the ligand apme of chapter 2 has been included into a macrocyclic ligand system.

Figure 9-3 (left) shows an abbreviation of the ligand bsm2py and its familiarity to the ligand apme.

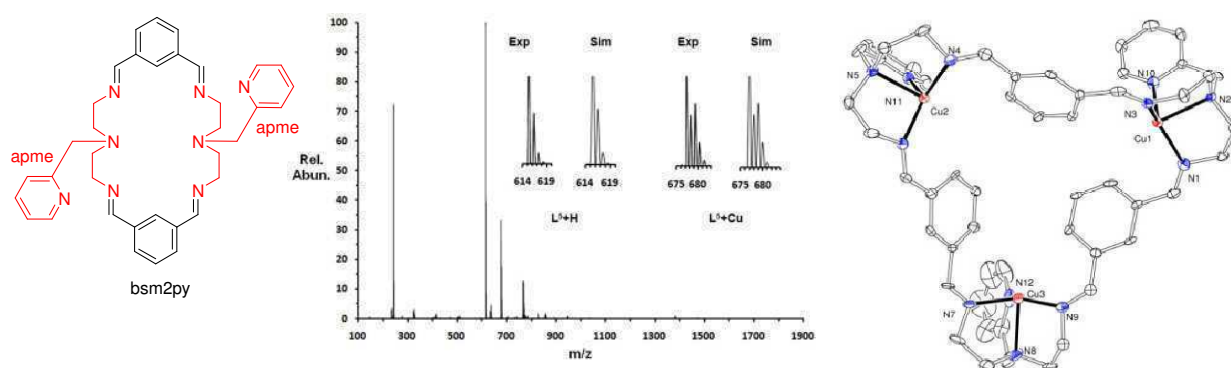


Figure 9-3: From left: Abbreviation of the ligand bsm2py (bsm2py = 6,20-bis(pyridin-2-yl)methyl, 3,6,9,17,20,23-hexaazatricyclo[23.3.1.1]triaconta-1(29),2,9,11(30),12(13),14,16,23,25,27-decaene); middle: ESI-MS spectra obtained for $[\text{Cu}_2(\text{bsm2PhOH})(\text{MeCN})_2](\text{CF}_3\text{SO}_3)_2$ in MeCN (middle) right: ORTEP plot of $[\text{Cu}_3(\text{L}^4)](\text{CF}_3\text{SO}_3)_3 \cdot 1\text{EtOEt}$.

The ligand bsm2py could be synthesized and characterized via NMR spectroscopy. Further the ligands bsm2PhOH and bsm2Et were synthesized and characterized. All these [2+2] compounds do not further undergo rearrangement reactions in solution, once they are formed, thus the [2+2] condensation is the favored product. In contrast to the reaction of the [2+2] condensation ligands, bsm2py and bsm2PhOH, with copper(I) complexes, generate a mixture of dinuclear $[\text{Cu}_2(\text{bsm2py})]^{2+}$ and $[\text{Cu}_2(\text{bsm2PhOH})(\text{MeCN})_2]^{2+}$ as well as trinuclear $[\text{Cu}_3(\text{L}^4)]^{3+}$ and $[\text{Cu}_3(\text{L}^5)(\text{MeCN})_3]^{3+}$ complexes that are in equilibrium in solution. These results are verified by X-Ray structure refinement (Figure 9-3 (right)), NMR spectroscopy and MS spectroscopy. The Figure 9-3 (middle) shows the ESI-MS spectrum of the complex $[\text{Cu}_2(\text{bsm2PhOH})(\text{MeCN})_2]^{2+}$. The molecular peaks could not be

identified but a series of fragments are found. For complex $[\text{Cu}_2(\text{bsm2PhOH})(\text{MeCN})_2]^{2+}$ key mono-charged peaks at 615 m/z (bsm2PhOH +H; highest intensity), 637 m/z (bsm2PhOH +Na), 677 m/z (bsm2PhOH +Cu), 739 (bsm2PhOH +Cu₂-1), and 766 (bsm2PhOH +Cu₂Na-3) could be identified. For complex $[\text{Cu}_3(\text{L}^5)(\text{MeCN})_3]^{3+}$ key peaks are found at 922 m/z (L⁵+H; highest intensity), 984 m/z (L⁵+Cu) and their corresponding doubly charged peaks at 461 m/z and 492 m/z respectively. The relative intensities of their peaks coincide perfectly with the simulated ones.

"Splitting" the parent macrocyclic ligand of bsm2py "mac" in half results in the ligand (7E)-N¹-benzylidene-N²-((E)-2-(benzylideneamino) ethyl)ethane-1,2-diamine (L¹) that has been used in the studies described in Chapter 4. ¹H NMR spectroscopy in CDCl₃ showed the presence of an aminor form (60%) beside the bisimine form (39%). IR spectroscopy and X-Ray analysis indicate that only the aminor form is present in the solid state. Reducing L¹ with LiAlH₄ leads to the ligand N¹-benzyl-N²-(2-(benzylamino)ethyl)ethane-1,2-diamine (L²). Complexes $[\text{Cu}(\text{L}^1)(\text{CH}_3\text{CN})]\text{PF}_6$, $[\text{Cu}_2(\text{L}^1)_2](\text{ClO}_4)_2$, $[\text{Cu}(\text{L}^1)(\text{PPh}_3)](\text{ClO}_4)$, $[\text{Cu}_2(\text{L}^1)_2(\text{OCH}_3)_2](\text{PF}_6)_2$, $[\text{Cu}_2(\text{L}^1)_2(\text{OH})_2](\text{PF}_6)_2$ and $[\text{Cu}_2(\text{L}^2)_2\text{Cl}_3]\text{PF}_6 \cdot 2\text{MeOH}$ were synthesized and structurally characterized. Copper(I) complexes of L¹ display an unusual anion effect: with PF₆⁻, the mononuclear complex $[\text{Cu}(\text{L}^1)(\text{CH}_3\text{CN})]\text{PF}_6$ was obtained, while using ClO₄⁻ as a counterion the dinuclear helical compound $[\text{Cu}_2(\text{L}^1)_2](\text{ClO}_4)_2$ was formed. Investigations in regard of the oxidation behavior of those complexes were performed using time resolved UV-vis spectroscopy. A peroxido species as well as the oxido compound $[\text{Cu}_2(\text{L}^1)_2\text{O}](\text{PF}_6)_2$ were detected during the reaction. However, observation of the peroxido species by UV-Vis spectroscopy was not possible. Furthermore, the reaction of $[\text{Cu}(\text{L}^2)(\text{CH}_3\text{CN})]\text{PF}_6$ with dioxygen was investigated, but a "dioxygen adduct" complex as a reactive intermediate could not be detected. To summarize the Chapters 2-4 interesting new reactions of tripodal and related ligands containing copper and dioxygen have been investigated that are important for further research in the area of finding copper complexes that could be used in catalytic oxidation reactions of organic substrates with dioxygen as an oxidant.

In Chapter 5 the investigations of the iron(II)-complexes with the ligand apme and its derivatives (Figure 9-1) are described. In the past it that iron(II) complexes with different tripodal ligands similar to apme (such as tmpa and derivatives) were observed showing a spin crossover (SCO) behavior.^{68, 75, 247} Thus investigating further variations of the ligand tmpa seemed quite promising in regard to obtain new SCO complexes that might become useful for electronic devices in the future.

During the crystallographic investigations of these complexes, interactions with the used solvent were detected. Formation of a new imine ligand: N¹-(propan-2-ylidene)-N²-(2-(propan-2-ylideneamino)ethyl)-N²-((pyridin-2-yl)methyl)ethane-1,2-diamine (Imine₂-apme) was observed and the complex [Fe(imine₂-apme)(NCS)₂] (Figure 9-4, left) could be structurally characterized.

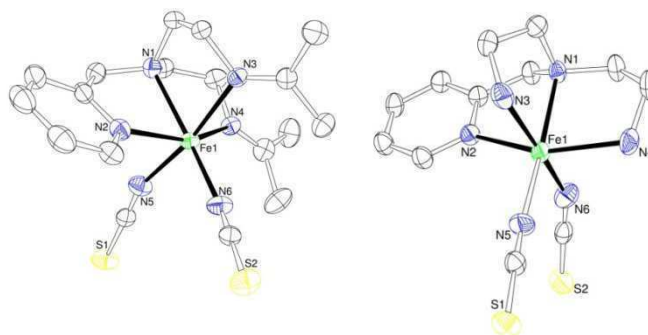


Figure 9-4: Molecular structure of left: [Fe(imine₂-apme)(NCS)₂] and right: [Fe(apme)(NCS)₂].

In contrast using acetonitrile as a solvent, [Fe(apme)(NCS)₂] was obtained and could be structurally characterized (Figure 9-4 (right)). A further interesting observation was made during the first efforts to prepare the complex [Fe(Me₄apme)(NCS)₂]. Here it was observed that the ligand was protonated and a third thiocyanate molecule coordinated instead of the protonated amine group. Further a methanol molecule is located with a hydrogen bonding to the protonated amine group and to one of the thiocyanate anions. Again switching solvents, here from methanol to acetone, did allow to prepare the complex [Fe(Me₄apme)(NCS)₂] that could be structurally characterized. Figure 9-5 shows the complexes [Fe(HMe₄apme)(NCS)₃] and [Fe(Me₄apme)(NCS)₂].

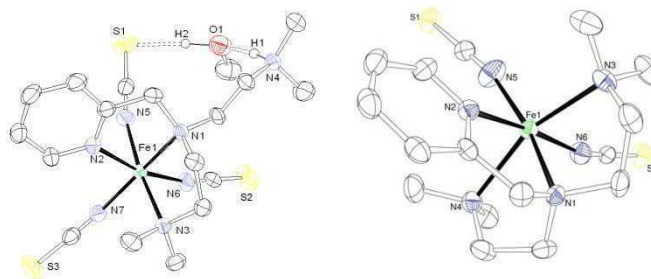


Figure 9-5: Molecular structure of left: $[\text{Fe}(\text{HMe}_4\text{apme})(\text{NCS})_3]$ and right: $[\text{Fe}(\text{Me}_4\text{apme})(\text{NCS})_2]$.

The complex $[\text{Fe}(\text{Me}_4\text{apme})(\text{NCS})_2]$ was further investigated in regard to its spin crossover behavior using Mößbauer Spectroscopy. No SCO could be detected between 298 K and 40 K. The spectra show doublets with an isomer shift δ_s of 1.01 mm s^{-1} and a quadrupole splitting of ΔE_Q of 1.65 mm s^{-1} at room temperature as well as an isomer shift δ_s and the quadrupole splitting ΔE_Q to 1.12 mm s^{-1} and 2.23 mm s^{-1} at 40 K, respectively. Regarding the complex $[\text{Fe}(\text{imine}_2\text{-apme})(\text{NCS})_2]$ magnetic susceptibility measurements were performed on recrystallized and powder samples using cooling and heating mode. No SCO could be detected between 300 K and 5 K, both samples are in a HS- state over the full temperature range.

In part one of Chapter 6 investigations of a related series of iron(II) complexes with a different set of tripodal ligands related to tmpa were carried out. It can be concluded, that small differences in ligand field strength or steric aspects at one of the arms of the tripodal ligand can lead to the preference of either *mer*- or *fac*- arrangement in the resulting crystallized complex. The ligands shown in Figure 9-6 were applied.

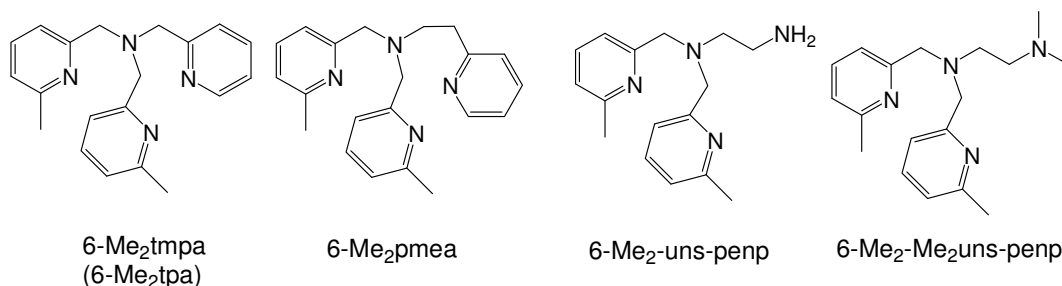


Figure 9-6: Abbreviations used for tripodal ligands: from left: tris((6-methylpyridin-2-yl)methyl)amine (6-Me₂tmpa), 2-(6-methylpyridin-2-yl)-N,N-bis((6-methylpyridin-2-yl)methyl)ethanamine (6-Me₂pmea), *N*¹,*N*¹-bis((6-methylpyridin-2-yl)methyl)ethane-1,2-diamine (6-Me₂-uns-penp) and *N*¹,*N*¹-dimethyl-*N*²,*N*²-bis((6-methylpyridin-2-yl)methyl)ethane-1,2-diamine (6-Me₂-Me₂uns-penp).

Furthermore, in the second part of Chapter 6 iron(II) complexes with derivatives of uns-penp as ligands are described. ([Fe(uns-penp)(NCS)₂] showed spin crossover behavior and had been described previously)⁶⁸. Figure 9-7 shows the ligands used for the complexes [Fe(L)(NCS)₂] (L = Me₂uns-penp, Imine-uns-penp, TMG-uns-penp).

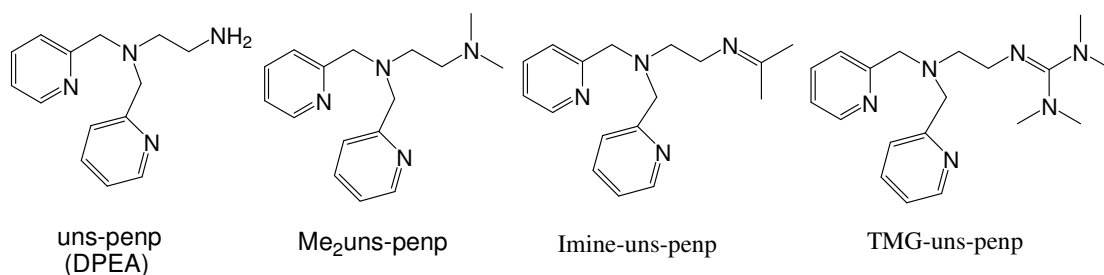


Figure 9-7: Abbreviation used for tripodal ligands: from left: 2-aminoethylbis(2-pyridyl-methyl)amine (uns-penp); N¹,N¹-Dimethyl-N²,N²-Bis(2-pyridylmethyl)-1,2-ethandiamine (Me₂uns-penp); N¹-(propan-2-ylidene)-N²,N²-bis((pyridin-2-yl)methyl)ethane-1,2-diamine (Imine-uns-penp); 2-(2-(bis((pyridin-2-yl)methyl)amino)ethyl)-1,1,3,3-tetramethylguanidine (TMG-uns-penp).

Investigations regarding spin crossover behavior were carried out for all complexes described in Chapter 6 using Mößbauer spectroscopy and magnetic susceptibility measurements. Figure 9-8 shows the summary of the magnetic susceptibility measurements (cooling mode only) for all seven complexes. No spin crossover behavior could be detected for any of the investigated complexes. All complexes were in the high spin state over the complete temperature range between 300 K and 5 K.

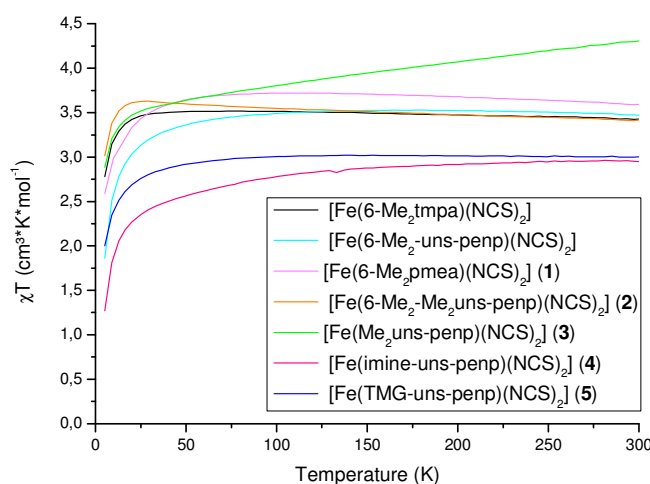


Figure 9-8: Magnetic susceptibility measurements for the compounds of Chapter 6 (cooling mode) between 300 K and 5 K.

In Chapter 7 the effect of chelate ring size in iron(II) complexes with tripodal ligands on the spin crossover behavior was investigated. Here the ligands tmpa, pmea, pmap and tepa (see Figure 9-9) were used to prepare the complexes of the general formula $[\text{Fe}(\text{L})(\text{NCS})_2]$. All of them were structurally characterized.

The difference in spin crossover behavior is clearly shown in magnetic susceptibility measurements (heating mode only) in Figure 9-10 (left) for these complexes. Whereas $[\text{Fe}(\text{tmpa})(\text{NCS})_2]$ shows a gradual spin crossover from low spin to high spin beginning above 180 K, that is not completed at 400 K, $[\text{Fe}(\text{pmea})(\text{NCS})_2]$ shows an abrupt spin crossover beginning at about 140 K (LS \rightarrow HS) to a plateau at $2.5 \text{ cm}^3 \text{ K}$ by reaching 210 K, followed by a gradual growing transition to the HS state monitored up to 400 K. Together with the Mößbauer results this clearly indicates a multistep spin transition.

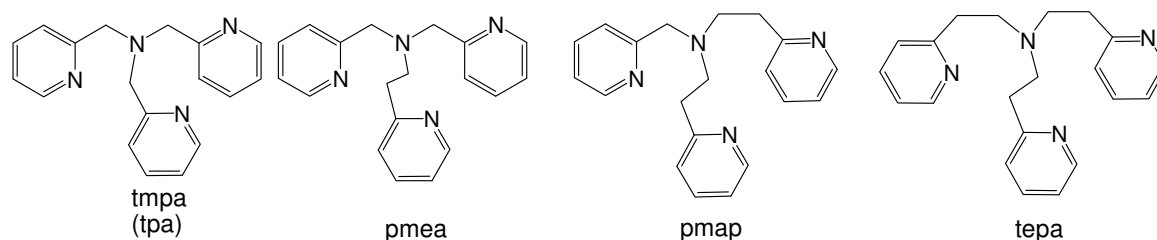


Figure 9-9: Abbreviations used for tripodal ligands: from left: tris(2-pyridylmethyl)amine (tmpa), N^2, N^2 -bis[(2-pyridyl)methyl]-2-(2-pyridyl)ethanamine (pmea), N^2, N^2 -bis[2-(2-pyridyl)ethyl]-(2-pyridyl)methylamine (pmap) and tris[2-(2-pyridyl)ethyl]amine (tepa).

Furthermore, Mößbauer studies were carried out for $[\text{Fe}(\text{pmea})(\text{NCS})_2]$. Figure 9-10 (right) shows ^{57}Fe Mößbauer spectra before and after light irradiation. Before light irradiation the complex $[\text{Fe}(\text{pmea})(\text{NCS})_2]$ is found in low spin state to 100% at 10 K. Under green light irradiation (514.5 nm ; 20 mW/cm^2) at 20 K a high spin state could be observed in addition to the low spin state (LIESST effect). After irradiation at 100 K, 100 % LS state is observed. Hence the photo-induced state is fully reversible and a photo-induced decomposition is excluded while at 175 K the thermal spin transition is still observed. Continuous red light irradiation (820 nm ; 40 mW/cm^2) at 170 K results in an alteration of the molar ratio. The effect of the light perturbed the thermal spin transition, this is called the LiPTH effect.²⁷⁸

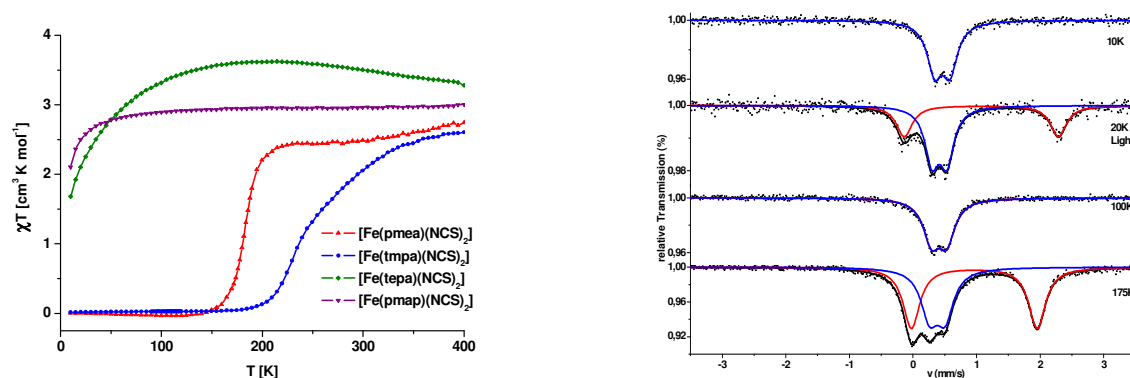


Figure 9-10: left: Magnetic susceptibility χT vs T plot (heating mode) for [Fe(tmpa)(NCS)₂], [Fe(pmea)(NCS)₂], [Fe(pmap)(NCS)₂] and [Fe(tepa)(NCS)₂] measured at 1 Tesla in a SQUID magnetometer between 6 and 400 K. Right: ⁵⁷Fe Mößbauer spectra of [Fe(pmea)(NCS)₂] before irradiation at 10 K shows 100% LS. At 20 K under green light irradiation (514.5 nm; 20 mW/cm²) clearly shows a light-induced excited spin state trapping (LIESST) effect. At 100 K after irradiation reversibility is indicated. While at 175 K still the thermal spin transition is reproduced.

Increasing the chelate ring sizes further using the ligands pmap and tepa has the consequence that in contrast to [Fe(tmpa)(NCS)₂] and [Fe(pmea)(NCS)₂] SCO behavior could not be observed anymore. The complexes [Fe(pmap)(NCS)₂] and [Fe(tepa)(NCS)₂] stayed in a high spin state from 6 to 400 K.

Most iron(II) complexes including two thiocyanate groups are found coordinating NCS-ligands in *cis*-position, including all complexes of the Chapters 5-7. Far less complexes are known with *trans*-coordinating positions of the NCS groups, because only rigid ligands will lead to *trans*-geometries more flexible ones will prefer α - or β -*cis* geometry.²⁸² In Chapter 8 the ligand 1,2-bis(6-(pyridin-2-yl)pyridin-2-yl)ethane (*o*-bipy) has been used that supports formation of a *trans*-complex. The *trans*-coordinated complex [Fe(*o*-bipy)(NCS)₂] could be prepared and was structurally characterized (Figure 9-11 (left)). Investigations in regard of spin crossover behavior were carried out using magnetic susceptibility in a SQUID magnetometer between 30 K and 300 K (heating and cooling modes). Figure 9-11 (right) shows the magnetic susceptibility χT vs T plot with no change in spin state, the complex is in high spin state over the complete temperature range.

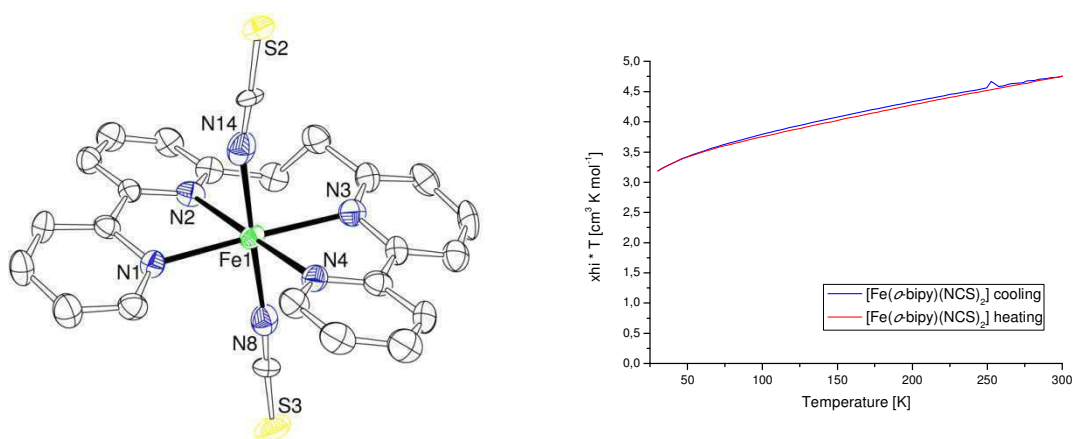
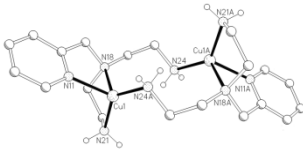
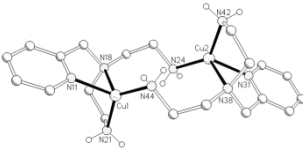
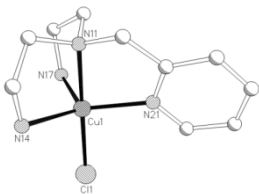
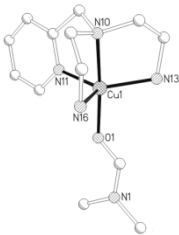
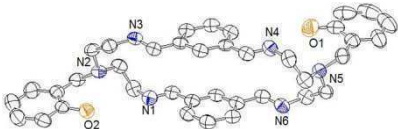
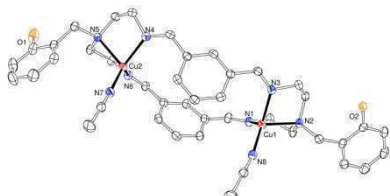
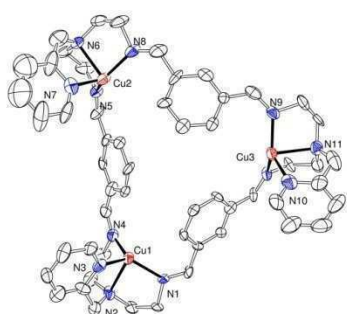


Figure 9-11: From left: ORTEP plot of the complex $[\text{Fe}(\text{o-bipy})(\text{NCS})_2]$. Right: Magnetic susceptibility χT vs T plot (cooling and heating modes) for $[\text{Fe}(\text{o-bipy})(\text{NCS})_2]$ between 30 and 300 K.

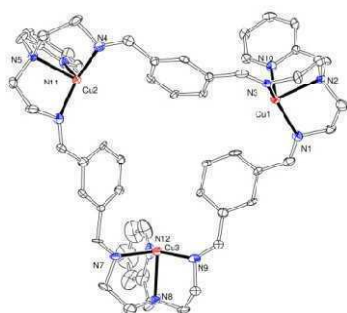
To summarize the Chapters 5-8 it could be demonstrated for the iron(II) complexes with tripodal ligands related to tmpa that so far $[\text{Fe}(\text{tmpa})(\text{NCS})_2]$ still showed the most interesting properties in regard to spin crossover behavior of these complexes. Despite a large number of ligand variations these changes did not lead to an optimization of spin crossover properties.

List of Crystal Structures

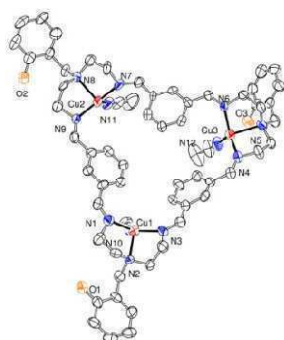
Ortep plot	Compound name, formula, formula weight [g mol ⁻¹]	Crystal System, Space group	Cell dimensions [Å], angles[°], Volumes [Å ³]
	1 [Cu ₂ (apme) ₂](ClO ₄) ₂ C ₁₀ H ₁₈ N ₄ CuClO ₄ 357.27	monoclinic; P2 ₁ /c	[a, b, c] = [9.6566(2), 10.1755(2), 14.5125(4)] [α, β, γ] = [90, 95.883(1), 90] V = 1418.50(6)
	2 [Cu ₂ (apme) ₂](CF ₃ SO ₃) ₂ C ₁₁ H ₁₈ N ₄ CuF ₃ O ₃ S 406.89	monoclinic; P2 ₁ /n	[a, b, c] = [14.7596(3), 10.1171(2), 21.7103(4)] [α, β, γ] = [90, 96.016(1), 90] V = 3224.0 (1)
	3 [Cu(apme)Cl] BPh ₄ C ₃₇ H ₄₅ N ₅ CuClBO 685.58	triclinic; P-1	[a, b, c] = [10.98030(10), 12.4384(2), 13.6573(2)] [α, β, γ] = [84.809(1), 71.945(1), 77.020(5)] V = 1727.68(4)
	4 [Cu(apme)(DMF)] BPh ₄ C ₆₄ H ₇₂ N ₆ CuB ₂ O ₂ 1042.44	monoclinic ; Cc	[a, b, c] = [17.9649(2), 12.8478(2), 25.478(4)] [α, β, γ] = [90, 101.224(1), 90] V = 5768.2 (4)
	5 bsm2PhOH C ₃₈ H ₄₂ N ₆ O ₂ 614.52	monoclinic ; P2 ₁	[a, b, c] = [13.357(5), 35.402(13), 14.629(6)] [α, β, γ] = [90, 101.776(7), 90] V = 6772(4)
	6 [Cu ₂ (bsm2PhOH)(MeCN) ₂](CF ₃ SO ₃) ₂ ·MeCN C ₄₈ H ₅₁ Cu ₂ N ₉ O ₈ F ₆ S ₂ 1163.16	monoclinic ; P2 ₁ /n	[a, b, c] = [15.203(3), 18.211(3), 19.084(3)] [α, β, γ] = [90, 99.371(3), 90] V = 5213.3(16)



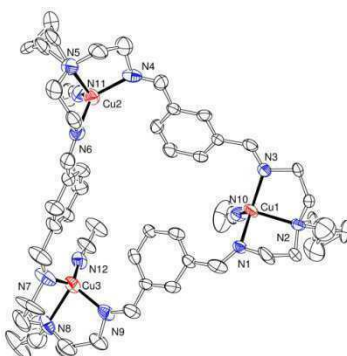
7 triclinic; P-1 [a, b, c] =
 $[\text{Cu}_3(\text{L}^4)](\text{PF}_6)_3$
 2.5THF·0.5H₂O·0.75MeOH
 $\text{C}_{64.75}\text{H}_{84}\text{Cu}_3\text{F}_{18}\text{N}_{12}\text{O}_{3.75}\text{P}_3$
 1715.97
 36.255(1)] [α , β , γ] =
 [80.620(2),
 81.518(2),
 82.902(2)]
 V = 7127.1(4)



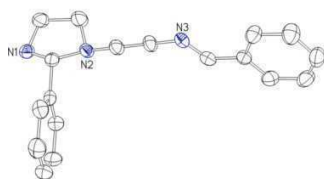
8 triclinic; P-1 [a, b, c] =
 $[\text{Cu}_3(\text{L}^4)](\text{SbF}_6)_3$
 $\text{C}_{54}\text{H}_{59}\text{Cu}_3\text{F}_{18}\text{N}_{12}\text{Sb}_3$
 1774.00
 36.255(1)] [α , β , γ] =
 [80.620(2),
 81.518(2),
 82.902(2)]
 V = 7127.1(4)



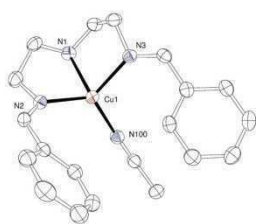
9 triclinic; P-1 [a, b, c] = [15.72(2),
 $[\text{Cu}_3(\text{L}^5)(\text{MeCN})_3](\text{CF}_3\text{SO}_3)_3$
 2 H₂O
 $\text{C}_{66}\text{H}_{76}\text{Cu}_3\text{F}_9\text{N}_{12}\text{O}_{14}\text{S}_3$
 1719.19
 16.73(2), 18.04(3)]
 [α , β , γ] = [104.45(3),
 111.79(3),
 106.39(3)]
 V = 3878(10)



10 triclinic; P-1 [a, b, c] = [11.383(6),
 $[\text{Cu}_3(\text{L}^6)(\text{CH}_3\text{CN})_3](\text{CF}_3\text{SO}_3)_3 \cdot$
 1EtOEt
 $\text{C}_{55}\text{H}_{76}\text{Cu}_3\text{N}_{12}\text{F}_9\text{O}_{10}\text{S}_3$
 1523.08
 14.732(8),
 20.652(11)] [α , β , γ]
 = [84.485(10),
 80.547(9),
 86.199(10)]
 V = 3396(3)

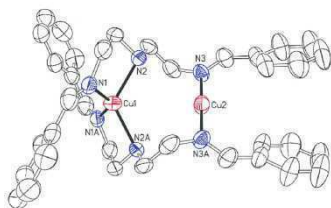


11 monoclinic ; [a, b, c] = [8.947(1),
 L^1
 P2_1
 $\text{C}_{18}\text{H}_{21}\text{N}_3$
 279.38
 5.515(1), 16.088(2)]
 [α , β , γ] = [90,
 90.93(1), 90]
 V = 784.2(2)



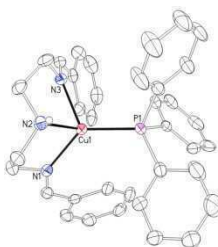
12
 $[\text{Cu}(\text{L}^1)(\text{CH}_3\text{CN})]\text{PF}_6$
 $\text{C}_{20}\text{H}_{24}\text{N}_4\text{CuPF}_6$
 528.94

triclinic; P1 $[a, b, c] = [8.8145(2), 11.2443(2), 12.2806(2)]$ $[\alpha, \beta, \gamma] = [110.282(1), 91.682(1), 95.242(1)]$
 $V = 1134.49(4)$



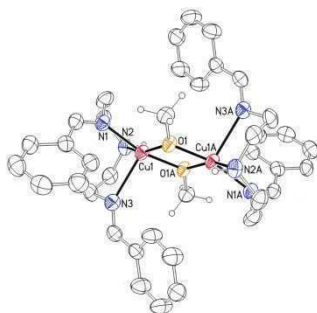
13
 $[\text{Cu}_2(\text{L}^1)_2](\text{ClO}_4)_2$
 $\text{C}_{36}\text{H}_{42}\text{N}_6\text{Cu}_2\text{Cl}_2\text{O}_8$
 884.74

monoclinic ; C2/c $[a, b, c] = [16.763(1), 15.213(1), 17.344(1)]$ $[\alpha, \beta, \gamma] = [90, 116.44(1), 90]$
 $V = 3960.3(5)$



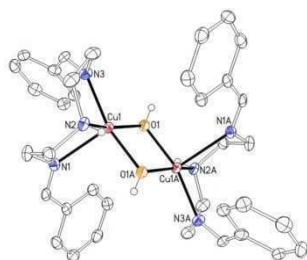
14
 $[\text{Cu}(\text{L}^1)(\text{PPh}_3)](\text{ClO}_4)$
 $\text{C}_{37.5}\text{H}_{39}\text{N}_3\text{CuCl}_{1.33}\text{PO}_{4.33}$
 742.83

trigonal ; R-3 $[a, b, c] = [35.126(1), 35.126(1), 15.4896(5)]$ $[\alpha, \beta, \gamma] = [90, 90, 120]$
 $V = 16550.7(9)$



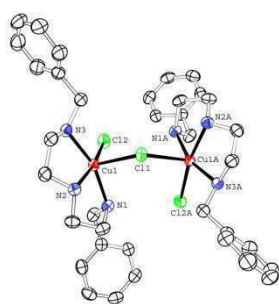
15
 $[\text{Cu}_2(\text{L}^1)_2(\text{OCH}_3)_2](\text{PF}_6)_2$
 $\text{C}_{38}\text{H}_{48}\text{N}_6\text{O}_2\text{Cu}_2\text{P}_2\text{F}_{12}$
 1037.84

monoclinic; $P2_1/n$ $[a, b, c] = [9.074(1), 11.193(1), 21.017(3)]$ $[\alpha, \beta, \gamma] = [90, 92.75(1), 90]$
 $V = 2132.1(4)$

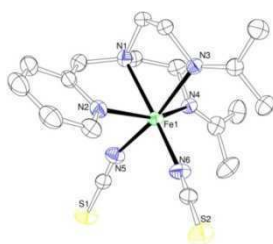


16
 $[\text{Cu}_2(\text{L}^1)_2(\text{OH})_2](\text{PF}_6)_2$
 $\text{C}_{42}\text{H}_{56}\text{N}_6\text{O}_4\text{Cu}_2\text{P}_2\text{F}_{12}$
 1125.95

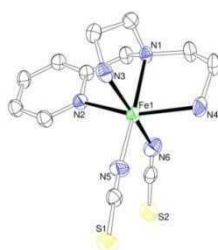
triclinic; P-1 $[a, b, c] = [9.4575(4), 10.6958(5), 12.4593(7)]$ $[\alpha, \beta, \gamma] = [101.657(4), 92.168(4), 104.018(3)]$
 $V = 1192.6(1)$



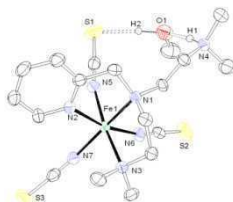
17
 $[\text{Cu}_2(\text{L}^2)_2\text{Cl}_3]\text{PF}_6 \cdot 2\text{MeOH}$
 $\text{C}_{38}\text{H}_{50}\text{Cl}_3\text{Cu}_2\text{F}_6\text{N}_6\text{O}_2\text{P}$
 1001.24
 monoclinic;
 $\text{C}2/c$
 $[a, b, c] =$
 $[22.0450(4),$
 $7.3390(2),$
 $27.4254(5)]$ $[\alpha, \beta, \gamma]$
 $= [90, 102.720(2),$
 $90]$
 $V = 4328.2(2)$



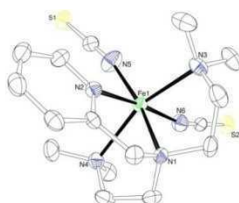
18
 $[\text{Fe}(\text{imine}_2\text{-apme})(\text{NCS})_2]$
 $\text{C}_{18}\text{H}_{26}\text{FeN}_6\text{S}_2$
 446.44
 orthorhombic;
 $\text{Pna}2_1$
 $[a, b, c] =$
 $[15.1739(2),$
 $8.9232(1),$
 $32.3826(6)]$ $[\alpha, \beta, \gamma]$
 $= [90, 90, 90]$
 $V = 4384.6(1)$



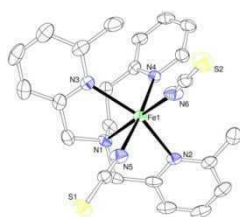
19
 $[\text{Fe}(\text{apme})(\text{NCS})_2]$
 $\text{C}_{12}\text{H}_{18}\text{FeN}_6\text{S}_2$
 366.29
 monoclinic;
 $\text{P}2_1/c$
 $[a, b, c] = [7.9242(3),$
 $13.2741(4),$
 $15.4981(5)]$ $[\alpha, \beta, \gamma]$
 $= [90, 92.338(3), 90]$
 $V = 1628.84(9)$



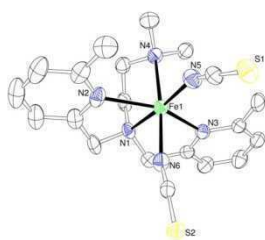
20
 $[\text{Fe}(\text{HMe}_4\text{apme})(\text{NCS})_3]$
 $\text{C}_{18}\text{H}_{31}\text{FeN}_7\text{OS}_3$
 513.53
 monoclinic;
 $\text{P}2_1/c$
 $[a, b, c] = [10.461(1),$
 $16.932(2),$
 $14.220(2)]$ $[\alpha, \beta, \gamma] =$
 $[90, 100.28(1), 90]$
 $V = 2478.4(4)$



21
 $[\text{Fe}(\text{Me}_4\text{apme})(\text{NCS})_3]$
 $\text{C}_{16}\text{H}_{26}\text{FeN}_6\text{S}_2$
 422.40
 monoclinic;
 $\text{P}2_1/n$
 $[a, b, c] = [9.769,$
 $15.934, 13.057]$
 $[\alpha, \beta, \gamma] = [90,$
 $93.23(3), 90]$
 $V = 2029.3(7)$



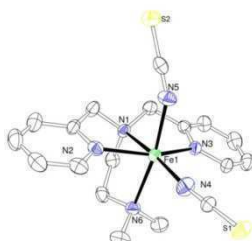
22
 $\text{Fe}(\text{6-Me}_2\text{pmea})(\text{NCS})_2]$
 $\text{C}_{23}\text{H}_{23}\text{FeN}_6\text{S}_2$
 503.44
 monoclinic ;
 $\text{P}2_1/n$
 $[a, b, c] =$
 $[10.5625(3),$
 $14.9136(4),$
 $15.1715(4)]$ $[\alpha, \beta, \gamma]$
 $= [90, 96.938(3), 90]$
 $V = 2372.4(1)$



23
 $\text{Fe}(6\text{-Me}_2\text{-Me}_2\text{uns-penp})(\text{NCS})_2$
 $\text{C}_{20}\text{H}_{26}\text{FeN}_6\text{S}_2$
 470.44

monoclinic ;
 $P 2_1/c$

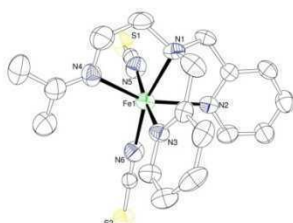
$[a, b, c] =$
 $[21.0056(8),$
 $12.1951(5),$
 $17.4014(7)]$ $[\alpha, \beta, \gamma]$
 $= [90, 93.406(4), 90]$
 $V = 4449.8(3)$



24
 $\text{Fe}(\text{Me}_2\text{uns-penp})(\text{NCS})_2$
 $\text{C}_{18}\text{H}_{22}\text{FeN}_6\text{S}_2$
 442.39

monoclinic;
 $P 2_1/n$

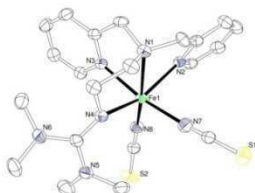
$[a, b, c] = [8.240(2),$
 $13.467(3),$
 $18.397(4)]$ $[\alpha, \beta, \gamma] =$
 $[90, 94.07(3), 90]$
 $V = 2036.4(7)$



25
 $\text{Fe}(\text{imine-uns-penp})(\text{NCS})_2$
 $\text{C}_{19}\text{H}_{22}\text{FeN}_6\text{S}_2$
 454.40

orthorhombic;
 $Pna2_1$

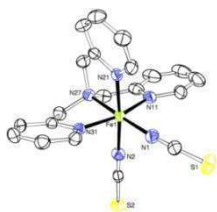
$[a, b, c] = [15.295(3),$
 $10.669(2),$
 $13.387(3)]$ $[\alpha, \beta, \gamma] =$
 $[90, 90, 90]$
 $V = 2184.5(8)$



26
 $\text{Fe}(\text{TMG-uns-penp})(\text{NCS})_2$
 $\text{C}_{21}\text{H}_{28}\text{FeN}_8\text{S}_2$
 512.48

triclinic; $P-1$

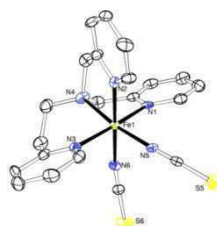
$[a, b, c] = [8.607(2),$
 $10.094(2),$
 $15.492(3)]$ $[\alpha, \beta, \gamma] =$
 $[86.01(3), 82.98(3),$
 $66.28(3)]$
 $V = 1222.6(4)$



27
 $[\text{Fe}(\text{tmpa})(\text{NCS})_2]$
 $\text{C}_{20}\text{H}_{18}\text{FeN}_6\text{S}_2$
 462.37

monoclinic;
 $P 2_1/c$

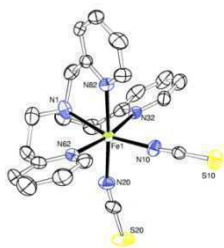
$[a, b, c] = [13.5652$
 $(2), 20.7575(4),$
 $15.1192(3)]$ $[\alpha, \beta, \gamma]$
 $= [90, 96.930(1), 90]$
 $V = 4226.2(1)$



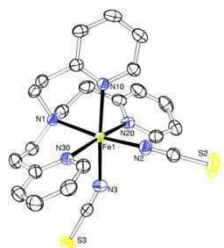
28
 $[\text{Fe}(\text{pmea})(\text{NCS})_2]$
 $\text{C}_{21}\text{H}_{20}\text{FeN}_6\text{S}_2$
 476.40

orthorhombic;
 $Pna2_1$

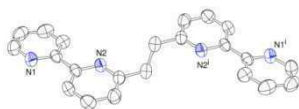
$[a, b, c] = [14.989(2),$
 $10.438(1),$
 $13.341(3)]$ $[\alpha, \beta, \gamma] =$
 $[90, 90, 90]$
 $V = 2087.3(6)$



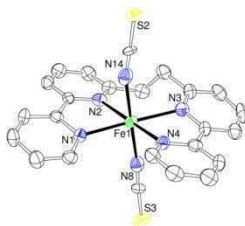
29 [Fe(pmap)(NCS) ₂] C ₂₂ H ₂₂ FeN ₆ S ₂ 490.43	orthorhombic; Pna2 ₁	[a, b, c] = [15.5048(5), 10.8670(3), 13.4399(4)] [α, β, γ] = [90, 90, 90] V = 2264.5(1)
---	---------------------------------	--



30 [Fe(tepa)(NCS) ₂] C ₂₃ H ₂₄ FeN ₆ S ₂ 504.45	orthorhombic; Pna2 ₁	[a, b, c] = [8.1210(2), 15.1714(3), 18.8912(6)] [α, β, γ] = [90, 90, 90] V = 2327.4(1)
---	---------------------------------	--



31 o-bipy C ₂₂ H ₁₈ N ₄ 338.40	monoclinic; P2 ₁ /n	[a, b, c] = [6.614(1), 12.157(2), 11.040(2)] [α, β, γ] = [90, 90.043(6), 90] V = 887.7(2)
---	--------------------------------	---



32 Fe(o-bipy)(NCS) ₂ C ₂₄ H ₁₈ FeN ₆ S ₂ 510.41	triclinic; P-1	[a, b, c] = [9.084(2), 9.346(2), 13.728(3)] [α, β, γ] = [98.33(3), 101.07(3), 100.85(3)] V = 1103.3(4)
--	----------------	---

Publications

- “Synthesis and Characterization of Iron(II) Thiocyanate Complexes with Derivatives of the Tris(2-pyridylmethyl)amine (tmpa) Ligand” (Kisslinger, S., Kelm, H., Zheng, S., Bonnet, S., Beitat, A., Würtele, C., Wortmann, R., Herres-Pawlis, S., Krüger, H.-J. and Schindler, S. submitted to *Z. Anorg. Allg. Chem.*, **2012**)
- “Effect of chelate ring size in iron(II) thiocyanate complexes with tetradentate tripyridyl-alkylamine tripodal ligands” (Leibold, M., Kisslinger, S., Heinemann, F., Hampel, F., Renz, F., Toftlund, H., Brehm, G., Schneider, S., Reiher, M. and Schindler, S. To be submitted to *Inorg. Chem.*, **2012**)
- “Ligand influence over the formation of [2+2] versus [3+3] Cu(I) Schiff Base Macrocyclic Complexes” (Arbuse, A., Mandal, S., Maji, S, Martínez, M. A., Fontrodona, X., Utz, D., Heinemann, F. W., Kisslinger, S., Schindler, S., Sala, X., Llobet, A. *Inorg. Chem.* **2011**, 50, 6878–6889. (doi: 10.1021/ic102185y))
- “Synthesis, characterization and properties of iron(II) complexes with a series of tripodal ligands based on the parent ligand tris(2- pyridylmethyl)amine” (Kisslinger, S., Kelm, H., Beitat, A., Würtele, C., Krüger, H.-J. and Schindler, S.. *Inorg. Chim. Acta* **2011**, 374, 540-545. (doi: 10.1016/j.ica.2011.02.062))
- “Syntheses, Characterization and Oxidation Behavior of Open-Chain Copper(I) Complexes” (Utz, D., Kisslinger, S., Heinemann, F. W., Hampel, F. and Schindler, S. *Chem. Eur. J.*, **2011**, 255–267. (doi: 10.1002/ejic.201000954))
- „Syntheses and characterization of copper complexes with the ligand 2-aminoethyl(2-pyridylmethyl)-1,2-ethanediamine (apme)“ (Utz D., Kisslinger, S., Hampel F., Schindler S. *J. Inorg. Biochem.* **2008**, 102, 1236–1245. (doi: 10.1016/j.jinorgbio.2008.01.028))

Presentations

- Poster Presentation: Spin Crossover Meeting of Bad Dürkheim (2010/3)
Spin Crossover Properties of Iron(II) Complexes with Tripodal Ligands”
- Oral Presentation: Koordinationschemie Tagung of Mainz (2010/2)
“Spin-Crossover Eigenschaften von Eisen(II)-Komplexen”
(<http://www.chemie.unimainz.de/AC/Dateien/Tagungsband.pdf>)
- Poster Presentation: EuChems Conference of Turin (2008/9)
“Systematic Study of the Spin Crossover Properties of Iron(II) Complexes with Tripodal Ligands”
- Poster Presentation: GdCh-Wissenschaftsforum of Ulm (2007/09)
“Effects of Chelating growth of mononuclear tripodal Iron(II)- Complexes”

The curriculum vitae was removed from the
electronic version of the paper.

Bibliography

- Hollemann, A. F.; Wiberg, E., *Lehrbuch der Anorganischen Chemie*. de Gruyter: Berlin, New York, 1995.
- Pascaly, M.; Jolk, I.; Krebs, B., *Chem. unserer Zeit* **1999**, 6, 334-341.
- Kaim, W.; Rall, J., *Angew. Chem., Int. Ed.* **1996**, 35, 43-60.
- Decker, H.; Dillinger, R.; Tuczek, F., *Angew. Chem. Int. Ed.* **2000**, 39, 1591-1595.
- Decker, H.; Schweikardt, T.; Tuczek, F., *Angew. Chem. Int. Ed.* **2006**, 45, 4546-4550.
- Matoba, Y.; T.Kumagai; Yamamoto, A.; Yoshitsu, H.; Sugiyama, M., *J. Biol. Chem.* **2006**, 281, 8981-8990.
- Tipler, P. A.; Llewellyn, R. A., *Moderne Physik*. Oldenbourg Wissenschaftsverlag GmbH: Oldenbourg - München - Wien, 2003; p 564-567.
- Min, K. S.; Swierczek, K.; DiPasquale, A. G.; Rheingold, A. L.; Reiff, W. M.; Arifa, A. M.; Miller, J. S., *Chem. Commun.* **2008**, 317-319.
- Biswas, B.; Salunke-Gawali, S.; Weyhermüller, T.; Bachler, V.; Bill, E.; Chaudhuri, P., **2008**, 2391-2395.
- Miyake, Y.; Watanabe, S.; Aono, S.; Nishinaga, T.; Miyazaki, A.; Enoki, T.; Miyasaka, H.; Otanic, H.; Iyoda, M., **2008**, 6167-6169.
- Weyhermüller, T.; Wagner, R.; Chaudhuri, P., *Eur. J. Inorg. Chem.* **2011**, 2547-2557.
- Abedi, A.; Safari, N.; Amanib, V.; Khavasi, H. R., *Dalton Trans.* **2011**, 40, 6877-6885.
- Baca, S. G.; Botezat, O.; Filippova, I.; Speldrich, M.; Jeanneau, E.; Kögerler, P., *Z. Anorg. Allg. Chem.* **2011**, 637, 821-823.
- Fuchs, M. G. G.; Dechert, S.; Demeshko, S.; Ryde, U.; Meyer, F., *Inorg. Chem.* **2010**, 49, 5853-5858.
- Zhang, Y.-J.; Liu, T.; Kanegawa, S.; Sato, O., *J. Am. Chem. Soc.* **2009**, 131, 7942-7943.
- Wen, H.-R.; Wang, C.-F.; Li, Y.-Z.; Zuo, J.-L.; Song, Y.; You, X.-Z., *Inorg. Chem.* **2006**, 45, 7032-7034.
- Janiak, C.; Klapötke, T. M.; Meyer, H.-J., *E. Riedel - Moderne Anorganische Chemie*. 2. Auflage ed.; de Gruyter: Berlin; New York, 2003; p 207-219.
- Gütlich, P., *Spin Crossover in Iron(II)-Complexes*. Springer Verlag: Berlin - Heidelberg - New York, 1981.
- Goodwin, H. A.; Sylva, R. N., *Aust. J. Chem.* **1968**, 21, 83-90.
- Fleisch, J.; Gütlich, P.; Hasselbach, K. M.; Müller, W., *Inorg. Chem.* **1976**, 15, 958-961.
- Baker, W. A.; Bobonich, H. M., *Inorg. Chem.* **1964**, 3, 1184-1188.
- Real, J. A.; Gaspar, A. B.; Munoz, M. C., *Dalton Transactions* **2005**, 2062-2079.
- Cambi, L.; Cagnasso, A., *Atti Accad. Naz. Lincencei* **1931**, 13, 809.
- Cambi, L.; Malatesta, L., *Ber. Dtsch. Chem. Ges* **1937**, 70, 2067-2078.
- Cambi, L.; Szegö, L., *Ber. Dtsch. Chem. Ges.* **1931**, 64, 259-264.
- Cambi, L.; Szegö, L.; Cagnasso, A., *Atti Accad. Naz. Lincencei* **1932**, 15, 266.
- Ewald, A. H.; Martin, R. L.; Ross, I.; A. H. White, P., *R. Soc. London, Ser. A* **1964**, 280, 235-257.
- White, A. H.; Roper, R.; Kokot, E.; Waterman, H.; Martin, R. L., *Aust. J. Chem.* **1964**, 17, 294-303.
- Gütlich, P.; Hauser, A.; Spiering, H., *Angew. Chem. Int. Ed.* **1994**, 33, 2024-2054.
- Gütlich, P.; Goodwin, H. A., *Top. Curr. Chem.* **2004**, 233, 1-47.
- Yousif, A. A.; Winkler, H.; Toftlund, H.; Trautwein, A. X.; Herber, R. H., *J. Phys.: Cond. Matt.* **1989**, 1, 7103-7112.
- Yu, Z.; Hsia, Y. F.; You, X. Z.; Spiering, H.; Gütlich, P., *J. Mat. Sci.* **1997**, 32, 6579-6581.
- Decurtins, S.; Gütlich, P.; Köhler, C. P.; Spiering, H., *Chem. Phys. Lett.* **1984**, 105, 1-4.
- Létard, J.-F.; Guionneau, P.; Gaux-Capes, L., *Top. Curr. Chem.* **2004**, 235, 221-249.
- Verdaguer, M., *Polyhedron* **2001**, 20, 1115-1128.

36. Lippard, S. J.; Berg, J. M., *Bioanorganische Chemie*. Spektrum Akademischer Verlag: Heidelberg- Berlin -Oxford, 1995; p 302-310.
37. Fischetti, M., *Spektrum der Wissenschaft - Dossier* 2005, pp 32-33.
38. Westerheide, L.; Müller, F. K.; Than, R.; Krebs, B.; Dietrich, J.; Schindler, S., *Inorg. Chem.* **2001**, *40*, 1951-1961.
39. Kryatov, S. V.; Rybak-Akimova, E. V.; Schindler, S., *Chem. Rev.* **2005**, *105*, 2175-2226.
40. LeCloux, D. D.; Barrios, A. M.; Mizoguchi, T. J.; Lippard, S. J., *J. Am. Chem. Soc.* **1998**, *120*, 9001-9014.
41. Que L., J.; Ho, R. Y. N., *Chem. Rev.* **1996**, *96*, 2607-2624.
42. Toftlund, H., *Coord. Chem. Rev.* **1989**, *94*, 67-108.
43. Fox, S.; Karlin, K. D., *Active Oxygen in Biochemistry*, Blackie Academic and Professional. Chapman & Hall: Glasgow, 1995; p 188-231.
44. Holm, R. H.; Kennepohl, P.; Solomon, E. I., *Chem. Rev.* **1996**, *96*, 2239-2314.
45. Kaim, W.; Schwederski, B., *Bioanorganische Chemie*. Teubner Verlag: Stuttgart, 1991.
46. Karlin, K. D.; Zuberbühler, A. D., *Bioinorganic Chemistry*. Teubner Verlag: 1999.
47. Kitajima, N., *Adv. Inorg. Chem.* **1992**, *39*, 1-77.
48. Reedijk, J.; Bouwman, E., *Bioinorganic Catalysis*. CRC: New York, 1999.
49. Jacobson, R. R.; Tyeklar, Z.; Farooq, A.; Zubieta, J.; Karlin, K. D.; Liu, S., *J. Am. Chem. Soc.* **1988**, *110*, 3690-3692.
50. Karlin, K. D.; Wei, N.; Jung, B.; Kaderli, S.; Niklaus, P.; Zuberbühler, A. D., *J. Am. Chem. Soc.* **1993**, *115*, 9506-9514.
51. Weitzer, M.; Schatz, M.; Hampel, F.; Heinemann, F. W.; Schindler, S., *Dalton Trans.* **2002**, 686-694.
52. Weitzer, M.; Schindler, S.; Brehm, G.; Schneider, S.; Hörmann, E.; Jung, B.; Kaderli, S.; Zuberbühler, A. D., *Inorg. Chem.* **2003**, *42*, 1800-1806.
53. Schatz, M.; Becker, M.; Thaler, F.; Hampel, F.; Schindler, S.; Jacobson, R. R.; Tyeklar, Z.; Murthy, N. N.; Ghosh, P.; Chen, Q.; Zubieta, J.; Karlin, K. D., *Inorg. Chem.* **2001**, *40*, 2312-2322.
54. Schatz, M.; Becker, M.; Walter, O.; Liehr, G.; Schindler, S., *Inorg. Chim. Acta* **2001**, *324*, 173-179.
55. Schatz, M.; Leibold, M.; Foxon, S. P.; Weitzer, M.; Heinemann, F. W.; Hampel, F.; Walter, O.; Schindler, S., *Dalton Trans.* **2003**, 1480-1487.
56. Thaler, F.; Hubbard, C. D.; Heinemann, F. W.; Eldik, R. v.; Schindler, S., *Inorg. Chem.* **1998**, *37*, 4022-4029.
57. Wei, N.; Murthy, N. N.; Chen, Q.; Zubieta, J.; Karlin, K. D., *Inorg. Chem.* **1994**, *33*, 1953-1965.
58. Würtele, C.; Gaoutchenova, E.; Harms, K.; Holthausen, M. C.; Sundermeyer, J.; Schindler, S., *Angew. Chem., Int. Ed.* **2006**, *45*, 3867-3869.
59. Solomon, E. I.; Sundaram, U. M.; Machonkin, T. E., *Chem. Rev.* **1996**, *96*, 2563-2606.
60. Schindler, S., *Eur. J. Inorg. Chem.* **2000**, 2311-2326.
61. Lewis, E. A.; Tolman, W. B., *Chem. Rev.* **2004**, *104*, 1047-1076.
62. Köhn, R. D.; Seifert, G.; Kociok-Köhn, G., *Chem. Ber.* **1996**, *129*, 1327-1333.
63. Kojima, T.; Leising, R. A.; Yan, S.; L. Que, J., *J. Am. Chem. Soc.* **1993**, *115*, 11328-11335.
64. Hazell, A.; McKenzie, C. J.; Nielsen, L. P.; Schindler, S.; Weitzer, M., *J. Chem. Soc., Dalton Trans.* **2002**, 313-317.
65. Chiou, Y.-M.; L. Que, J., *J. Am. Chem. Soc.* **1995**, *117*, 3999-4013.
66. Ha, E. H.; R. Y. N., Ho; Kisiel, J. F.; Valentine, S. J., *Inorg. Chem.* **1995**, *34*, 2265-2266.
67. Blackman, A. G., *Polyhedron* **2005**, *24*, 1-39.
68. Matouzenko, G. S.; Bousseksou, A.; Lecoq, S.; Koningsbruggen, P. J. v.; Perrin, M.; Kahn, O.; Collet, A., *Inorg. Chem.* **1997**, *36*, 2975-2981.
69. Zang, Y.; Kim, J.; Dong, Y.; Wilkinson, E. C.; Appelman, E. H.; Lawrence Que, J., *J. Am. Chem. Soc.* **1997**, *119*, 4197-4205.
70. Sugano, S.; Tanabe, Y., *J. Phys. Soc. Jpn.* **1958**, *13*, 43-48.
71. Buchen, T.; Toftlund, H.; Gütllich, P., *Chem. Eur. J.* **1996**, *2*, 1129-1133.

72. Matouzenko, G. S.; Bousseksou, A.; Lecoq, S.; Koningsbruggen, P. J. v.; Perrin, M.; Kahn, O.; Collet, A., *Inorg. Chem.* **1997**, *36*, 5869-5879.
73. Renz, F.; Oshio, H.; Ksenofontov, V.; Waldeck, M.; Spiering, H.; Gütllich, P., *Angew. Chem.* **2000**, *112*, 3832-3834.
74. Yu, Z.; HSIA, Y. F.; YOU, X. Z.; Spering, H.; Gütllich, P., *Journal of Material Science* **1997**, *32*, 6579-6581.
75. Brehm, G.; Reiher, M.; Guennic, B. L.; Leibold, M.; Schindler, S.; Heinemann, F. W.; Schneider, S., *J. Raman Spectra.* **2006**, *37*, 108-122.
76. Brehm, G.; Reiher, M.; Schneider, S., *J. Phys. Chem.* **2002**, *106*, 12024-12034.
77. Li, B.; Wei, R.-J.; Tao, J.; Huang, R.-B.; Zheng, L.-S., *Inorg. Chem.* **2010**, *49*, 745-751.
78. Li, B.; Wei, R.-J.; Tao, J.; Huang, R.-B.; Zheng, L.-S.; Zheng, Z., *J. Am. Chem. Soc.* **2010**, *132*, 1558-1566.
79. Wei, R.-J.; Li, B.; Tao, J.; Huang, R.-B.; Zheng, L.-S.; Zheng, Z., *Inorg. Chem.* **2011**, *50*, 1170-1172.
80. Wei, R.-J.; Huo, Q.; Tao, J.; Huang, R.-B.; Zheng, L.-S., *Angew. Chem Int. Ed.* **2011**, *50*, 8940-8943.
81. Garber, T.; Wallendaal, S. V.; Rillema, D. P.; Kirk, M.; Hatfield, W. E.; Welch, J. H.; Singh, P., *Inorg. Chem.* **1990**, *29*, 2863-2868.
82. Solomon, E. I.; Sarangi, R.; Woertink, J. S.; Augustine, A. J.; Yoon, J.; Ghosh, S., *Acc. Chem. Res.* **2007**, *40*, 581-591.
83. Lerch, K., in *Enzymatic Browning and Its Prevention*. ACS Symposium Series: 1995; Vol. 600, p 64-80.
84. Hatcher, L. Q.; Karlin, K. D., *J. Biol. Inorg. Chem.* **2004**, *9*, 669-683.
85. Mirica, L. M.; Ottenwaelder, X.; Stack, T. D. P., *Chem. Rev.* **2004**, *104*, 1013-1045.
86. Cramer, C. J.; Tolman, W. B., *Acc. Chem. Res.* **2007**, *40*, 601-608.
87. Itoh, S.; Fukuzumi, S., *Acc. Chem. Res.* **2006**, *40*, 592-600.
88. Suzuki, M., *Acc. Chem. Res.* **2006**, *40*, 609-617.
89. Mukherjee, R., *Comprehensive Coordination Chemistry II: From Biology to Nanotechnology*. Pergamon: 2004; Vol. 5, p 747-910.
90. Schatz, M.; Raab, V.; Foxon, S. P.; Brehm, G.; Schneider, S.; Reiher, M.; Holthausen, M. C.; Sundermeyer, J.; Schindler, S., *Angew. Chem. Int. Ed.* **2004**, *43*, 4360-4363.
91. Tyeklar, Z.; Jacobson, R. R.; Wei, N.; Murthy, N. N.; Zubieta, J.; Karlin, K. D., *J. Am. Chem. Soc.* **1993**, *37*, 2677-2689.
92. Zhang, C. X.; Kaderli, S.; Costas, M.; Kim, E.-I.; Neuhold, Y.-M.; Karlin, K. D.; Zuberbühler, A. D., *Inorg. Chem.* **2003**, *42*, 1807-1824.
93. Becker, M.; Heinemann, F. W.; Schindler, S., *Chem. Eur. J.* **1999**, *5*, 3124-3129.
94. Komiyama, K.; Furutachi, H.; Nagatomo, S.; Hashimoto, A.; Hayashi, H.; Fujinami, S.; Suzuki, M.; Kitagawa, T., *Bull. Chem. Soc. Jpn.* **2004**, *77*, 59-72.
95. Prigge, S. T.; Eipper, B. A.; Mains, R. E.; Amzel, L. M., *Science* **2004**, *304*, 864-867.
96. Fenton, D. E.; Rossi, G., *Inorg. Chim. Acta* **1985**, *98*, L29-30.
97. Adams, H.; Bailey, N. A.; Carlisle, W. D.; Fenton, D. E.; Rossi, G., *Dalton Trans.* **1990**, 1271-1283.
98. Adams, H.; Elsegood, M. R. J.; Fenton, D. E.; Heath, S. L.; Ryan, S. J., *Dalton Trans.* **1999**, 2031-2037.
99. Barbarin, C. O. R. d.; Bailey, N. A.; Fenton, D. E.; He, Q.-Y., *Dalton Trans.* **1997**, 161-166.
100. Skinner, M. G. E.; Cawnig, D. A.; Mountford, P., *Chem. Commun.* **2000**, *13*, 1167-1168.
101. Skinner, M. G. E.; Li, Y.; Mountford, P., *Inorg. Chem.* **2002**, *41*, 1110-1119.
102. Cheng, T.-H.; Wang, Y.-M.; Lee, W.-T.; Liu, G.-C., *Polyhedron* **2000**, *19*, 2027-2037.
103. Abdel-Magid, A. F.; Carson, K. G.; Harris, B. D.; Maryanoff, C. A.; Shah, R. D., *J. Org. Chem.* **1996**, *61*, 3849-3862.
104. Britovsek, G. J. P.; England, J.; White, A. J. P., *Inorg. Chem.* **2005**, *44*, 8125-8134.
105. Weitzer, M.; Brooker, S., *Dalton Trans.* **2005**, 2448-2454.
106. Chiu, Y.-H.; Canary, J. W., *Inorg. Chem.* **2003**, *42*, 5107-5116.
107. Gerdemann, C.; Eicken, C.; Krebs, B., *Acc. Chem. Res.* **2002**, *35*, 183-191.

108. Addison, A. W.; Rao, T. N.; Reedijk, J.; Rijn, J. v.; Verschoor, G. C., *Dalton Trans.* **1984**, 1349-1356.
109. Chen, C. H.; Cai, J.; Chen, X. M., *Acta Cryst., Sec. C* **2002**, C58, m59-m60.
110. Laskowski, E. J.; Duggan, D. M.; Henrickson, D. N., *Inorg. Chem.* **1975**, 14, 2449-2459.
111. Karlin, K. D.; Hayes, J. C.; Juen, S.; Hutchinson, J. P.; Zubieta, J., *Inorg. Chem.* **1982**, 21, 4106-4108.
112. Henrick, P. M. J. K.; McPartlin, M.; Tasker, P. A.; Turner, R. W., *Inorg. Chim. Acta* **1981**, L265-L266.
113. Henrick, P. M. J. K.; Owston, P. G.; Peters, R.; Tasker, P. A.; Turner, R. W., *Chem. Commun.* **1983**, 1253-1254.
114. Cheng, P.-H. C. H.-Y.; Lee, C.-F.; Peng, S.-M., *Inorg. Chim. Acta* **1991**, 145-147.
115. Becker, M.; Schindler, S.; Karlin, K. D.; Kaden, T. A.; Kaderli, S.; Palanche, T.; Zuberbühler, A. D., *Inorg. Chem.* **1999**, 38, 1989-1995.
116. Börzel, H.; Comba, P.; Hagen, K. S.; Kerscher, M.; Pritzkow, H.; Schatz, M.; Schindler, S.; Walter, O., *Inorg. Chem.* **2002**, 41, 5440-5452.
117. Klinman, J. P., *Chem. Rev.* **1996**, 96, 2541-2561.
118. Klinman, J. P., *J. Biol. Chem.* **2005**, 281, 3013-3016.
119. Maiti, D.; Lee, D.-H.; Gaoutchenova, K.; Würtele, C.; Holthausen, M. C.; Sarjeant, A. A. N.; Sundermeyer, J.; Schindler, S.; Karlin, K. D., *Angew. Chem.* **2007**, 120, 88-91.
120. Leonard, J.; Lygo, B.; Procter, G., *Praxis der organischen Chemie*. VCH-Verlag: Weinheim, 1996.
121. Kubas, G. J., *Inorg. Synth.* **1979**, 19, 90-92.
122. Sheldrick, G. M., *Acta Crystallogr. A* **2008**, 64, 112-122.
123. Cromer, D. T., *Int. Tables X-Ray Crystallogr.* **1974**, 4, 71-147.
124. Alexander, V., *Chem. Rev.* **1995**, 95, 273.
125. Caltagirone, C.; Gale, P. A., *Chem. Soc. Rev.* **2009**, 38, 520-563.
126. Collinson, S. R.; Fenton, D. E., *Coord. Chem. Rev.* **1996**, 148, 19-40.
127. Draho, B. S.; Kotek, J.; Hermann, P.; Like, I.; Toth, E., *Inorg. Chem.* **2010**, 49, 3224-3238.
128. Fenton, D. E., *Appl. Chem.* **1986**, 58, 1437.
129. Fenton, D. E.; Okawa, H., *Chem. Berl.* **1997**, 130, 433.
130. Vigato, P. A.; Tamburini, S.; Bertolo, L., *Coord. Chem. Rev.* **2007**, 251, 1311-1492.
131. Brooker, S., *Coord. Chem. Rev.* **2001**, 222, 33-56.
132. Martell, A. E.; Penitka, J.; Kong, D., *Coord. Chem. Rev.* **2001**, 216-217, 55-63.
133. Nelson, J. V.; McKee, G. M., *Progress in Inorganic Chemistry*. JohnWiley&Sons: New York, 1998; Vol. 47.
134. Nelson, S. M., *Pure & Appl. Chem.* **1980**, 52, 461 - 2476.
135. Costas, M.; Ribas, X.; Poater, A.; Valbuena, J. M. L.; Xifra, R.; Company, A.; Duran, M.; Sola, M.; Llobet, A.; Uson, M. A.; Mahia, J.; Solans, X.; Shan, X.; Benet-Buchholz, J., *Inorg. Chem.* **2006**, 45, 3569-3581.
136. Brooker, S.; McKee, V.; Shepard, W. B.; Pannell, L. K., *Dalton Trans.* **1987**, 11, 2555-2562.
137. Fenton, D. E.; Kitchen, S. J.; Spencer, C. M.; Tamburini, S.; Vigato, P. A., *Dalton Trans.* **1988**, 685-690.
138. Aspinall, H. C.; Moore, S. R.; Smith, A. K., *Dalton Trans.* **1993**, 709-714.
139. Brooker, S.; Kelly, R. J.; Sheldrick, G. M., *Chem. Commun.* **1994**, 487-488.
140. Tandon, S. S.; Thompson, L. K.; Bridson, J. N.; Benelli, C., *Inorg. Chem.* **1995**, 34, 5507-5515.
141. Brooker, S.; McKee, V.; Metcalfe, T., *Inorg. Chim. Acta* **1996**, 246, 171-179.
142. Givaja, G.; Blake, A. J.; Wilson, C.; Schröder, M.; Love, J. B., *Chem. Commun.* **2005**, 4423-4425.
143. Lui_Ma, C. T.; MacLachlan, M. J., *Angew. Chem Int. Ed.* **2005**, 44, 4178-4182.
144. Gallant, A. J.; Hui, J. K.-H.; Zahariev, F. E.; Wang, Y. A.; MacLachlan, M. J., *Org. Chem.* **2005**, 70, 7936-7946.
145. Radecka-Paryzek, W.; Patroniak, V.; Lisowski, J., *Coord. Chem. Rev.* **2005**, 249, 2156-2175.
146. Nabeshima, T.; Miyazaki, H.; Iwasaki, A.; Akine, S.; Saiki, T.; Ikeda, C., *Tetrahedron* **2007**, 63, 3328-3333.

147. Ikeda, C.; Sakamoto, N.; Nabeshima, T., *Organic Letters* **2008**, *10*, 4601-4604.
148. Akine, S.; Nabeshima, T., *Dalton Trans.* **2009**, 10395-10408.
149. Anda, C.; Llobet, A.; Salvado, V.; Motekaitis, R.; Riebenspies, J.; Martell, A. E., *Inorg. Chem.* **2000**, *39*, 2986-2999.
150. Anda, C.; Llobet, A.; Martell, A. E.; Donnadieu, B.; Parella, T., *Inorg. Chem.* **2003**, *42*, 8545-8550.
151. Anda, C.; Llobet, A.; Martell, A. E.; Riebenspies, J.; Solans, X., *Inorg. Chem.* **2004**, *43*, 2793-2802.
152. Anda, C.; Llobet, A.; Salvado, V.; Motekaitis, R.; Martell, A. E., *Inorg. Chem.* **2000**, *39*, 3000-3008.
153. Arbuse, A.; Anda, C.; Martínez, M. A.; Perez-Mirón, J.; Jaime, C.; Parella, T.; Llobet, A., *Inorg. Chem.* **2007**, *46*, 10632 -10638.
154. Costas, M.; Sola, M.; Robles, J.; Xifra, R.; Llobet, A.; Parelle, T.; Stoeckli-Evans, H.; Neuburger, M., *Inorg. Chem.* **2003**, *42*, 4456-4468.
155. Wenzel, M.; Bruere, S. R.; Knapp, Q. W.; Tasker, P. A.; Plieger, P. G., *Dalton Trans.* **2010**, *39*, 2936-2941.
156. Llobet, A.; Martell, A. E.; Martínez, M. A., *J. Mol. Cat. A: Chem.* **1998**, *129*, 19-26.
157. Poater, A.; Ribas, X.; Cavallo, L.; Llobet, A.; Sola, M., *J. Am. Chem. Soc.* **2008**, *130*, 17710-1771.
158. Company, A.; Jee, J. E.; Ribas, X.; Lopez-Valbuena, J. M.; Gomez, L.; Llobet, A.; Mahia, J.; Benet-Buchholz, J.; Eldik, R. v., *Inorg. Chem.* **2007**, *46*, 9098-9110.
159. Dioury, F.; Sylvestre, I.; Siaugue, J.-M.; Wintgens, V.; Ferroud, F.; Favre-Reguillon, A.; Foos, J.; Guy, A., *Eur. J. Org. Chem.* **2004**, 4424-4436.
160. Ngwenya, M. P.; Chen, D.; Martell, A. E.; Reibenspies, J. H., *Inorg. Chem.* **1991**, *30*, 2732-2736.
161. Ngwenya, M. P.; Martell, A. E.; Reibenspies, J. H., *Chem. Commun.* **1990**, 1207-1208.
162. Becker, M.; Schindler, S.; Eldik, R. v., *Inorg. Chem.* **1994**, *33*, 5370-5371.
163. Ma, H.; Allmendinger, M.; Thewalt, U.; Lentz, A.; Klinga, M.; Rieger, B., *Eur. J. Inorg. Chem.* **2002**, 2857-2867.
164. Menif, R.; Martell, A. E.; Squattrito, P. J.; Clearfield, A., *Inorg. Chem.* **1990**, *29*, 4723-4729.
165. Utz, D.; Heinemann, F. W.; Hampel, F.; Richens, D. T.; Schindler, S., *Inorg. Chem.* **2003**, *42*, 1430-1436.
166. Claus, H.; Decker, H., *Syst. Appl. Microbiol.* **2006**, *29*, 3-14.
167. Fusi, V.; Llobet, A.; Mahía, J.; Micheloni, M.; Paoli, P.; Ribas, X.; Rossi, P., *Eur. J. Inorg. Chem.* **2002**, *4*, 987-990.
168. Vigato, P. A.; Tamburini, S., *Coord. Chem. Rev.* **2004**, *248*, 1717-2128.
169. Hutin, M.; Bernardinelli, G.; Nitschke, J. R., *Proc. Nat. Acad. Sci.* **2006**, *103*, 17655-17660.
170. Veauthier, J. M.; Tomat, E.; Lynch, V. M.; Sessler, J. L.; Mirsaidov, U.; Markert, J. T., *Inorg. Chem.* **2005**, *44*, 6736-6743.
171. Utz, D.; Kisslinger, S.; Hampel, F.; Schindler, S., *J. Inorg. Biochem.* **2008**, *102*, 1236-1245.
172. Song, B.; Reuber, J.; Ochs, C.; Hahn, F. E.; Lügger, T.; Orvig, C., *Inorg. Chem.* **2001**, *40*, 1527-1535.
173. Sheldrick, G. M. *Program for Crystal Structure Refinement, Universität Göttingen, Bruker Advanced X-ray Solutions. SHELXTL Version 6.14*, 2000-2003: 1997.
174. Spek, A. L. *PLATON, A Multipurpose Crystallographic Tool*, Utrecht University, Utrecht, The Netherlands: 2005.
175. Garcia-Borron, J. C.; Solano, F., *Pigment Cell Res.* **2002**, *15*, 162-173.
176. Karlin, K. D.; Tyeklár, Z., *Bioinorganic Chemistry of Copper*. Chapman & Hall, Inc.: New York, London, 1993.
177. Marusek, C. M.; Trobaugh, N. M.; Flurkey, W. H.; Inlow, J. K., *J. Inorg. Biochem.* **2006**, *100*, 108-123.
178. Sánchez-Ferrer, A.; Rodríguez-López, J. N.; García-Cánovas, F.; García-Carmona, F., *Biochim. Biophys. Acta* **1995**, *1247*, 1-11.
179. Solomon, E. I.; Chen, P.; Metz, M.; Lee, S.-K.; Palmer, A. E., *Angew. Chem., Int. Ed.* **2001**, *40*, 4570-4590.

180. Wang, N.; Hebert, D. N., *Pigm. Cell Res.* **2006**, *19*, 3-18.
181. Battaini, G.; Casella, L.; Gullotti, M.; Monzani, E.; Nardin, G.; Perotti, A.; Randaccio, L.; Santagostini, L.; Heinemann, F. W.; Schindler, S., *Eur. J. Inorg. Chem.* **2003**, 1197-1205.
182. Casella, L.; Gulotti, M.; Pallanza, G.; Rigoni, L., *J. Am. Chem. Soc.* **1988**, *110*, 4221-4227.
183. Casella, L.; Gulotti, M.; Partosek, M.; Pallanza, G.; Lauretini, E., *J. Chem Soc., Chem. Commun.* **1991**, 1235-1237.
184. Cruse, R. W.; Kaderli, S.; Karlin, K. D.; Zuberbühler, A. D., *J. Am. Chem. Soc.* **1988**, *110*, 6882-6883.
185. Gelling, O. J.; Meetsma, A.; Bolhuis, F. v.; Feringa, B. L., *J. Chem Soc., Chem. Commun.* **1988**, 552-554.
186. Gosh, D.; Mukherjee, R., *Inorg. Chem.* **1998**, *37*, 6597-6605.
187. Karlin, K. D.; Hayes, J. C.; Gultneh, Y.; Cruse, R. W.; McKnown, J. W.; Hutchinson, J. P.; Zubieta, J., *J. Am. Chem. Soc.* **1984**, *106*, 2121-2139.
188. Karlin, K. D.; Nasir, M. S.; Cohen, B. I.; Cruse, R. W.; Kaderli, S.; Zuberbühler, A. D., *J. Am. Chem. Soc.* **1994**, *116*, 1324-1336.
189. Li, L.; Sarjeant, A. N.; Karlin, K. D., *Inorg. Chem.* **2006**, *45*, 7160-7172.
190. Mandal, S.; Mukherjee, R., *Inorg. Chim. Acta* **2006**, *359*, 4019-4026.
191. Nasir, M. S.; Karlin, K. D.; McGowty, D.; Zubieta, J., *J. Am. Chem. Soc.* **1991**, *113*, 698-701.
192. Palavicini, S.; Granata, A.; Monzani, E.; Casella, L., *J. Am. Chem. Soc.* **2005**, *127*, 18031-18036.
193. Sander, O.; Henß, A.; Näther, C.; Würtele, C.; Holthausen, M. C.; Schindler, S.; Tucek, F., *Chem. Eur. J.* **2008**, *14*, 9714 – 9729.
194. Menif, R.; Martell, A. E., *J. Chem Soc., Chem. Commun.* **1989**, 1521-1523.
195. Company, A.; Gómez, L.; Mas-Balleste, R. n.; Korendovych, I. V.; Ribas, X.; Poater, A.; Parella, T.; Fontrodona, X.; Benet-Buchholz, J.; Sola, M.; Lawrence Que, J.; Rybak-Akimova, E. V.; Costas, M., *Inorg. Chem.* **2007**, *46*, 4997-5012.
196. Poater, A., *J. Phys. Chem. A* **2009**, *113*, 9030-9040.
197. Adams, H.; Bailey, N. A.; Fenton, D. E.; Hempstead, P. D.; Westwood, G. P., *J. Incl. Phenom. Mol. Rec.* **1991**, *11*, 63-69.
198. Childs, L. J.; Alock, N. W.; Hannon, M. J., *Angew. Chem. Int. Ed.* **2001**, *40*, 1079-1080.
199. Comba, P.; Fath, A.; Hambley, T. W.; Reichens, D. T., *Angew. Chem. Int. Ed.* **1995**, *34*, 1883-1884.
200. Solanki, N. K.; Wheatley, A. E. H.; Radojevic, S.; McPartlin, M.; Halcrow, M. A., *Dalton Trans.* **1999**, 521-523.
201. Hanton, L. R.; Lee, K., *J. Chem. Soc., Dalton Trans.* **2000**, 1161-1166.
202. Sharma, C. V. K.; Griffin, S. T.; Rogers, R. D., *Chem. Commun.* **1998**, 215-216.
203. Withersby, M. A.; Blake, A. J.; Champness, N. R.; Hubberstey, P.; Li, W. S.; Schroder, M., *Angew. Chem. Int. Ed.* **1997**, *36*, 2327-2329.
204. Hasenkopf, B.; Lehn, J.-M.; Boumediene, N.; Dupont-Gervais, A.; Dorsselaer, A. v.; Kneisel, B.; Fenske, D., *J. Am. Chem. Soc.* **1997**, *119*, 10956-10962.
205. Hannon, M. J.; Painting, C. L.; Plummer, E. A.; Childs, L. J.; Alcock, N. W., *Chem. Eur. J.* **2002**, *8*, 2225-2238.
206. Schiessl, W.; Puchta, R.; Bugarcic, Z. D.; Heinemann, F. W.; Eldik, R. v., *Eur. J. Inorg. Chem.* **2007**, 1390-1404.
207. Pots, K. T.; Keshavarz-K, M.; Tham, F. S.; Abruna, H. D.; Arana, C., *Inorg. Chem.* **1993**, *32*, 4450-4456.
208. Balasubramanian, R.; Smith, S. M.; Rawat, S.; Yatsunyk, L. A.; Stemmler, T. L.; Rosenzweig, A. C., *Nature* **2010**, *465*, 115-U131.
209. Woertinka, J. S.; Smeetsa, P. J.; Groothaert, M. H.; Vancea, M. A.; Selsb, B. F.; Schoonheydt, R. A.; Solomon, E. I., *PNAS* **2009**, *106*, 18908-18913.
210. Himes, R. A.; Karlin, K. D., *PNAS* **2009**, *106*, 1877-1878.
211. Karlin, K. D.; Gultneh, Y.; Hayes, J. C.; Zubieta, J., *Inorg. Chem.* **1984**, *23*, 519-521.
212. Holland, P. L.; Rodgers, K. R.; Tolman, W. B., *Angew. Chem. Int. Ed.* **1999**, *38*, 1139-1142.

213. Itoh, S.; Fukuzumi, S., *Bull. Chem. Soc. Jpn.* **2002**, 75, 2081-2095.
214. Taki, M.; Teramae, S.; Nagamoto, S.; Tachi, Y.; Kitagawa, T.; Itoh, S.; Fukuzumi, S., *J. Am. Chem. Soc.* **2002**, 124, 6367-6377.
215. Ryan, S.; Adams, H.; Fenton, D. E.; Becker, M.; Schindler, S., *Inorg. Chem.* **1998**, 37, 2134-2140.
216. Scafani, J. A.; Maranto, M. T.; Sisk, T. M.; Armin, S. A. v., *J. Org. Chem.* **1996**, 61, 3221-3222.
217. Astner, J.; Weitzer, M.; Foxon, S. P.; Schindler, S.; Heinemann, F. W.; Mukherjee, J.; Gupta, R.; Mahadevan, V.; Mukherjee, R., *Inorg. Chim. Acta* **2007**, 361, 279-292.
218. Gentshev, P.; Feldmann, A. A.; Lüken, M.; Möller, N.; Sirges, H.; Krebs, B., *Inorg. Chem. Commun.* **2002**, 5, 64-66.
219. Kani, Y.; Ohba, S.; Ito, S.; Nishida, Y., *Acta Cryst., Sect. C: Cryst. Struct. Commun.* **2000**, 56, e195-e195.
220. Karlin, K. D.; McKnown, J. W.; Hayes, J. C.; Hutchinson, J. P.; Zubieta, J., *Trans. Met. Chem.* **1984**, 9, 405-406.
221. Blessing, R. H., *Acta Cryst.* **1995**, A51, 33-38.
222. Kahn, O.; Launay, J. P., *Chemtronics*. 1988; Vol. 3, p 140-151.
223. Salmon, L.; Donnadiou, B.; Bousseksou, A.; Tuchagues, J.-P., *Acad. Sci. Ser. II c* **1999**, 305-309.
224. Bernarding, J.; Buntkowski, G.; Macholl, S.; Hartwig, S.; Burghoff, M.; Trams, L., *J. Am. Chem. Soc.* **2006**, 128, 714-715.
225. Goodwin, H. A., *Top. Curr. Chem.* **2004**, 233, 59-90.
226. Hauser, A., *Adv. Polym. Sci.* **2004**, 233, 49-58.
227. Koningsbruggen, P. J. v.; Maeda, Y.; Oshio, H., *Top. Curr. Chem.* **2004**, 233, 259-324.
228. Murray, K. S.; Kepert, C. J., *Top. Curr. Chem.* **2004**, 233, 195-228.
229. Paulsen, H.; Grünstreudel, H.; Meyer-Klaucke, W.; Gerdan, M.; Grünstreudel, H. F.; Chaumakov, A. I.; Rüffer, R.; Winkler, H.; Toftlund, H.; Trautwein, A. X., *Eur. Phys. J. B* **2001**, 23, 463-472.
230. Renz, F.; Oshio, H.; Ksenofontov, V.; Waldeck, M.; Spiering, H.; Gütlich, P., *Angew. Chem. Int. Ed.* **2000**, 39, 3699-3700.
231. Sato, O.; Tao, J.; Zhang, Y.-Z., *Angew. Chem. Int. Ed.* **2007**, 46, 2152-2187.
232. Toftlund, H.; McGarvey, J. J., *Top. Curr. Chem.* **2004**, 233, 151-166.
233. Paulsen, H.; Grünstreudel, H.; Meyer-Klaucke, W.; Gerdan, M.; Grünstreudel, H. F.; Chaumakov, A. I.; Rüffer, R.; Winkler, H.; Toftlund, H.; Trautwein, A. X., *Eur. Phys. J. B* **2001**, 23, 463-472.
234. Wei, R.-J.; Li, B.; Tao, J.; Huang, R.-B.; Zheng, L.-S.; Zheng, Z., *Inorg. Chem.* **2010**, *Inorg. Chem.* **2011**, 50, 1170-1172.
235. Mandel, J.; Douglas, B., *Inorg. Chim. Acta* **1989**, 155, 55-69.
236. Gütlich, P., *Struct. Bonding* **1981**, 44, 83-195.
237. Baker, W. A.; Long, G. J., *Chem. Commun.* **1965**, 15, 368-369.
238. Herber, R.; Casson, L. M., *Inorg. Chem.* **1986**, 25, 847-852.
239. Herber, R. H., *Inorg. Chem.* **1987**, 26, 173-178.
240. König, E., *Coord. Chem. Revs.* **1968**, 3, 471-495.
241. König, E.; Majeda, K., *Spectrochim. Acta A* **1967**, 23A, 45-54.
242. Ericson, N. E.; Sutton, N., *Inorg. Chem.* **1966**, 5, 1834-1835.
243. Kempf, N.; Wortmann, R.; Hoppe, T.; Beitat, A.; Bienemann, O.; Herres-Pawlis, S.; Würtele, C., manuscript in preparation. In.
244. CrysAlisPro Oxford Diffraction Ltd., Version 1.171.33.66
245. Sheldrick, G. M. *SHELXS-97, Crystal Structure Solution*, University of Göttingen, Germany: 1990.
246. Sheldrick, G. M. *SHELXL-97, Crystal Structure Refinement*, University of Göttingen, Germany: 1997.
247. Højland, F.; Toftlund, H.; Yde-Andersen, S., *Acta Chem. Scand. A* **1983**, 37, 251-257.
248. Toftlund, H.; Pedersen, E.; Yde-Andersen, S., *Acta Chem. Scand. A* **1984**, 38, 693-697.
249. Gütlich, P., In *Mossbauer Spectroscopy Applied to Inorganic Chemistry*, Long, G. J., Ed. Plenum Press: New York, 1984; Vol. 1.
250. Gütlich, P.; Goodwin, H., *Topics in Current Chemistry Volumes 233 – 235*. Springer Verlag: Heidelberg, 2004.

251. Krüger, H.-J., *Coord. Chem. Rev.* **2009**, 2450-2459.
252. Halcrow, M. A., *Polyhedron* **2007**, 26, 3523–3576.
253. Arcis-Castillo, Z.; Zheng, S.; Siegler, M. A.; Roubeau, O.; Bedoui, S.; Bonnet, S., *Chem. Eur. J.* **2011**, 17, 14826–14836.
254. Gamez, P.; Costa, J. e. S.; Quesadaa, M.; Aromí, G., *Dalton Trans.* **2009**, 7845–7853.
255. Löw, P.; Kim, B.; Takama, N.; Bergaud, C., *Small* **2008**, 4, 908–914.
256. Šalitroš, I.; Madhu, N. T.; Bocă, R.; Pavlik, J.; Ruben, M., *Monatsh Chem* **2009**, 140, 695–733.
257. Bousseksou, A.; Molnár, G. b.; Salmon, L.; Nicolazzi, W., *Chem. Soc. Rev.* **2011**, 40, 3313–3335.
258. Kisslinger, S.; Kelm, H.; Beitat, A.; Würtele, C.; Krüger, H.-J.; Schindler, S., *Inorg. Chim. Acta* **2011**, 374, 540-545.
259. Miyazaki, Y.; Nakamoto, T.; Ikeuchi, S.; Saito, K.; Inaba, A.; Sorai, M.; Tojo, T.; Atake, T.; Matouzenko, G. S.; Zein, S.; Borshch, S. A., *J. Phys. Chem. B* **2007**, 111, 12508-12517.
260. Chansou, B.; Salmon, L.; Bousseksou, A.; Tuchagues, J.-P.; Hazell, A.; Toftlund, H., Hydrogen-Bond Interaction Versus p-Stacking: Effect on the Spin -Crossover Phenomenon Illustrated by the Crystal Structures of Four New Phases of [Fe(tpa)(NCS)₂] (tpa=tris(2-pyridylmethyl)amine). In p 20.
261. Chiou, Y.-M.; L. Que, J., *Inorg. Chem.* **1995**, 117, 3999-4013.
262. Zang, Y.; L. Que, J., *Inorg. Chem.* **1995**, 34, 1030-1035.
263. Guionneau, P.; Gac, F. L.; Kaiba, A.; Costa, J. S.; Chasseau, D.; Létard, J.-F., *Chem. Commun.* **2007**, 3723-3725.
264. Ménage, S.; Zang, Y.; Hendrich, M. P.; L. Que, J., *J. Am. Chem. Soc.* **1992**, 114, 7786-7792.
265. Gallois, B.; Real, J.-A.; Hauw, C.; Zerembowitch, J., *Inorg. Chem.* **1990**, 29, 1152-1158.
266. Gultneh, Y.; Yisgedu, T. B.; Tesema, Y. T.; Butcher, R. J., *Inorg. Chem.* **2003**, 42, 1857-1867.
267. Canary, J. W.; Wang, Y.; Jr., R. R.; Jr., L. Q.; Miyake, H., *Inorg. Synth.* **1998**, 32, 70-74.
268. Dietrich, J.; Heinemann, F. W.; Schrod, A.; Schindler, S., *Inorg. Chim. Acta* **1999**, 288, 206-209.
269. Murthy, N. N.; Ghosh, P.; Chen, Q.; Zubieta, J.; Karlin, K. D., *Inorg. Chem.* **2001**, 40, 2312-2322.
270. McKenzie, E., *Coord. Chem. Rev.* **1971**, 6, 187-216.
271. Carbonera, C.; Kilner, C. A.; Létarda, J.-F.; Halcrow, M. A., *Dalton Trans.* **2007**, 1284-1292.
272. Weber, B.; Kaps, E.; Weigand, J.; Carbonera, C.; Létard, J.-F.; Achterhold, K.; Parak, F. G., *Inorg. Chem.* **2008**, 47, 487-496.
273. Grünsteudel, H.; Paulsen, H.; Meyer-Klaucke, W.; Winkler, H.; Trautwein, A. X.; Grünsteudel, H. F.; Baron, A. Q. R.; Chumakov, A. I.; Rüffer, R.; Toftlund, H., *Hyperfine Interactions* **1998**, 113, 311–317.
274. Gülich, P.; Garcia, Y.; Goodwin, H. A., *Chem. Soc. Rev.* **2000**, 29, 419-427.
275. Grünsteudel, H.; Paulsen, H.; A.X.Trautwein; Toftlund, H., *Hyperfine Interactions* **1999**, 123/124, 841-846.
276. Yu, Z.; Hsia, Y. F.; You, X. Z.; Spering, H.; Gülich, P., *J. Mat. Sci.* **1997**, 32, 6579-6581.
277. Kondo, M.; Yoshizawa, K., *Chem. Phys. Lett.* **2003**, 372, 519–523.
278. Renz, H.; Spiering, H.; Goodwin, P.; Gülich, P., *Hyperfine Interactions* **2000**, 126, 155-158.
279. Oshio, H.; Spiering, H.; Ksenofontov, V.; Renz, F.; Gülich, P., *Inorg. Chem.* **2001**, 40, 1143-1150.
280. Hatfield, W. E., *Theory and Application of Molecular Paramagnetism*. Wiley and Sons: New York, 1976; p 491-495.
281. XSCAnS, 2.31; Bruker Analytical Instruments: 1999.
282. Britovsek, G. J. P.; England, J.; White, A. J. P., *Dalton Trans.* **2006**, 1399–1408.
283. Konno, M.; Mikadi-Kido, M., *Bull. Chem. Soc. Jpn.* **1991**, 64, 339-345.
284. Costa, J. S.; Lappalainen, K.; Ruiter, G. d.; Quesada, M.; Tang, J.; Mutikainen, I.; Turpeinen, U.; Grunert, C. M.; Gülich, P.; Lazar, H. Z.; Létard, J.-F.; Gamez, P.; Reedijk, J., *Inorg. Chem.* **2007**, 46, 4079-4089.
285. Bonnet, S.; Siegler, M. A.; Costa, J. S.; Molnár, G.; Bousseksou, A.; Spek, A. L.; Gameza, P.; Reedijk, J., *Chem. Commun.* **2008**, 5619–5621.